Modelleren van de hepatische perfusie van macro- tot microniveau ter ondersteuning van levertransplantatie

Multi-Level Modelling of Hepatic Perfusion in Support of Liver Transplantation Strategies

Charlotte Debbaut

Promotoren: prof. dr. ir. P. Segers, prof. dr. D. Monbaliu
Proefschrift ingediend tot het behalen van de graad van
Doctor in de Ingenieurswetenschappen: Biomedische Ingenieurstechnieken

Vakgroep Civiele Techniek
Voorzitter: prof. dr. ir. P. Troch
Faculteit Ingenieurswetenschappen en Architectuur
Academiejaar 2012 - 2013

UNIVERSITEIT GENT

ISBN 978-90-8578-626-9
NUR 954
Wettelijk depot: D/2013/10.500/59

Supervisors:

Prof. dr. ir. Patrick Segers
Prof. dr. Diethard Monbaliu

Research lab:

Institute Biomedical Technology
Biofluid, Tissue and Solid Mechanics for Medical Applications (bioMMeda)
Ghent University
De Pintelaan 185 - Blok B
B–9000 Gent
Belgium

Members of the exam committee:

Chairman:	
Prof. dr. ir. Jan Van Campenhout	Faculty of Engineering and Architecture, UGent
Secretary:	
Prof. dr. ir. Pascal Verdonck	Faculty of Engineering and Architecture, UGent
Reading committee:	
Dr. ir. Irène Vignon-Clementel	INRIA Paris Rocquencourt, France
Prof. dr. ir. Gerardo Catapano	University of Calabria, Italy
Prof. dr. ir. Jan Vierendeels	Faculty of Engineering and Architecture, UGent
Other members:	
Prof. dr. ir. Piet Claus	Faculty of Medicine, KULeuven
Prof. dr. ir. Sunny Eloot	Faculty of Medicine and Health Science, UGent
Dr. ir. Abigail Swillens	Faculty of Engineering and Architecture, UGent
Prof. dr. ir. Patrick Segers	Faculty of Engineering and Architecture, UGent
Prof. dr. Diethard Monbaliu	Faculty of Medicine, KULeuven

This research was funded by a research grant of the Agency for Innovation by Science and Technology in Flanders (IWT/101115).

Ode to the liver

There, inside,
you filter and apportion,
you separate and divide,
you multiply and lubricate,
you raise and gather
the threads and the grams of life,
the final distillate,
the intimate essences.

From you I hope for justice,
I love life.
Do not betray me!
Work on!
Do not arrest my song.

Pablo Neruda
(Translated by Oriana Josseau Kalant)

Preface

Taking a look back

At the end of this PhD, I would like to stand still for a moment and take a look back at the past four years. The course of a PhD is like an adventurous journey. At the start, you don't know exactly where the journey will lead you or where the scientific adventure will guide you. Along the way, however, you meet a lot of people. Some of them guide and join you on your trip, while others give you advice on which road to take, where to stop or what to do. In this respect, I would like to share with you the most important and inspiring people I met on my journey and acknowledge them for their contributions.

A 4-year scientific adventure

First and foremost, I would like to thank my promotor, prof. dr. ir. Patrick Segers, for giving me the opportunity to start as a PhD student at bioMMeda. Although Patrick has a busy agenda, the door of his office was always open. I always felt welcome when I knocked on his door to ask or discuss something. I really appreciated his enthusiasm, motivating words and enormous scientific insights and expertise. In the end, I have an enormous respect for Patrick and, honestly, cannot think of a better promotor. Patrick, thank you for guiding me on my 4-year trip towards this dissertation.

Being a biomedical engineer, it was extremely enriching to collaborate with medical doctors. In that respect, I would like to thank my copromotor, prof. dr. Diethard Monbaliu, for submerging me in the topics of liver transplantation and preservation, for the interesting discussions and his enormous enthusiasm. Similar to some parts of the journey being rather difficult to predict, the moment at which a human liver becomes available for research is highly unpredictable. Therefore, I would like to dedicate a special thank you to Diethard and his team for all logistical arrangements and support enabling the human liver perfusion experiments.

While digging deep in a PhD research topic, one may lose touch with the research that is going on outside. However, I was able to join the Belgian National Committee on Biomedical Engineering as a youngster member, which allowed me to zoom out to the larger picture capturing biomedical research at national level. Hence, I would like to thank prof. dr. ir. Pascal Verdonck for this opportunity.

As none of this journey would have been possible without financial support, I also want to thank the Agency for Innovation by Science and Technology (IWT) for funding this project by a doctoral grant Strategic Basic Research.

Meeting people along the way

Next, I would like to thank all other people with whom I had the pleasure to collaborate and who joined me during part of my trip.

I would like to thank Organ Recovery Systems for the liver perfusion machine they supplied, and especially Bert for the technical assistance. Jurgen, thank you for your technical support during a number of long days to perform all required perfusion measurements. Pieter, Christophe and other colleagues at the Department of Morphology, thank you for the vascular corrosion casting and for adjusting your agenda at the moment that a human liver was available, even on days like 'Sinterklaas'. Denis, Manuel and other colleagues at the UGCT, thank you for performing the challenging micro-CT scans of our liver casts. Jan, Jennifer and Rodolfo, thank you for the interesting discussions on how to optimise the liver microcirculation models. Ye-Dong, thank you for the interesting discussions on the impact of partial hepatectomy procedures. Benedict, thank you for the support concerning the bumper cluster. Prof. em. Valeer Desmet, thank you for your input on how to interpret our data on the human liver (micro)vascular architecture. David, Geert, Alexandre, Laurent and Nathan, thank you for your interesting master theses.

Furthermore, I thank my previous and current office mates (Abigail, Benjamin, Bram, Francisco, Geert, Joris, Nic, Paula, Sebastian, Thomas & Tom) for joining me along the way, for the pleasant atmosphere and for the nice conversations. Additionally, I would like to thank all other colleagues and ex-colleagues for their support: Alessandra, Annette, Ayfer, Daniel, Danilo, Darya, David, Dieter, Francesco, Frederic, Gianluca, Guillermo, Guivey, Iris, Jan, Koen, Liesbeth, Luis, Lynn, Margo, Mathias, Matthieu, Michele, Peter, Sofie, Sander, Tim, Tomas & Wouter. Additionally, I would like to dedicate a special thank you to Saskia for all administrative and practical arrangements.

At some point during the trip, you might decide to change directions and go looking elsewhere to learn new things and come back with a bunch of new ideas. Therefore, I want to thank everybody who made it possible for me to go to Toronto (Canada) for an internship. John and all other colleagues at MICe, thank you for all the advice and interesting discussions. David, Dolores and Luc, thank you for the warm welcome and your generous hospitality.

Additionally, I thank all the members of the jury for their interest and for reading this dissertation.

The walk of life

On your way called life, you meet lots of people of whom some in particular deserve special attention. Without these supporters, I would probably not have reached the point where I am today.

First of all, I would like to thank my parents and my brother for their unconditional support, for giving me a good foundation on how to handle life, teaching me about right and wrong and about how to persist, while always stimulating what I was going for. Thank you so much for all efforts. By providing me with the necessary luggage, you brought me up to the point where I was able to start a PhD. I also want to thank my grandparents, who - unfortunately - cannot share this moment with us anymore. This brings me to also thank my family and friends, who were always supportive and interested in my research.

Finally, there is one more person that I would like to thank, being the person to whom I'm indebted the most: my husband. Bob, I want to thank you for your unconditional love and support, for your never-ending encouragements, for being my listening ear, for being my soundboard, for just always being there for me, even during difficult times. In this respect, I would like to mention that - in antiquity - the liver was perceived as being the seat of soul, life, intelligence, passion and love, illustrating its importance. Therefore, Bob, instead of saying *"I love you with all my heart!"*, I would like to end by saying: *"I love you with all my liver!"*

Charlotte Debbaut
Gent, September 2013

Samenvatting
Summary

Samenvatting

Inleiding

Het blijvend tekort aan geschikte donorlevers voor transplantatie heeft onderzoekers ertoe aangezet om nieuwe mogelijkheden te zoeken om de donorpool te vergroten. De donorpool bestaat hoofdzakelijk uit overleden donoren en een kleiner aandeel levende donoren. Hoewel er volgens de standaardcriteria gewerkt wordt met hersendode donoren, worden steeds vaker donorlevers gebruikt afkomstig van donoren die overleden aan de gevolgen van circulatoir arrest of van hersendode donoren met contra-indicaties (bijv. leversteatose). Aangezien deze organen gevoeliger zijn aan ischemie-reperfusieschade en koude temperaturen (zoals het geval is bij de huidige gouden standaard van statische koude bewaring) dan organen van standaardcriteria donoren, werd er gezocht naar betere bewaringstechnieken. Bijgevolg kende machineperfusie (MP) gedurende de laatste decennia een snelle opmars als alternatieve bewaringsmethode voor donorlevers met een betere en langere preservatie dan statische koude bewaring. Desondanks zijn de optimale MP-instellingen om beschadiging te voorkomen (bijv. mogelijke beschadiging van de sinusoïdale endotheelcellen) en om homogene perfusie te waarborgen nog niet eenduidig bepaald (vooral voor hypothermische MP; HMP), en wordt MP nog steeds geconfronteerd met een aantal logistieke problemen (vooral bij normothermische MP; NMP). Verder werden ook alternatieve transplantatietechnieken voorgesteld om het orgaantekort te verhelpen, zoals levertransplantaties met levende donoren (LDLT), waarbij een gezonde persoon een deel van zijn lever afstaat aan een patiënt met leverfalen. Helaas lopen deze donoren en ontvangers het risico om complicaties te ontwikkelen zoals het 'small-for-size'-syndroom. Daarnaast is er het aanhoudende debat omtrent de optimale hoeveelheid bij de donor te verwijderen leverweefsel alsook omtrent de resectielocatie. Binnen deze klinische context zouden modellen van de leverperfusie dus ingezet kunnen worden om meer inzicht te verschaffen in de hemodynamische impact van MP alsook van een partiële hepatectomie.

De unieke bouw en de complexe vasculaire architectuur van de lever spelen ongetwijfeld een belangrijke rol in de hierboven aangehaalde proble-

men. Daarom wordt er in deel I eerst een overzicht gegeven van de anatomie, fysiologie, pathologie en transplantatie van de lever, gevolgd door een samenvatting van de beschikbare literatuur omtrent het modelleren van de (perfusie van de) lever. Vervolgens focussen deel II en deel III op het onderzoek dat binnen dit doctoraat uitgevoerd werd. Deel II bespreekt hoe een stromingsmodel van de globale leverperfusie ontwikkeld werd om de interne hepatische stromingspatronen te bestuderen, bijv. tijdens MP. Aangezien de microcirculatie een sleutelrol speelt bij leverbeschadiging, handelt deel III over het ontrafelen en modelleren van de perfusie-eigenschappen van de hepatische microcirculatie. Tenslotte worden in deel IV de belangrijkste conclusies en toekomstperspectieven opgelijst. Hieronder wordt de inhoud van ieder hoofdstuk kort samengevat.

Deel I. De lever: van anatomie tot model

Hoofdstuk 1. Anatomie en fysiologie van de lever

Hoofdstuk 1 geeft een overzicht van de macro- en microscopische anatomie van de lever met de focus op de unieke vasculaire architectuur van de lever. Zo is de lever voorzien van twee afferente vatensystemen (de hepatisch arteriële (HA) en de portaal veneuze (PV) vaatboom) en één efferent vatensysteem (de hepatisch veneuze vaatboom (HV)). Op het microscopische niveau bestaat de lever uit leverlobules (opgebouwd uit o.a. hepatocyten), die de sinusoïden (kleinste hepatische bloedvaten afgelijnd door endotheelcellen) bevatten.

Verder worden de belangrijkste leverfuncties aangehaald, zoals de regulerende functies van de lever in de bloedcirculatie, de lymfe- en galproductie, de metabolische rol, detoxificatie, leverregeneratie enz.

Hoofdstuk 2. Pathologie van de lever

Leverpathologieën worden onderverdeeld in hepatocellulaire en cholestatische ziektes. Hepatocellulaire ziektes (bijv. steatose, fibrose, hepatitis en cirrose) zijn de frequentste leverpathologieën en worden gekenmerkt door inflammatie en necrose van de levercellen. Deze ziektes worden vaak gecompliceerd door vasculaire aandoeningen zoals portale hypertensie. Cholestatische ziektes (bijv. cholestasis en biliaire cirrose) duiden op een inhibitie of obstructie van de galafvloei. In een vergevorderd stadium kunnen leverziektes leiden tot leverfalen. In het geval van ongeneeslijke leverziektes is levertransplantatie op dit moment de enige behandeling.

Hoofdstuk 3. Levertransplantatie

De donorpool voor levertransplantatie bevat zowel overleden als levende donoren. Hierbij worden de overleden donoren onderverdeeld in hersendode donoren (standaardcriteria), donoren overleden aan een circulatoir

arrest en hersendode donoren met bijkomende complicaties (bijv. leversteatose of een hoge leeftijd). De transplantatieprocedure start met de identificatie en aanmelding van een donor bij Eurotransplant, gevolgd door de toewijzing van de beschikbare donororganen aan de ontvangers. Vervolgens worden de organen gepreleveerd en getransporteerd om nadien getransplanteerd te worden. Er bestaan verschillende technieken voor levertransplantatie, zoals de standaardtechniek van orthotope levertransplantatie en alternatieve technieken zoals LDLT en gesplitste levertransplantatie. Daarnaast wordt ook een vergelijking gemaakt tussen verschillende preservatietechnieken voor donorlevers, zijnde de gouden standaard van statische koude bewaring en de opnieuw ontdekte MP-techniek.

Vervolgens worden een aantal HMP-experimenten besproken om meer inzicht te verwerven in het perfusiegedrag van geïsoleerde (varkens)levers, en in het bijzonder in de stromingscompetitie tussen de HA and PV. Aangezien dit fenomeen kan leiden tot een onevenwichtige perfusie en de HMP-stabiliteit in gevaar kan brengen, is het essentieel om de determinanten van stromingscompetitie te onderzoeken. Zo werd in deze studie de invloed van HMP-randcondities op het gedrag van de geperfundeerde lever onderzocht. De resultaten toonden aan dat stromingscompetitie kon uitgelokt worden door de HA-druk te verhogen alsook door een obstructie aan te brengen ter hoogte van de hepatische outflow. Deze fenomenen konden gerelateerd worden aan veranderingen van de intrasinusoïdale druk en zouden in rekening moeten gebracht worden bij het ontwerp van HMP-protocollen.

Hoofdstuk 4. Modelleren van de lever

Hoofdstuk 4 geeft een overzicht van de reeds ontwikkelde modellen van de lever (experimentele modellen en computermodellen van de leveranatomie, -perfusie, -mechanica en -functies), die relevant zijn voor dit manuscript. Verschillende technieken en modellen werden eerder aangewend om de hepatische vasculatuur te bestuderen op zowel het macroscopische als het microscopische niveau (bijv. vasculaire afgietsels, classificatie van de vertakkingstopologie gebaseerd op bloedvatengeneraties enz.). Hoewel de vasculaire architectuur reeds het onderwerp was van vele studies, werd er nooit eerder een analyse uitgevoerd van het complete spectrum van bloedvaten gaande van de macrocirculatie tot de microcirculatie van één en dezelfde lever.

Verschillende experimentele diermodellen (gebruikmakende van ratten, muizen, varkens, honden enz.) werden reeds ontwikkeld om de normale alsook verstoorde leverperfusie (bijv. na een partiële hepatectomie, in het geval van cirrose enz.) te karakteriseren, maar hierbij valt op te merken dat diermodellen niet altijd representatief zijn voor de mens. Verder werden ook verschillende computermodellen ontwikkeld om leverperfusie te

simuleren: compartimentele modellen, elektrisch analoge modellen en numerieke vloeistofdynamische (Computational Fluid Dynamics; CFD) modellen.

Naast de levervasculatuur en -perfusie werden ook andere aspecten van de lever gemodelleerd. Zo werd de mechanica van leverweefsel reeds experimenteel (bijv. trek- en compressietesten) alsook numeriek bestudeerd (bijv. poroviscoelastische materiaalmodellen). Verder focusten verschillende studies op het modelleren van leverfuncties zoals het verwijderen van chemicaliën en leverregeneratie.

Deel II. De hepatische macrocirculatie: van experiment tot elektrisch analoog model

Hoofdstuk 5. Analyse van de vasculaire architectuur van de humane lever aan de hand van vasculaire afgietsels en micro-CT beeldvorming

Hoewel een goed inzicht in de hepatische circulatie belangrijk is voor levertransplantatie, -chirurgie en -pathologie, is er nog steeds weinig geweten omtrent de topografische organisatie van de levervasculatuur. Daarom werd in dit hoofdstuk de humane hepatische vasculatuur gematerialiseerd, gevisualiseerd en morfologisch geanalyseerd op verschillende schalen, zijnde de macro- en mesocirculatie.

Een vasculair afgietsel (replica van de bloedvaten) van een humane lever werd verkregen door een simultane injectie van polymeervloeistof in de HA en PV. Een micro-CT-scan van de volledige replica op hoge resolutie (110 µm) liet toe om gedetailleerde data te verzamelen van de macrovasculatuur, zijnde de grootste bloedvaten. Vervolgens werd een sample gedissecteerd (representatief voor de mesocirculatie startende bij bloedvatengeneratie 5; 88 mm x 68 mm x 80 mm) en gescand met een resolutie van 71 µm. Segmentaties en drie-dimensionale (3D) reconstructies maakten het mogelijk om de topologie (volgens de waargenomen vertakkingspatronen en dus niet volgens de anatomische segmentatie) en geometrische eigenschappen van de HA-, PV- en HV-vaatboom te kwantificeren tot op het niveau van de 13e bloedvatengeneratie (stralen varieerden van 13.2 mm tot 80 µm; lengtes van 74.4 mm tot 0.74 mm).

Door de techniek van vasculaire afgietsels te combineren met micro-CT scans konden de vertakkingstopologie en geometrische eigenschappen van de hepatische vasculatuur gekwantificeerd worden aan de hand van een multischaalaanpak.

Hoofdstuk 6. Studie van de humane leverhemodynamica en -perfusie: van vasculaire replica tot elektrisch analoog model

Niettegenstaande HMP gezien wordt als een potentieel betere preservatiemethode (in het bijzonder voor levers afkomstig van donoren overleden aan

een circulatoir arrest of donoren met contra-indicaties zoals steatose) in vergelijking met statische koude bewaring, zijn de optimale perfusieprotocollen momenteel nog niet eenduidig gedefinieerd voor deze niet-fysiologische bewaringsmethode, waarbij hypothermie in se een potentieel probleem vormt. Hierbij worden o.a. de mogelijke beschadiging van de sinusoïdale endotheelcellen en heterogene perfusie gezien als hinderpalen. Daarom werd in dit hoofdstuk een elektrisch analoog model ontwikkeld van de humane hepatische bloedcirculatie om interne druk- en debietverdelingen in de lever te bestuderen tijdens HMP en om verschillende HMP-condities uit te testen. De gedetailleerde geometrische eigenschappen van de hepatisch humane vasculatuur, verkregen in hoofdstuk 5, werden gebruikt om de componenten van het elektrisch model te berekenen.

Het model kon de effecten van drukgestuurde HMP op de leverhemodynamica simuleren en kon observaties zoals stromingscompetitie tussen de HA en PV reproduceren. Onze simulaties tonen verder ook aan dat, gezien vanuit een puur biomechanisch (schuifspanning) standpunt, drukgestuurde HMP met lage drukken niet resulteert in endotheelschade en dat de vloeistofviscositeit geen effect heeft op de schuifspanning die tijdens drukgestuurde HMP heerst ter hoogte van de levermicrovasculatuur. Deze resultaten impliceren een mogelijke toepasbaarheid van deze techniek om perfusiecondities virtueel uit te testen.

Hoofdstuk 7. Validatie en kalibratie van een elektrisch analoog model van de hepatische perfusie op basis van HMP-experimenten

In hoofdstuk 6 werd een elektrisch analoog model ontwikkeld van de humane hepatische perfusie tijdens HMP. Hierbij dienden een aantal veronderstellingen gemaakt te worden als gevolg van enkele ongekende parameters. Om het elektrisch analoog model te toetsen aan experimentele data wordt er in dit hoofdstuk een methodologie toegelicht om het initiële elektrische model (ontwikkeld in hoofdstuk 6) te valideren en te tunen voor een specifieke lever. Een aantal HMP-experimenten werden uitgevoerd om het perfusiegedrag van humane levers te karakteriseren aan de hand van simultane druk- en debietmetingen. De berekening van HA- en PV-ingangsimpedanties liet toe om compacte Windketelmodellen te fitten aan de globale hepatische perfusie-eigenschappen. Vervolgens werden deze globale eigenschappen gebruikt om het leverspecifiek elektrisch analoog model te tunen.

Hoofdstuk 8. Modelleren van de impact van partiële hepatectomie op de hepatische hemodynamica gebruikmakende van een rattenmodel

LDLT biedt een mogelijkheid om de donorpool uit te breiden, maar kan tevens leiden tot het 'small-for-size'-syndroom, waarbij een te klein levervolume als het ware te veel bloedstroming te verwerken krijgt. Aangezien de

hemodynamische effecten van een partiële hepatectomie nog niet volledig duidelijk zijn, ontwikkelden we een elektrisch model van de bloedcirculatie doorheen de rattenlever (gebaseerd op het model van hoofdstuk 6) om de hemodynamica van de normale lever te vergelijken met die van een lever waaruit een deel geresecteerd werd.

Gedetailleerde 3D-reconstructies en geometrische data van de levervasculatuur van twee ratten werden verzameld door vasculaire afgietsels te combineren met micro-CT scans en beeldverwerking. Deze data lieten toe om een druk- en een debietgestuurd elektrisch model te ontwikkelen van de totale rattenlever. Vervolgens werden virtuele resecties uitgevoerd om een 70%, 80% en 90% partiële hepatectomie te modelleren en de impact hiervan op de hemodynamica te voorspellen. De resultaten demonstreerden duidelijke hyperperfusie met portale hypertensie en verhoogde PV-debieten per lob. De vergelijking van twee 90% resectietechnieken demonstreerde verschillen in totale HA-debieten, portale en sinusoïdale drukken, wat mogelijks zou kunnen resulteren in betere overlevingskansen voor lagere portale en sinusoïdale drukken. Naar de toekomst toe kunnen deze nieuwe modellen geëxtrapoleerd worden naar de humane context en kunnen ze mogelijks bijdragen tot een betere planning van partiële hepatectomieën.

Deel III. De hepatische microcirculatie: van visualisatie van de sinusoïdale geometrie tot microschaal-CFD-modellen

Hoofdstuk 9. Perfusiekarakteristieken van de humane hepatische microcirculatie gebruikmakende van 3D-reconstructies en CFD-analyse

De hepatische microcirculatie bezit een unieke en complexe structurele organisatie en is gevoelig voor abnormale omgevingsfactoren (bijv. een verhoogde schuifspanning tijdens HMP of na een partiële hepatectomie). Aangezien de microcirculatie daarenboven een sleutelrol speelt in het proces van leverbeschadiging en aangezien relatief weinig geweten is omtrent de hepatisch microvasculaire hemodynamica, was het aangeraden om de perfusiekarakteristieken van de levermicrocirculatie verder te bestuderen. Hoewel de hepatische microstructuur door vloeistofdynamische modellen tot nu toe vaak geanalyseerd werd als zijnde opgebouwd uit geïdealiseerde functionele eenheden gebaseerd op poreuze media, is uitgebreider onderzoek essentieel om de validiteit van deze aanpak te onderzoeken en om een adequate en kwantitatieve karakterisatie van de levercirculatie toe te laten. In dit hoofdstuk onderzoeken we daarom de perfusiekarakteristieken van de humane levermicrocirculatie.

Een microvasculair staal met drie leverlobules werd gedissecteerd uit de vasculaire replica van een humane lever. Het staal werd vervolgens ingescand met een micro-CT scanner op een resolutie van 2.6 μm. Na de

beeldvorming werd een kubusvolume, gevuld met tortueuze en intergeconnecteerde sinusoïden, uit de 3D-gereconstrueerde beelden geïsoleerd om het vloeistofdomein te definiëren. Aan de hand van deze kubus werden drie computationele vloeistofdynamische (CFD) modellen bestudeerd om de stroming langs drie orthogonale richtingen te simuleren (i.e. parallel aan de centrale vene, radiaal en in de circumferentiële richting van de lobule).

Verwerking van de resultaten liet toe om de perfusiekarakteristieken van de microvasculatuur te visualiseren en te kwantificeren, alsook om de 3D-porositeit en de permeabiliteitstensor met bijhorende permeabiliteitshoofdrichtingen te berekenen. De CFD-simulaties resulteerden o.a. in data over drukverschillen, stroomlijnen en wandschuifspanningen. Deze nieuwe data tonen aan dat de humane hepatische microcirculatie gekarakteriseerd wordt door een hogere permeabiliteit in de richting van de centrale vene, en een ongeveer twee maal kleinere permeabiliteit in de radiale en circumferentiële richting ten opzicht van een lobule. Aangezien de permeabiliteitscoëfficiënten afhangen van de stromingsrichting, zouden (poreuze media) modellen van de levermicrocirculatie deze sinusoïdale anisotropie in rekening moeten brengen.

Hoofdstuk 10. Een 3D poreus medium model van een leverlobule: het belang van vasculaire septa en anisotrope permeabiliteit voor homogene perfusie

Gebruikmakend van de perfusiekarakteristieken verkregen in hoofdstuk 9 ontwikkelden we in dit hoofdstuk een 3D-micromodel van een leverlobule om de rol van vasculaire septa en de invloed van anisotrope permeabiliteiten te onderzoeken. De lobule werd gemodelleerd als een hexagonaal prisma (met of zonder vasculaire septa) en het leverweefsel werd behandeld als een poreus medium (isotrope of anisotrope permeabiliteit). De modellen werden opgelost met CFD.

De inclusie van vasculaire septa resulteerde in een betere perfusie van de zones tussen de portale triades in vergelijking met modellen zonder vasculaire septa, alsook in een spatiaal homogenere perfusie van de lobule. Anisotrope permeabiliteit resulteerde in duidelijk verschillende stromingspatronen met stroomlijnen die, in vergelijking met een isotrope permeabiliteit, een grotere axiale snelheidscomponent hadden. Een parameterstudie toonde aan dat de resultaten het gevoeligst zijn aan de circumferentiële lobulediameter en de radiale drukval. Ons model verschaft inzicht in de hepatische microhemodynamica en suggereert dat vooral de inclusie van vasculaire septa leidt tot perfusiepatronen die de fysiologische werkelijkheid hoogst waarschijnlijk beter benaderen. Verder heeft het model potentieel om ook aangewend te worden voor andere doeleinden zoals de microhemodynamica in niet-fysiologische en pathologische situaties.

Deel IV. Conclusies

Hoofdstuk 11. Conclusies en toekomstperspectieven

Dit hoofdstuk geeft een overzicht van de belangrijkste bevindingen en conclusies van dit manuscript. De hoofdboodschap van dit werk is dat er verschillende modellen (anatomische modellen van de hepatische vasculatuur, elektrisch analoge modellen van de hepatische perfusie en CFD-modellen van de hepatische microcirculatie) ontwikkeld werden om de hepatische perfusie te simuleren op verschillende niveaus (macro-, meso- en microcirculatie). Dit geheel aan modellen werd toegepast binnen het kader van levertransplantatie en resulteerde in unieke morfologische en geometrische data van humane levers en rattenlevers, alsook in nieuwe inzichten in de hemodynamische impact van MP-preservatie en partiële hepatectomieën (bijv. bij LDLT procedures) en in de perfusiekarakteristieken van de hepatische microcirculatie. Op deze manier waren we in staat om een aantal stukjes van de puzzel omtrent leverperfusie te verzamelen. Verder onderzoek (zoals validatie van de micromodellen en het bestuderen van meer levers) is ongetwijfeld nodig om de volledige puzzel op te lossen. De veelzijdige modellen die binnen dit doctoraatswerk ontwikkeld werden, zijn niet enkel toepasbaar voor hemodynamische vraagstukken gerelateerd aan levertransplantatie, maar ook voor leverpathologieën (bijv. cirrose), chirurgische ingrepen (bijv. de Fontanprocedure) enz. Deze laatste zijn slechts enkele voorbeelden van mogelijke toekomstige onderzoeksrichtingen.

Summary

Introduction

The substantial shortage of suitable donor livers for transplantation has forced researchers to investigate possibilities to increase the donor pool. The donor pool contains mainly deceased donors and a smaller amount of living donors. Although the standard criteria donors are donation after brain death donors (DBD), more and more livers from donation after circulatory death donors (DCD) and extended criteria donors (ECD; e.g. liver steatosis) are being used. As DCD and ECD livers are more succeptible to ischaemia-reperfusion injury and cold temperatures (as is the case for the golden standard of static cold storage) than DBD organs, alternative preservation methods were explored. As such, machine perfusion (MP) revived during the last decades and was proposed as an alternative preservation method for donor livers, allowing for better and longer preservation compared to cold storage. However, liver MP encountered some problems (e.g. occasional endothelial cell damage) and the most optimal perfusion settings to prevent microcirculatory damage, while assuring a sufficient homogeneous perfusion, are still unknown (especially for hypothermic MP; HMP). In addition, MP is still confronted with logistical problems (especially for normothermic MP; NMP). Furthermore, alternative transplantation techniques have been suggested to help overcome the organ shortage. In living donor liver transplantation (LDLT) for instance, a healthy person donates part of his liver to a patient with liver failure. Unfortunately, LDLT donors and patients are succeptible to the 'small-for-size' syndrome and the most optimal amount of liver tissue to resect as well as the resection planes are still a matter of debate. Within this clinical context, models of liver perfusion would help to gain more insight into the haemodynamic impact of MP as well as partial hepatectomy procedures.

These open questions are unevitably linked to the unique and complex vascular architecture of the liver. Therefore, part I provides a background overview of liver anatomy, physiology, pathology and transplantation, followed by a summary of previous modelling studies on the liver (perfusion).

Parts II and III focus on the original research performed within the framework of this PhD. Part II deals with the development, validation and application of an electrical analog model of the global liver perfusion, e.g. during MP. As the microcirculation plays a key role in liver damage, part III goes deeper into unraveling and modelling the perfusion characteristics of the hepatic microcirculation. Part IV ends this dissertation by listing the main conclusions and future perspectives. Below, the content of each chapter is briefly summarised.

Part I. The liver: from anatomy to model

Chapter 1. Anatomy and physiology of the liver

Chapter 1 starts by discussing the macro- as well as the microscopic anatomy of the liver with the focus on its unique vascular organisation. The liver has two afferent vessel systems (the hepatic arterial (HA) and the portal venous (PV) tree) and one efferent vessel system (the hepatic venous tree (HV)). At the microscopic level, the liver contains liver lobules (containing a.o. the hepatocytes) including the sinusoids, being the smallest hepatic blood vessels lined by endothelial cells.

In addition, the most important liver functions are addressed, such as the liver's regulatory functions in the blood flow, its lymph and bile production, its metabolic role, detoxification, liver regeneration etc.

Chapter 2. Liver pathology

Liver pathologies are divided in hepatocellular and cholestatic diseases. Hepatocellular diseases (e.g. steatosis, fibrosis, hepatitis and cirrhosis) are the most frequent liver pathologies and are characterised by inflammation and necrosis of liver cells. These diseases are often complicated by hepatic vascular disorders such as portal hypertension. Cholestatic diseases (e.g. cholestasis and biliary cirrhosis) are characterised by an inhibition or obstruction of the bile flow. In an advanced stage, they may lead to end-stage liver failure. In the case of incurable liver diseases, liver transplantation is the only possible treatment at this moment.

Chapter 3. Liver transplantation

The donor pool for liver transplantation contains deceased as well as living donors. Deceased donors are classified in DBD (standard criteria), DCD and ECD donors (with contraindications such as steatosis or advanced age). The transplantation procedure starts with the identification and registration of the donor to Eurotranplant, followed by the allocation of the available donor organs to recipients. Subsequently, the donor organs are prelevated

and transported to be transplanted afterwards. Several types of liver transplantation procedures exist, such as the most frequently applied orthotopic liver transplantation technique and alternative techniques such as LDLT or split liver transplantation. Next, different preservation techniques for donor livers are discussed, comparing static cold storage with the reviving technique of MP.

Furthermore, a set of HMP experiments are presented to gain more knowledge on the perfusion behaviour of isolated (porcine) livers, more specifically in the flow competition between the HA and PV. Since this phenomenon may lead to unbalanced MP and thus affects HMP stability, it is essential to gain more insight into the determinants of flow competition. To this end, we investigated the influence of HMP settings on the isolated liver behaviour. The results showed that flow competition could be evoked by increasing the HA pressure as well as by obstructing the hepatic outflow. These phenomena could be related to intrasinusoidal pressure alterations and should be taken into account for the design of liver HMP protocols.

Chapter 4. Modelling the liver

Chapter 4 lists the previously developed models of the liver (experimental models and computer models of liver anatomy, perfusion, mechanics and function), relevant to the work performed in this manuscript. As such, several techniques and models (vascular corrosion casting, branching topology classifications based on blood vessel generations etc.) have been used to study the hepatic vasculature on both the macroscopic and microscopic scale. Although the hepatic vascular architecture has been the topic of many studies, a vascular analysis of the complete spectrum of blood vessels ranging from the macrocirculation to the microcirculation of one and the same liver has not yet been performed.

Previous studies are almost exclusively based on experimental animal models (using rats, mice, pigs, dogs etc.). These models were developed to assess normal liver perfusion as well as disturbed liver perfusion characteristics (e.g. after a partial hepatectomy, in the case of cirrhosis). Note, however, that animal models are not always representative for humans. Several modelling approaches have been applied to simulate liver perfusion: compartment models, electrical analog models as well as computational fluid dynamics (CFD) models.

Besides the liver vasculature and perfusion, liver mechanics have been studied experimentally (tensile and compression tests etc.) as well as numerically by e.g. poroviscoelastic material models. Finally, the literature overview also briefly adresses studies focussing on modelling liver functions, such as the removal of chemicals and liver regeneration.

Part II. The hepatic macrocirculation: from experiments to electrical analog models

Chapter 5. Analysing the human liver vascular architecture by combining vascular corrosion casting and micro-CT scanning

Though a full understanding of the hepatic circulation is important for liver transplantation, surgery and pathology, relatively little is known about the topographical organisation of the liver vasculature. In this chapter, the human hepatic vasculature was materialised, visualised and morphologically analysed at different scales (being the macro- and mesocirculation).

A unique human liver vascular corrosion cast was obtained by simultaneous resin injection in the HA and PV. A high resolution (110 μm) in globo micro-CT scan of the cast allowed gathering detailed data on the macrovasculature. Subsequently, a sample representing the mesocirculation (starting at blood vessel generation 5; 88 mm by 68 mm by 80 mm) was dissected and imaged at a 71 μm resolution. Segmentations and three-dimensional (3D) reconstructions allowed quantifying the macro- and mesoscale topology (according to the observed branching patterns; not according to the anatomical segments) and geometrical features of the HA, PV and HV trees up to 13 generations (radii ranging from 13.2 mm to 80 μm; lengths from 74.4 mm to 0.74 mm).

Combining vascular corrosion casting and micro-CT imaging allows quantifying the branching topology and geometrical features of the hepatic vasculature by using a multiscale approach.

Chapter 6. From vascular corrosion cast to electrical analog model for the study of human liver haemodynamics and perfusion

While HMP is experiencing a revival in organ preservation (especially for DCD and ECD livers), perfusion protocols are still poorly defined for this non-physiological preservation method, for which hypothermia is a potential problem. Hereby, potential sinusoidal endothelial cell injury and heterogeneous perfusion are concerns. In order to enlighten internal pressure and flow distributions during HMP and test different HMP settings, an electrical model of the human liver blood circulation is presented in this chapter. The detailed human hepatic vascular data, obtained in chapter 5, were used to set up the electrical model.

The model was able to simulate effects of pressure-driven HMP on liver haemodynamics and reproduced observations such as flow competition between the HA and PV. Our simulations further indicated that, from a pure biomechanical (shear stress) point of view, pressure-controlled HMP with low pressures should not result in organ damage, and that fluid viscosity has no effect on the shear stress experienced by the liver microcirculation during

pressure-driven HMP. These findings imply that this modelling technique may be applicable to virtually test perfusion conditions.

Chapter 7. Validation and calibration of an electrical analog model of hepatic perfusion based on human liver HMP experiments

In chapter 6, an initial electrical analog model was developed to investigate the human hepatic perfusion during HMP. Due to unknown parameters, a number of assumptions had to be made. To test the electrical analog model against experimental data, this chapter presents a methodology to validate and tune the initial electrical model (as developed in chapter 6) for a specific liver. A number of HMP experiments were aimed at capturing the perfusion behaviour of human liver grafts by performing simultaneous pressure and flow measurements. The calculation of HA and PV input impedances enabled fitting compact Windkessel models to represent the global hepatic perfusion properties. Subsequently, these global properties were used to tune an extended liver-specific electrical analog model.

Chapter 8. Modelling the impact of partial hepatectomy on the hepatic haemodynamics using a rat model

LDLT may help expanding the donor pool, but is often confronted with the 'small-for-size' syndrome, in which a small liver has to deal with too much blood flow. Since the haemodynamic effects of partial hepatectomy are not fully understood, we developed an electrical model of the blood circulation through the rat liver (derived from the model discussed in chapter 6) in order to compare the normal liver haemodynamics with those of partially resected livers.

Detailed geometrical data and 3D reconstructions of the liver vasculature of two rats were gathered by combining vascular corrosion casting, micro-CT scanning and image processing. Data extrapolations allowed obtaining a total liver pressure- and flow-driven electrical analog model. Subsequently, virtual resections led to 70%, 80%, or 90% partial hepatectomy models. Results demonstrated hyperperfusion effects such as portal hypertension and elevated lobe-specific PV flows. Comparison of two 90% resection techniques demonstrated different total arterial flows, portal and sinusoidal pressures, possibly resulting in better survival for lower portal and sinusoidal pressures. These models may be extrapolated to human livers and help to optimise hepatectomy planning.

Part III. The hepatic microcirculation: from imaging the sinusoidal geometry to microscale CFD models

Chapter 9. Perfusion characteristics of the human hepatic microcirculation based on 3D reconstructions and CFD analysis

The hepatic microvasculature has a unique and complex organisation, and is susceptible to abnormal stressors, possibly arising during MP or after a partial hepatectomy procedure etc. As the microcirculation plays a pivotal role in liver perfusion and function, and since relatively little is known about the microvascular haemodynamics, it is advisable to put more effort in unraveling the microcirculation perfusion properties. Previously, perfusion models of the liver microcirculation were often analysed in terms of idealised functional units (e.g. hexagonal liver lobules) based on a porous medium approach, while more elaborate research is essential to assess the validity of this approach and to provide a more adequate and quantitative characterisation of the liver microcirculation. Therefore, we investigated the perfusion characteristics of the liver microcirculation in this chapter.

A microvascular sample representing three liver lobules, was dissected from a human liver vascular corrosion cast and scanned using a high resolution (2.6 μm) micro-CT scanner. Following image processing, a cube representing a sample of intertwined and interconnected sinusoids, was isolated from the 3D reconstructed dataset to define the fluid domain. Three computational fluid dynamics (CFD) models were studied to simulate flow along three orthogonal directions (i.e. parallel to the central vein and in the radial and circumferential directions of the lobule).

Post-processing allowed visualising and quantifying the microvascular flow characteristics, calculating the permeability tensor and corresponding principal permeability axes, as well as the 3D porosity. The CFD simulations provided data on pressure differences, preferential flow pathways and wall shear stresses. Our data indicate that the human hepatic microcirculation is characterised by a higher permeability along the central vein direction, and an about two times lower permeability along the radial and circumferential directions of a lobule. Since the permeability coefficients depend on the flow direction, (porous medium) liver microcirculation models should take into account sinusoidal anisotropy.

Chapter 10. A 3D porous media liver lobule model: the importance of vascular septa and anisotropic permeability for homogeneous perfusion

Using the perfusion characteristics acquired in chapter 9, we developed a 3D microcirculatory liver lobule model to investigate the role of vascular septa (VS) and anisotropic permeability. The lobule was modelled as a hexagonal

prism (with or without VS) and the tissue was treated as a porous medium (isotropic or anisotropic permeability). Models were solved using CFD.

VS inclusion resulted in better perfusion of the zones lying between portal tracts as well as a more spatially homogeneous perfusion of the lobule compared to models neglecting the VS. Anisotropic permeability resulted in clearly different flow patterns with streamlines that are oriented closer to the lobule axes compared to isotropic permeability. A parameter study revealed that results are most sensitive to the lobule circumferential diameter and radial pressure drop. Our model provides insight into hepatic microhaemodynamics, and suggests that especially the inclusion of VS in the model leads to perfusion patterns that are likely to better reflect physiological reality. The model has also potential for other applications such as unphysiological and pathological conditions.

Part IV. Conclusions

Chapter 11. Conclusions and future perspectives

This chapter gives an overview of the key findings and most important conclusions of this manuscript. The take home message of this work is that a multi-level modelling framework (anatomical models of the hepatic vasculature, electrical analog models of the hepatic perfusion and CFD models of the hepatic microcirculation) was developed to simulate hepatic perfusion at different scales (macro-, meso- en microcirculation). This framework was applied in the context of liver transplantation and resulted in unique 3D morphological and geometrical data on human and rat livers, as well as novel insights into the haemodynamic impact of MP preservation of donor livers, partial hepatectomy procedures (such as LDLT), and into the perfusion characteristics of the liver microcirculation. Doing so, we collected some missing pieces of the puzzle on liver perfusion, but further research (such as validation of the micromodels and investigating more livers) is necessary to reveal the complete picture. The versatile modelling tools that were generated within this PhD work, are not only applicable to hepatic haemodynamic issues related to liver transplantation, but also to liver pathologies (e.g. cirrhosis), surgical interventions (e.g. the Fontan procedure) etc. These represent only a few of the potential future research directions to go from here.

Contents

List of Figures

List of Tables

Abbreviations and Symbols

Abbreviations

1D	One-dimensional
2D	Two-dimensional
3D	Three-dimensional
AC	Anterior (ventral) caudate lobe
AMC BAL	Academic Medical Centre bio-artificial liver
AST	Aspartate aminotransferase
CBDL	Common bile duct ligation
CCl_4	Carbon tetrachloride
CFD	Computational fluid dynamics
CS	Cold storage
CT	Computer tomography
CV	Central vein
DBD	Donation after brain death
DCD	Donation after circulatory death
DICOM	Digital imaging and communication in medicine
DNA	Deoxyribonucleic acid
ELAD	Extracorporeal liver assist device
FPSA	Fractionated plasma separation and adsorption
HA	Hepatic artery / hepatic arterial
HABR	Hepatic arterial buffer response
HCC	Hepatocellular carcinoma
HL	Human liver
HMP	Hypothermic machine perfusion
HTK	Histidine-tryptophan-ketoglutarate
HV	Hepatic veins / hepatic venous
INR	International normalised ratio
IRL	Inferior (caudal) right lobe
KOH	Potassium hydroxide
KPS	Kidney preservation solution
LDLT	Living donor liver transplantation

LLL	Left lateral lobe
LML	Left median lobe
MARS	Molecular adsorbents recirculating system
MELD	Model for end-stage liver disease
MELS	Modular extracorporeal liver support
MFU	Macro-functional units
MP	Machine perfusion
MR(I)	Magnetic resonance (imaging)
NASH	Non-alcoholic steatohepatitis
NMP	Normothermic machine perfusion
NO	Nitrogenoxide
PC	Posterior (dorsal) caudate lobe
PhD	Doctor of philosophy
PIV	Particle image velocimetry
PPVL	Partial portal vein ligation
PT	Portal triad
PV	Portal vein / portal venous
RML	Right median lobe
RMSE	Root mean square error
ROS	Reactive oxygen species
SEM	Scanning electron microscopy
SFSS	Small-for-size syndrome
SLT	Split liver transplantation
SNMP	Subnormothermic machine perfusion
SPAD	Single pass albumin dialysis
SRL	Superior (cranial) right lobe
SSI	Supersonic shear imaging
TIPS	Transjugular intrahepatic portosystemic shunts
UNOS	United network for organ sharing
US	Ultrasound
USA	United States of America
UW	University of Wisconsin
VCI	Vena cava inferior
VCS	Vena cava superior
VS	Vascular septa
WK	Windkessel model

Operators

Δ	Difference
$\int$	Integral

$\nabla\cdot$	Divergence
∇	Gradient
∂	Partial derivative
$\sum$	Sum

Symbols

%	Percentage	
α	Angle	[°]
λ	Eigenvalue	
μ	Dynamic viscosity	[Pa · s]
ω	Angular frequency	[rad]
ϕ	Phase angle	[°]
π	Pi	
ρ	Density	[kg/m³]
σ	Standard deviation	
σ	Stress	[Pa]
τ	Shear stress	[Pa]
θ	Azimuthal angle (cylindrical coordinate)	[°]
ε	Porosity	
$\vec{e}$	Eigenvector	
$\vec{v}$	Velocity vector	[m/s]
A	Area	[m²]
a	Real part	
b	Imaginary part	
C	Capacitance	[m⁵/N]
c_p	Pulse wave velocity	[m/s]
C_{xy}	Coherence between signals x and y	
E	Young's elasticity modulus	[Pa]
f	Frequency	[Hz]
f	Generation number	
f_C	C factor	
f_L	L factor	
f_{R_p}	R_p factor	
G_{xx}	Autospectral density of signal x	
G_{xy}	Cross-spectral density between signals x and y	
h	Wall thickness	[mm]
j	Imaginary unit	
K	Permeability tensor	
k	Permeability coefficient	[m²]
L	Inertia	[Ns²/m⁵]

L	Length	[mm]
l	Length	[mm]
m	Mass	[kg]
n	Number of vessels	
o	Order number	
P	Pressure	[mmHg]
p	Pressure	[mmHg]
Q	Flow	[ml/min]
q	Flow	[ml/min]
R	Vascular resistance	[mmHg·min/ml]
r	Radius	[mm]
R^2	Determination coefficient	
t	Time	[s]
V	Volume	[m^3]
v	Velocity	[m/s]
w	Weighting factor	
WSS	Wall shear stress	[Pa]
x	Generation number	
Z	Impedance	[mmHg·min/ml]
z	Length	[m]

Units

μm	Micrometer
°	Degrees
cm	Centimeter
g	Gram
Hz	Hertz
kg	Kilogram
l	Litre
min	Minute
ml	Millilitre
mm	Millimeter
mmHg	Millimeters of Mercury
N	Newton
Pa	Pascal
rad	Radials
s	Second
V	Volt

Introduction

Introduction

The liver: a mythical organ

The first reports on the liver and its anatomy date back from many centuries ago. The ancient Greek culture already provided two tales involving the liver. One of them is the myth of Prometheus, written by the poet Hesoid (700-750 BC). According to one of the versions of this myth, Prometheus, who created mankind, offered the best meat of a cow to mortal humans, while giving only bones and fat to the gods. Zeus, king of the gods, was furious about this and punished mankind by taking their fire. Prometheus stole the fire back, but he was caught. Zeus punished Prometheus by chaining him to a rock on the mountain Caucasus and making an eagle eat from his liver daily (Fig. 1). His liver grew back overnight and the hungry eagle returned each morning, leaving Prometheus in eternal pain [282, 336]. While the myth of Prometheus is generally well-known, less is known about the myth of Tityus. Tityus, son of Zeus, was another mythical figure who was so gigantic that his body was believed to cover nine acres. Tityus made the mistake of attempting to rape Leto, mother of Apollo. She cried for help resulting in Apollo trying to kill Tityus with his arrows, but he could not kill the immortal Tityus. Nonetheless, Zeus punished Tityus by exiling him to Hades, kingdom of the dead, where he was tied down. Two vultures (or a snake according to another version of this myth) were released to fed on his regenerating liver. This resulted in eternal torture, similar to the punishment of Prometheus [406, 468].

These mystical tales illustrate that the ancient Greek already had some knowledge of the liver and its ability to regenerate (see section 1.2.12). However, as stated by Lehman et al. [282], the liver remains - to some extent - '*a fragile bleeding mystery*'…

Clinical context and research goals

Since liver transplantation became a true and successful treatment for liver failure, a substantial discrepancy arose between the supply of donor livers

Figure 1: *Prometheus Bound*, 1611-1612. Photographic reproduction of an oil painting by Peter Paul Rubens (Flemish painter who lived from 1577 to 1640). Source: [10].

and the demand for liver transplantation during the last decades. As a consequence, there is now a substantial shortage of liver grafts for patients with liver failure and waiting lists are becoming longer. Patients die while waiting for a transplant liver. This urged research, aiming to reduce the waiting list and increase the number of available liver grafts.

Machine perfusion

One of the proposed options to expand the donor pool is the use of organs that are currently uncommonly used for transplantation (e.g. livers from donation after circulatory death donors or extended criteria donors with contraindications such as liver steatosis, advanced age etc.) [345]. Compared to standard criteria organs (donation after brain death), these organs are more succeptible to ischaemia-reperfusion injury, which is partly aggravated by the current gold standard of static cold storage. Consequently, machine perfusion (MP) preservation (see also section 3.3.2) was proposed

as a potential alternative preservation technique for donor organs, different from and better than static cold storage. MP can be hypothermic (non-physiological cold perfusion) or (sub)normothermic (with normothermic MP mimicking normal *in vivo* liver perfusion) [341]. Experimental studies gave evidence of a better organ viability after MP preservation, especially in the case of extended criteria donor livers (see section 3.1.3). Other advantages of MP are the possibility of longer preservation periods compared to static cold storage, as well as the possibility to monitor the behaviour and viability of the organ by measuring perfusion parameters. Nonetheless, liver MP also encountered some non-negligible disadvantages. As such, the two blood inlets of the liver may start to compete during MP. Furthermore, it is known that the unique and complex hepatic microvasculature is prone to abnormal stressors which may arise due to hyperperfusion and lead to endothelial injury. In the end, the challenge is to define the most optimal perfusion settings to prevent microcirculatory damage while assuring sufficient and homogeneous perfusion. It would thus be insightful to clarify the intrahepatic haemodynamics at both the macro- and microscale during (hypothermic) MP and to develop a liver perfusion model to test different settings.

Alternative transplantation techniques

Another possibility to circumvent the donor liver shortage is to use alternative transplantation techniques, such as living donor liver transplantation (LDLT; see section 3.2.3.2) and split liver transplantation (SLT; see section 3.2.3.1). In LDLT, a healthy living person donates a part of his liver to a patient with liver failure, while SLT stands for a deceased donor liver being split into two liver grafts to be transplanted into two recipients. The disadvantage of these transplantation techniques is the risk of developing the small-for-size syndrome (SFSS). SFSS is characterised by a liver that is too small compared to the patient's body and may lead to serious complications or even liver graft failure. In this context, it is for instance not completely clear how much liver tissue can be safely removed from a living donor, or what the optimal resection planes are. More insight into the haemodynamics before and after partial hepatectomy is thus desired.

Research goals

Since hepatic haemodynamics are shown to play an important role in different liver transplantation strategies, this dissertation focused on clarifying and modelling hepatic haemodynamics and perfusion across different length scales. Three major research goals were defined:

Goal 1. *Development of a methodology for the quantitative analysis of the human liver vasculature from the macro- down to the microscopic level.*

Goal 2. *Development of computer models to study the intrahepatic haemodynamics and quantify biomechanical stressors on the macro- and microscale level.*

Goal 3. *Validation and application of the acquired models.*

Structure overview

This dissertation is divided into four major parts.

Part I gives a background overview starting with the liver anatomy and physiology (chapter 1). Subsequently, the different categories of liver pathologies are discussed followed by the treatment options, of which liver transplantation is the ultimate treatment for patients with end-stage liver failure (chapter 2). Chapter 3 deals with the donor pool for liver transplantation, the transplantation procedure and liver preservation techniques with the focus on MP. Chapter 4 gives a literature overview of previous modelling approaches to study the hepatic vasculature and perfusion as well as a short overview of liver mechanics and function models.

In part II, chapter 5 first focuses on acquiring detailed data on the hepatic vascular architecture. These data are used in chapter 6 to develop an electrical analog model of the human liver perfusion in order to study the internal hepatic flow patterns during MP. Chapter 7 discusses how the electrical analog model is validated and tuned to a specific liver based on MP experiments to acquire the hepatic perfusion characteristics. Subsequently, the electrical liver model is adapted to the rat liver in order to investigate the effect of partial hepatectomy on the hepatic haemodynamics (chapter 8).

While part II mainly focuses on the hepatic macrocirculation, part III goes deeper into the hepatic microcirculation. In chapter 9, a CFD model, based on a real 3D geometry of sinusoids, is developed to quantify the perfusion characteristics of the hepatic microcirculation. Chapter 10 applies the acquired permeability data to develop a porous media model of the blood flow through a liver lobule.

Finally, part IV sums the most important conclusions of this dissertation, as well as the future perspectives (chapter 11).

List of publications

First author peer-reviewed papers

- Debbaut C., Monbaliu D., Casteleyn C., Cornillie P., Van Loo D., Maschaele B., Pirenne J., Simoens P., Van Hoorebeke L., and Segers P.

"From vascular corrosion cast to electrical analog model for the study of human liver hemodynamics and perfusion." IEEE Transactions on Biomedical Engineering, 58(1):25-35, 2011.

- Debbaut C., Vierendeels J., Casteleyn C., Cornillie P., Van Loo D., Simoens P., Van Hoorebeke L., Monbaliu D., and Segers P. *"Perfusion characteristics of the human hepatic microcirculation based on three-dimensional reconstructions and computational fluid dynamic analysis."* Journal of Biomechanical Engineering, 134(1):011003, 2012.

- Debbaut C.*, De Wilde D.*, Casteleyn C., Cornillie P., Van Loo D., Van Hoorebeke L., Monbaliu D., Fan Y.-D., and Segers P. *"Modeling the impact of partial hepatectomy on the hepatic hemodynamics using a rat model."* IEEE Transactions on Biomedical Engineering, 59(12):3293-3303, 2012.
  **Debbaut C. and De Wilde D. contributed equally to this study.*

- Debbaut C., Vierendeels J., Siggers J., Repetto R., Monbaliu D., and Segers P. *"A 3D porous media liver lobule model: the importance of vascular septa and anisotropic permeability for homogeneous perfusion"*, Computer Methods in Biomechanics and Biomedical Engineering, in press (e-publication ahead of print, 2012).

- Debbaut C., Segers P., Cornillie P., Casteleyn C., Dierick M., Laleman W., and Monbaliu D. *"Analyzing the human liver vascular architecture by combining vascular corrosion casting and micro-CT scanning: a feasibility study"*, submitted for publication.

- Debbaut C., Monbaliu D., Segers P. *"Validation and calibration of an electrical analog model of hepatic perfusion based on human liver hypothermic machine perfusion experiments"*, submitted for publication.

Coauthor peer-reviewed papers

- Monbaliu D., Debbaut C., Hillewaert W., Brassil J., Laleman W., Sainz-Barriga M., Kravitz D., Pirenne J., and Segers P. *"Flow competition between hepatic arterial and portal venous flow during hypothermic machine perfusion preservation of porcine livers."* International Journal of Artificial Organs, 35(2):119-131, 2012.

- Monbaliu D., Vandersmissen J., De Hertogh G., Van Assche G., Hoffman I., Knops N., Debbaut C., Heye S., Pirenne J., and Maleux G. *"Portal hypertension after combined liver and intestinal transplantation, a diagnostic and therapeutic challenge?"* Pediatric Transplantation, 16(7):E301-E305, 2012.

- Monbaliu D., Liu Q., Libbrecht L., De Vos R., Vekemans K., Debbaut C., Detry O., Roskams T., van Pelt J., and Pirenne J. *"Preserving the morphology and evaluating the quality of liver grafts by hypothermic machine perfusion: A proof-of-concept study using discarded human livers."* Liver Transplantation, 18(12):1495-1507, 2012.

One

The liver: from anatomy to model

CHAPTER 1

Anatomy and physiology of the liver

Before adressing the research and findings of this PhD dissertation (part II-IV), it is important to give a general background overview. In this chapter, the anatomy of the liver will be discussed from the macroscopic to the microscopic level. We will further discuss its major regulatory and metabolic functions.

1.1 Anatomy of the liver

1.1.1 Macroscopic anatomy of the liver

1.1.1.1 General characteristics

The liver is the largest organ in the human body. The human liver accounts for approximately 2-2.5% of the body weight, which corresponds to a liver weight of 1.4 kg for the average adult. At birth, however, the liver is proportionally larger, occupying approximately 5.5% of the body weight. The wedge-shaped liver typically has a brown-reddish colour and is located in the right upper quadrant of the abdominal cavity, just below the diaphragm (Fig. 1.1). Due to its location, the liver is partially protected by the rib cage of the thorax. Furthermore, the liver is embedded in the visceral peritoneum, except for the location where the liver touches the diaphragm (bare area; Fig. 1.2). The liver is also covered by a thin layer of connective tissue: the liver capsule (also called the capsule of Glisson). The gallbladder is located at the

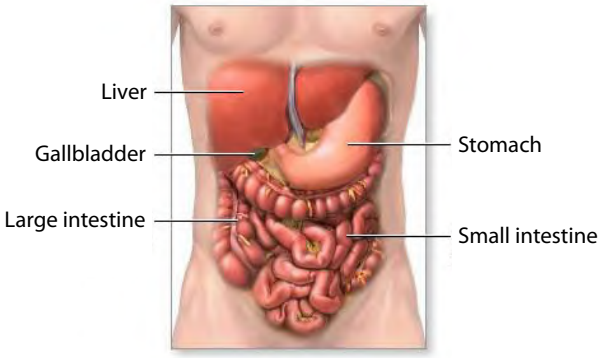

Figure 1.1: The human liver is located in the upper right quadrant of the abdominal cavity. Adapted from [4].

inferior side of the liver and acts as a storage location for bile produced by the liver and the bile ducts [118, 122, 164, 278, 311, 351, 400, 496].

The human liver is traditionally divided into four primary anatomic liver lobes (Fig. 1.2). The right lobe (lobus dexter) is the largest lobe, and has approximately six times the size of the left lobe (lobus sinister). The two

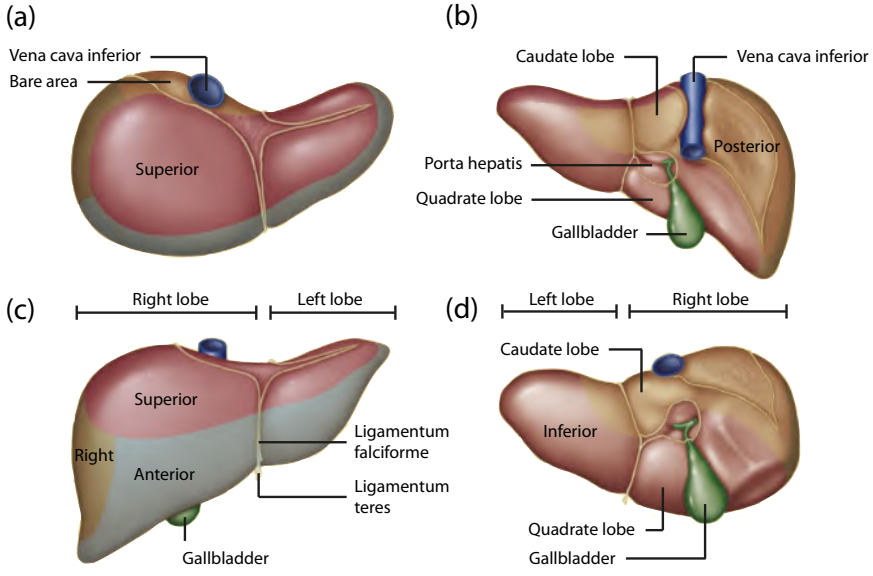

Figure 1.2: Different views of the human liver based on the classical view of four lobes: (a) superior, (b) posterior, (c) anterosuperior and (d) posteroinferior view of the liver. Adapted from [122].

smaller lobes are visible in a posteroinferior view of the liver: the caudate lobe (lobus caudatus) and the quadrate lobe (lobus quadratus). The liver is attached to its surrounding structures by a number of ligaments. The ligamentum falciforme (visible on the anterosuperior view of the liver) attaches the liver to the diaphragm and separates the right from the left lobe. Below the ligamentum falciforme lays the remnant of the foetal umbilical vein: the ligamentum teres. The gallbladder is situated between the right lobe and the quadrate lobe. It is a thin-walled greenish muscular sac having a length of approximately 10 cm and a volume of approximately 50 ml [311, 377].

In addition to the traditional division of the human liver in four anatomic lobes, there is a more functional schematisation dividing the liver in lobes and segments. Several hepatic functional classifications [78, 79, 133, 176, 177, 437, 443] have been proposed, such as the system described by Couinaud (and later refined by Bismuth [38] by dividing segment 4 in segment 4a and 4b) which is accepted by the transplantation community in Europe, North America and Asia [213]. Couinaud divided the liver into a functional left and right liver by a main portal scissurae containing the middle hepatic vein running from the middle of the gallbladder fossa anteriorly to the inferior vena cava posteriorly. Typically, each segment has its own blood supply and biliary drainage, without anastomoses between these segments (Fig. 1.3). In the centre of each segment there is a branch of the portal vein, hepatic artery and bile duct. In the periphery of each segment, there is vascular outflow through the hepatic veins. Hereby, the liver is divided into eight main segments (or nine segments when defining the caudate lobe as a separate posteriorly located segment). This compartmental segmental subdivision is applied clinically, e.g. in liver surgery to help planning segmental resections of the liver [122, 176, 213, 409, 460].

1.1.1.2 Macroscopic hepatic vasculature

At rest, 25-30% of the total cardiac output flows into the liver. The human liver receives a total flow of approximately 1.5 l/min or 100-130 ml/min/100 g liver tissue [377]. This corresponds to an oxygen consumption of approximately 25% of all oxygen consumed in the body. The liver has a unique vasculature with a dual afferent vascular system. Blood is supplied to the liver through the hepatic artery (arteria hepatica; HA) and the portal vein (vena portae; PV) as illustrated in Fig. 1.4. Both vessels enter the liver through the porta hepatis (hilum) and branch into vessels with smaller diameters to form vascular trees, supplying the liver parenchyma with blood [55, 169, 233].

The vessels of the HA and PV vascular trees typically run parallel in the so-called portal tracts or portal triads (PTs; Fig. 1.5). The PTs also contain vessels of the biliary tree, running parallel to the HA and PV vessels. Note, however, that the bile flow in the biliary tree is directed opposite to the blood

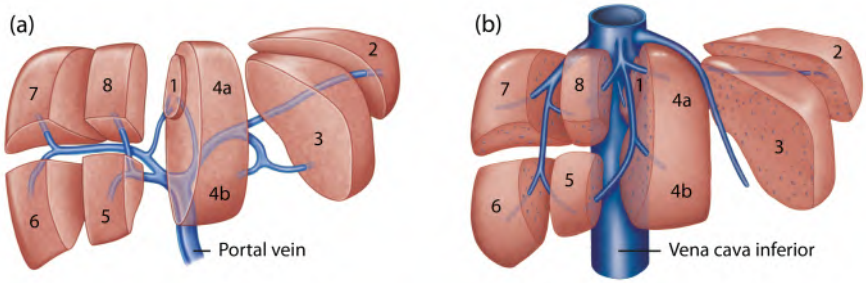

Figure 1.3: Segmental subdivision of the human liver in correspondence to (a) the portal veins and (b) the hepatic veins: the caudate lobe (1), the lateral superior segment (2), the lateral inferior segment (3), the medial superior (4a) and medial inferior segment (4b), the anterior inferior segment (5), the posterior inferior segment (6), the posterior superior segment (7) and the anterior superior segment (8). Adapted from [122].

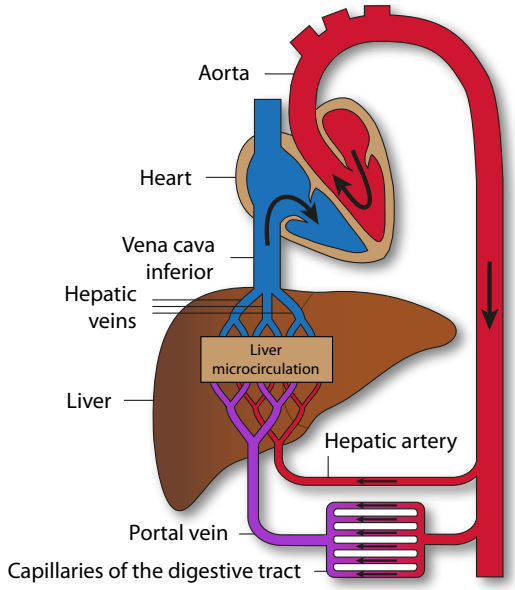

Figure 1.4: Schematic overview of the macroscopic vasculature of the human liver and its relation to the systemic circulation.

flow through the HA and PV vascular trees. After passing the liver microcirculation, blood leaves the liver via the hepatic veins (venae hepaticae; HV) and drains into the vena cava inferior (VCI). The VCI leads the deoxygenated blood to the right atrium of the heart (Fig. 1.4) [311, 377].

As one of the afferent vessel systems of the liver, the common hepatic artery is a side branch of the coeliac trunk which directly originates from

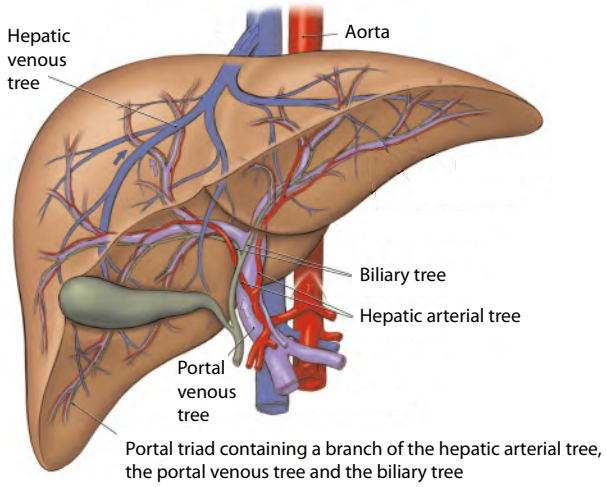

Figure 1.5: The vascular trees of the human liver: the hepatic arterial (HA) tree, the portal venous (PV) tree and the hepatic venous (HV) tree. The biliary tree is also visible. Adapted from [5].

the aorta. The coeliac trunk gives rise to the splenic artery, the left gastric artery and the common hepatic artery. Along its course, the common hepatic artery gives rise to the gastroduodenal artery, and enters the porta hepatis as the proper hepatic artery. Usually, after the origin of a side branch (right gastric artery), it splits into a left and right branch, bringing oxygen-rich blood to the liver (Fig. 1.5) [122, 213]. The HA assures approximately 25% of the total blood flow to the liver, resulting in a pulsatile HA inflow with a mean value of 350-400 ml/min at a mean pressure of 100 mmHg (comparable to the aortic pressure). In this way, the HA accounts for 50-80% of the oxygen supply to the liver. In addition to the perfusion of liver parenchyma, the HA tree also includes a subtree providing blood flow to the gallbladder. Unlike liver tissue, the gallbladder has only one afferent vascular system. The HA vascular tree also nourishes the bile ducts by a network of capillaries, called the peribiliary plexus [377].

The PV supplies the remaining 75% of the blood flow into the liver, as well as the remaining oxygen. The nutrient-rich PV blood originates from the gastro-intestinal tract: the small and large intestines (superior and inferior mesenteric veins), the spleen (splenic vein), the stomach (coronary and pyloric veins), the pancreas (pancreaticoduodenal veins) and the gallbladder (cystic vein). The PV blood is partially deoxygenated and carries a lot of nutrients as well as waste products. The PV has a length of approximately 6-8 cm and a diameter of 1-1.2 cm. The PV is characterised by a mean continuous blood flow of 1.1 l/min at a pressure of 7-10 mmHg. The PV vascular tree has no valves, resulting in the pressure being freely transmitted

to the afferent vessels. After passing through the porta hepatis, the PV also splits into left and right branches and further splits into segmental branches (Fig. 1.5) [42, 169, 309, 377, 382].

Deoxygenated blood is removed from the liver through the HV tree by its major HV draining into the VCI. The continuous outflow is characterised by a mean flow of approximately 1.5 l/min and a 3-5 mmHg pressure [377]. The HV vascular tree counts three major vessels (the right, left and middle hepatic vein), complemented by a number of accessory hepatic veins. Usually, the middle hepatic vein drains into the left vein just before its termination in the VCI [377]. The HV tree also lacks valves [169, 254].

The unique vascular organisation of the human liver is studied in detail in chapter 5, as the hepatic vascular architecture is important to take into account when modelling liver perfusion.

Next to the vascular trees of the hepatic blood circulation, there is also the biliary tree. The intrahepatic bile ducts, which drain the bile produced by the liver, merge into a right and left hepatic duct, which in turn fuse together at the porta hepatis into the common hepatic duct. This duct receives the cystic duct from the gallbladder. From the confluence of the cystic duct, the hepatic duct is termed the common bile duct or ductus choledochus, draining bile both from the gallbladder and intrahepatic bile ducts into the duodenum at the papilla of Vater [311].

1.1.2 Microscopic anatomy of the liver

1.1.2.1 Liver lobules and sinusoids

In literature, the microscopic anatomy of the liver is usually schematically represented in terms of structural units, called classic liver lobules. Classically, these liver lobules are proposed to have the shape of a hexagonal prism and have a circumscribed diameter of 0.7-2 mm and a length up to several millimetres (Fig. 1.6 and 1.7a). Of interest, a more recent quantitative study revealed that pentagonal lobules predominate over hexagonal ones in pigs [118]. Liver lobules are assumed to be configured in a tessellating pattern, similar to the organisation of hexagonal wax cells in the honeycombs of bees (Fig. 1.6 and 1.7b). Every lobule consists of plates of hepatocytes (main liver parenchymal cells; see also section 1.1.2.3), which account for 80% of the liver mass and 65% of the liver cells (Fig. 1.6 and 1.8a) [305, 309, 311]. In chapter 10, a liver microperfusion model is developed based on liver lobules.

At every corner of a lobule, there is a PT, containing three structures: a hepatic artery , a portal vein branch and a portal or interlobar bile duct (Fig. 1.7 and 1.8a). However, Crawford et al. [81] showed that variations in PTs are possible (e.g. a portal vein branch and a portal bile duct accompanied by three instead of one hepatic artery branch). There are also lymph vessels and nerves running along the PTs, but these are difficult to distinguish. A

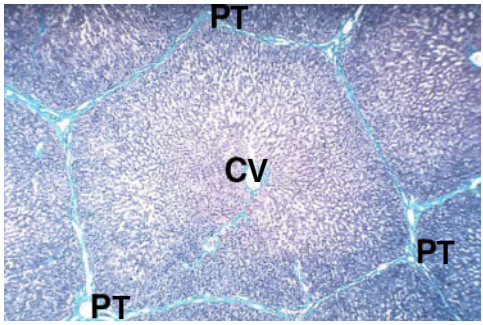

Figure 1.6: Representative histological image of liver lobules. The delineation of a lobule and its neighbouring lobules is clearly visible, demonstrating the tessellating organisation of liver lobules. Adapted from [2].

fraction of the blood from the PTs enters the vascular septa (VS), which are the continuous vascular surfaces between neighbouring lobules, bordered at opposite edges by two PTs. As such, the VS supply blood to the tissue between PTs by a number of microvessels (septal branches) branching off the PTs.

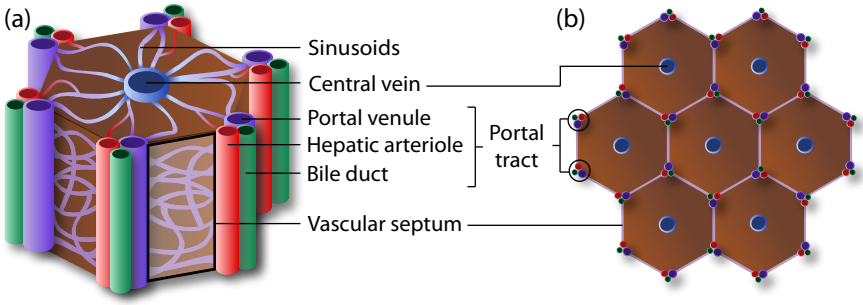

Figure 1.7: Schematic representation of the liver microcirculation: (a) liver lobule, (b) organisation of liver lobules in a tessellating pattern.

Subsequently, blood flows from the PTs and VS into the interconnected network of tortuous hepatic-specific capillaries, called the sinusoids (Fig. 1.7 and 1.8). The hepatic arterioles in the PTs do not always drain directly into the sinusoids. The hepatic arterioles either drain into the peribiliary plexus, the periportal plexus or the sinusoids. Hereby, the peribiliary plexus supplies blood to the intrahepatic bile ducts before draining into the sinusoids. In the periportal plexus, the arterioles first nourish the PV branches before draining into the sinusoids. As a third option, arterial blood can directly

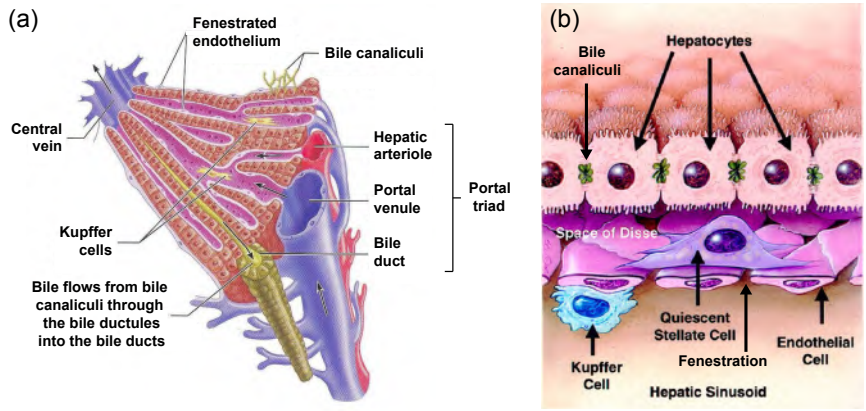

Figure 1.8: Microanatomy of the liver: (a) segment of a liver lobule and (b) illustration of the space of Disse between the sinusoidal endothelial cells and the hepatocytes. Adapted from [143, 311].

enter the sinusoids through arteriosinus twigs which terminate in the sinusoids close to the origin of portal venules [237, 322, 324, 409, 465, 496].

Blood flow through a sinusoid can be portal venous, hepatic arterial or a mix of both. The sinusoids are located between the plates of hepatocytes, and are lined by endothelial cells of which the flat extensions are provided with pores or fenestrations (fenestrae) (Fig. 1.8b). Fenestrations are clustered together (typically 10-15 pores per cluster) forming sieve plates. Human sinusoids have a diameter of 7-15 μm and a length of 223-477 μm [309, 382, 496, 517]. Blood solutes (nutrients, toxic substances etc.) can pass through the fenestrations ending up into the space of Disse. The space of Disse is the region between the endothelial cells lining the sinusoids and the hepatocytes (Fig. 1.8b). Proteins as well as blood plasma are able to enter into the space of Disse through the fenestrae (typically having a diameter of approximately 175 nm [509]) contrary to the larger red blood cells. As such, the endothelial cells with fenestrations act as a filter. Due to these characteristics, the hepatocytes are able to take up nutrients, oxygen etc. from blood. Furthermore, the space of Disse contains a low density extracellular matrix (supporting the overall structure of the liver) and is responsible for approximately half of the lymph production. The exchange of fluids, solutes, particles etc. between sinusoidal blood and the microvilli of hepatocytes is bidirectional. Next to endothelial cells, the sinusoids also contain Kupffer cells (Fig. 1.8b). These liver-resident macrophages remove bacteria and worn-out blood cells, and play an important role in inflammation processes of the liver [309, 311].

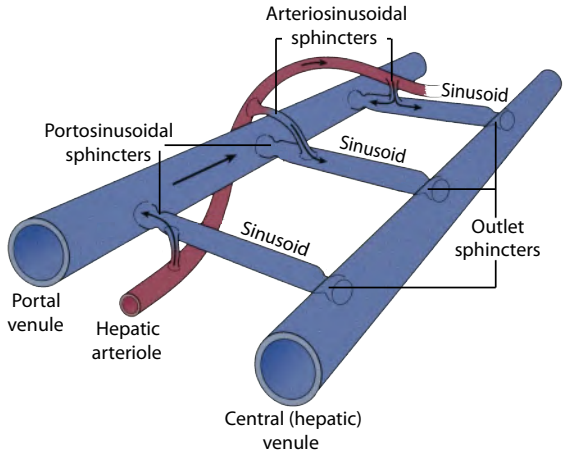

Figure 1.9: Schematic illustration of the sphincters in the liver microcirculation. Adapted from [409].

Sinusoids also contain two types of sphincters at their inlets (Fig. 1.9). The portosinusoidal sphincters contain large endothelial cells combined with hepatic stellate cells. They are located at the connection between the terminal portal venule and sinusoid. The arteriosinusoidal sphincters are located at the connections of terminal hepatic arterioles with sinusoids and are contractile smooth muscle sphincters [53, 324, 382, 409]. In addition, after flowing through the sinusoids, blood passes through the outlet or efferent sphincters composed of sinusoidal endothelial cells (Fig. 1.9) [216].

The blood flow in the sinusoidal network is heterogeneous. As such, the periportal sinusoids form an interconnected polygonal network, while the pericentral sinusoids are more organised as parallel vessels provided with intersinusoidal connections and draining radially into the central vein (CV; also called centrolobular vein) [323, 409]. The haemodynamics in the sinusoids are characterised by a low pressure (2-5 mmHg) and a low blood velocity. As a consequence, this enables hepatocytes to interact metabolically with blood that slowly passes by [169]. At the centre of every lobule, there is a central vein, oriented along the longitudinal axis of the lobule (Fig. 1.6-1.9). The blood is drained from the sinusoids into the CV, and from there into the HV and VCI [311].

1.1.2.2 Bile secretion

The hepatocytes produce bile, playing an important role in the digestion of lipids. Bile is drained into the bile canaliculi lining the hepatocytes (Fig. 1.8), and subsequently into the canals of Hering. Through these canals, bile flows towards the portal bile duct in the PTs and leaves the liver through

the biliary tree, guiding bile towards the porta hepatis. Furtheron, bile is transported either to the gallbladder, where it is stored and concentrated up to 20-fold the original concentration, or to the duodenum. Note, however, that bile flows in the opposite direction of the HA and PV blood flow in the PTs [82, 272, 309, 311, 409].

1.1.2.3 Liver cells

The liver counts six major types of cells, of which a few were already mentioned earlier in the text. Here, we give a short overview of the major cell types and their functions [509].

- ***Hepatocytes*** are the main liver parenchymal cells. These polygonal epithelial cells are organised in plates with a thickness of one or two cell layers. At their sinusoidal side, they line the interstitial space of Disse by their microvilli. On the other side, at the middle of their intercellular surface, a groove is formed representing a so-called hemicanaliculus which together with a similar groove from the adjacent hepatocyte forms a separate biliary compartment which is the beginning of the bile canaliculus. The functions of hepatocytes include processing of nutrients, bile production, storage of fat-soluble vitamins, and detoxification [309, 351, 377].

- ***Endothelial cells*** form the lining of the sinusoids. In this way, parenchymal cells are separated from the sinusoidal blood. In contrast to other capillary endothelia, the sinusoidal endothelial cells have no visible basement membrane and are perforated at their flat extensions by fenestrations [382].

- ***Kupffer cells*** are star-shaped mobile macrophages, attached to the sinusoidal endothelial lining, and are mainly located in the periportal area. These phagocytes remove debris such as bacteria, old blood cells, viruses etc. by the process of endocytosis. Kupffer cells can become activated by several agents (endotoxins, interferon-gamma etc.) as well as by shock or sepsis. Activated Kupffer cells can produce proinflammatory cytokines (inflammation initiators) [377].

- ***Pit cells*** (also called the hepatic specific natural killer cells) are located in the space of Disse. These liver-associated lymphocytes play an active role in the immune system [41, 377, 409].

- ***Stellate cells*** (also called perisinusoidal cells, fat storing cells or Ito cells) contain lipid droplets which store vitamin A. Their main features are the long cytoplasmatic extensions which may regulate blood flow.

They contain actin and myosin to contract in response to endothelin-1 etc. Hepatic stellate cells play an important role in fibrogenesis (synthesis of extracellular matrix) and are found in the space of Disse. They produce extracellular matrix proteins (both in normal conditions as well as excessively in the fibrotic liver) and play a role in liver regeneration. Stellate cells account for 5-8% of all liver cells [377, 382, 409].

- ***Cholangiocytes*** (or bile ductular cells) are epithelial cells lining the bile ducts [41].

1.1.2.4 Liver units

Although the ***classic hexagonal liver lobule*** (Fig. 1.10a; used in chapter 10) as first described by Kiernan [252] is probably the most frequently used liver unit, there is an ongoing debate about the most suitable morphological or functional liver unit. This has to do with the fact that the peripheral polygonal boundaries of classic liver lobules are not easy to recognise (partially due to sinusoidal anastomoses between lobules), except for a few species. As such, the liver lobules of pigs, camels and polar bears are well-defined by interlobular septa of connective tissue, while connective tissue is sparser in the human liver. Furthermore, liver lobules are not always perfect prisms, and variations are frequently observed in the number of PTs per lobule as is also observed in chapter 9 (e.g. polyhedral lobules with four, five or seven corners instead of six). Consequently, other units have been proposed in the past. Below, we give an overview of a number of alternative functional units [118, 119, 303, 309, 377, 409, 417, 466, 496].

Mall [305] favoured the ***portal lobule*** (also called the portal unit) as the true structural unit of the liver. Hereby, the portal lobule is centred around

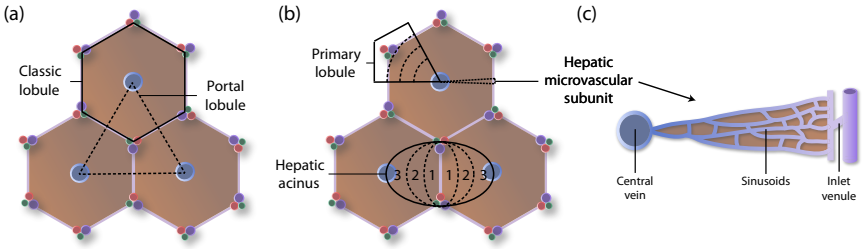

Figure 1.10: Schematic illustration of several structural and functional liver units: (a) the classic hexagonal lobule centred around a central vein (CV) and the portal lobule centred around a portal tract (PT); (b) the primary lobule with sickle zones and the hepatic acinus with its corresponding zonation (periportal zone 1, intermediate zone 2 and pericentral zone 3); (c) the hepatic microvascular subunit.

a PT and extends to the closest three CVs. Hence, a portal lobule has a triangular shape (Fig. 1.10a).

The ***hepatic acinus*** proposed by Rappaport et al. [394] is probably the second most used liver unit (after the classic lobule). It was defined as a unit related to the afferent vessels of the microcirculation. The simple hepatic acinus represents a parenchymal mass having an irregular size and shape, bordered by two PTs and two CVs (Fig. 1.10b). Its shortest axis is the connection between two PTs, including connective tissue and a vascular septum. An acinus is arbitrarily divided in three zones implying zonal heterogeneity: zone 1 lies closest to the PTs (periportal), zone 3 is closest to the CVs (pericentral) and zone 2 lies in between zones 1 and 3 (intermediate). In this interpretation, zone 1 is thought to receive most nutrients and oxygen, while zone 3 receives partially deoxygenated blood carrying fewer nutrients. However, there are a number of papers, in which metabolic activity is experimentally measured, stating that the acinar zonation is not the most optimal zonation method [466, 532]. The simple acinus occupies parts of two neighbouring lobules in 2D. The locations of the terminal afferent vessels of neighbouring acini are called the nodal points of Mall. The concept of simple acini was also extended to ***complex acini***, containing at least three simple acini and the parenchyma around the preterminal portal venule accompanied by its arteriole and bile duct. On its turn, the ***acinar agglomerate*** consisted of three or four complex acini [271, 377, 382, 394].

The ***primary lobule*** of Matsumoto et al. [317, 318] contains a group of sinusoids that are supplied by a single portal inlet venule (and its neighbouring terminal hepatic arteriole) and drain into a CV (Fig. 1.10b). The classic lobule consists of 6-8 primary lobules, and is consequently named the ***secondary lobule***. The concept of the primary lobule seems to give evidence of another type of zonation, called sickle zones. Sickle zones seem to correspond better with the actual liver physiology than the zonation based on the hepatic acinus [317, 465]. Furthermore, Matsumoto clearly highlighted the role of VS [317, 322, 409].

Bloch [40] and McCuskey [320] proposed the ***hepaton*** as the hepatic functional unit, as they suggested that the functional liver unit should be the minimum amount of tissue required to perform liver function. As such, the hepaton was defined as a single sinusoid with a cylinder of surrounding tissue including afferent and efferent blood vessels, biliary vessels and lymphatic connections [309, 377, 409].

Later, the ***choleon*** was introduced by Hoffman [202] as the exocrine secretory unit consisting of a group of hepatocytes drained by a single portal bile duct [409].

Following the report of the hepaton, Ekataksin and Wake [119] came to a similar conclusion that most terminal portal vessels preferentially perfused a certain column of sinusoids. These can be interpreted as having a

conical shape with a wider base at the lobule perimeter and a point end at the lobule centre. They called this pyramidal group of sinusoids the ***hepatic microvascular subunit*** (Fig. 1.10c) [119, 409]. Furthermore, Ekataksin and Wake [119] showed that the choleon spatially overlaps with the pyramidal column of sinusoids of a hepatic microvascular subunit. The parenchymal mass of liver cells associated with this overlap is thus equipped with all necessary structures to perform exocrine and endocrine liver functions. Hence, this configuration was called the ***choleohepaton***, being a combination of a hepaton and a choleon [116, 119, 409].

In his turn, Teutsch et al. [465, 466] introduced the ***primary unit*** or primary module and the ***secondary unit*** or secondary module based on three-dimensional reconstructions using serial cryosections. The liver module is compatible with the primary lobule of Matsumoto, but with more irregularities in shape. In the modular concept of Teutsch, the complexity of the real shapes in liver units is represented in the marked variation of size, in shape, in number of facets, in concavity or convexity of the facets, and also in the number of primary units assembled into the secondary modules [465]. One should realise that hexagons and pentagons are considered as geometrically idealised perfections of the real lobular shape [104].

In addition to the described liver units, a number of other units were proposed during the last decades, but never really permitted acceptance (e.g. the metabolic lobule of Lamers, the modified zonal microcirculatory unit, the hepatom, the billion, the porton etc.) [119, 271].

1.1.3 Individual and interspecies hepatic anatomical differences

Although the general characteristics of the hepatic macro- as well as microanatomy are similar among individual humans and different mammalian species, there are individual variations as well as interspecies anatomical differences. Since human and rat livers are being used in this PhD dissertation (part II and III), it is worth having a look at these differences.

1.1.3.1 Individual anatomical variations

Macroscopically, individual human livers differ in size, weight and shape. Additionally, a lot of variations have been observed previously when analysing the branching patterns of the hepatic vasculature as well as the biliary tree [255, 301]. Below, we briefly discuss a few of these variations.

For the HA tree, Gruttadauria et al. [172] reported HA anomalies in 42% of 701 individuals. In most cases, the HA arises from the coeliac artery (or trunk as mentioned earlier) and provides blood flow to several arterial vessels (see section 1.1.1.2). Anatomical variations have been described of which the most frequent ones are a replaced or accessory right HA arising from the

superior mesenteric artery, or a replaced or accessory left HA arising from the left gastric artery [172, 377].

The PV tree also displays a substantial degree of variations. Gupta [176] reported that the PV of approximately 80% of the individuals splits into a right and left branch at the porta hepatis. In contrast, about 10% of the individuals have a PV dividing into three branches (two to the right and one to the left [133]).

Concerning the HV tree, the middle hepatic vein usually drains into the left hepatic vein just before its termination, but variations of this organisation have been described. In addition, there are variations of the number of accessory hepatic veins [122, 177].

These individual variations and differences in vascular anatomy are especially relevant in the context of surgical planning (e.g. for living donor liver transplantation or segmental liver resection; see also chapter 8) [255].

1.1.3.2 Interspecies anatomical differences

Next to individual differences between humans, it is important to take into account the more outspoken anatomical differences between species. Tremendous differences between species (e.g. pigs, dogs, rats, primates, humans) have been reported when studying the hepatic anatomy, histological features and vasculature [377]. Caution is thus needed when extrapolating results obtained in animals to the human setting. A few examples of species-dependent hepatic variations are provided showing that animal models may not always be a good tool to compare with human liver properties [80, 117, 203, 305, 312, 400, 417, 465, 526].

Macroscopically, the liver size and weight as well as the number of liver lobes and their relative sizes differ between species (Fig. 1.11). For instance, the rat liver has a small size and a different division in liver lobes compared to the human liver [257, 258, 312, 323, 466]. Its VCI is completely intrahepatic, which is not the case for human livers. Furthermore, the PV of the rat trifurcates while in the normal human liver, the PV only bifurcates. Also, the rat (as well as the horse and deer) has no gallbladder, in contrast to humans, dogs, pigs, mice etc. [312]. The external morphology of the porcine liver also clearly differs from the human liver morphology. The pig liver has three main lobes (the right lateral, the median and the left lateral lobe), while the human liver is known to count four main lobes (see section 1.1.1.1). The segmental anatomy is similar to that of the human liver, albeit there are substantial differences in the relative volumes of segments compared to the human liver [80, 526].

Also microscopically, there are a number of remarkable interspecies differences. For instance, the lobules of the porcine liver are clearly delineated by septa of connective tissue between the portal tracts, while the human liver

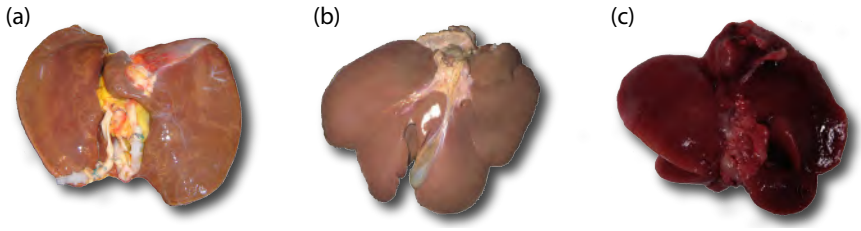

Figure 1.11: Comparison of the liver of different species: (a) human liver, (b) porcine liver (adapted from [80]), (c) rat liver (adapted from [533]).

typically contains less connective tissue [417]. In addition, the frequency of arterioportal anastomoses in the microvasculature is said to be species-dependent. For instance, the presence of arterioportal anastomoses is frequent in rats, but not in hamsters and humans [322, 324, 417]. Teutsch [465] reported that sinusoids are typically longer in humans than in rats, and that the branching pattern of the CV tree is different.

1.2 Liver functions

The metabolic activity of the liver is without any doubt a very complex phenomenon. The liver is responsible for more than 500 functions, contributing to the homeostasis of the body. These functions range from the synthesis, storage and breakdown of proteins and cholesterol to the degradation of toxic substances. All these activities depend on the well-functioning of the blood circulation, which is the main topic of this manuscript. Below, a short overview of the most important liver functions is given [311, 409].

1.2.1 Regulation mechanisms of hepatic blood flow

1.2.1.1 Sphincters

The sinusoids contain inlet and outlet sphincters, as mentioned in section 1.1.2.1. These sphincters are able to regulate the sinusoidal blood flow. The arterial inflow regulation is possibly triggered by the need for oxygen: if the oxygen concentration is too low, sphincters may react by altering the ratio of arterial to portal blood inflow [169, 321, 377].

1.2.1.2 Stellate cells and endothelial cells

Hepatic stellate cells have been suggested to play a role in controlling the hepatic vascular resistance to blood flow due to their cytoplasmic processes and contractility [267, 409]. Endothelial cells are able to expand or contract as a response to a variety of vasoactive substances. Hereby, the diameter of the sinusoidal lumen is changed, resulting in alterations of the vascular resistance and blood flow [377].

1.2.1.3 Hepatic arterial buffer response (HABR)

The hepatic arterial buffer response (HABR) is the compensatory response of the HA to changes in PV blood flow. For instance, an increase of the PV flow will lead to a decrease of the HA flow. This mechanism is thought to be based on the adenosine washout: the metabolic washout hypothesis [114]. Adenosine is produced at a constant rate and released into the space of Mall, surrounding the HA resistance vessels and the PV branches. The adenosine concentration in the space of Mall depends on the adenosine washout by the blood flow through the neighbouring PV and HA vessels. When PV flow decreases, less adenosine will be washed away, resulting in higher adenosine concentrations surrounding the HA vessels. This will trigger the HA vessels to dilate, resulting in a higher HA flow. Also, the opposite response is present: when the PV flow rises, more adenosine will be washed away, resulting in more constricted HA vessels and a lower HA flow. This mechanism is thus intended to preserve a nearly constant hepatic blood flow, maintaining the hepatic clearance functions and adequate blood levels of nutrients, hormones, oxygen etc. In addition to the adenosine washout hypothesis, some studies report that other mediators may also play a role in the HABR regulation (e.g. nitric oxide, carbon monoxide, H_2S etc.). It is also believed that - in physiological conditions - a similar response does not exist for the PV. As such, it is thought that the PV flow doesn't change as a response to an altered HA flow [114, 169, 216, 275, 276, 278, 377, 401, 409, 496].

The HABR is, to some extent, related to the flow competition phenomenon between the HA and PV that we observed during previous perfusion experiments with isolated porcine livers (see section 3.3.3). For instance, the PV flow was altered as a response to HA pressure changes and this phenomenon was reversible when decreasing the arterial inflow. This PV response is not accounted for by the HABR. An elevated pressure in the VCI was also able to provoke flow competition in our experiments. Note, however, that we observed flow competition *ex vivo* in isolated organs, while the HABR has been observed *in vivo* under physiological conditions [342].

1.2.1.4 Nervous control

Two plexuses of nerve fibres are found near the PTs of the liver: parasympathetic (hepatic branches of the vagus nerve) and sympathetic fibres [41]. The fibres extend into the parenchymal tissue and tend to run along sinusoids (mainly sympathetic fibres). Neurotransmitters may be released from the intrasinusoidal fibres and may affect the lipid and carbohydrate metabolism as well as the intrahepatic haemodynamics by changing the vascular resistance. However, transplanted livers also have the ability to function satisfactorily, while they are denervated during the transplantation procedure and not reconnected afterwards. Consequently, some authors suggest that the neural regulatory mechanisms are less important [377, 409].

1.2.2 Hepatic lymph flow

In normal circumstances, the liver produces about 1 to 2 litres of lymph per day by which the liver is the largest source of lymph in the body. Hepatic lymph typically has a high protein content and a high content of cells (mainly lymphocytes and macrophages). The hepatic lymph flow rate is proportional to the hepatic blood flow rate: approximately 0.5 ml lymph for every litre of blood flow. Hepatic lymph production is mainly situated in the space of Disse between the hepatocytes and the endothelial cells (protein-rich lymph), supplemented by a small amount of lymph production in the peribiliary capillary plexus of the PTs (protein-poor lymph).

The terminal vessels of the lymphatic tree are a fine plexus associated with the finest arterial ramifications in the interstitium of the small PTs. Larger lymph vessels are also associated with PV and biliary branches, resulting in a fourth element in the PTs (Fig. 1.12). In addition, two other types of smaller (and less important) lymphatic plexuses have been described: one associated with hepatic veins and one with the capsule of Glisson. The lymphatic vessels exit the liver at the porta hepatis and drain into the hepatic lymph nodes or alternatively via the falciform ligament or the bare area.

The lymph system is responsible for several functions including the formation of lymphocytes and antibodies, the removal of dead bacteria and waste products, the transportation of fats and fat-soluble vitamins etc. If the pressure in the sinusoids rises, the lymph production will increase. Doing so, the excess fluid and proteins of the interstitial spaces are drained, resulting in a protein-rich ascitis fluid [277, 309, 369, 377, 409].

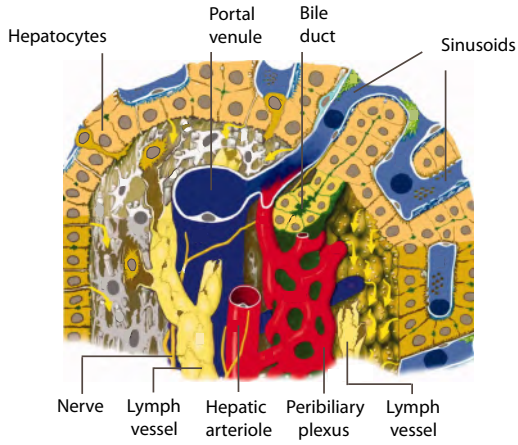

Figure 1.12: Illustration of the microscopic liver anatomy showing a lymph vessel in the interstitial tissue of a portal tract (PT). Adapted from [369].

1.2.3 Bile production and secretion

The hepatocytes of the liver produce bile for export to the duodenum. In normal conditions, 600 to 1200 ml bile is secreted daily. Bile is a yellow-greenish fluid composed of water, bilirubin, bile salts, phospholipids, proteins, cholesterol etc. [311, 377].

Bilirubin, the major bile pigment, is a product of the breakdown of normal haeme - a component of haemoglobin present in red blood cells - which takes place in the spleen, liver and bone marrow. Daily, 250-300 mg bilirubin is produced. Free bilirubin is not water-soluble. Most of the free bilirubin is attached to albumin proteins for transport. The rest is partially attached to glucuronic acid. This form of bound bilirubin is water-soluble and can be secreted in bile. After transport by bile into the small intestine, bilirubin is transformed by bacteria into urobilinogen, which is responsible for the brown colour of faeces [311, 409].

Bile salts are derived from cholesterol and play an important role in the digestion of fats by emulsifying them. In this way, fats are decomposed into smaller particles, which are easier to handle by the digestive enzymes. Furthermore, bile salts are important for the absorption of cholesterol. The conversion of cholesterol into bile acids by the liver is the most important way of cholesterol decomposition in the human body. Though several substances in bile leave our body through faeces, there is a recycling process for bile salts: the enterohepatic circulation. About 90% of the bile salts are reabsorbed in this process at the level of the intestines. Subsequently, the bile salts are brought back to the liver through the PV and can be resecreted in the newly formed bile [233, 434].

1.2.4 Immunological barrier

The Kupffer cells of the liver are important for the immune system because of their phagocytosis function. Kupffer cells are able to remove 99% of the bacteria in PV blood coming from the intestines when it reaches the sinusoids and before it enters the blood circulation. This filtration system prevents e.g. colon bacilli from contaminating the systemic circulation before entering the general circulation [309].

1.2.5 Detoxification

The liver is able to remove hormones, medication, alcohol and other biological active molecules from the blood through bile production and by phagocytosis by Kupffer cells as well as through chemical reactions at the level of the hepatocytes [309, 311]. For instance, the liver possesses an enzyme to transform ammonia into urea. Subsequently, the liver secretes urea, after which urea is cleared from the blood by the kidneys and removed via the urine [434]. Moreover, the liver inactivates steroid hormones, different types

of medication and other xenobiotics by modifications of their chemical structure. As a result, these substances are less active, more water-soluble and thus easier to excrete by the kidneys.

1.2.6 Carbohydrate metabolism

The liver helps regulating the blood glucose homeostasis. Keeping the glucose concentration within a narrow range is important for the human body to ensure adequate glucose delivery to the cells [409]. After a meal rich in carbohydrates, the liver is able to remove glucose from the PV blood. First, the glucose is transformed into glycogen (glycogenesis) to fill up the glycogen supply, and secondly into triglycerides for storage (lipogenesis). Hepatocytes can store up to 8% of their weight as glycogen and an average adult liver stores approximately 80 g of glycogen. After a period of fasting, the liver will secrete glucose into the blood by the conversion of stored glycogen (glycogenolysis) or the conversion of other molecules (lactate, amino acids, glycerol and pyruvate) if no more glycogen is available (gluconeogenesis) [311]. The carbohydrate metabolism is regulated by hormones (e.g. insulin, glucagon, adrenaline) and the nervous system [409].

1.2.7 Lipid metabolism

The liver is essential for the lipid metabolism in the body, e.g. because of its ability to emulsify fats, to store fats, to produce lipoproteins and to synthesise fats from proteins and carbohydrates. Lipids (e.g. triglycerides, fatty acids, cholesterol esters) are not soluble in water and need lipoproteins for transport in the plasma. According to the density, three types of lipoproteins are distinguished: very low (chylomicrons), intermediate and high density lipoproteins. Chylomicrons (containing dietary fats) lose their triglycerides due to the action of lipoproteins. The rest of the chylomicrons (including cholesterol) is further metabolised by the liver. High density lipoproteins transport cholesterol from the tissues to the liver [409]. Concerning the fatty acid metabolism, the liver is active in the oxidation of fatty acids to acetyl coenzyme A for the production of energy. Alternatively, the acids are used to form triglycerides, phospholipids or cholesterol esters. When there is an excess of energy, glucose is converted by the liver to fatty acids. These acids are used to synthesise triglycerides (lipogenesis; also mentioned in section 1.2.6) [311, 409].

1.2.8 Protein metabolism

The hepatic protein metabolism assures the breakdown of amino acids (deamination), the formation of urea to remove ammonia (highly toxic) from the human body, the synthesis of most plasma proteins, coagulation factors and non-essential amino acids as well as the conversion of amino acids into

other amino acids (transamination). The hepatic synthesis of proteins (mainly plasma proteins) accounts for 15% of the proteins produced in the human body. This synthesis is influenced by several factors such as the nutritional state (when fasting, protein synthesis drops), hormones (e.g. insulin), tissue injury or inflammation etc. The most important proteins secreted by the liver are albumin, transferrin, ceruloplasmin etc. Albumin accounts for approximately 70% of the plasma proteins and is an important constituent of blood, acting as an acid-base buffer which binds drugs and electrolytes in the blood. Most plasma globulins are also produced in the liver. These globulins perform several functions such as the transport of cholesterol, triglycerides, steroid hormones etc. Furthermore, most components necessary for coagulation are synthesised in the liver, as well as many of the proteins active in fibrinolysis and proteins playing a role in the complement system (important for the immune response). The liver also releases amino acids destined to be used by other tissues [311, 409]. Next to protein production, the liver also breaks down proteins to amino acids, which are reused to synthesise new proteins or to produce energy [409].

1.2.9 Vitamin metabolism

The liver is responsible for the storage of vitamins such as vitamin A, D and B_{12}. Large quantities of vitamin A are stored in the hepatic stellate cells, complemented by vitamin D and B_{12} [309, 311].

1.2.10 Iron metabolism

Except for the iron in haemoglobin molecules, the liver is the biggest storage location for iron as ferritin. The liver functions as an iron buffer. When excess iron is available in the body fluid, the liver will convert iron into ferritin destined for storage. When the level of circulating iron decreases to low levels, iron is released from the ferritin stored in the liver [309, 311].

1.2.11 Biotransformation

The liver plays a crucial role in the metabolism of drugs to protect the body against harmful chemicals (xenobiotics) by converting drugs and alcohol into inactive products that can be secreted by the kidneys. Most water-soluble xenobiotics are eliminated via the kidneys, while the non-water-soluble xenobiotics are first metabolised by the liver to less lipophilic substances, which are easier to eliminate by the kidneys. This involves two subsequent phases: first the oxidation, reduction, hydrolysis and hydration reactions, and secondly, the conjugation with hydrophilic ligands, making the molecules more water-soluble. Afterwards, the kidney or bile flow can eliminate the resulting conjugated metabolite [309, 311, 409].

1.2.12 Liver regeneration

The liver possesses the unique property of regeneration to re-establish the appropriate ratio between liver size and body size. This means that the liver is capable of growing back to a sufficient liver size after a partial hepatectomy (resection of up to 70% of the liver tissue; see also chapter 8). The liver is capable of healing rapidly and replacing damaged tissue in a time window of only a few weeks/months. Regeneration happens by proliferation of hepatocytes such that the critical mass, necessary for a normal liver function, is achieved [151, 239, 265, 309, 329–331, 409, 415, 464].

After liver injury, the hepatocytes secrete vascular endothelial growth factors. These factors bind to receptors of the sinusoidal endothelial cells. Hence, the sinusoidal endothelial cells proliferate and release other growth factors, among which interleukin 6 and hepatic growth factor. The latter promotes the proliferation of hepatocytes by induction of DNA synthesis in the hepatocytes [253, 409].

Interestingly, the growth of the liver remnant happens by enlargement of the remaining part, rather than a morphogenetic restoration of the liver shape. This phenomenon is called compensatory hyperplasia, because the remaining part enlarges due to hepatocyte proliferation, while the resected part does not grow back. The liver actually has two different types of growth mechanisms: liver regeneration and postnatal liver growth. In the case of liver regeneration, the enlargement of lobules is responsible for the growth following partial hepatectomy, resulting in liver lobules having a more complex and irregular shape. In contrast, postnatal liver growth is not only due to the enlargement of lobules, but also to the multiplication of lobules and the enlargement of hepatocytes [375].

Liver regeneration has consequences for liver transplantation. When a transplanted liver is too small for the host, the liver will grow to the optimal mass for this person. The inverse is also true: when a transplant liver is too big for the host, the liver will decrease in size [336, 409].

Chapter 2

Liver pathology

Liver pathologies range from mild infections to life-threatening liver failure. In general, symptoms of liver diseases seem to be negligible in the initial stage. When symptoms become more severe and start attracting attention, the condition is usually quite serious. An early and effective detection of liver disease is thus very important. A well-known example of a symptom is jaundice. The yellow colour of the eyes and skin indicates that bilirubin is no longer sufficiently filtered from the blood. Liver pathologies are often classified in two categories. The first category contains the hepatocellular diseases, characterised by inflammation and necrosis leading to liver damage. The cholestatic diseases make up the second category and are characterised by inhibition or obstruction of bile flow. A number of hepatic vascular disorders may be associated with hepatocellular or cholestatic diseases, which is especially relevant for the research concerning liver perfusion in this dissertation. In this chapter, we will discuss the major liver pathologies and hepatic vascular disorders, liver failure and the treatment options [214, 287].

2.1 Hepatocellular pathologies

2.1.1 Steatosis

Steatosis or fatty liver (Fig. 2.1b) is associated with a disturbance in the fat metabolism and leads to the accumulation of fat inside the liver. Steatosis occurs when the triglyceride synthesis is higher than the export or lipolysis (breakdown of lipids) capacity of the liver [409].

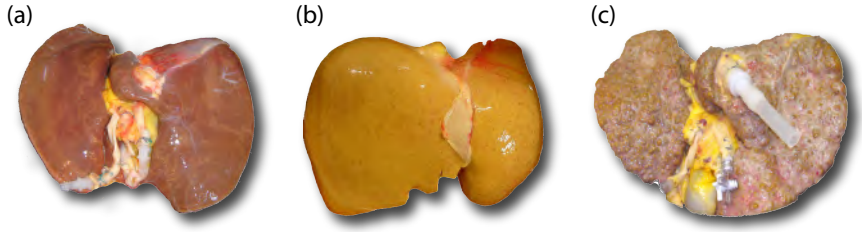

Figure 2.1: Illustration of the macroscopic differences between (a) a normal liver, (b) a steatotic liver and (c) a cirrhotic liver.

There are two types of fatty liver disease: macrovesicular and microvesicular steatosis (Fig. 2.2). Also, a mixture of macro- and microvesicular steatosis is possible.

The most frequent causes of macrovesicular steatosis are a fatty diet or obesity, chronic alcohol abuse, diabetes mellitus, drug abuse or hyperlipidemia. The cell architecture of hepatocytes is disturbed by large fat vacuoles, displacing the cell nucleus to the periphery of the cell (Fig. 2.2a). The accumulation of fat in the cytoplasm of hepatocytes results in an increasing cell volume, reducing the sinusoidal space up to 50% of its normal size, as well as the volume of the space of Disse. These microvascular changes result in an increased intrahepatic resistance due to narrow and irregular sinusoids and blood cell adhesion to sinusoidal walls. This may lead to sinusoidal obstructions. Consequently, the access of blood solutes to the ballooned hepatocytes is restricted, possibly leading to chronic hypoxia. Macrovesicular steatosis is often benign, but makes the liver severely susceptible to ischaemic injury and may even lead to liver failure. Macrovesicular steatosis is potentially reversible by taking away the cause, e.g. by stopping alcohol consumption [190, 217, 444].

Microvesicular steatosis is mostly caused by toxins or drugs, impairing mitochondrial beta-oxidation (one of the processes in the fat metabolism) and inducing inflammatory changes. Multiple small vacuoles are dispersed in the cytoplasm (Fig. 2.2b), but do not displace the nucleus or change the sinusoidal diameter, as is the case for macrovesicular steatosis. Nonetheless, severe microvesicular steatosis can lead to fulminant liver insufficiency, multiorgan failure, coma or even death. As such, microvesicular steatosis is more severe than macrovesicular steatosis [190, 217].

When the cause of steatosis is not taken away, fat accumulation can evolve to inflammation of the liver (hepatitis), as is the case in non-alcoholic steatohepatitis (NASH). NASH may result in liver fibrosis, and leads to cirrhosis in 20% of the cases (see section 2.1.4) [409, 444]. The severity of

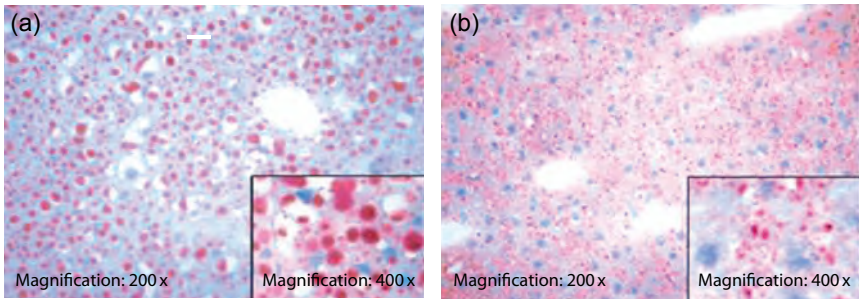

Figure 2.2: Oil red staining of steatotic cells: (a) macrovesicular steatosis showing large vacuoles, (b) microvesicular steatosis showing numerous small vacuoles. Adapted from [408].

steatosis is classified in three degrees: mild, moderate and severe steatosis corresponding to maximally 30%, 30-60% and more than 60% of the hepatocytes containing fatty inclusions, respectively [444].

The incidence of steatosis is continuously increasing, mainly due to the increasing number of cases of non-alcoholic fatty liver disease among the general population. Fatty liver disease is the most common liver disease in the Western civilisation with a non-alcoholic fatty liver disease prevalence of 17-33% in the United States [132, 408, 444].

2.1.2 Hepatitis

Hepatitis or inflammation of the liver is most often caused by a viral infection (virus of hepatitis A, B, C, D, E and G). Drugs, alcohol, medication etc. may also induce hepatitis (e.g. by a toxic overdose of paracetamol or ibuprofen). In addition, autoimmune hepatitis may be encountered when the immune system attacks the own liver.

Hepatitis A accounts for approximately 32% of the hepatitis cases and is a benign form with only an acute phase and no chronic stage. It is transmitted through the oral-faecal route by contaminated water, food etc.

Hepatitis B is responsible for more than 40% of the hepatitis infections in the United States and is transmitted by blood transfusions, sexual contact, contaminated needles, in utero from mother to unborn child etc. Patients with hepatitis B have 5% chance to develop a chronic infection. Vaccines for hepatitis A and B are available.

Hepatitis C may lead to chronic liver disease, which can be life-threatening. Hepatitis C patients have a 20% chance to develop cirrhosis and a 25% chance to develop hepatocellular carcinoma (HCC).

Hepatitis E is transmitted similar to hepatitis A and is known to cause waterborne epidemics in developing countries [103, 309, 311, 391].

2.1.3 Fibrosis

Chronic liver disease is mostly associated with liver fibrosis. Hepatic fibrosis is the process of excessive accumulation of extracellular matrix in the liver (Fig. 2.3). The deposition of a certain amount of extracellular matrix (fibrogenesis) is necessary for wound healing, but an excessive deposition can be pathological. Hepatic fibrosis is a dynamic and regulated process, in which an increase in the synthesis and a decrease in the degradation of extracellular matrix results in excess extracellular matrix in the liver, disposed in the form of vascularised septa in the space of Disse (perisinusoidal fibrosis). The latter results in a loss of fenestrations of the sinusoidal endothelial cells, a loss of hepatocyte microvilli and the formation of basement membranes lining the endothelial cells. The combination of fenestration losses with the presence of capillary basal membranes is called sinusoidal capillarisation [246, 486]. Fibrosis has a substantial impact on the mechanical behaviour of the liver, because the liver tissue becomes stiffer due to excess extracellular matrix. Since there is a cross-talk between the mechanical properties and the vascular perfusion of the liver, fibrosis may result in higher hepatic vascular resistances which alter the hepatic haemodynamics.

As a result of fibrosis, the liver function is impaired as the ability to exchange substances between blood and hepatocytes is reduced. Hepatic stellate cells play a key role in this process. They are activated by liver injury to become myofibroblasts and represent the main source of accumulated extracellular matrix in case of chronic liver injury. Liver fibrosis may lead to cirrhosis and increases the risk for HCC [285, 470].

Liver fibrosis is classified in five stages according to its location. As such, the METAVIR scale defines the F0, F1, F2, F3 and F4 stage as no fibrosis, portal fibrosis, periportal fibrosis, bridging fibrosis (reaching from a portal area to another portal area) and cirrhosis, respectively [22, 154, 388].

2.1.4 Cirrhosis

Liver cirrhosis (Fig. 2.1c) is the (later) end-stage of any chronic and long lasting liver disease, characterised morphologically by a combination of fibrosis and regenerative parenchymal nodules, and functionally by a progressive loss of liver function, finally ending in liver failure. Liver cirrhosis is the most frequent reason for liver transplantation and is amongst the most important causes of death in the Western world. It is the twelfth most frequent cause of death in the United States and has a 5-year mortality rate higher than 50% [24, 311, 467].

Frequent causes of cirrhosis are the chronic or repetitive injuries due to alcohol abuse, long term infections of hepatitis B or C, fatty liver disease, diseases related to the biliary tree, inherited liver pathologies, drug abuse or intoxication etc. [24, 311].

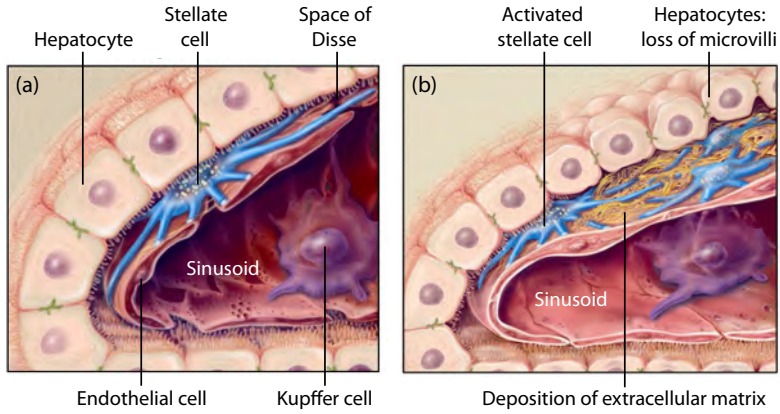

Figure 2.3: Illustration of the deposition of extracellular matrix in liver fibrosis: (a) normal liver; (b) injured liver with activated stellate cells. Adapted from [306].

Cirrhosis is the result of repetitive and sustained inflammatory liver injuries (cell death by necrosis) and healing responses (nodular regrowth of hepatocytes). It causes an excessive production of extracellular matrix and disorganised proliferation of hepatocytes. Liver cirrhosis is not limited to a local part of the liver, but is a diffuse process affecting the whole liver (Fig. 2.1c). The current definition of cirrhosis is based on morphological grounds, as described by Anthony et al. [22]: *"Liver cirrhosis is a diffuse process characterised by fibrosis and the conversion of normal architecture into structurally abnormal (regenerative) nodules"*. Liver fibrosis (see section 2.1.3) is the early stage of cirrhotic liver disease, while the formation of regenerative nodules is the more advanced stage. Regenerative nodules are lumps of liver tissue, surrounded by fibrous bands (Fig. 2.4).

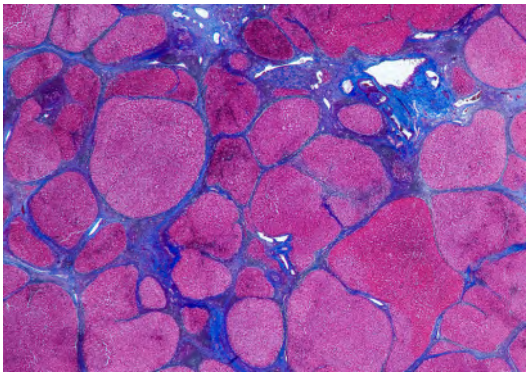

Figure 2.4: Histological image of advanced cirrhotic liver disease showing regenerative nodules surrounded by fibrous tissue. Source: [13].

According to the morphological characteristics, cirrhosis is usually classified in three main groups: micronodular cirrhosis, macronodular cirrhosis and a mixture of both. Micronodular cirrhosis is characterised by thin regular bands of connective tissue and small regenerative nodules with a diameter of 3 mm or less, containing no portal tracts or hepatic venules. Typically, the nodules have a uniform size and lack a lobular organisation, while terminal hepatic venules and portal triads are distorted. Micronodular livers may have an enlarged size (e.g. due to steatosis). Cirrhosis often begins with micronodular entities and may progress towards macronodular cirrhosis, but there are exceptions to this course of events. Macronodular cirrhosis is associated with regenerative nodules, having a diameter of more than 3 mm and possibly containing portal tracts and/or terminal hepatic venules. Macronodules vary considerably in diameter (3-50 mm) and are surrounded by broad fibrous bands of varying thickness. The concentration of portal triads in the fibrous scars suggests a collapse of the normal hepatic architecture. Macronodular livers may be reduced in size when they are severely scarred. In many cases, mixed cirrhosis is observed, which is a mixture of approximately equal portions of micro- and macronodules [22, 192].

Due to the morphological alterations in which newly formed masses replace normal liver tissue, cirrhosis has a devastating effect on the hepatic (micro)architecture resulting in a step-by-step loss of normal lobular structure and an altered mechanical behaviour due to the higher stiffness of distorted liver tissue. As such, scattered focal necrosis may occur and hepatic arterial (HA), portal venous (PV) and hepatic venous (HV) vessels may be tangled with each other. Abnormal branching patterns (e.g. parallel portal vessels of the same order), sharp bends, tortuosity and branching angles have been observed in blood vessels such as PV vessels in cirrhotic livers. An increased intrahepatic vascular resistance and the capillarisation of sinusoids result in a deteriorated hepatic perfusion and a loss of hepatic metabolic functions. Fibrous bridging may occur between portal tracts or between a portal tract and a central vein. Furthermore, new vessels may arise to create new blood supply and venous draining routes in regenerative nodules. Consequently, nodules give evidence of a complex and conspicuous vasculature [181]. Lymphatic vessels may be enlarged [497] and lymph flow increased, which may result in ascites when the remaining filtrated fluid passes into the peritoneal cavity [169]. Cirrhosis may also lead to the compression of biliary tracts impairing normal drainage, which may result in jaundice. In addition, patients may be confronted with other severe complications or symptoms such as portal hypertension, the formation of shunt vessels bypassing the hepatocytes (shunts between portal venules and hepatic venules) and arterioportal shunts (capillary shunting between arterioles or capillaries and portal venules) [47, 192, 212], the formation and bleeding of oesophageal

varices, ascites, hepatic encephalopathy, the hepatopulmonal or hepatorenal syndrome, liver cancer and even death. A number of these complications is more elaborately discussed in section 2.3 [55].

Since cirrhosis is characterised by a continuous disease spectrum of deteriorating liver function, cirrhosis is not a static disease, but rather a dynamic and potentially bidirectional process [154]. Hence, cirrhosis is clinically often classified in two stages: compensated and decompensated cirrhosis. In the first stage, compensated cirrhosis will induce liver damage, but the liver has the ability to compensate for the damage and functions normally. Compensated cirrhosis may thus be non-symptomatic and can be further divided in different substages, being with or without portal hypertension, with or without oesophageal varices. However, when extensive damage occurs, the liver is no longer able to function normally and decompensation takes place. Decompensated cirrhosis is associated with clinically evident complications which can be classified in three categories: portal hypertension (section 2.3), liver failure (section 2.4) and hepatocellular carcinoma (section 2.1.5) [154].

The severity and prognosis of cirrhosis can be estimated by using different scoring systems, of which a few examples are briefly discussed. The Child-Pugh score is used to classify patients based on their circulating levels of bilirubin and albumin, prothrombin time (international normalised ratio; INR), the presence and severity of ascites and encephalopathy. This score was originally intended to assess the risk of patients undergoing surgery (e.g. placement of a portosystemic shunt). The model for end-stage liver disease score (MELD; more elaborately discussed in section 3.1) is based on the risk of dying while the patient is waiting for a liver transplantation. Furthermore, there is the recently developed cirrhosis relative wellness index, which is based on desirability functions of 10 mostly uncorrelated parameters: prothrombin time, portosystemic encephalopathy mental status score, the quantities of aspartate aminotransferase (AST), creatinine, platelets, white blood cells, albumin, total bilirubin, sodium and haemoglobin [157].

2.1.5 Liver cancer

Primary liver cancer or hepatocellular carcinoma (HCC) is initiated within the liver. Most HCC patients have liver cirrhosis before evolving towards HCC. HCC is the third most common cause of cancer-related deaths worldwide and the fifth most frequent cancer [287]. Hepatitis B and C infections are the most important risk factors for HCC. Hepatic resection is not an option for the majority of patients with primary liver malignancies. This may be due to a severe hepatic dysfunction, the tumour size, the tumour location, multifocality and distant metastases. In the case of an unresectable liver cancer, patient survival is estimated at 2-10 months [89, 302].

Secondary liver cancer or metastasis means that the cancer originates from another organ and was spread to the liver.

Liver cancer is difficult to diagnose in an early stage, because the symptoms may be vague (weight loss, less appetite, fatigue, debility, jaundice, fever etc.). Often, liver cancer is diagnosed during surveillance radiological examination in the case of known cirrhosis.

2.1.6 Alcoholic liver disease

Alcoholic liver disease may originate when heavily drinking alcohol for a certain period of time. After consumption, alcohol is absorbed at the level of the gastrointestinal tract. Subsequently, the liver receives about 90% of the alcohol to be detoxified. The oxidative metabolism of ethanol in the liver may result in the formation of acetaldehyde (toxic molecule contributing to liver damage), highly reactive oxygen species (ROS; may lead to inflammation, necrosis and apoptosis) etc. Alcohol overconsumption may thus result in an alcohol overload and liver damage [124].

Often, patients with alcoholic liver disease first develop steatosis and then progressively evolve towards hepatitis and cirrhosis. The occurrence and progress of alcoholic liver disease depends on the drinking behaviour of the patient (the amount of alcohol consumed, the duration of alcohol consumption, binge drinking versus steady drinking etc.). Also, the type of alcoholic beverages may be important, since certain types of alcohol may be more toxic to the liver than others. More specifically, some studies state that wine drinkers are at lower risk of developing alcoholic cirrhosis compared to spirit or beer drinkers [171, 307]. Below, a short overview of the different (stages of) alcoholic liver disorders is given.

- ***Alcoholic fatty liver***

  Approximately 20% of the alcoholics develop steatosis, often associated with an enlarged liver (hepatomegaly). This condition may be reversible when alcohol consumption is stopped. However, alcoholic fatty liver can lead to death if alcohol consumption is not reduced or stopped. Furthermore, the liver may show inflammatory changes as an early sign of more severe liver disease.

- ***Alcoholic hepatitis***

  Usually, alcoholic hepatitis is diagnosed when a liver biopsy shows inflammatory changes, liver degeneration, fibrosis or other abnormal liver cell changes. Symptoms may include a swollen liver, nausea, vomiting, abdominal pain, fever, jaundice, liver failure, bleeding etc. In severe cases of alcoholic hepatitis, the mortality rate is 50%. When these patients continue to drink heavily, they have a 40% chance of developing cirrhosis [316].

- ***Alcoholic cirrhosis***

  Alcoholic cirrhosis is responsible for serious illness and many deaths. Approximately 10-15% of the individuals with alcoholism develop alcoholic cirrhosis. Possible symptoms are liver enlargement, capillary dilations leading to palm redness, finger muscle shortening due to toxic effects and fibrous changes etc.

Alcohol abuse may also be a risk factor in the context of other forms of liver disease. For instance, heavy drinking in combination with a hepatitis B or C infection substantially increases the risk of developing liver cirrhosis and people having alcohol-related cirrhosis have a much higher chance of developing liver cancer [124, 307].

2.1.7 Inherited liver diseases

Some liver diseases are inheritable, but do not show any symptoms until adulthood. An example is haemochromatosis, in which the iron metabolism is disturbed and the liver stores more iron from food than needed for the body. When haemochromatosis is not diagnosed, it can be lethal. Another inheritable liver pathology is the disease of Wilson. Here, too much copper is stored within the liver. When the excess copper enters the blood stream, this can lead to psychological symptoms or physical disorders (going from trembling, having difficulty to speak etc. to liver failure).

2.2 Cholestatic pathologies

2.2.1 Cholestasis

Cholestasis stands for a stagnation of bile flow in the liver. The causes may be intrahepatic (parenchymal diseases, pathology of intrahepatic bile ducts) and/or extrahepatic (problems with the extrahepatic bile duct conduits e.g. gall stones). Gall stones are caused by too much cholesterol or too little bile salts, resulting in cholesterol crystallisation. The stones obstruct the bile flow and may cause severe pain when the gallbladder contracts. Furthermore, the blockage of bile drainage may lead to an accumulation of bile pigments in blood and subsequently to jaundice [85, 103, 311, 434].

2.2.2 Primary sclerosing cholangitis

This pathology is associated with a chronic inflammation of the bile canals leading to destruction of the intrahepatic and/or extrahepatic bile ducts. Bile is no longer sufficiently drained from the liver (bile stasis) resulting in liver damage. Primary sclerosing cholangitis leads to hepatic fibrosis which can evolve towards cirrhosis, end-stage liver disease with liver failure and the

need for transplantation. Often, primary sclerosing cholangitis is preceded by inflammatory bowel disease. It takes a median time period of 12-18 years for a patient to go from the diagnosis of primary sclerosing cholangitis to end-stage liver disease [435].

2.2.3 Primary biliary cirrhosis

This chronic autoimmune liver pathology leads to slow, progressive damaging of the bile ducts. The slow progression of primary biliary cirrhosis may extend over several years with varying rates and disease severity among individual patients. Similar to primary sclerosing cholangitis, bile acids remain in the liver due to poor bile drainage and lead to damage of liver cells, fibrosis, cirrhosis and eventually liver failure. Primary biliary cirrhosis is histopathologically characterised by immune-mediated destruction of the intrahepatic bile ducts and portal inflammation [241, 288].

2.2.4 Cholangiocarcinoma

The bile ducts can also be afflicted by cancer. For example, cholangiocarcinoma is often the consequence of primary sclerosing cholangitis. It is characterised by malignant tumourous tissue in the intrahepatic bile ducts and has a poor prognosis with a mean survival time of less than two years [309, 435].

2.3 Hepatic vascular disorders

Most liver pathologies are associated with a number of complications, among which vascular disorders. Different vascular disorders often interact with each other (e.g. portal hypertension (see also chapter 8) and the formation or bleeding of collaterals). Below, an overview is given of the most frequent hepatic vascular disorders [385].

2.3.1 Portal hypertension

Portal hypertension is defined as an increased blood pressure in the PV. Any condition hampering the flow to the portal vein will lead to portal hypertension. The most important factors leading to portal hypertension are an increased vascular resistance of the liver and/or an increased blood flow in the splanchnic circulation. For instance in case of cirrhosis, which is the most common cause of portal hypertension, the intrahepatic resistance is increased, followed by an increase of the splanchnic blood flow in a more advanced cirrhotic stage.

The increased intrahepatic vascular resistance to blood flow is the result of a combination of structural and functional causes. Structural factors account for 70% of the resistance and include fibrosis, distortion of blood

vessels by regenerative nodules, capillarisation of sinusoids etc. Functional factors account for 30% of the resistance and are modifiable. Here, the hepatic stellate cells play a major role. Studies revealed that stellate cells are able to contract and relax in response to endothelium-derived vasoactive molecules. This response is enhanced during liver injury (stellate cell activation) and may lead to narrowing of the sinusoids. Nonetheless, the response of stellate cells can be modulated by the administration of vasoactive substances (e.g. nitric oxide). In the case of cirrhosis, a net increase of the hepatic resistance is due to the imbalance between vasoconstrictor and vasodilator agents.

Next to an increased vascular resistance, a higher splanchnic blood flow is the result of splanchnic arteriolar vasodilatation. This vasodilatation is caused by increased levels of circulating vasodilators and a reduced sensitivity to vasoconstrictors. When the intrahepatic vascular resistance is elevated, the increased blood flow maintains and further aggravates portal hypertension. Chronic vasodilatation increases the PV blood flow and may induce the formation of portosystemic varices. Splanchnic vasodilatation and an increased portal flow may result in a hyperdynamic circulation, which is a combination of a low arterial pressure, a low overall vascular resistance due to systemic vasodilatation, an increased heart rate, an increased plasma volume and an increased cardiac output.

The major complications of portal hypertension (related to cirrhosis) include the development of varices (collateral circulation), ascites, splenomegaly, hepatic encephalopathy and renal dysfunction. A severely elevated PV pressure increases the risk of variceal bleeding (see also section 2.3.2) [186, 267, 269, 405, 427, 467, 483].

Portal hypertension can be classified into three types, corresponding to the location of increased vascular resistance: prehepatic, intrahepatic (sinusoidal) or posthepatic. Fig. 2.5 schematically shows the potential causes of portal hypertension.

2.3.1.1 Prehepatic causes of portal hypertension

An impaired PV inflow may be caused, for instance, by a thrombosis or compression by a tumour in the PV or splenic vein. The consequences of blockage of the extrahepatic PV go from being well tolerated to catastrophic complications with death as a consequence. Impaired PV inflow or PV occlusion is often accompanied by abdominal pain, ascites, portal hypertension and principally oesophageal varices, prone to rupture [55, 83].

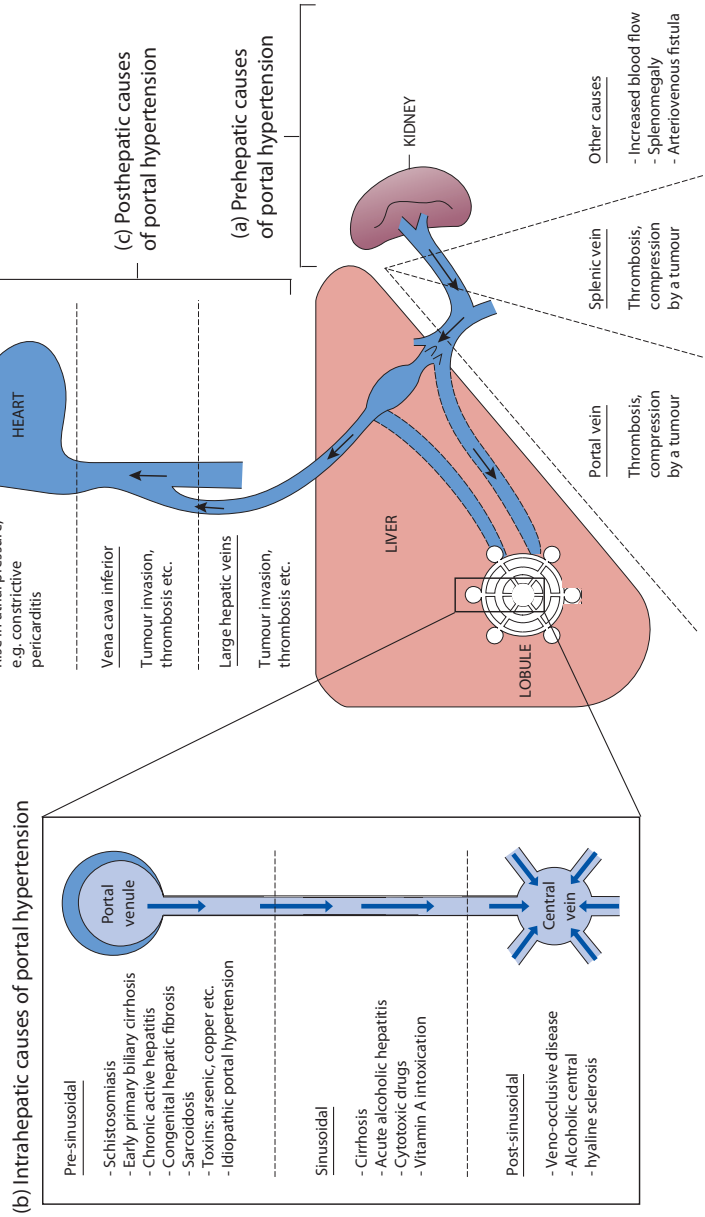

Figure 2.5: Causes of portal hypertension: (a) prehepatic, (b) intrahepatic and (c) posthepatic causes. Adapted from [55].

2.3.1.2 Intrahepatic causes of portal hypertension

Impairment of blood flow through the microvascular hepatic bed results in a major loss of physiological function. Cirrhosis is the most common cause of sinusoidal blood flow obstruction. This impairment is caused by capillarisation of the sinusoids, activated stellate cells constricting the sinusoidal lumen, fibrosis etc. Another disorder is the veno-occlusive disease, which may impair the hepatic flow and is characterised by the obstruction of microvascular HV vessels. This disease occurs primarily in patients receiving bone marrow transplantation and in cancer patients receiving chemotherapy [55, 83].

2.3.1.3 Posthepatic causes of portal hypertension

Typically, the obstruction of only one major HV is clinically silent, but an obstruction of two or more HV results in the Budd-Chiari syndrome, characterised by liver enlargement, ascites and pain. It is caused by the blood flow not being able to shunt around the blocked portion of the HV, inducing an increased intrahepatic blood pressure. The obstruction may be caused by an HV thrombosis as well as an obstruction of the inferior vena cava. When HV obstruction develops acutely, the liver is red-purple and swollen. Acute HV thrombosis has a high mortality when left untreated [55, 83].

2.3.2 Development of collateral circulation

When the pressure gradient between the PV and HV reaches a certain threshold (for instance in the case of portal hypertension), one often observes the development of a network of collaterals which decompresses the portal system. Doing so, blood is diverted into alternative routes from the PV tree to the systemic veins and bypasses the liver. The portosystemic collateral circulation is created by opening, dilation and hypertrophy of pre-existing vascular channels as well as by neoangiogenesis. By bypassing the liver, collaterals carry portal blood containing toxic substances (e.g. drugs) to the systemic circulation, which can result in severe complications such as encephalopathy, bleeding and sepsis. Despite the fact that collaterals lead to a decreased portosystemic resistance, the portal pressure usually remains elevated due to the persistent high portal inflow [382, 483].

Examples of the development of the collateral circulation are oesophageal and gastric varices. These vessels are fragile and prone to rupture. Hence, they can cause severe oesophageal and gastric variceal bleeding [55, 83, 222]. In cirrhosis, there is also a significant collateral flow into smaller veins that connect branches of the portal with the hepatic veins (portocaval shunts) [382].

2.3.3 Arteriovenous and portovenous shunts

Portovenous and arteriovenous shunt vessels may bypass the sinusoids and hepatocytes. These typically occur in case of cirrhosis. When a parenchymal region becomes extinct, the corresponding liver tissue collapses, resulting in a portal tract lying close to and adjacent to a terminal HV. This is an opportunity for the portal tract vessels to directly drain in the HV vessel and, hence, leads to the creation of shunt vessels [83].

2.4 Liver failure

In the case of liver failure, liver cells are so severely damaged that the liver is no longer able to function sufficiently. As a consequence, substances like bilirubin and ammonia start to accumulate in the body. This leads to symptoms such as jaundice, hepatic encephalopathy etc. A second consequence of liver failure is the absence of the synthesis functionality, resulting in hypoalbuminemia, coagulopathy etc. Liver failure can be life-threatening. Basically, there are four types of liver failure.

- ***Acute liver failure*** corresponds to an acute absence or drop in liver function in a time span of a few days or weeks. A whole range of clinical problems abruptly appears. Acute liver failure is rare, and - unfortunately - most of the times fatal.
- ***Chronic liver failure*** is more frequent than acute failure. Here, the liver is progressively damaged during a period of years. Hepatitis B or alcohol abuse are possible causes.
- ***Acute-on-chronic liver failure*** occurs when a patient with chronic liver failure develops a superimposed complication including acute liver failure.
- ***Primary liver dysfunction*** of a donor liver is sometimes observed in the context of liver transplantation. In this case, the donor organ is not working properly.

2.5 Treatment options for liver disease

In this section, different treatment options for liver failure are addressed: medical treatments, liver transplantation, (bio)-artificial livers and potential future treatments.

2.5.1 Medical treatments

Medical treatments focus on (early) detection of complications and the use of general supportive measures. This includes monitoring blood parameters (e.g. the glucose level), measuring the intracranial pressure etc. Classic medical treatments include the administration of drugs (e.g. to slow down or reverse the progression of fibrosis, to dissolve gall stones, antibiotics to treat patients with severe bacterial infections), surgical procedures (e.g. to remove the gallbladder or tumourous tissue) etc. Nevertheless, classic treatments are not sufficient to help patients with end-stage liver failure, whose only option to survive may be transplantation [24, 134, 161, 311].

2.5.2 Liver transplantation

Liver transplantation is often the only solution for patients suffering from incurable liver disease. More detailed information on this technique will be given in chapter 3.

2.5.3 The (bio-)artificial liver

The (bio-)artificial liver systems are - to some extent - comparable to acute kidney dialysis systems. They are intended to act as a bridge towards transplantation to gain time to find a suitable donor organ for patients, or to allow the liver to recover spontaneously. The best treatment for irreversible liver failure is liver transplantation, but unfortunately, the demand for donor livers is higher than the supply and some people die while being on the waiting list. These patients could be helped with an alternative or temporary solution, such as the artificial or bio-artificial liver. These systems could also help patients for whom liver transplantation is not an option due to contraindications, or for recipients in whom the liver graft does not function properly, but recovery may be expected [290, 359, 360, 381].

2.5.3.1 The artificial liver

Artificial liver systems only contain mechanical components and provide detoxification of blood through filtration and/or adsorption. They are not able to perform other liver functions such as the synthesis of substances. Filters with semipermeable membranes are used to separate the blood or plasma flow from the dialysis solution. Water-soluble particles are displaced from the blood compartment to the dialysis solution through diffusion or convection. Additionally, adsorption columns are used and contain activated charcoal or resin as adsorbent. In this way, the columns make sure that protein-bound toxins (especially albumin-bound toxins) are drained by adsorption or ion exchange. A few examples of artificial livers are the MARS system (Molecular Adsorbents Recirculating System, Gambro, Lund,

Sweden [9, 27, 107, 461]; Fig. 2.6a), the FPSA or Prometheus system (Fractionated Plasma Separation and Adsorption, Fresenius, Bad Homburg, Germany [8, 263]) and the SPAD system (Single Pass Albumin Dialysis) [161, 290, 309, 359, 360, 363, 381].

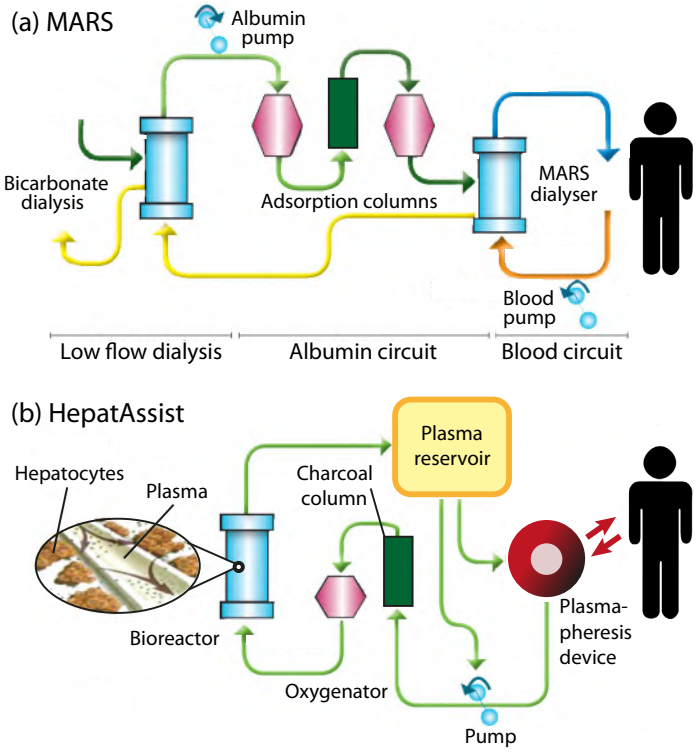

Figure 2.6: Schematisation of (a) the MARS system (Molecular Adsorbents Recirculating System; artificial liver) and (b) the HepatAssist system (bio-artificial liver). Adapted from [57].

2.5.3.2 *The bio-artificial liver*

Whereas artificial liver systems only provide detoxification, bio-artificial liver systems have the ability to also perform metabolic functions (protein synthesis, gluconeogenesis etc.). These systems contain one or more bioreactors filled with hepatocytes. Plasma flows through these bioreactors and is able to interact metabolically with the hepatocytes in the bioreactor. These hepatocytes can have different origins. The ELAD system (Extracorporeal Liver Assist Device [333]) works with immortalised C3A human hepatocytes, derived from a human hepatoblastoma cell line. In contrast, the HepatAssist system uses porcine hepatocytes (Fig. 2.6b). Porcine as well as human hepatocytes are being used in the MELS (Modular Extracorporeal Liver Support

[416]) and AMC BAL (Academic Medical Centre Bio-Artificial Liver [364]) systems [325, 381]. Previously, our group developed numerical models to simulate the flow and mass transport in the AMC BAL [309]. During the last decade, however, researchers shifted their focus more to the artificial liver instead of the bio-artificial liver for several reasons, such as safety concerns about the use of porcine cells (risk of zoonosis) and the use of human cell lines derived from liver tumour cells [363].

Using (bio-)artificial systems, improvements have been achieved such as a decrease of jaundice, more stable haemodynamics, reduction of portal hypertension, lowering of the intracranial pressure and improvements of hepatic encephalopathy. However, these beneficial effects are often of short duration, while the long term survival time, which is a crucial parameter, did not change significantly. Hence, more elaborate and long term research is necessary to improve and optimise these systems [363].

2.5.4 Future perspective on liver disease therapy

Currently, experimental technologies such as adult hepatocyte transplantation, foetal hepatocyte transplantation and bone marrow stem cell transplantation are being explored as possible future therapies for liver failure. Several clinical studies on these therapies attempted to enhance liver regeneration. They showed clinical improvements, but the mechanisms leading to these improvements are still unknown [403]. Since no overall survival benefit was observed without transplantation, these therapies should still be considered as experimental treatments and more research is necessary [44]. However, when up and running, these technologies have the potential of establishing an unlimited supply of hepatocytes. This would facilitate hepatocyte transplantation [20, 367, 529].

CHAPTER 3

Liver transplantation

The history of liver transplantation, which is the main research context of this manuscript, started in 1955, the year in which Welch [504] used the term 'liver transplantation' for the first time in the scientific literature. He reported on a canine liver transplantation experiment. During the following years, versatile transplantation procedures were tested and optimised on dogs. Eventually, in 1963, Starzl performed the first series of human liver transplantations [446, 447, 450]. Unfortunately, the first donor liver recipients died within the first 3 weeks after transplantation. A few years later, liver transplantation had become more successful. In 1967, the first human liver transplantation with a survival time of more than one year was accomplished [447, 448]. At that time, the estimated chance to survive one year after liver transplantation was about 30%. Survival chances luckily augmented substantially during the eighties with the introduction of cyclosporin [58, 449], an immunosuppressive drug to prevent rejection. From that moment on, chances to survive at least one year after liver transplantation increased up to 80% [248, 282, 447, 449, 481]. At present, survival chances are even 85% according to international registry data or higher (for instance higher than 90% in the University Hospitals Gasthuisberg, Leuven, Belgium [383]). The major reasons for these increased survival chances are optimised surgical procedures, better preservation techniques, better immunosuppressive agents, better patient selection, better prophylaxis and infection treatments, and an improved care during the peri- and postoperative period [454].

Irreversible acute or chronic liver failure is ideally treated by liver transplantation. The primary indications for liver transplantation in Europe, according to the European Liver Transplant Registry, are given in Fig. 3.1 for

the period 1988-2010 [6]. The total number of liver transplantations in this period was 86764. Liver cirrhosis was responsible for more than half (58%) of these liver transplantations.

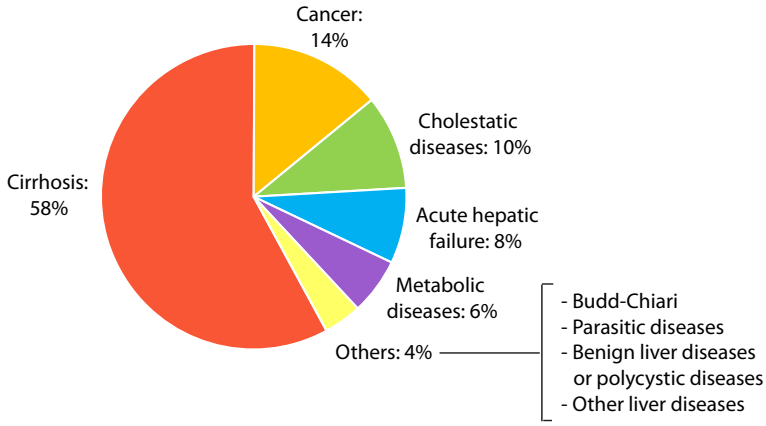

Figure 3.1: Primary indications for liver transplantation from January 1988 until December 2010 according to the data of the European Liver Transplant Registry [6].

3.1 The donor pool

Although liver transplantation is now a successful therapy for end-stage liver disease, there is a large shortage of donor livers. The evolution of the shortage of donor livers is illustrated in Fig. 3.2. Since the number of patients on the waiting list substantially outnumbers the availability of donor livers (in 2012 by approximately 33% based on Fig. 3.2), patients are dying while waiting for transplantation. As such, 660 patients with liver failure died in 2012 in the Eurotransplant region while waiting for an organ (see also section 3.2.1.1) [127]. The number of patients on the waiting list has been increasing enormously during the past 20 years. In fact, the number of patients waiting for a liver in 2012 is approximately the ten-fold of that in 1991, while the number of transplantations rose to approximately its three-fold. The elongation of the waiting list is due to different factors, such as the increasing number of patients with liver cirrhosis (for instance following steatosis or hepatitis C infections), new indications for transplantation etc. A lot of research efforts are invested in tackling the donor shortage problem by searching for new resources to enlarge the donor pool, for instance by the usage of extended criteria donor livers. As a result, the donor pool for liver transplantation represents different types of donors, based on their origin. Basically, there are deceased donors and living donors. Hereby, deceased donors are classified in three types: donation after brain death donors (DBD), donation

after circulatory death donors (DCD) and extended criteria donors (ECD) [68, 248, 345, 355, 481].

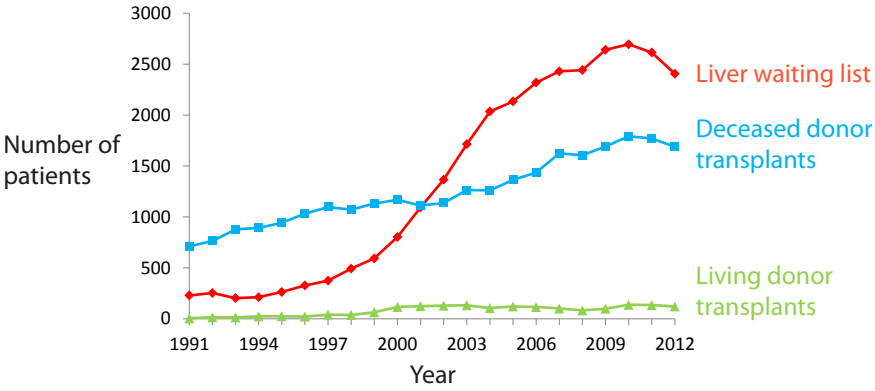

Figure 3.2: Evolution of the number of patients on the waiting list for liver transplantation within the Eurotransplant region (red), the number of deceased donor liver transplantations (blue) and the number of living donor liver transplantations (green) between 1991 and 2012 according to the data of Eurotransplant [127].

3.1.1 Donation after brain death

The major portion of the transplanted donor livers originates from donation after brain death donors (DBD). In the case of DBD donors, cerebral death is diagnosed because of severe brain damage and irreversible cessation of all brain functions. The blood circulation in all organs (except for the brain) is still intact, implying that the liver receives blood and oxygen until the onset of the organ procurement procedure. Though DBD donor organs are generally of good quality, they do not generate a sufficient donor pool to help all patients on the waiting list [454].

3.1.2 Donation after circulatory death

Donation after circulatory death (DCD) donors, previously referred to as non-heart-beating donors, are declared dead based on cardiorespiratory criteria and are characterised by the irreversible cessation of circulation. This implies that, at the moment of procurement, the organs are exposed to a certain period of warm ischaemia. Because of the stagnating blood circulation, several processes of organ damage are initiated, e.g. blood coagulation and anoxia under normothermic conditions. Since this hampers the chances of a successful transplantation and affects early graft function as well as survival, it is of utmost importance to shorten the period of warm ischaemia as much as possible [50, 292, 327, 389, 454].

Livers originating from DCD donors represent a potential resource to substantially enlarge the donor pool. Although the quality of DCD is known to be inferior to that of DBD donors (mainly due to an increased risk of ischaemic type biliary strictures), they are increasingly being used to decrease the shortage of transplantable organs. At the moment, DCD donors account for 10-20% of the donor pool in several countries [74, 345]. However, these organs are very susceptible to additional hypothermic preservation induced damage, which implies that it is very important to optimise preservation methods (such as machine perfusion; see also section 3.3 and chapter 6 and 7) for donor livers in order to improve the quality of these organs [54, 74]. DCD donors are divided in four categories [74, 259, 340, 345].

- ***Category 1: Dead on arrival at the hospital***
  These patients are declared dead upon arrival at the hospital. In this uncontrolled type of donor, the exact moment of cardiac arrest as well as the moment of onset of warm ischaemia is unknown.

- ***Category 2: Unsuccessful resuscitation after cardiac arrest***
  In this case, the patient fails to respond to cardiopulmonary resuscitation after witnessed cardiac arrest.

- ***Category 3: Cardiac arrest after withdrawal of life-sustaining therapy***
  In these patients, life-sustaining support (e.g. a ventilator) is withdrawn at a planned moment. This category mostly includes patients with irreversible brain injury who do not meet the criteria of cerebral death. After removing life sustaining therapy, irreversible circulatory arrest is awaited and a 'no touch' waiting period is respected before starting the organ procurement procedure.

- ***Category 4: Cardiac arrest in a brain-dead donor***
  This category includes brain-dead patients undergoing a sudden cardiac arrest.

In general, controlled DCD donors (category 3 and 4) provide organs which are suffering less from ischaemia than uncontrolled ones (category 1 and 2). The organs from controlled DCD donors result in a better posttransplant outcome.

With careful selection of donors and recipients (e.g. patients who can tolerate some degree of partial liver function), DCD liver grafts can be safely used to expand the donor pool, but until now no objective viability criteria have been defined [463]. Finally, euthanasia may potentially result in a new source of donor organs in countries where this is legal [345].

3.1.3 Extended criteria donors

The usage of extended criteria donors (or so called marginal donors) is clearly increasing, although their organs were previously believed to be untransplantable. Extended criteria donor organs are of less good quality compared to DBD donor organs. They are associated with a higher risk of physiological dysfunction and potential transmission of diseases. Furthermore, extended criteria organs are more succeptible to ischaemia-reperfusion injury, potentially resulting in an initially non-functioning graft, early graft dysfunction or severe damage of the biliary tract. Extended criteria include advanced age (older than 70 years), increased ischaemic time, prolonged stay in the intensive care unit, prolonged hypotensive episodes, macrovesicular steatosis, previous malignancy, hepatitis C infection etc. In fact, deceased after circulatory death (DCD) donors are also extended criteria donors, but they are discussed separately in section 3.2.2 [50, 135, 165, 282, 326, 341, 345, 355]. Below, we shortly discuss a few extended criteria.

- ***Advanced age***
  Since the life expectancy is generally increasing, the age of potential donors also increases. There is no universal age limit that is considered as a contraindication for donation. However, there are indications that the use of donors older than 70 years is associated with less favourable outcomes compared to younger donors. As such, advanced age is e.g. associated with an impaired drug metabolism and a higher susceptibility to toxins, which may be due to a reduced sinusoidal flow through aged livers. The loss of hepatic clearance capacity in the elderly is probably caused by a combination of leukocyte accumulations in the sinusoids, pseudocapillarisation of the sinusoids (thickening of the basement membrane and defenestration, deposition of collagen etc.) and dysfunction of liver sinusoidal endothelial cells [221, 496, 501]. In selected cases, equally good results have been reported after the transplantation of older livers compared to younger organs. Therefore, age should never be considered a contraindication for donation and transplantation. On the other hand, additional risk factors (such as steatosis or a prolonged ischaemic time) should be avoided [266, 345].

- ***Steatosis***
  Since the prevalence of steatosis (see also section 2.1.1) caused by obesity or alcohol intake is increasing, especially in developed countries, it is likely that more and more steatotic liver grafts will be encountered in clinics. Though many steatotic donor livers are discarded for transplantation, it has been reported that steatotic livers can be transplanted

with good results. Of course, it is recommended to only use grafts with a low or mild steatosis and without any extra extended criterion [183].

- ***Hepatitis C infection***
  Due to the shortage of donor livers, grafts with hepatitis C infections can be safely used to transplant hepatitis C positive patients. This procedure has been shown to be safe and leads to long-term survival of the recipient, comparable to using hepatitis C negative grafts. However, it is important to only use hepatitis C positive grafts without fibrosis, severe inflammation or cirrhosis [183].

Though the results seem to be promising, many transplant centres are still relatively reluctant to use extended criteria donor organs for transplantation because of the risk of lower organ viability and the higher chance of (initial) liver graft dysfunction. Attention should be paid to optimise preservation techniques for these organs. The latter is one of the research objectives of this thesis (see chapter 6 and 7).

3.1.4 Living donors

In the case of living donor liver transplantation, a healthy volunteer donates a part of his liver to a patient with liver failure (see also section 3.2.3.2).

3.2 Transplantation procedure

3.2.1 Organ allocation

3.2.1.1 The role of Eurotransplant

The Eurotransplant International Foundation is a non-profit organisation that coordinates the allocation and distribution of donor organs for the Eurotransplant countries, being Belgium, Austria, Germany, Luxembourg, The Netherlands, Slovenia and Kroatia. Transplantation centres in these countries have access to the Eurotransplant computer database, in which they can enter patient data to put patients on the international waiting list.

When a donor comes available, Eurotransplant first collects all relevant information about the donor and his/her specific organs. Subsequently, the Eurotransplant allocation computer algorithm determines the best donor-recipient matches for each organ taking into account valid medical and ethical criteria that are supported by the transplant community. The matching procedure is based upon a combination of several factors, such as the expected outcome and the national organ balance, since a reasonable balance is pursued in the exchange of organs between countries. More specifically, the general characteristics used to find a suitable recipient for an organ are the clinical urgency, the waiting time, virology, the ABO blood group rules,

the country balance, the centre and recipient profile, the presence or absence of sepsis, meningitis, malignant tumours, drug abuse etc. Since the cold ischaemic period must be limited to only a few hours (for some organs in particular such as the heart), transportation logistics are also taken into account to bring the donor organ from the country of origin to the potential recipient. In addition, there are some criteria specifically used when allocating donor livers: the weight (and height) of the donor as well as the MELD-score of potential recipients (see section 3.2.1.2).

When the physician treating the potential recipient accepts the donor organ, the patient is contacted and admitted to the hospital. Simultaneously, Eurotransplant establishes contacts between the donor hospital and recipient transplant centre, and arranges the transportation of the donor organ. When there is no suitable recipient found within the Eurotransplant region, other transplantation centres are contacted through other organ allocation organisations. Since the cold ischaemic period between organ procurement and implantation is limited (e.g. to approximately 12 hours for livers and 24 hours for kidneys), the whole process must run very smoothly [7]. The development of better preservation techniques allowing longer preservation times would be welcome to facilitate this process (see also section 3.3 and chapter 7).

3.2.1.2 Model for end-stage liver disease

The model for end-stage liver disease (MELD) score is helpful as one of the allocation criteria for liver transplantation. As shown in eq. 3.1, the MELD-score incorporates three different and objective lab parameters of the patient: serum creatinine (mg/dl), serum bilirubin (mg/dl) and the international normalised ratio (INR; reflecting blood coagulation) [236, 304].

$$\begin{aligned} \text{MELD} = {} & 9.6 \ln(\text{creatinine}) + 3.8 \ln(\text{bilirubine}) + 11.2 \ln(\text{INR}) \\ & + 6.4 \cdot (\text{aetiology: 0 if cholestatic or alcoholic, 1 otherwise}) \end{aligned} \tag{3.1}$$

The MELD score varies between 6 and 40. It reflects the condition of the patient, since it is a measure of the severity of the patient's illness and his/her probability of mortality within three months. A MELD score of 40 shows a patient with severe illness and an urgent need for transplantation, while a score of 6 shows a less diseased patient. In the case of organ allocation, donor livers are first allocated to patients with a more severe condition. In 2002, the United Network for Organ Sharing (UNOS) decided that the MELD score was a good measure to use in donor liver allocation. In 2003, Eurotransplant also started using the MELD score [7].

3.2.1.3 Contraindications for liver transplantation

Not all patients with end-stage liver disease are suitable for liver transplantation. The goal of these contraindications is to use the scarce amount of donor livers to gain a maximum of successes and advantages for the recipients. Contraindications are divided into absolute and relative counterarguments. Absolute contraindications include liver cancer with metastases, advanced cardiopulmonary pathologies, active alcohol abuse, as well as patients who are unable to accept the procedure or who are unable to understand and cooperate with the medical care after transplantation. Relative contraindications endanger a successful transplantation when balancing the disadvantages and advantages. Examples of relative counterarguments are chronic kidney diseases, old age, severe cardiovascular problems etc. Potential candidates for transplantation are thus first evaluated by a multidisciplinary liver transplantation team. If the result of the evaluation is positive, the patient is added to the waiting list [370].

3.2.2 Orthotopic liver transplantation

The most frequently used liver transplantation technique is orthotopic liver transplantation. Below, the donor procedure and the recipient procedure are discussed.

3.2.2.1 Donor procedure

According to the dead donor rule, procurement procedures can only start after the declaration of death. First, an incision is made in the donor body to provide exposure for multiorgan procurement. A thorough abdominal exploration can be performed to exclude any contraindications such as malignancy etc. In the next step, cannulas are placed in the aorta (and the inferior mesenteric vein) to flush the abdominal organs with a cold preservation fluid (4-6°C). As such, the blood of the donor is removed from the organ and the organs are rapidly cooled down. The peritoneal and pericardial cavities are filled with slushed ice to speed up the cooling process. The procurement of thoracic organs can start when flushing is initiated. Then, the abdominal organs are procured starting with a hepatectomy by mobilising the liver and by dissecting and transecting its blood vessels. Subsequently, the pancreas is removed en bloc with the duodenum and spleen, followed by the kidneys. Thereafter, the donor body is closed with respect. After procurement, the donor organs are packed for transport to the recipient transplant centre. Organ retrieval techniques may vary between different transplant centres. As such, possible variations are: single (aorta) versus dual cannulation (aorta and the inferior mesenteric vein or the portal vein), dissection in cold versus warm conditions, single versus en bloc organ removal, the usage of different preservation solutions etc. [50, 175, 454, 510].

During this normothermic process, organ ischaemia is absent in DBD donors, since the administration of cold preservation solution occurs shortly after circulatory arrest. In contrast, DCD donors (especially uncontrolled DCD donors) suffer more from normothermic ischaemia due to the prolonged period between cardiac arrest and cooling [345].

3.2.2.2 Recipient procedure

Once the donor liver has arrived at the recipient's transplantation centre, the organ is carefully inspected. When the liver is judged transplantable, benching of the liver graft is performed, meaning that unneeded tissue is removed and the hilar structures as well as the infra- and suprahepatic vena cava are dissected. Simultaneously, the recipient is prepared for transplantation. The recipient procedure counts three steps: the pre-anhepatic, the anhepatic and the post-anhepatic phase.

- ***Pre-anhepatic phase***

  During this phase, an abdominal subcostal incision is made and the recipient liver is mobilised to prepare for its removal. The bile duct and major blood vessels (hepatic artery (HA), portal vein (PV), suprahepatic vena cava (or vena cava superior; VCS) and infrahepatic vena cava (or vena cava inferior; VCI) will be isolated.

- ***Anhepatic phase***

  Vascular clamps are placed on the bloods vessels and the liver is removed. This hepatectomy is a dangerous intervention with risks of coagulopathy and major bleeding related to the portal hypertension. The occlusion of the PV and VCI results in a decreased venous return to the heart. Sometimes, a veno-venous bypass is used to prevent a drop in venous return. Doing so, blood from the lower body and bowel is bypassed towards the upper body, resulting in a better haemodynamic stability. After a successful hepatectomy, the donor liver can be implanted. The donor liver is placed in the recipient's body in an orthotopic position. First, the VCS is anastomosed followed by the VCI and the PV (Fig. 3.3).

- ***Post-anhepatic phase***

  Subsequently, the clamps of the PV and VCI are removed, allowing for reperfusion of the donor liver by restoring blood flow through the liver. Before or after reperfusion, the HA is also anastomosed (Fig. 3.3). Often, hypotension, arrhythmia or coagulopathy may occur during reperfusion. Next, the bile duct system is reconstructed.

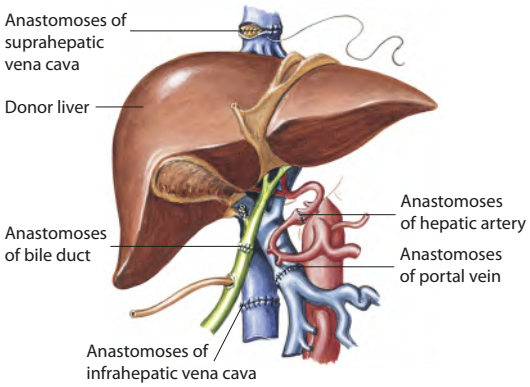

Figure 3.3: Implantation of a donor liver in a recipient. Adapted from [493].

Variations of the liver transplantation technique have been reported. For example, the piggy-back technique preserves the recipient's VCI implying no need to completely cross clamp the VCI, in contrast to the technique described above [515].

After transplantation, post-operative care is important to stabilise the major organs systems, to evaluate the graft function and immunosuppression, to monitor and possibly treat complications [214].

3.2.3 Alternative transplantation techniques

Due to the donor shortage despite the increasing use of extended criteria donors to enlarge the donor pool, new and innovative liver transplantation techniques have been developed. The alternative transplantation techniques have a positive, but modest influence on the number of liver transplantations.

3.2.3.1 Split liver transplantation

In the 1980s, split liver transplantation (SLT) was performed for the first time to increase the number of liver transplantations. During SLT, the donor liver is split into two liver grafts (Fig. 3.4). In this way, the two partial liver grafts are transplanted in two recipients. The regeneration capacity of the liver enables each part to regrow to a normal liver size in both recipients [68, 155, 205, 398, 521].

In most SLT procedures, one adult liver is split among one adult and one child. Doing so, the liver is split in a smaller portion for the child (the left lateral superior and inferior segment; see Fig. 1.3 and 3.4) and a larger portion for the adult (the extended right lobe). To obtain two liver grafts of a sufficient size aimed at transplanting two adults, division of the liver has to be done differently, i.e. by transection of the liver midplane to divide the liver

in its anatomical right (60% of the liver tissue) and left liver lobe (40% of the liver tissue). However, it is practically impossible at this moment to predict the functionality of the splitted liver grafts, resulting in a risk of developing the small-for-size syndrome (SFSS). In chapter 8, we developed a model to gain more insight into this problem. Though SLT is an attractive alternative to enlarge the donor pool, careful donor and recipient selection is necessary. As such, SLT is often restricted to 'ideal donors', being young and stable with a short period of hospitalisation [214].

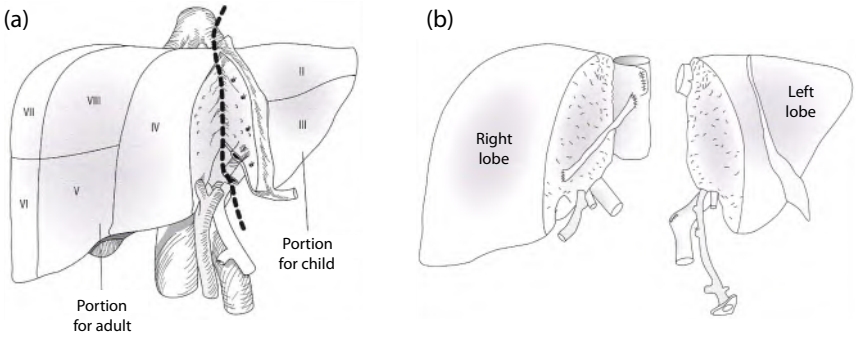

Figure 3.4: Split liver transplantation. (a) Liver split in a small portion for a child (left lateral superior and inferior segment) and a large portion for an adult (extended right lobe); (b) liver split in its anatomical left and right lobe, both destined to transplant an adult. Adapted from [214].

3.2.3.2 Living donor liver transplantation

At the end of the 1990s, living donor liver transplantation (LDLT) became feasible. LDLT involves a healthy person who is willing to donate a part of his liver to be implanted in a patient with liver failure (Fig. 3.5). Similar to SLT, the LDLT technique leans on the regeneration capacity of the liver. During approximately three months after the procedure, the regeneration capacity enables the liver parts in the donor and recipient to regrow to a sufficient liver size to maintain liver function of the body. The LDLT procedure is only performed when both the donor and recipient are stable. The main problem is the substantial mortality risk for the donor of a right lobe. Since a partial hepatectomy of the living donor is a major surgical procedure and to ensure that there are no risk factors that would contraindicate donation, potential donors are preoperatively carefully screened for their medical condition to rule out major diseases and to check biochemical markers of liver function etc. Some centres also perform a liver biopsy to check for steatosis or other liver diseases. Additionally, their psychosocial condition is checked. The

donor should be made aware of the risks and possible complications, and has to be able to come to a personal decision without being coerced by anyone else. Before performing LDLT, surgical planning is being done with specially developed software packages using CT images of the liver to study the liver anatomy and volume of both donor and recipient. This is done to estimate the best splitting location so that both the donor and recipient would hopefully possess sufficient viable liver tissue to sustain life after transplantation. As such, a current guideline says that the donor should retain at least 40% of the original liver and that the graft to body weight ratio should be higher than 0.8% [59, 129, 130, 155, 410].

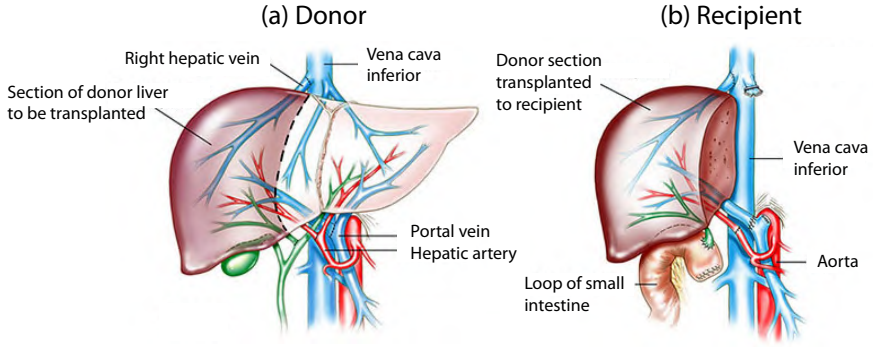

Figure 3.5: Adult living donor liver transplantation: the right lobe of the donor (a) is being resected to be transplanted in the recipient (b). Adapted from [14].

In the beginning, LDLT as well as SLT were mainly applied in the paediatric context, since it was difficult to find donor organs with good size matches for smaller children. As the number of patients on the waiting list kept growing, however, these techniques were extended to the adult setting. In the case of a paediatric recipient, a graft containing the left lateral superior and inferior segments (representing approximately 25% of the liver tissue) is most frequently used. For larger children, the total left lobe may be used. For adult recipients, the most frequently used graft is the right liver lobe, although a left lobe as well as a combination of two left liver lobes (called 'dual donor LDLT' involving two donors) also have been reported as successful measures. Removal of the right lobe is more drastic than removal of the left lobe [374, 507]. In contrast to paediatric LDLT, adult LDLT is still more likely to lead to complications and a substantial risk of death for the healthy volunteering donor (approximately 0.5-1%). Since the greatest concern in LDLT is the risk of death for the donor, adult LDLT has not gained general acceptance yet [159, 214, 345].

A major complication associated with LDLT (and SLT) is SFSS. SFSS can occur in both the donor and recipient and is usually the consequence of a graft size mismatch. A living donor develops SFSS when an excessive liver resection leads to progressive liver dysfunction and failure. SFSS is basically caused by an insufficient amount of hepatocytes, resulting in an unbalance between an accelerated liver regeneration and an increased demand of liver function. SFSS is characterised by overperfusion of the portal system, typically accompanied by portal hypertension, and may cause other complications, such as delayed or no synthetic function, prolonged cholestasis, biliary problems (e.g. poor biliary drainage due to bile duct stricture, bile leak from cut surface), coagulopathy etc. It is thus of vital importance to do a careful donor and recipient selection and to preserve a sufficient volume of remnant liver in the donor [64, 151, 189, 214, 218, 374, 392, 415, 430, 431, 462, 474, 513]. To gain more insight into this delicate balance, we developed an electrical analog model to simulate the impact of a partial hepatectomy on the liver haemodynamics (see chapter 8).

LDLT can take place between family members, as well as between non-related people. The results of this technique are favourable for paediatric living donation. As such, a parent may donate part of his liver to save his/her child's life [243]. LDLT has the big advantage of bypassing the waiting time for a deceased donor liver. In this way, liver transplantation can be done before the condition of the patient with liver failure further deteriorates. Typically, LDLT happens more frequently in areas of the world where deceased donation is (almost) not performed, such as Asia and the Middle East [355, 366, 436].

Alternative techniques have been reported to procure living donor grafts using less invasive methods such as laparoscopic and hand assisted techniques, but these methods are still under exploration in dedicated and experienced centres (e.g. the transplantation centre of Ghent University Hospital, Ghent, Belgium) [70, 218].

3.2.3.3 Domino transplantation

This rare form of liver transplantation involves a patient with a metabolic disease undergoing liver transplantation, while at the same time donating his own liver to another patient. In this way, the second patient receives a donor liver which is carrier of a metabolic disorder, most likely to be familial amyloidotic polyneuropathy. The only curative treatment for this disorder is liver transplantation. Familial amyloidotic polyneuropathy is an inherited mutation disorder, which takes about 15 years or more to develop symptoms in genetically affected individuals and usually never manifests during the lifetime of most carriers. Since it is thought that a similarly long incubation period is needed to develop symptoms in a domino transplant recipi-

ent, these disorders are an interesting source of donor organs especially for stable older recipients [123].

3.2.3.4 Xenotransplantation

The persistent donor shortage has led to an increased interest in xenotransplantation. Xenotransplantation is a procedure during which an organ from one species is implanted in another species. In that way, animals would be a potential resource of organs to transplant into humans. The pig seems to be the best candidate due to the similarity in size and the unlimited supply. At the moment, further research is mandatory, since xenotransplantation is not feasible yet due to safety reasons. Problems include rejection due to the immune response, risks of zoonosis (potentially resulting in the transmission of infectious agents from the graft to the recipient), and thrombocytopenia with spontaneous haemorrhage immediately after graft reperfusion. Furthermore, a number of ethical and regulatory issues should be dealt with. It is believed that after solving the current issues (e.g. by genetic modification) in the next coming years, clinical trials may be feasible to test xenotransplantation as a bridge to allograft transplantation [121, 248].

3.2.4 Complications associated with liver transplantation

The surgical procedure of liver transplantation is very complex and there is a continuous risk of rejection of the donor liver by the recipient body. Moreover, the lifelong consumption of immunosuppressive medication by the recipients makes them more sensible for infections and malignity. Most surgery-related complications after liver transplantation occur within the first weeks. An increased postoperative chance for complications is observed for partial-liver transplantations (e.g. SFSS in SLT and LDLT) as well as for patients who are critically ill at the time of transplantation. The most common complications are haemorrhage, vascular complications (e.g. thrombosis, stenosis, variceal bleeding etc.), liver dysfunction, biliary leaks or obstructions, wound infection or haematoma, primary liver dysfunction, recurrence of disease (e.g. HCC recurrence after transplantation) etc. [17, 139, 184, 214, 347, 384, 439].

The biggest future challenges will be finding solutions for the reduced motivation for donation and the high costs of maintaining potential donors on life support, as well as to improve storage solutions and techniques (e.g. by machine perfusion; see also chapters 6 and 7), to improve intraperitoneal cooling etc. [54].

3.3 Donor liver preservation

The time span during which a donor liver can be safely preserved is limited. This time limitation is stricter for extended criteria donor organs (such as

DCD donors) than for DBD donors. When aiming at expanding the use of extended criteria donor organs, better preparation and preservation methods will be necessary for these organs, prone to ischaemia-reperfusion injury [481].

During liver transplantation, the preservation period starts at the moment of organ procurement and lasts until the moment of implantation in the recipient. Hereby, the moment of removal of the liver from the donor body (or the moment of death in case of DCD donors) initiates a cascade of processes by which the organ starts to get damaged. From that moment on, the liver is no longer perfused by blood until it is reperfused after implantation in the recipient. To bridge the ischaemic period between removal and implantation, the liver has to be preserved in such a way that the ischaemic damage is minimised and the organ viability maintained. Though static cold storage is usually applied to preserve donor livers, the upcoming use of extended criteria donors resulted in a revival of machine perfusion [187]. In addition, total donor perfusion is a technique to perfuse the donor organs in situ during organ procurement.

3.3.1 Cold storage and its limitations

The current standard for the preservation of donor livers is cold storage (CS). After an initial flush to remove blood [469] and hepatectomy, the liver is packed in a special bag filled with preservation fluid. From that moment on, the preservation time is started. The bag is immersed in a box filled with melting ice. To prevent direct contact between the organ and ice, a second bag (filled with a salt solution) is placed around the first bag and a third bag is used for sterility reasons. Once the organ is packed, it can be transported. During the preservation period, the water/ice temperature has to be kept constant between 2 and 4°C. Cooling of the organ implies a strongly reduced metabolic need (approximately 10% of the normal cellular metabolic activity at 37°C). As a consequence, nutrients and oxygen are less needed [283, 441, 479, 481].

Though CS is the most widely used preservation technique for liver transplantation, some CS-related problems are encountered. Livers of extended criteria donors do not tolerate prolonged cold ischaemia and thus cannot be optimally preserved by CS. During CS, there is no circulation through the liver resulting in no oxygen or nutrient delivery as well as no waste removal. A cascade of detrimental events (ATP depletion, cellular swelling etc.) is initiated and may progressively damage the organ upon reperfusion. When reperfusing the organ after cold ischaemia, this may lead to the production of radical oxygen species initially, inflammation and cell death [46, 168, 283, 326, 378, 440]. Moreover, CS offers no possibility to assess viability markers of the liver graft. As a consequence, alternative preservation

techniques (e.g. machine perfusion) may be a solution to these limitations [188, 297, 344, 442].

3.3.2 The revival of machine perfusion

In 1813, le Gallois was the first to propose perfusion as a method to preserve donor organs. However, it took a long time before Carell and Lindberg reported on the first perfusion pump system in 1935, used to preserve thyroid glands [61, 109, 346]. The system was able to maintain a pulsatile fluid circulation through living organs. Nevertheless, the interest in perfusion decreased during the following decades in favour of CS. During the last decades, however, the increasing shortage of donor organs has forced transplantation centres to consider using (more) extended criteria donors, having a reduced ischaemic tolerance. Simultaneously, this resulted in a revival of machine perfusion (MP) to revitalise or resuscitate extended criteria organs [56, 110, 111, 146, 223, 227, 279, 282, 296, 340, 341, 343, 346, 387, 475, 519].

The goal of MP preservation is to mimic - to some extent - the physiological blood circulation in order to limit ischaemic liver damage [92]. MP aims to optimise the quality and viability of donor organs in order to prevent organ damage and complications after transplantation. In addition, MP may enable longer preservation times. MP is already elaborately tested [338, 352] and clinically used for kidneys. Liver MP prototypes have been developed and experiments and trials are ongoing, but liver MP systems are not yet commercially available. This is due to a number of substantial differences with kidneys, mainly caused by the complexity of the liver (such as its dual afferent vasculature with flow competition ([342]; see also section 3.3.3) and its complex microvasculature with endothelial cells susceptible to damage) [35, 110, 111, 175, 361, 378, 478, 479]. Nevertheless, liver MP has shown potential to be a better preservation technique than CS. The advantage is that dynamic MP ensures active perfusion. There is a continuous supply of nutrients (metabolic substrates) supporting the metabolism, the possibility of oxygen and therapeutic agent delivery and removal of metabolic waste products and toxins. Moreover, MP better preserves the microvascular integrity and offers a unique time window between procurement and transplantation to assess the viability of organs prior to transplantation [25, 26, 35, 173, 340, 346, 378]. As a result, MP can improve the clinical outcome and enable prolonged preservation times without increased preservation damage. Moreover, MP leads to economic benefits due to lower graft dysfunction, shorter hospital stays and better graft survival rates [341, 343].

Different MP systems have been developed. In essence, an MP machine contains an organ chamber and is typically equipped with one or two pumps (an HA and/or PV pump) to pump perfusion fluid from the reservoir into the liver (Fig. 3.6). Fig. 3.6a shows a schematic example of a liver perfusion

machine, while Fig. 3.6b and 3.7 show pictures of liver MP systems. Below, some important characteristics of liver MP systems are addressed as well as the extension of MP to extracorporeal donor body perfusion. Furthermore, we describe the MP device that was used for the liver MP experiments presented in this dissertation (see section 3.3.3 and chapter 7).

3.3.2.1 Perfusion system

Several studies have investigated different perfusion modes, e.g. HA and/or PV perfusion, pulsatile versus continuous perfusion [476] etc. Hereby, perfusion of both the HA and PV leads to the best results according to certain studies [488]. Roughly, there are two types of pump systems: pressure- and flow-controlled pumps. Systems with flow-control (e.g. displacement pumps with a piston) deliver a certain flow, independent of any occlusion or increased vascular resistance in the circuit. This can lead to the generation of enormous pressures and shear stresses, which may affect and damage the sinusoidal endothelial cells. In contrast, pressure-controlled pumps are essential to prevent endothelial cell damage due to overperfusion. When assuming that the law of Poiseuille is valid (eq. 3.2 with Δp [Pa] the pressure drop, R [Ns/m^5] the vascular resistance, q [m^3/s] the flow, μ [Pa·s] the dynamic viscosity, l [m] the length and r [m] the radius), pressure-control implies that the flow depends on the vascular resistance.

$$\Delta p = Rq = \frac{8\mu l}{\pi r^4} q \tag{3.2}$$

As such, the flow as well as the corresponding shear stress is restricted by the pressure. Pressure-control is possible by using for instance pressure-controlled rotation pumps. Normally, rotation pumps result in a continuous flow, but by controlling and varying their rotational speed, a pulsatile flow can be generated. The latter type of pumps is used in the LifePort Workstation (Organ Recovery Systems, Zaventem, Belgium; Fig. 3.7), the MP system that we used to perform HMP experiments as described in section 3.3.3 and chapter 7. The MP system is also provided with controllers to monitor the pumps and adjust the settings when necessary.

3.3.2.2 Temperature

There is an ongoing debate on the most optimal perfusion temperature. MP systems are subdivided in hypothermic (HMP), subnormothermic (SNMP) and normothermic perfusion (NMP) [187, 238, 371].

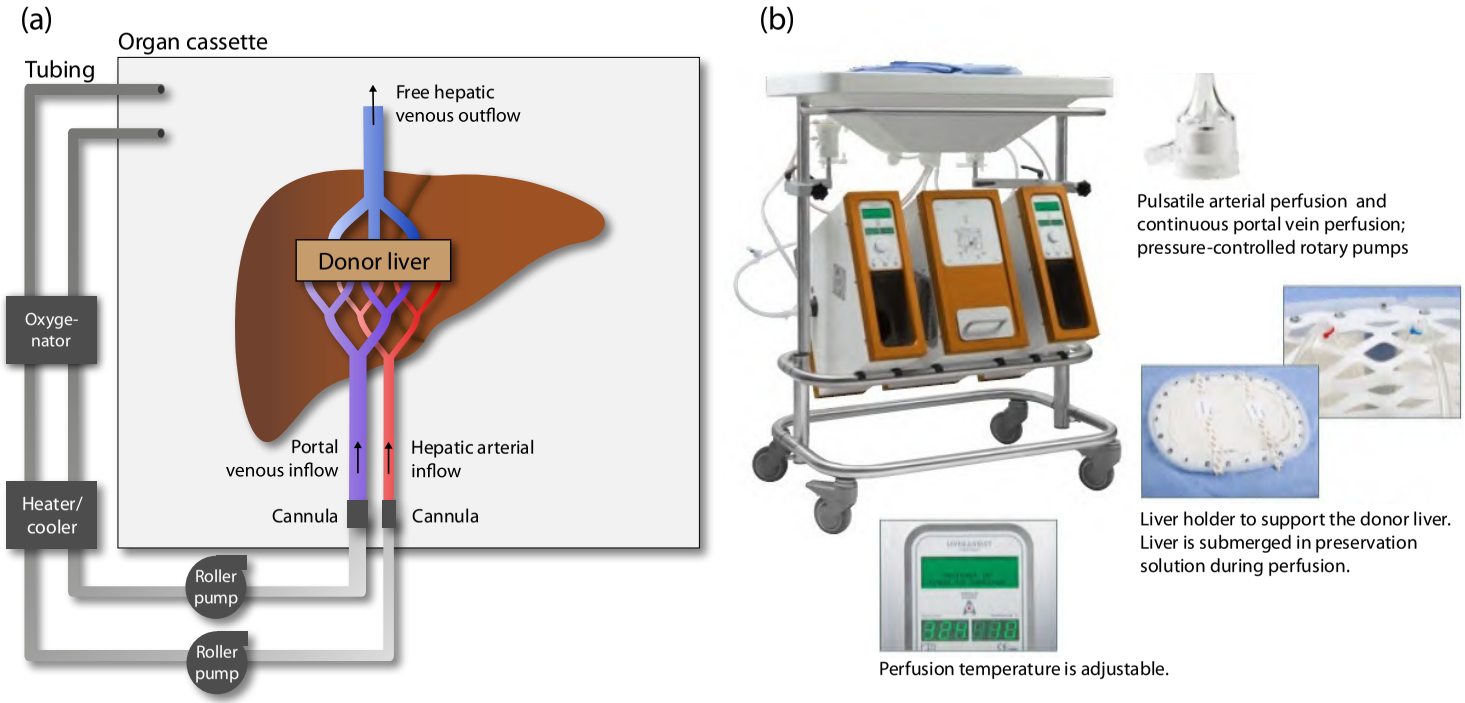

Figure 3.6: Liver machine perfusion (MP). (a) Schematic illustration of a liver MP system with two pumps. Preservation fluid is pumped into the liver through the tubing and cannulas. When leaving the liver, the perfusion fluid drains into the organ cassette and is subsequently recirculated. (b) Example of a liver MP system (Liver Assist, Organ Assist, The Netherlands; adapted from [11]).

- ***Hypothermic MP (HMP)*** implies a preservation temperature between 4-6°C. This temperature ensures a lower metabolic activity resulting in a lower need for nutrients as well as a lower production of waste products. HMP thus combines the advantages of hypothermic preservation with continuous perfusion [35, 36, 111–113, 173, 340, 458, 478, 479, 481]. The low HMP temperatures induce a vasoconstrictive response of the blood vessels [481]. A decrease of the radius of the blood vessels results in a substantial increase of the vascular resistance, as illustrated by Poiseuille's law (eq. 3.2) in which the resistance is inversely proportional with the fourth power of the radius. However, after approximately 30 minutes of MP, the effect of vasoconstriction is slowly diminishing.

  Different microscopic studies observed morphological changes of endothelial cells after HMP [110, 227]. Endothelial cells seem to get partially detached from their surrounding tissue and change from an elongated shape to a round shape indicating swollen cells. These changes can lead to flow heterogeneity, an increased vascular resistance and obstruction of the sinusoidal lumen and flow, which may result in loss of the barrier between vascular and interstitial spaces. As such, the vasculature may be torn and oedema may develop. This course of events may induce irreversible damage to the donor organ. Maintaining the integrity of endothelial cells is thus one of the biggest challenges for HMP of donor livers [35]. Therefore, HMP should avoid rapidly varying shear stresses. Since preservation happens at low temperatures, fluid viscosity values will be higher compared to conditions of normal physiological temperatures, corresponding with a higher vascular resistance (eq. 3.2). As such, lower perfusion flows should be used to prevent damage of fragile endothelial cells.

  HMP has been shown to reduce molecular markers of preservation injury and to improve graft viability and function compared to CS [187, 187, 226]. Guarrera et al. [174] demonstrated in a first clinical HMP trial with human livers that HMP is safe and feasible. HMP preserved livers showed shorter postoperative recovery, less biliary complications and hepatic injury compared to simple CS [25]. HMP was performed during patient preparation and recipient hepatectomy, thus only during a part of the preservation time after a certain period of cold ischaemia. Dutkowski et al. [111] also suggested that a short period (e.g. one hour) of oxygenated HMP prior to transplantation is able to improve cold ischaemic induced energetic disturbances and injuries. Human liver HMP experiments of Monbaliu et al. [343] showed well-preserved parenchyma and an intact endothelial cell lining

after 24 hours of HMP. Furthermore, oxygenation in HMP has been shown to be important to protect from mitochondrial and nuclear injury [419]. Though HMP gives evidence of good results in normal livers, its use for the preservation of extended criteria grafts may lead to increased Kupffer cell activation and endothelial cell destruction [141, 188]. An inherent limitation of HMP is the fact that the cellular activity may remain quiescent. As such, a more correct assessment of viability may be possible in more physiological conditions as seen in (sub)normothermic perfusion [343].

- ***Subnormothermic MP (SNMP)*** may be a promising intermediate approach in between HMP and NMP by perfusing at 20-28°C close to room temperature [341]. As such, Olschewski et al. [371] and Vairetti et al. [477] showed that SNMP results in a better preservation of the hepatic functional capacity and a reduction in damage of steatotic livers compared to HMP. Gringeri et al. [170] reported the resuscitation of DCD livers using SNMP. However, one has to be careful to avoid a progressive oxygen debt by using a solution with an adequate oxygen-carrying capacity [188]. In the end, SNMP is able to avoid the disadvantages of hypothermia, while circumventing the logistic difficulties of normothermic perfusion [371].

- ***Normothermic MP (NMP)*** is being performed at a normal body temperature (37°C) [49, 144, 228, 341, 395, 495]. Since these preservation conditions mimic normal physiological conditions, one of the advantages of NMP is the ability to perform a more advanced assessment of the organ viability by measuring key functional parameters correlating with function after transplant, such as bile flow, urea production, oxygen uptake etc. [519]. In theory, NMP preservation avoids ischaemia-reperfusion injuries and could even last for several days [110, 494]. NMP has been shown to be superior over CS, and to have the ability to resuscitate DCD grafts after warm ischaemia [219, 420]. A potential disadvantage is that NMP is a complex undertaking with a high risk of organ damage when not performed correctly or in case of any technical failure [326, 420, 494]. Drawbacks are the complex logistics of NMP and the risk of infection. One of the major challenges in NMP is to use a carrier providing sufficient oxygen without inducing any vascular damage. Often, (diluted) autologous blood is used with adequate additives of nutrients required to regulate homeostasis of the high liver metabolism, heparin etc. [110, 146, 188, 341]. Hessheimer et al. [188] stated that NMP appears to be the best option in liver transplantation to improve the viability of extended criteria organs. Other studies on the perfusion of extended criteria livers also

indicated that higher temperatures (approaching 37°C) improved the graft preservation when adequate oxygen supply was provided [188].

3.3.2.3 Perfusion solution

Perfusion solutions aim at protecting the donor liver by maintaining a normal intravascular osmotic and oncotic pressure, by regulating the pH and limiting reperfusion damage. In the first MP experiments, blood was used to perfuse the liver. However, due to several problems (such as blood coagulation and limited availability), the switch was made to acellular perfusion fluids such as KPS (Kidney Preservation Solution), Celsior, UW (University of Wisconsin solution), HTK (Histidine-Tryptophan-Ketoglutarate), Vasosol, Polysol etc. Modifications of these fluids are possible by using additives to administer nutrient or medication. For instance, anti-apoptotic drugs are added to reduce ischaemia/reperfusion damage and nitrogenoxide (NO) precursors are added to protect mitochondria against warm ischaemia. Furthermore, the perfusion fluid can be oxygenated [21, 48, 175, 187, 283, 296, 297, 326, 335, 519].

Acellular preservation solutions are different from blood and also act differently concerning their flow behaviour. Blood is a non-Newtonian fluid and - to some extent - behaves like a shear thinning fluid, showing lower viscosity values for higher shear rates and vice versa. In addition, the hematocrit (the percentage of red blood cells in blood) influences the viscosity. Several models have been proposed to describe the viscosity behaviour of blood as a function of shear rate (e.g. the Quemada model including hematocrit effects and the Casson model including yield stress) [339]. Furthermore, blood gives rise to the Fahraeus-Lindqvist effect (diameter-dependent viscosity decrease due to red blood cell aggregation in the centre of small blood vessels) [128, 185]. In contrast to blood, acellular perfusion solutions don't show these effects [28, 480].

3.3.2.4 The role of oxygen

The liver consumes oxygen during preservation. Also in the case of HMP with a lower metabolic activity, the liver is assumed to consume a certain amount of oxygen for oxidative energy production (aerobic metabolism) [110, 487]. This implies that optimal preservation should include the administration of oxygen to reduce the risk of cell damage due to hypoxia. However, oxygenation is a double-edged sword and can also result in the production of reactive oxygen species (ROS), damaging cellular structures such as membranes. To prevent ROS formation, ROS scavengers may be added to the perfusion fluid [343, 457, 481].

An alternative technique to administer oxygen is persufflation of gas through the vessels, more specifically by a retrograde venous insufflation

of humidified pure oxygen. In several experiments, this technique showed improvements of liver graft viability and is now evaluated clinically [187, 274, 296, 335, 456].

In the end, several studies have shown the beneficial effect of oxygenation resulting in less overall damage and improved liver function [110, 187, 429, 487].

3.3.2.5 Monitoring

Careful monitoring of perfusion characteristics (such as pressures, flows and vascular resistances) may enable estimating the viability of the organ after preservation. In kidney HMP, the intrarenal resistance is used as a measure of kidney quality, but should not be used to discard organs for transplantation [232]. An elevated resistance may indicate microvascular disturbances such as cell swelling and oedema, which may result in a decreased viability [115, 173]. Using pressure sensors close to the HA and PV of the liver, the perfusion pressure can be monitored and controlled. In this way, twisted or loosening cannulas can be detected. Flows may be estimated by using the pump rotation speed or by using flow probes. Calculating the vascular resistances may allow estimating the liver viability. Furthermore, a temperature sensor is advised to detect and correct for temperature variations. In addition, biochemical analysis of the perfusate (e.g. enzymatic markers such as aspartate transaminase, lactic dehydrogenase etc.) may be interesting to provide information to the clinicians about the viability [26, 343].

3.3.2.6 The quest for optimal MP parameters

The balance between good perfusion parameters and the occurrence of damage at the endothelial level is crucial. However, the optimal manner to perform MP is still a matter of debate [188]. Many different MP protocols have been proposed: single versus dual perfusion, different pressure or flow settings, pulsatile versus non-pulsatile perfusion, oxygenation or not, the perfusion temperature etc. [342, 488]. For example, a study of 't Hart et al. [457] postulates that - to minimise cellular damage - the perfusion pressure should be set at 25% of the *in vivo* pressures in physiological conditions. However, these settings still result in some cellular damage. Another important factor is the usability of the system. As such, a practical MP machine should be easy to transport, not expensive and user friendly [341]. More research is thus necessary to refine perfusion systems and parameters so that a balance is found between stable and complete MP and endothelial injury [25, 26, 92, 371, 458, 481]. The latter is also the research objective of chapter 6.

3.3.2.7 *Extracorporeal MP of the donor body*

Similar to the extracorporeal perfusion support during cardiac surgery, extracorporeal MP of the donor body enables the recirculation of blood or perfusion fluid through the donor organs during procurement. This approach may allow changing the period of warm ischaemia after cardiac arrest (especially relevant in the case of DCD donors) to a preconditioning period. In this way, the potential donor and his/her organs may be evaluated [140, 156]. Similar to MP, different types of extracorporeal support systems have been developed, using different temperatures (hypothermic versus normothermic) [235, 300]. Usage of these systems may allow expanding the donor pool by improved graft function and performing controlled and unhurried organ procurements [50, 188, 300, 407].

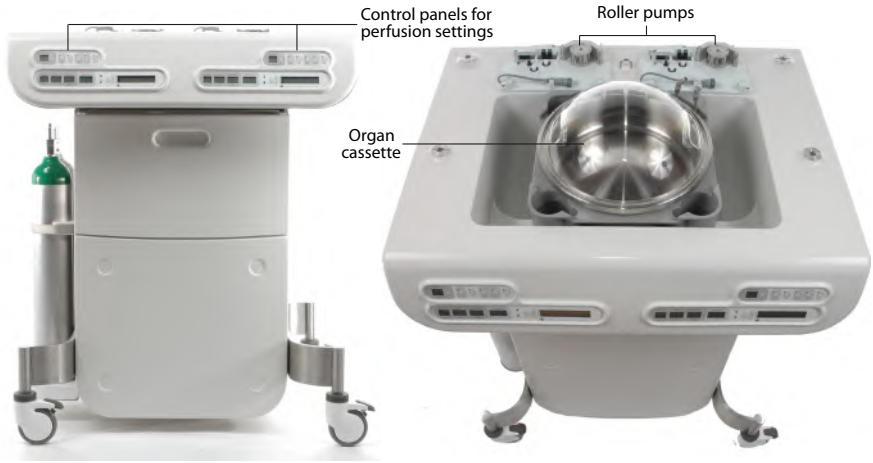

Figure 3.7: The LifePort Workstation (Organ Recovery Systems, Zaventem, Belgium). This liver machine perfusion (MP) prototype was used to perform porcine and human liver hypothermic machine perfusion (HMP) experiments.

3.3.2.8 *The LifePort Workstation (Organ Recovery Systems, Zaventem, Belgium)*

The LifePort Workstation (Organ Recovery Systems, Zaventem, Belgium) was used for all experiments discussed in section 3.3.3 and chapter 7 (Fig. 3.7). Two roller pumps are included to pump perfusion solution from the reservoir (organ cassette) to the HA and PV (Fig. 3.6a and 3.7). The LifePort Workstation prototype generates pressure-controlled MP, meaning that the perfusion flow through the organ is secondary to the pressure, which is set by the operator (pressure range of 5-99 mmHg). Optionally, a flow limitation can be added by specifying the maximum allowed flow for each pump

(with an absolute maximum flow of approximately 700 ml/min). Perfusion regimes are either continuous or pulsatile with pulsatile perfusion being implemented as the generation of sinusoidal pressure curves. The perfusion circuit of each pump also includes a dampener (accordion-like reservoir filled with water and air; Fig. 7.3) to reduce unwanted pressure fluctuations generated by the pumps. Porcine as well as human livers are perfused with 2 litres of KPS-1, which is a perfusion solution that is often used for renal HMP (see also section 3.3.2.3) [201]. During HMP, livers are placed in a dome-shaped organ cassette and are partially immersed in the KPS-1 solution (Fig. 3.6a and 3.7). The organ cassette is placed in a tub, filled with ice water to cool the organ and perfusion solution (see Fig. 7.3). A tubing circuit guides the preservation solution from the organ cassette to the pumps, which generate flow to the cannulated inflow vessels (HA and PV). After leaving the liver through its hepatic venous (HV) system, the perfusion fluid drains into the organ cassette, after which it is recirculated (Fig. 3.6a). Optionally, an oxygenator and a heater/cooler system can be added to the circuit in order to oxygenate and heat/cool the perfusion solution before entering the donor organ (Fig. 3.6a). Furthermore, the device is designed to regularly flush the tubing for a short period of time (wash cycle of 10 seconds after every 10 minutes of perfusion).

3.3.3 Porcine HMP experiments to study flow competition

As flow competition between the HA and PV may lead to unbalanced liver MP and thus hampers perfusion homogeneity, a set of porcine HMP experiments was conducted to enlighten this phenomenon. This section discusses the key points of "*Flow competition between hepatic arterial and portal venous flow during hypothermic machine perfusion preservation of porcine livers*", as published in the International Journal of Artificial Organs, 35(2):119-131,2012. For more detailed information on this study, please consult the full paper [342].

3.3.3.1 Background and aim

Several papers focused on the hepatic flow characteristics during HMP feasibility studies with some HMP experiments showing a progressive decrease and/or a complete cessation of the PV flow whilst the HA flow was increasing [102, 340, 487]. This phenomenon, defined as flow competition, was occasionally observed during HMP of porcine as well as human livers discarded for clinical transplantation, which illustrates that the observation was not species-specific. As flow competition disturbs the HA-PV flow distribution, it may interfere with a homogeneous perfusion. Therefore, the aim of this study was to evaluate whether flow competition could be reproduced in an

animal model. We hypothesised that the PV flow may be hampered as a consequence of an elevated sinusoidal pressure, reducing the pressure difference between the PV and the sinusoids. To test this hypothesis, an increased intrasinusoidal pressure was evoked by either increasing the HA pressure or obstructing the hepatic outflow. In addition, the reversibility of flow competition was investigated.

3.3.3.2 Materials and methods

This study was approved by the local animal care committee of the University Hospitals Leuven (Belgium) and was carried out in accordance with the Belgian federal guidelines. Five porcine livers (average weight 600 g, from 30-35 kg pigs) were procured. After cannulating the HA, PV and infrahepatic vena cava inferior (VCI) and clamping the suprahepatic VCI, the livers were perfused with 2 liters of non-oxygenated 4-6°C KPS-1®. The LifePort Workstation (see section 3.3.2.8) allowed for pressure-controlled, flow-unlimited continuous perfusion through the HA and pressure-controlled, flow-limited continuous perfusion through the PV. PV flow was limited to 0.5 ml/g/min, because it was previously observed that PV pressure-control alone gave rise to very high flow rates, which may induce a high shear stress during HMP, possibly damaging the sinusoidal endothelial lining. Pressures (P_{HA}, P_{PV} and P_{HV}) and flows (Q_{HA} and Q_{PV}) were measured continuously with a sampling frequency of 1 Hz (for more details on the data acquisition: see [342]). HMP was initiated by applying the following conditions: P_{PV}≤7 mmHg and Q_{PV}≤300 ml/min for the PV inlet, and P_{HA}=25 mmHg with unlimited Q_{HA} for the HA inlet. A stable perfusion regime was awaited before starting the experimental measurements. Two experimental settings were designed to increase the sinusoidal pressure in order to evoke flow competition in the porcine livers. First, P_{HA} was incrementally increased (steps of 10 mmHg) until a significant decrease in Q_{PV} was observed. When flow competition was observed, the reversibility was investigated by a step-wise decrease of the P_{HA}. Secondly, an outflow obstruction was evoked by clamping the VCI cannula to increase the P_{HV}, whilst complete cessation of the hepatic outflow was avoided.

3.3.3.3 Results and discussion

Increasing the P_{HA} evoked gradual flow competition with Q_{PV} cessations at the highest P_{HA} (Fig. 3.8). Flow competition could be reversed by lowering P_{HA} (and/or increasing P_{PV}). During severe outflow obstruction, a repetitive pattern of alternating increases/decreases between the Q_{HA} and Q_{PV} was observed (Fig. 3.9). This interaction repeated itself and was eventually observed to be self-limiting. Comparison of the flow competition phenomena evoked by P_{HA} alterations and VCI obstructions reveals a clear differ-

ence. Where P_{HA} increases led to competition in one direction (Q_{HA} increased while Q_{PV} decreased), VCI obstructions affected both Q_{HA} and Q_{PV} in an alternating and repetitive way.

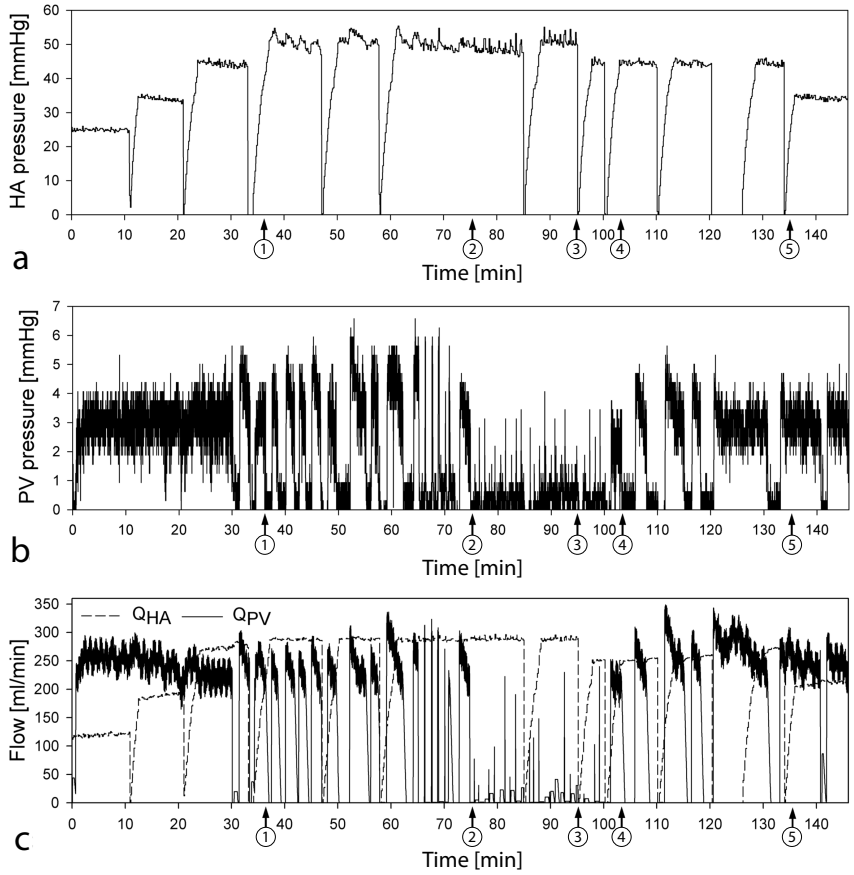

Figure 3.8: Hypothermic machine perfusion (HMP) measurements of a porcine liver when evoking flow competition by increasing the hepatic arterial pressure (P_{HA}). Panel a depicts P_{HA} and panel b depicts the portal venous pressure (P_{PV}), while panel c depicts the hepatic arterial flow (Q_{HA}) and the portal venous flow (Q_{PV}). P_{HA} was incrementally increased every 10 minutes starting from 25 mmHg, resulting in an incremental Q_{HA} increase. A P_{HA} of 50 mmHg (time stamp 1; t=37 min) evoked a series of decreasing but initially self-restoring Q_{PV}. These flow oscillations occur as the precursors of a flow instability. Eventually, Q_{PV} was hampered indicating the initiation of the flow competition (time stamp 2; t=75 min). To reverse the flow competition, P_{HA} was lowered (time stamp 3; t=95 min). Portal flow was gradually restored by also increasing the P_{PV} (time stamp 4; t=103 min). Further decreasing the P_{HA} (time stamp 5; t=135 min), resulted in a decreased Q_{HA}, allowing the full restoration of Q_{PV}.

Under normal *in vivo* conditions, intrinsic autoregulation mechanisms regulate the flow through the hepatic vascular bed. As such, the hepatic

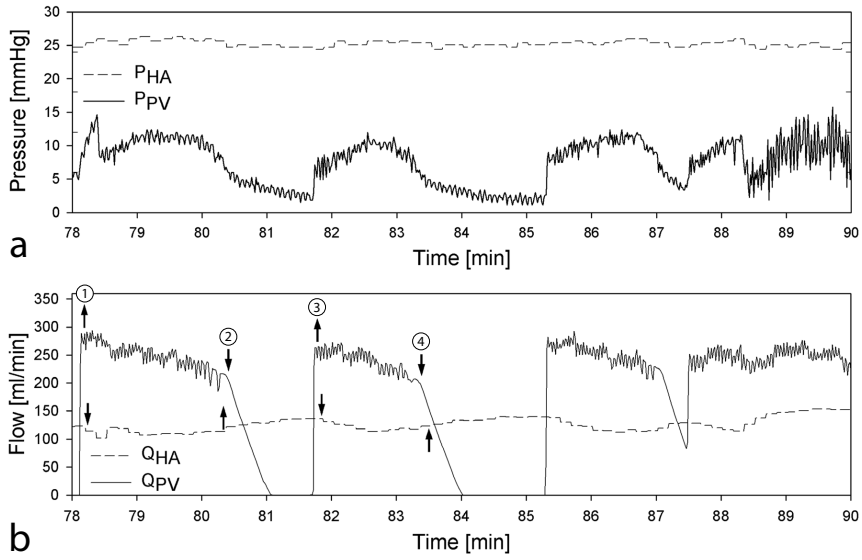

Figure 3.9: Hypothermic machine perfusion (HMP) measurements of a porcine liver when evoking flow competition by a vena cava inferior (VCI) outflow obstruction. Panel a and b display the hepatic arterial (HA) and portal venous (PV) pressure and flow measurements, respectively. When initiating a severe outflow obstruction, an alternating increase/decrease between the HA flow (Q_{HA}) and PV flow (Q_{PV}) was evoked (time stamp 1-4), also detectable in the HA pressure (P_{HA}) and PV pressure (P_{PV}) measurements.

arterial buffer response (HABR; section 1.2.1) implies that Q_{PV} may directly influence Q_{HA} *in vivo*. In contrast, the response observed during *ex vivo* HMP experiments in our study showed that the Q_{HA} may directly influence the Q_{PV} (Fig. 3.8). Similar observations of flow competition - albeit in a different perfusion model using cirrhotic rat livers - were made by Zipprich et al. [531]. However, most studies concerning liver perfusion did not report any occurrence of flow competition between the HA and PV.

When theoretically interpreting the hepatic circulation as a passive system, the observation of flow competition evoked by an increased P_{HA} would analogously lead to flow competition evoked by an increased P_{PV} leading to a decreased Q_{HA}. However, we did not manage to evoke flow competition by increasing P_{PV}, as this cannot be reached within the physiological P_{PV} ranges. Since the P_{HA} is higher compared to the P_{PV}, a P_{PV} increase will substantially affect the pressure difference between the PV and sinusoids, while it will only mildly affect the HA pressure difference. These observations are theoretically illustrated by the electrical liver model of chapter 6 (Fig. 6.7a), where even large P_{PV} variations only result in minor Q_{HA} changes. However, when increasing the P_{HA} similar to the HMP experiments (Fig. 3.8), the

mathematical liver model clearly illustrates the appearance of flow competition. These results support our hypothesis that when changing the arterial flow, portal flow changes through an altered sinusoidal perfusion.

Due to the absence of equipment to directly measure sinusoidal pressure and flow in an intact organ, our data do not allow analysing the mechanisms of the observed flow competition more profoundly. However, the observations made in this study showed that flow competition could be consistently reproduced, justifying the nature of our hypothesis. Consequently, these observations might have important implications on the design and flow control for clinical *ex vivo* MP devices.

3.3.3.4 Conclusion

In this study, flow competition between the HA and PV was observed during liver HMP. Flow competition could be evoked by increasing P_{HA} or obstructing the outflow, suggesting that this phenomenon is related to alterations of pressure differences between the HA, PV, sinusoids and HV. In the end, flow competition should be taken into account when designing appropriate dual perfusion protocols for hepatic HMP control.

Chapter 4

Modelling the liver

An overview of the liver anatomy and physiology was given in chapter 1, while chapter 2 addressed liver pathologies affecting hepatic functionality. In chapter 3, liver transplantation was discussed together with the current challenges concerning optimal preservation methods for donor livers, surgical planning etc. Experimental as well as numerical models may be helpful to gain more insight into these liver-related topics and challenges.

The goal of this PhD thesis was to develop computer models of the hepatic vasculature and perfusion to better understand the inner liver haemodynamics. Before addressing this work in the following chapters, an overview is given of the state-of-the-art in hepatic modelling. Models are classified as models of the liver vascular architecture, liver perfusion and other hepatic models on liver mechanics and liver function.

4.1 Modelling the liver vascular architecture

An intact hepatic vascular architecture is one of the cornerstones of a well-functioning liver. An altered blood circulation (e.g. due to disease or surgical complications) may result in organ damage and even liver failure. Lehmann et al. [282] underlined the importance of the hepatic architecture: *"Anatomic insights provide the fundamental basis for hepatic surgery"*. One could even extend this statement to the broader field of liver-related medical applications (including quantitative diagnosis, outcome assessment, monitoring disease progression etc.). Below, we discuss the available hepatic architectural models on the macro- and microvascular level.

4.1.1 Hepatic macrovascular architecture

The architecture of the largest vessels of animal and human livers has been investigated using different techniques. One of those techniques is vascular corrosion casting, which results in physical replicas of vascular systems [62, 63, 77, 203]. Practically, casting resin is injected in situ or in an isolated organ after cannulation of the blood vessel(s) and/or bile duct of interest. It is typically a polymeric mixture of several substances, such as the Batson's corrosion kit (Polysciences, Florida, USA) which was used in this dissertation (see chapters 5, 6, 8 and 9). After hardening of the injected resin, the specimen is immersed in a bath of potassium hydroxide or chloride acid solution to macerate the tissue during a period up to several days. After rinsing, a polymeric replica of the vessel system is obtained. For example, in 1906, Mall [305] used corrosion specimens of dog livers to study the branching pattern and geometrical characteristics of the hepatic vasculature. Zanchet et al. [526] and Court et al. [80] studied the hepatic segmental architecture of porcine liver casts (Fig. 4.1), while Shirai et al. [432] focused on the vasculature and bile ducts of bovine liver casts. Van Steenkiste et al. [484] made vascular corrosion casts of the venous system of mice and rats to compare normal animals with portal hypertensive and cirrhotic animals. Human liver casts were used by Gupta et al. [176, 177] to study the hepatic segmental structure and the architecture of the HV tree. Fasel et al. [133] combined vascular corrosion casting of human livers with subsequent CT (computer tomography) scanning to investigate the intrahepatic PV architecture, while Hahn et al. [178] similarly analysed the PV and HV trees.

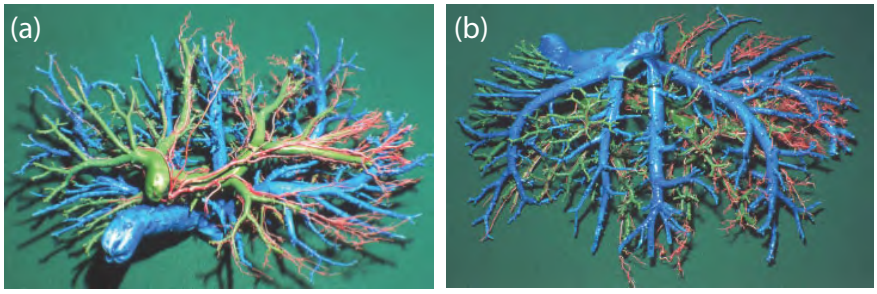

Figure 4.1: Vascular corrosion cast of the hepatic arterial (HA; red), portal venous (PV; green) and hepatic venous (HV; blue) tree of a porcine liver: (a) anterior and (b) posterior view. Adapted from [80].

The recent progress in high resolution (small animal) imaging modalities enabled researchers to more precisely describe the liver. As such, Fiebig et al. [18] used *in vivo* micro-CT scanning in combination with injections of

contrast agents to study the macroscopic anatomy of the murine liver and hepatic vessels. Micro-CT scanning typically results in higher resolutions and more detailed images compared to conventional CT scanners. Some studies combine Microfil (Flow Tech., Inc., Carver, MA, USA) injections with micro-CT scanning. Microfil is a radiopaque liquid silicone polymer containing lead and is being used to inject vascular systems. After polymerisation, the tissue is fixated (e.g. in formalin) and immersed in several glycerine solutions followed by immersion in bioplastic. Wan et al. [500], Masyuk et al. [315] and Op Den Buijs et al. [52] combined Microfil injections with micro-CT scanning to study the architecture of the rat liver. More specifically, Wan et al. [500] studied the HA tree, while Op Den Buijs et al. [52] studied one lobe of the rat PV tree. Masyuk et al. [315] and Kline et al. [256] used three types of rat liver casts of which the HA, PV or biliary tree was injected.

Several methods have been developed and adopted to analyse and quantify the geometrical features of vascular systems. As such, the concept of blood vessel generations has widely been used to analyse the topology of the placental vasculature, the bronchial tree etc. [167, 206, 207, 524, 525]. In this approach, generation 1 is the main trunk of the vascular tree (Fig. 4.2a). Subsequently, when a mother vessel of generation x splits in two (or more) similar daughter vessels, the daughter vessels belong to generation x+1. Mall [305] used this approach to study the vascular trees of the dog liver, while Op Den Buijs et al. [52] and Kline et al. [256] used generations to quantify the geometrical characteristics of a rat liver lobe.

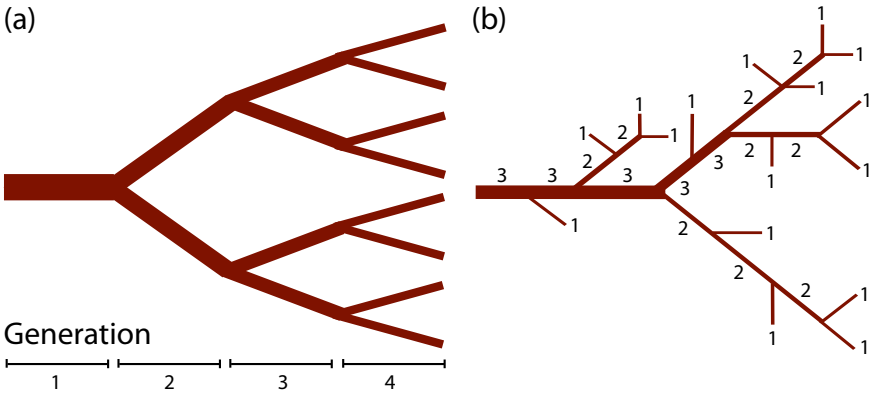

Figure 4.2: Illustration of the principle of (a) blood vessel generations and (b) the Strahler ordering system

Another classification system for vascular trees is the Strahler ordering system [453]. In contrast to vessel generations, the Strahler ordering system

starts by assigning order 1 to the terminal vessels (Fig. 4.2b). Subsequently, if all daughter vessels have the same order number o, the mother vessel is assigned to order o+1. If the daughter vessels have different order numbers, the mother vessel is assigned to the highest order number of the daughter vessels. The Strahler ordering system has been used to study the topology of e.g. renal vascular trees [365], the pulmonary arterial tree [230, 365, 453], the coronary arterial tree [337] and the largest vessels of the PV and HV hepatic trees [178].

In addition to vessel generation and ordering models, other morphometric studies [18, 244, 245, 337] and fractal models have been used to describe vascular branching patterns. In the latter approach, vascular trees are interpreted as self-similar structures for which each generation of the tree is obtained from the generation preceding it [149, 179, 502, 522–525] (Fig. 4.3a). For instance, Op Den Buijs et al. [52] and Hahn et al. [178] applied this approach to analyse the PV vessels of a rat liver lobe and the human PV and HV trees, respectively. Also, 3D models of hepatic vascular trees (see Fig. 4.3b for an example) have been generated by creating binary trees based on constrained constructive optimisation methods [37, 179, 234, 261, 262, 328]. For instance, digital hepatic trees were generated as phantoms for dynamic image formation models to study the performance of contrast-enhanced CT [37, 261] or dynamic contrast-enhanced MRI (magnetic resonance imaging) [328] e.g. to better detect and understand the complexity of hepatic tumourous tissue.

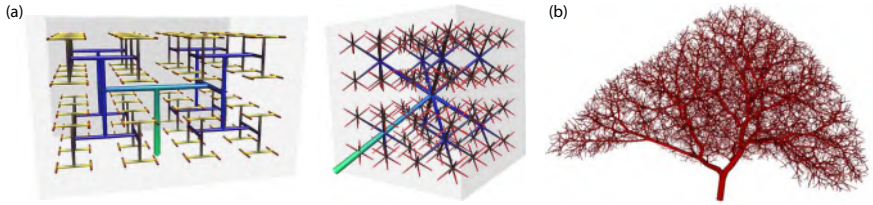

Figure 4.3: Examples of (a) self-similar fractal tree structures (adapted from [179]) and (b) a portal venous (PV) tree generated by a constrained constructive optimisation method (adapted from [234]).

In the clinical context, patient-specific models of the liver architecture may be very helpful to plan surgical interventions and transplantations. After a CT or MRI angiography, the patient-specific imaging data is processed to create 3D reconstructions as input for surgical planning models [23, 60, 362, 396, 414, 425, 514, 516]. As such, several geometrical and structural analysis methods based on vascular territories have been proposed to facilitate living donor liver transplantation (LDLT) and oncologic partial hepatectomy procedures (see Fig. 4.4 for an example) [45, 354, 356, 418, 423, 424]. In this way,

computer-assisted decision-making models enable planning the optimal resection surface based on the best solution for blood supply and drainage (e.g. for both donor and recipient in the case of LDLT) and preventing intraoperative heavy bleeding etc. Furthermore, the concept of resection maps (or risk maps) has been suggested as an intraoperative navigation tool in liver surgery [182, 270].

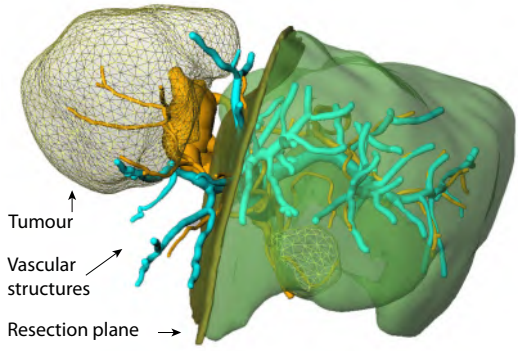

Figure 4.4: Surgical planning for a tumour resection. Adapted from [182].

4.1.2 Hepatic microvascular architecture

The hepatic microstructural architecture is still not fully understood. There is an ongoing debate on the best suited model to describe the structural or functional liver unit (see section 1.1.2.4). Nevertheless, several techniques have been applied to investigate and model the hepatic microvascular architecture. For example, Teutsch et al. [465, 466] obtained 3D reconstructions of the hepatic microvasculature by registering photographs of serial sections. Also, a combination of vascular corrosion casting and scanning electron microscopy (SEM) has been used to study the hepatic microvascular architecture in detail for normal conditions ([162]; Fig. 4.5) as well as liver pathologies (e.g. capillary shunting in cirrhosis [192]). Vollmar et al. [496] gave an excellent overview of available techniques to study the hepatic microcirculation (e.g. *in vivo* fluorescence microscopy, orthogonal polarised spectral imaging etc.).

In conclusion, the hepatic vascular architecture has been the topic of many studies, but some questions are still unanswered. Most macrovascular studies focused on a part of the hepatic vascular system, but never simultaneously studied the HA, PV and HV tree of the same liver. Furthermore, a vascular analysis of the complete spectrum of blood vessels going from the macrocirculation to the microcirculation of a liver was not performed yet.

Therefore, one of the aims of this PhD thesis was to study all hepatic vascular trees simultaneously and at different spatial scales for one and the same liver (see chapters 5 and 9).

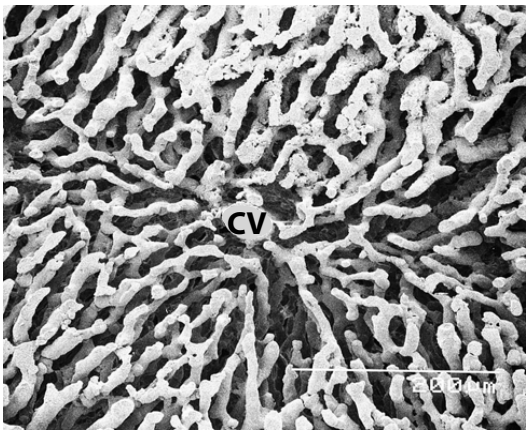

Figure 4.5: SEM image of the centre of a liver lobule. The sinusoids clearly drain in the central vein (CV). Source: [162].

4.2 Modelling liver perfusion

In this section, we will focus both on experimental studies and numerical models of the hepatic macro- and microvascular perfusion.

4.2.1 Experimental animal (and human) models

Several studies used animal experiments to assess hepatic haemodynamic parameters in normal physiological circumstances [34, 42, 180, 293–295, 358, 401]. As such, Bohlen et al. [42] measured hepatic pressures in rats, dog puppies and rabbits. Pressures were in the same order of magnitude for all three species with hepatic venous pressures of 5.1 ± 1.0, 6.4 ± 1.1 and 5.4 ± 1.0 mmHg in rats, puppies and rabbits, respectively. Bohlen et al. [42] and Maass-Moreno et al. [293] used rabbits to show that - in normal conditions - the major resistance to hepatic blood flow must lie upstream to the major hepatic veins. Subsequently, Maass-Moreno et al. [295] measured microvascular pressures in vascular networks close to the liver surface of rabbits by using a servo-null micropipette pressure-measuring system. Their results showed a gradual pressure decrease from the portal venules to the hepatic venules with average pressures of 5.7 ± 0.8, 5.4 ± 0.7 and 4.7 ± 0.6 mmHg for the portal venules, sinusoids and initial hepatic venules, respectively. Richter et al. [401] performed *in vivo* HA and PV flow measurements in rats using

ultrasonic flow probes. Their results confirmed the hepatic arterial buffer response (HABR; see section 1.2.1) and suggest that there are arteriolo-portal venular shunts, which regulate the ratios of HA and PV flow.

Next to invasive measurement techniques, Halavaara et al. [180] imaged rabbits by functional CT scanning after a bolus injection of an iodinated experimental intravascular contrast agent. This enabled measuring hepatic flows. They estimated the total hepatic flow to be 241.1 ± 33.6 ml/min per 100 g of liver tissue. Chen et al. [69] demonstrated the ability of perfusion CT with contrast agents to assess hepatic microvascular changes in patients with cirrhosis. Lueck et al. [291] used contrast-enhanced ultrasound by injecting microbubbles to assess liver perfusion. MRI techniques are also being used to study the liver perfusion, such as perfusion MRI with contrast agents (e.g. to analyse hepatic blood flow parameters). Yzet et al. [520] tested two non-invasive techniques to assess liver haemodynamics. The performance of human free breathing phase contrast MRI was compared with that of Doppler ultrasound (US) by measuring blood velocities and flow rates in the HA and PV. Phase contrast MRI provided reliable non-invasive measurements of hepatic flow parameters with a lower variability and higher reproducibility compared to Doppler US.

Often, animal models are used to test and optimise novel and alternative transplantation techniques or surgical procedures [105, 211, 231, 530]. As such, a number of rodent and porcine models have been developed to study the haemodynamic effects of partial hepatectomy [19, 86–88, 106, 131, 140, 209, 210, 280, 313, 348, 349, 386, 485, 511]. For instance, Fan et al. [131, 485] and Dahmen et al. [86, 209] performed rat liver resections up to 90% and 97% removal of liver tissue, respectively. Consecutive resections demonstrated a clear increase of the portal pressure and the portal flow per gram of liver tissue. Partial hepatectomy rat models illustrate the importance to prevent the small-for-size syndrome (SFSS; see section 3.2.3.2) by preserving a sufficient amount of functional liver mass and avoiding outflow obstructions [87, 210]. Outflow obstructions may arise when the middle hepatic vein is not incorporated in the liver graft (e.g. in LDLT) [88, 386]. Dirsch et al. [106] showed that this can lead to centrilobular necrosis in the early postoperative phase or even to SFSS. However, they also demonstrated that the liver may recover due to dilation of sinusoids forming vascularised canals.

Large animal experiments were done by Fondevila et al. [140], who used a porcine LDLT model to perform partial (70%) liver transplantations and to study SFSS, while Mortensen et al. [349] used pigs to look into the regenerative response in the liver remnant. Studies on human patient data also demonstrated that SFSS is characterised by an excessive portal venous inflow and pressure and is considered as one of the most important causes of liver graft dysfunction in LDLT [65, 431, 513, 528].

To reduce SFSS risks, partial hepatectomy rat models have been used to test the effect of portosystemic shunts (Fig. 4.6; shunt between a PV and a HV vessel [314]), showing an improved early survival rate [145]. Additionally, Glanemann et al. [163] and Eipel et al. [114] performed splenectomy procedures in rats, resulting in a reduced risk for postoperative hyperperfusion. Troisi et al. [472] used portocaval shunts to decompress the portal system in patients and also illustrated that graft inflow modulation reduces the risk of SFSS complications.

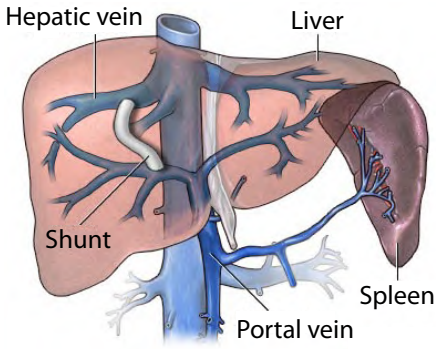

Figure 4.6: Illustration of a portosystemic shunt connecting a portal venous (PV) and a hepatic venous (HV) vessel. Adapted from [4].

Machine perfusion (MP) is a potentially better preservation technique for donor livers than cold storage (CS). Numerous experimental studies have been performed to compare MP protocols with CS, as well as to test several MP parameters, such as the perfusion pressures or flows, temperature, preservation solutions etc. For more detailed information on this topic, the reader is referred to section 3.3.2 [25, 26, 92, 138, 188, 289, 341, 342, 371, 457, 458, 481, 488].

Experimental animal models have also been used to elucidate the pathogenesis, architectural changes and haemodynamic impact of liver pathologies. As such, Spannbauer et al. [444] and Rosenstengel et al. [408] developed rat models of steatosis by administering either a fatty diet or ethanol. Peterson et al. [379] modelled fibrosis in pigs by adding yellow phosphorus to their feed. Welsch et al. [505] developed a porcine model of cystic fibrosis by genetic modifications. Chen et al. [67] ligated the common bile ducts of piglets to model the impact of bile duct obstruction, as is the case in cholangitis or other cholestatic diseases (see section 2.2). Maksan et al. [302] used a rat model of hepatocellular carcinoma (HCC) to investigate the hepatic and tumourous microcirculation with intravital fluorescence microscopy. Additionally, several experimental studies attempted to develop animal models

of liver cirrhosis [24, 246, 268, 486, 527, 531]. For instance, Laleman et al. [268] showed that thioacetamide intoxication of rats during 18 weeks results in a reproducible model of cirrhosis including portal hypertension and endothelial dysfunction. Other models, however, did not succeed in developing full blown cirrhosis [24, 527].

4.2.2 Mathematical models

4.2.2.1 Hepatic macroperfusion models

Macrocirculatory perfusion models range from compartmental models to 3D computational fluid dynamics studies accounting for the largest hepatic vessels.

4.2.2.1.1 Compartmental modelling. Compartmental models may help clarifying the major characteristics of the hepatic vascular system [71, 136, 240, 413]. Traditionally, open two-compartment models were used (with a hepatic vascular and interstitial compartment; Fig. 4.7a) to measure liver perfusion with contrast-enhanced functional CT scanning, but they did not provide unique solutions for blood and interstitial volume fractions. Therefore, an open-four compartment model was proposed by splitting the hepatic vascular space in three compartments: the impermeable supplying vessels (HA and PV tree), the permeable microcirculation and the impermeable draining vessels (Fig. 4.7b) [240]. Differential equations, derived from the conservation of mass, allowed solving this four-compartment model and led to more accurate results (HA and PV flows, blood and interstitial volume fractions etc.) than those obtained from the two-compartment model.

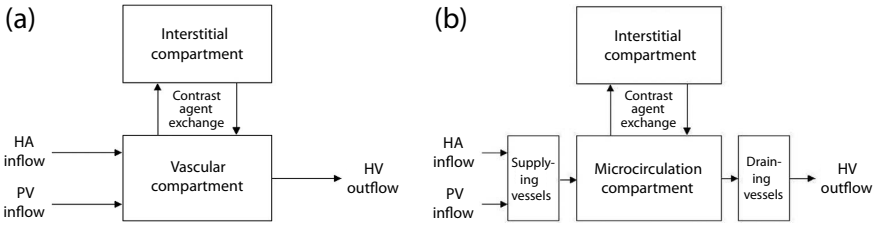

Figure 4.7: Compartment models used by Kapanen et al. [240]: (a) two-compartment model and (b) four-compartment model.

4.2.2.1.2 Electrical analog modelling. Reduced order models such as electrical analog models provide a concise way to analyse complicated vascular networks. They are often used to improve our understanding of the circulatory system [428, 459]. As such, several studies used electrical analog models

to simulate the total body haemodynamics (e.g. the human cardiovascular system [16, 29], the arterial system [264, 281], the perinatal cardiovascular system [357] etc.), while others focused on a specific organ or a specific vascular bed (e.g. the cerebral blood flow [445], the respiratory flow in lungs [220], lymph flow [108, 452] etc.). The idea behind electrical analog modelling is the analogy between the fluid flow through (blood) vessels and the electrical current through an electrical circuit. Here, we will focus on electrical models of liver perfusion.

A number of lumped parameter models have been applied to model the hepatic haemodynamics. Lumped parameters are basically quantities in which the bulk properties of a large number of vessels are condensed to only a few parameters. As such, Rypins et al. [411] investigated the haemodynamic impact of portocaval shunts used in the context of portal hypertension using a Wheatstone bridge circuit (Fig. 4.8). In this model, the HA resistance determines the pressure drop from the mean aortic pressure to the sinusoidal pressure, while the splanchnic arterial resistance represents the vascular system that supplies blood to the PV. The PV vessels are represented by the presinusoidal resistance forming the bridge. At the sinusoidal pressure point, the HA and PV flows meet and blood is drained through the HV tree (postsinusoidal resistance) towards the VCI. In addition, two flow paths are available between the portal pressure and VCI. The collateral bed resistance represents the presence of collaterals that shunt PV blood flow directly to the VCI (see also section 2.3.2), while the portocaval graft is modelled as a variable shunt resistance to investigate the impact of shunting blood to decompress the portal system. When varying the latter resistance, the bridge can be balanced so that no flow passes through the PV vessels. By modulating the resistance, higher values result in a positive PV flow, while lower values would lead to a reversed PV flow. Adding on the model of Rypins et al. [411], H. Ho et al. [194] developed a 1D model to study the haemodynamic impact of portocaval shunts. Simulation results confirmed a substantially reduced (or even reversed) PV flow when a portocaval shunt was present.

Mynard [357] developed a computer model of perinatal cardiovascular (dys)function. Within this model, a lumped parameter model of the liver haemodynamics was embedded (Fig. 4.9). The vascular bed model contains an HA inflow compartment (Z_{art}, C_{art} and R_{art}) including resistance arteries (R_{art}) that cause the pressure to fall to $p_{p/a}$, where the HA and PV inflows meet. Subsequently, blood flows through the lobules (R_{lob}) accounting for the pressure drop to venous pressure (p_{ven}), followed by the HV draining system.

In literature, different types of electrical analog models have been proposed to model the blood flow through a blood vessel (e.g. L-elements, inverted L-elements, T-elements, π-elements etc.) [90, 91, 148, 196, 197, 225,

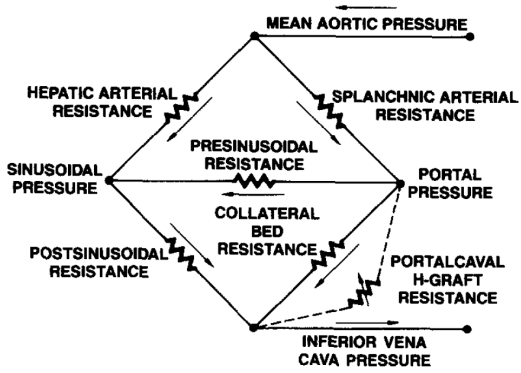

Figure 4.8: The Wheatstone bridge model of Rypins et al. [411] to investigate the effect of portocaval shunting on liver perfusion.

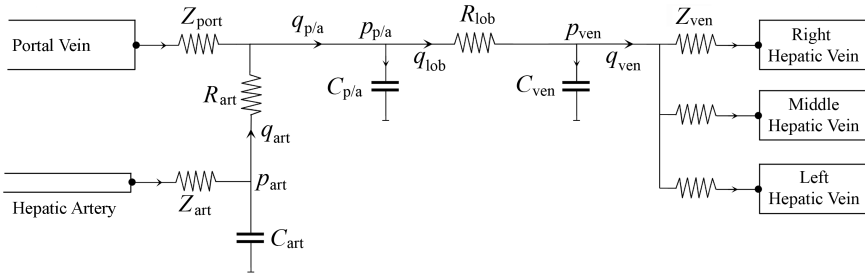

Figure 4.9: Lumped parameter model of the hepatic haemodynamics by Mynard [357] with Z being impedance, R resistance, C capacitance, p pressure, q flow, $port$ portal venous vessels, art hepatic arterial vessels, ven hepatic venous vessels and p/a being combined properties of portal venules and arterioles.

332, 372, 428, 445, 482]. In this dissertation, the π-element model of de Pater [90, 91] is used (see chapters 6 and 7). De Pater [90, 91] developed an electrical analogue of the circulatory system to get a better insight in the important and vital phenomena of the circulation. An electrical analog model for blood vessels can be derived starting from the Navier-Stokes equations and the continuity equation describing the fluid flow. These equations were simplified to two differential equations by making a number of assumptions: laminar flow (no rotational motion), no gravitational forces, blood being an incompressible Newtonian fluid (constant density and viscosity), the blood vessel being a horizontal axisymmetric and elastic tube. With these assumptions and by using a cylindrical coordinate system (r, θ, z) as illustrated in Fig. 4.10, the Navier-Stokes equations (eq. 4.22 and 4.23 in section 4.2.2.1.3) were simplified to eq. 4.1 and 4.2 describing the radial and longitudinal pressure gradients with p the pressure, v the velocity, ρ the density and μ the

dynamic viscosity. The continuity equation (conservation of mass) becomes eq. 4.3.

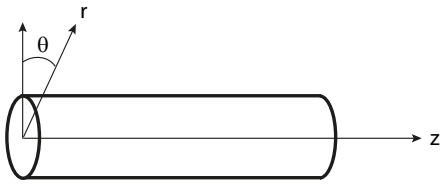

Figure 4.10: Cylindrical coordinate system with the z-axis aligned along the axis of the blood vessel.

$$-\frac{\partial p}{\partial r} = \rho\left(\frac{\partial v_r}{\partial t} + v_r\frac{\partial v_r}{\partial r} + v_z\frac{\partial v_r}{\partial z}\right) - \mu\left(\frac{\partial^2 v_r}{\partial r^2} + \frac{1}{r}\frac{\partial v_r}{\partial r} - \frac{v_r}{r^2} + \frac{\partial^2 v_r}{\partial z^2}\right) \tag{4.1}$$

$$-\frac{\partial p}{\partial z} = \rho\left(\frac{\partial v_z}{\partial t} + v_r\frac{\partial v_z}{\partial r} + v_z\frac{\partial v_z}{\partial z}\right) - \mu\left(\frac{\partial^2 v_z}{\partial r^2} + \frac{1}{r}\frac{\partial v_z}{\partial r} + \frac{\partial^2 v_z}{\partial z^2}\right) \tag{4.2}$$

$$\frac{\partial v_r}{\partial r} + \frac{v_r}{r} + \frac{\partial v_z}{\partial z} = 0 \tag{4.3}$$

In addition, de Pater [90, 91] assumed an incompressible, homegeneous and isotropic vessel wall material, obeying Hooke's law. The blood vessel is assumed to have a constant length and the wall thickness is assumed to be small compared to the radius. These assumptions allow integrating eq. 4.1-4.3 over the cross-section of the blood vessel, resulting in equations 4.4 and 4.5 describing the relation between pressure and flow (for more details on this derivation: see [91]) with q the flow, E_{wall} the Young's elasticity modulus of the wall, h_{wall} the wall thickness and μ_{wall} the viscosity of the visco-elastic wall material.

$$-\frac{\partial p}{\partial z} = \frac{8\mu}{\pi r^4}q + \frac{4\rho}{3\pi r^2}\frac{\partial q}{\partial t} \tag{4.4}$$

$$-\frac{\partial q}{\partial z} = \frac{3\pi r^3}{2E_{wall}h}\frac{\partial p}{\partial t} + \frac{\mu_{wall}}{E_{wall}}\frac{\partial^2 q}{\partial z \partial t} \tag{4.5}$$

When restricting to harmonic signals, the flow can be rewritten using the complex notation based on eq. 4.6-4.7 with q the flow as a function of time, q_m the flow magnitude, j the imaginary unit, t the time, ϕ the phase angle, ω the angular frequency and Q the complex flow as a function of the angular frequency.

$$q = q_m e^{j(\omega t+\phi)} = q_m e^{j\phi} e^{j\omega t} = Q e^{j\omega t} \tag{4.6}$$

$$Q = q_m e^{j\phi} = q_m(\cos(\phi) + j\sin(\phi)) = a + bj \tag{4.7}$$

Doing so, eq.4.4 can be rewritten as eq. 4.8, demonstrating that the pressure gradient depends on the vascular impedance (Z, eq. 4.9) and the flow q. The first term of the vascular impedance Z represents the vascular resistance in the longitudinal direction, while the second term represents the inertia of the fluid flow. Note the resemblance to the law of Poiseuille (eq. 3.2). Eq. 4.5 was derived from the continuity equation and shows the relation between the flow gradient and the material properties of the vessel wall.

$$-\frac{\partial p}{\partial z} = ZQ \tag{4.8}$$

$$Z = \frac{8\mu}{\pi r^4} + j\omega\frac{4\rho}{3\pi r^2} \tag{4.9}$$

Eq. 4.4 and 4.5 show a clear resemblance with the equations relating the voltage and current of an electrical transmission line. Fig. 4.11a shows a lumped parameter model of a segment (length z) of a transmission line with a serial resistance R_{s1}, a series inductance L_1, a parallel capacitance C_1 and a parallel resistance R_{p1} per unit of length.

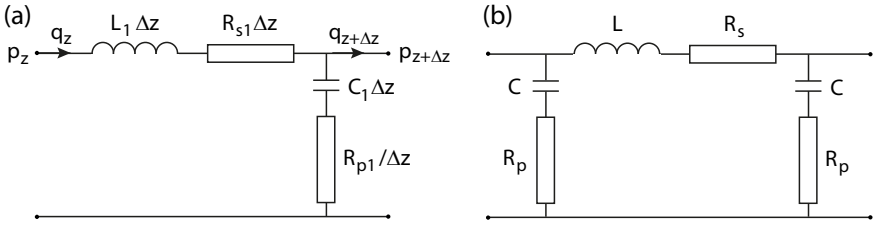

Figure 4.11: Electrical analog models: (a) electrical equivalent of a transmission line segment; (b) π element as an electrical anolog model of a blood vessel as defined by de Pater [90, 91].

Since voltage and current are analog to pressure and flow, the relations between voltage and current for this transmission line model can be written as:

$$p_z - p_{z+\Delta z} = L_1\Delta z\frac{\partial q}{\partial t} + R_{s1}\Delta z q \tag{4.10}$$

$$\frac{\partial p_{z+\Delta z}}{\partial t} = \frac{\partial(q_z - q_{z+\Delta z})}{\partial t}\frac{R_{p1}}{\Delta z} + \frac{q_z - q_{z+\Delta z}}{C_1\Delta z} \tag{4.11}$$

For Δz going to 0, these equations result in eq. 4.12 and 4.13.

$$-\frac{\partial p}{\partial z} = R_{s1} q + L_1 \frac{\partial q}{\partial t} \tag{4.12}$$

$$-\frac{\partial q}{\partial z} = C_1 \frac{\partial p}{\partial t} + C_1 R_{p1} \frac{\partial^2 q}{\partial z \partial t} \tag{4.13}$$

Except for the coefficients, the relation between voltage and current of the latter two equations is the same as the relation between pressure and flow in eq. 4.4 and 4.5. As such, there is a clear analogy between the electrical model of a transmission line and the flow equations of a blood vessel. Consequently, the corresponding coefficients should be equal. However, to model a blood vessel of a finite length l, de Pater [90, 91] adapted the electrical model to a π-filter (Fig. 4.11b). Hereby, the length was taken into account, resulting in the following coefficients:

$$R_s = R_{s1} l = \frac{8\mu}{\pi r^4} l \tag{4.14}$$

$$L = L_1 l = \frac{4\rho}{3\pi r^2} l \tag{4.15}$$

$$C = C_1 \frac{l}{2} = \frac{3\pi r^3}{2 E_{wall} h} \frac{l}{2} \tag{4.16}$$

$$R_p = R_{p1} \frac{2}{l} = \frac{2\mu_{wall} h}{3\pi r^3} \frac{2}{l} \tag{4.17}$$

Since literature values of E_{wall}, μ_{wall} and h are very scarce and/or inaccurate, de Pater [90, 91] chose to use the Moens-Korteweg equation (eq. 4.18) to calculate values of C using the pulse wave velocity c_p (eq. 4.19).

$$c_p^2 = \frac{E_{wall} h}{2\rho r} \tag{4.18}$$

$$C = \frac{l^2}{2 c_p^2 L} \tag{4.19}$$

Since values of μ_{wall} are only roughly known, de Pater [90, 91] defined R_p by eq. 4.20. This was thought to be an acceptable assumption as the influence of R_p seemed rather limited.

$$R_p = \frac{2 \cdot 10^{-6}}{C} \tag{4.20}$$

By now, an electrical analog model of a blood vessel is derived, of which the electrical components (eq. 4.14, 4.15, 4.19, 4.20) can be calculated by using the dimensions of the blood vessel (radius and length), the physical properties of the fluid (density and viscosity) and the pulse wave velocity.

Van der Plaats et al. [482] combined the modelling approach of de Pater [90, 91] with the hepatic vascular architecture data of Mall [305] to develop an electrical analog model of the hepatic perfusion in the dog liver. To do so, the hepatic vasculature was schematised as two inlet vascular trees (HA and PV) leading blood to the sinusoids, and one outflow vascular tree (HV) to drain blood into the VCI (Fig. 4.12).

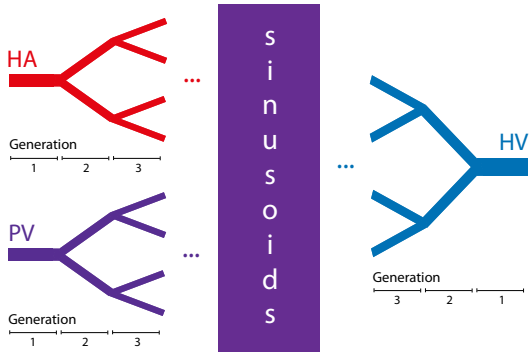

Figure 4.12: Schematic representation of the hepatic vascular trees and their generations.

Each of these trees was interpreted as a sequence of blood vessel generations, in which each generation represents a number of parallel blood vessels. As a consequence, each generation could be represented by a π-filter by adjusting the electrical components for the number of parallel blood vessels (n) (eq. 4.21 for R_s, analogous for the other components).

$$R_s = \frac{8\mu l}{n\pi r^4} \tag{4.21}$$

Doing so, each vascular tree was represented by a series of π-filters, resulting in the electrical model of a total liver as shown in Fig. 4.13. Using this model, van der Plaats et al. [482] simulated the perfusion of the dog liver. In chapter 6, we use a similar modelling approach to simulate the perfusion of the human liver based on detailed anatomical data acquired in chapter 5. Recently, two papers have been published that build further on the human liver model that we developed in chapter 6. As such, H. Ho et al. [195–197] used a simplified version of our model to simulate the HABR effect [196]. Furthermore, they used a similar simplified model to investigate the effect of transjugular intrahepatic portosystemic shunts (TIPS; see Fig. 4.6) [197] and to model the effect of a right lobectomy [195].

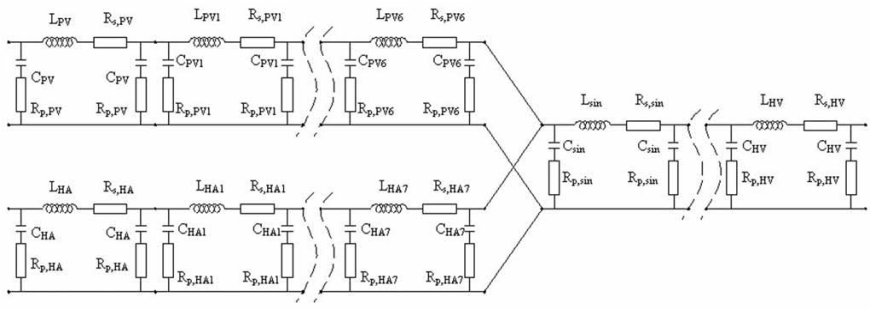

Figure 4.13: Electrical analog model of a liver. Source: [482].

4.2.2.1.3 3D modelling. In addition to the reduced order models discussed above, a number of 3D models of the blood flow through the largest hepatic vessels have used computational fluid dynamics (CFD) [251, 492]. This numerical modelling technique is based on the principles of conservation of mass and momentum. When assuming an incompressible Newtonian fluid and neglecting gravitational forces, the mathematical formulation of these principles results in the Navier-Stokes equations and the continuity equation (eq. 4.22 and 4.23) with ρ the fluid density, $\vec{v}$ the flow velocity field, t the time, p the pressure and $\bar{\tau}$ the shear stress tensor [506].

$$\rho \frac{\partial \vec{v}}{\partial t} + \rho \vec{v} \cdot \nabla \vec{v} = -\nabla p + \nabla \cdot \bar{\tau} \tag{4.22}$$

$$\nabla \cdot \vec{v} = 0 \tag{4.23}$$

In most cases, it is impossible to obtain an analytical solution for this set of non-linear partial differential equations. CFD overcomes this problem by discretising the fluid domain. For instance, Fluent (used in chapters 9 and 10; Ansys, Pennsylvania, USA) applies the finite volume method to divide the domain in a number of control volumes. As a result, a numerical grid of cells, called a 'mesh', is obtained. In this context, Yuan et al. [518] developed an interesting method to mesh tubular structures with a tree topology using centrelines. The performance of their method was tested by using MR images of a hepatic vascular tree. Next to discretisation in space, the governing equations also have to be discretised in time in the case of non-steady-state (transient) simulations. In this PhD dissertation, however, only steady-state CFD simulations were performed.

After discretisation of the fluid domain, fluid properties (e.g. the viscosity) have to be defined as well as the boundary conditions at the borders of the fluid domain. Subsequently, the governing equations are converted into

algebraic equations for all control volumes. The solution of this system of equations is approximated in an iterative way until the solution converges up to an error lower than a predefined threshold.

Several papers focused on modelling the PV flow using CFD. Petkova et al. [380] modelled the flow through the first branches of an idealised PV tree to investigate the influence of PV thrombosis. PV thrombosis was modelled as local vessel narrowing and was found to result in substantial increases of the velocity magnitude and shear stress. C.-M. Ho et al. [193] focused on the portal haemodynamic changes in the case of a right liver partial hepatectomy for LDLT. Three CFD simulations were performed using a patient-specific PV geometry: before, immediately after and one month after partial hepatectomy (Fig. 4.14). Their results clearly showed altered haemodynamics with elevated pressure immediately after hepatectomy. After one month, pressure values were again decreased to normal values and the remnant liver was regenerated, but had a different structural pattern compared to the liver before resection due to regenerative PV remodelling.

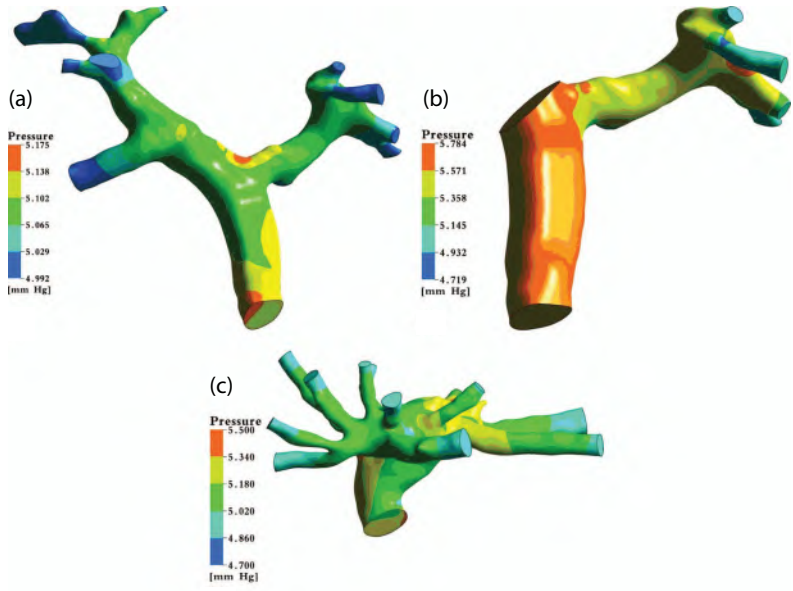

Figure 4.14: Results of the portal venous (PV) computational fluid dynamics (CFD) simulations of C.-M. Ho et al. [193]: pressure maps (a) before, (b) immediately after and (c) one month after right lobe hepatectomy.

Similarly, H. Ho et al. [195] also simulated the impact of a lobe hepatectomy in the case of LDLT, but they incorporated the splenic vein and the superior mesenteric vein (which merge into the PV) into their simulation

geometry (Fig. 4.15). As a result of the fact that the left PV receives the full PV flow after hepatectomy, the 3D simulations of the complex flow revealed substantial increases in the flow velocity and wall shear stress after partial hepatectomy compared to the baseline haemodynamics before resection. Also, strong helical flows seemed to develop after hepatectomy at the level of the merging point of the splenic vein and superior mesenteric vein. Next to partial hepatectomy, H. Ho et al. [197] also studied the liver haemodynamics induced by a TIPS procedure by using a patient-specific TIPS geometry reconstructed from CT images. Simulations showed helical flow distal to the merging point of the splenic and mesenteric flow.

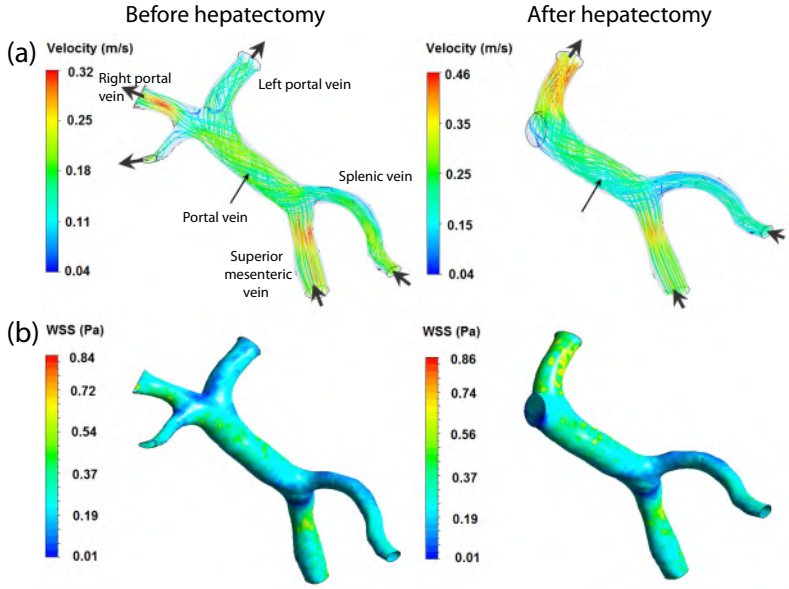

Figure 4.15: Simulation results of the potal venous (PV) system by H. Ho et al. [195]: (a) velocity magnitudes and (b) wall shear stresses before and after partial hepatectomy.

George [158] used idealised geometries as well as patient-specific geometries of the PV system (including the splenic and superior mesenteric vein) to investigate the PV flow in normal conditions, as well as in patients with cirrhosis and portal hypertension. Though a small sample size, cirrhotic patients showed a significantly increased PV cross-sectional area (1.75 cm^2 versus 0.97 cm^2) and a decreased average blood velocity per liver volume compared to normal patients ($5.8{\cdot}10^{-3}$ $1/(cm^2 s)$ versus 10^{-2} $1/(cm^2 s)$).

In addition, Van Steenkiste et al. [484] used 3D geometries of the portal system of rats to compare normal portal haemodynamics (sham operated rats) with those of portal hypertensive (common bile duct ligation; CBDL) and cirrothic (partial PV ligation; PPVL) rats (4.16). Sham operated rats

clearly showed lower wall shear stresses compared to portal hypertensive and cirrhotic rats, with the highest wall shear stress values located at the PV ligation of the cirrothic rat model. Furthermore, their results illustrated the decompressing effect of collaterals with lower wall shear stress values when collaterals were incorporated in the simulation geometry.

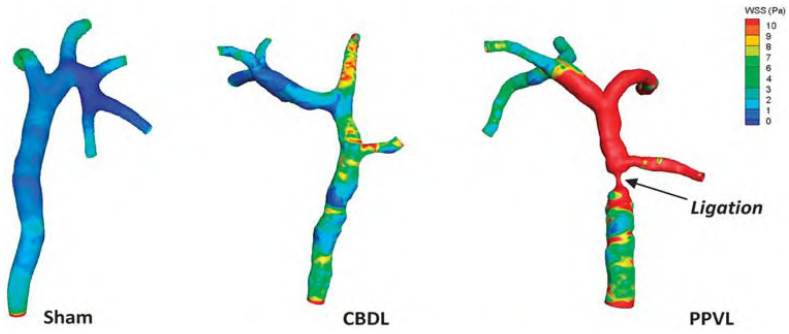

Figure 4.16: Simulation results of the potal venous (PV) system by Van Steenkiste et al. [484]: Time-averaged (over a cardiac cycle) wall shear stress distribution in the PV system of sham operated, common bile duct ligated (CBDL) and partial PV ligated (PPVL) rats.

Next, a number of CFD simulations studied the blood flow through the HA tree in order to assess the transport of microspheres (Yttrium-90) for radioembolisation of tumours [30, 31, 250]. Ideally, all injected microspheres should reach the periphery of the tumour via the blood vessels. Kennedy et al. [250] and Basciano et al. [31] used a representative idealised HA geometry based on literature values to study microsphere release and targeting (Fig. 4.17). Their CFD simulations showed that many variables influence the microsphere trajectories (vessel geometry, particle characteristics, spatial and temporal particle injection conditions etc.). Richards et al. [399] experimentally validated the simulation methodology, enabling targeting the microspheres to flow into individual branches. In the end, patient-specific computational analysis may help to optimise microsphere injection for liver tumour treatment.

In contrast to the CFD models of the hepatic haemodynamics, Ooi et al. [373] modelled the bile flow to investigate the influence of the cystic duct geometry and resistance to bile flow on the formation of gall stones. Idealised as well as actual patient-specific cystic duct geometries were modelled. Cystic ducts contain a number of valves, called the 'valves of Heister', narrowing the cross-section. The size and number of valves were found to be the most significant parameters affecting the resistance to bile flow. In the end, this modelling approach may help to assess the risk of gall stone formation in patients.

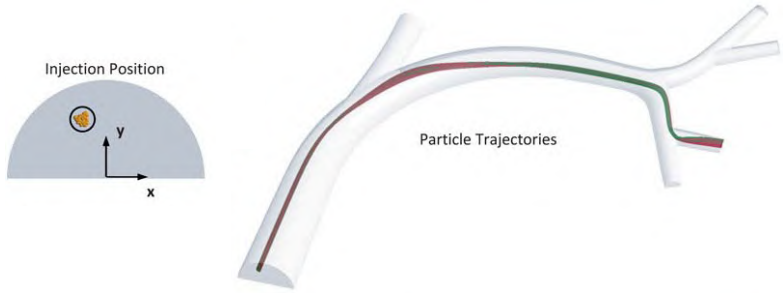

Figure 4.17: Illustration of the computational fluid dynamics (CFD) model of Basciano et al. [31] showing that individual branches can be targeted by choosing the corresponding injection location.

Particle image velocimetry (PIV) is an experimental technique, which may be applied to investigate and quantify perfusion in order to validate CFD models. Hereby, small particles are added to a fluid that is flowing through a transparent simulation geometry. The flow is illuminated so that particles can be observed and images are captured by a camera for flow analysis. For example, Lara et al. [273] studied the haemodynamics of the HV confluences using PIV to better understand abnormal HV flows due to cardiovascular venous disease.

4.2.2.2 Hepatic microperfusion models

Until now, relatively little papers have taken up the challenge of modelling the hepatic microperfusion. This is probably due to the uniqueness and complexity of the hepatic microcirculation as well as the difficulties associated with the acquisition of anatomical and functional data at sufficient resolution.

Kretowski et al. [261] coupled their hepatic macrovascular model (see section 4.1.1) with macro-functional units (MFU) to enable computing the local contrast agent concentration, e.g. for a functional CT scan. Each unit is a compartment model representing the hepatic microcirculation and counts three compartments: the sinusoids, the extracellular space and a hepatic venule (Fig. 4.18). Differential equations based on the conservation of mass allow solving the model to study the variations in concentrations in different compartments. However, this model could be improved, e.g. by incorporating communication between the sinusoids and hepatic venules.

Other hepatic microperfusion models are based on porous media [43, 302, 433] in which the sinusoids are represented by pores that are imbedded in a parenchymal matrix. Darcy's law (eq. 4.24) is used to prescribe the fluid

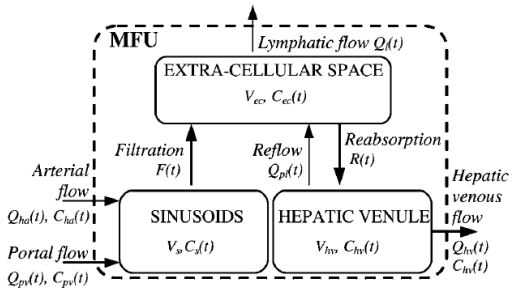

Figure 4.18: Compartmental model of the hepatic microcirculation. Source: [261].

flow through such a porous medium with p [Pa] the sinusoidal blood pressure, μ [Pa·s] the dynamic viscosity of blood, k [m²] the permeability and $\vec{v}_{porous}$ [m/s] the Darcy velocity.

$$\vec{v}_{porous} = -\frac{k}{\mu}\nabla p \tag{4.24}$$

Bonfiglio et al. [43] developed a 2D model of the blood flow through a liver lobule based on porous media. They studied the flow patterns in a hexagonal cross-section of a lobule (Fig. 4.19). Furthermore, they analysed the effects of isotropic versus 2D anisotropic permeability conditions (radial versus circumferential) as well as the influence of non-Newtonian fluid properties. Both modifications were shown to only have a small effect on the behaviour. In this way, the model gives insight in the pressure and velocity distribution in liver lobules.

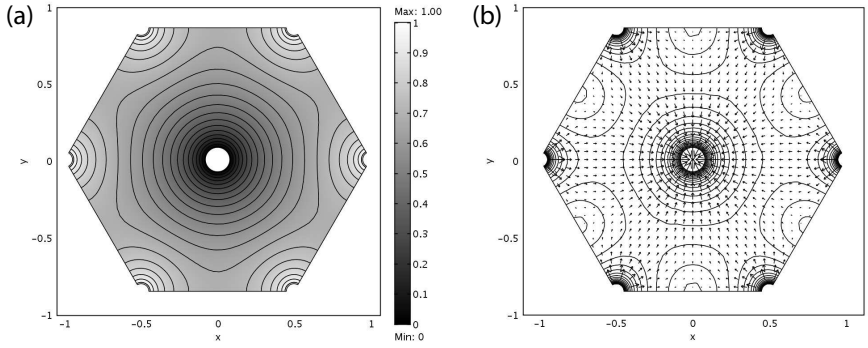

Figure 4.19: Results of the lobule model of Bonfiglio et al. [43]: (a) non-dimensional pressure and (b) velocity field.

Similarly, Siggers et al. [433] used a 2D symmetric triangular porous medium model to represent one-sixth of a hexagonal cross-section of a lobule. The model was solved analytically and PT inflows and CV outflows were modelled as point sources and point sinks, respectively. Siggers et al. [433] investigated the effect of VS by modelling them as line sources connecting two PT inflows. It was suggested that VS lead to a better spatial distribution of nutrients.

Ricken et al. [402, 508] developed a 2D biphasic mechanical model of liver lobules using porous media. The aim of this study was to describe the vascular remodelling process in normal conditions as well as after an outflow obstruction, for instance due to a liver resection. The modelling domain was an idealised geometry of a 2D longitudinal cross-section of liver lobules (Fig. 4.20). A transverse isotropic permeability was introduced in the direction of the vein as well as a relationship between the pressure gradient and direction of sinusoidal blood flow. The results for normal conditions are clearly different from those for an outflow obstruction, which results in redirecting the sinusoidal flow towards neighbouring hepatic venules that are not obstructed (Fig. 4.20).

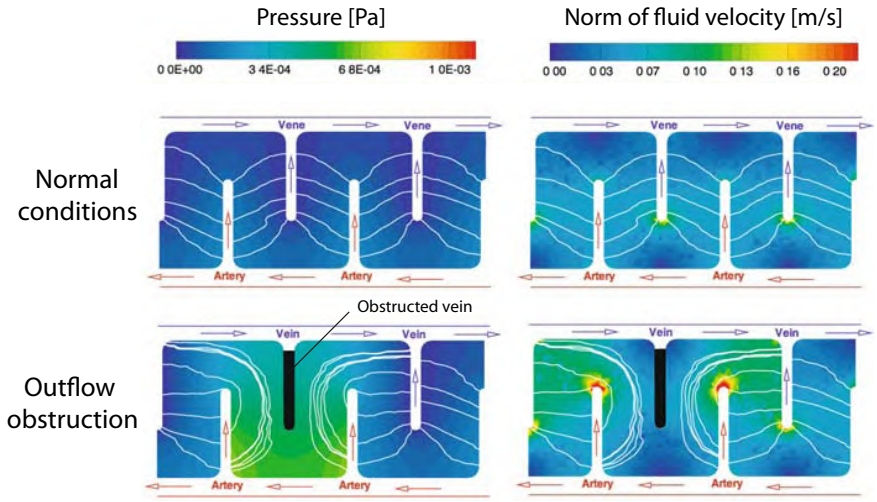

Figure 4.20: Results of the biphasic hepatic micromodel of Ricken et al. [402]. The pressure (left) and velocity (right) distributions are given for normal conditions as well as for an outflow obstruction.

Rani et al. [393] developed a 3D finite volume blood flow model of the hepatic microcirculation in a segment of a lobular structure. The idealised 3D geometry included a high pressure terminal hepatic arteriole, a low pressure portal venule and a hepatic venule (CV) as well as two fenestrated sinusoids (Fig. 4.21). Non-Newtonian blood properties were used to study the

flow features. As expected, pressures decreased from the inflow HA and PV vessels towards the sinusoids and hepatic venule.

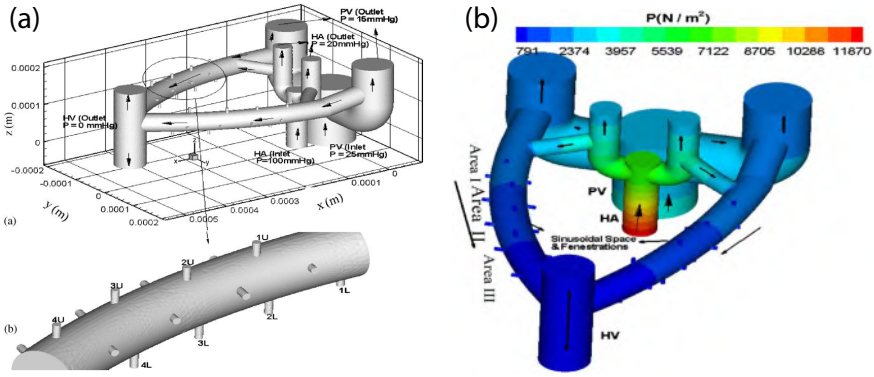

Figure 4.21: Hepatic microcirculation model of Rani et al. [393]: (a) simulation geometry and (b) pressure distribution.

Since modelling the hepatic microcirculation started only a few years ago, it is still in its infancy and more work has to be done to extend and improve these models. For example, all the discussed hepatic micromodels are based on idealised geometries, while it may be important to take into account the real 3D structure of the sinusoids. Therefore, chapter 9 discusses a CFD model of the hepatic microcirculation based on micro-CT acquired 3D imaging data.

4.3 Other liver models

Although the focus of this dissertation is modelling the liver vascular architecture and perfusion, we will shortly highlight other hepatic modelling approaches (liver mechanics and liver function) for completeness.

4.3.1 Liver mechanics

As the liver is a very vascular organ, liver tissue can be interpreted as a sponge-like porous structure with blood vessels running through it. A simple linear elastic or visco-elastic material model would thus be insufficient to model liver tissue. Therefore, constitutive models need to consider the poro-visco-elastic behaviour of liver tissue and dynamic testing is necessary to unravel its behaviour.

Several experimental studies have focused on characterising the mechanical behaviour of liver tissue by performing tensile, compression and/or shear deformation tests etc. [51, 72, 73, 150, 249, 319, 390]. For example, the

results of Chui et al. [73] suggest that the mechanical behaviour of liver tissue is anisotropic, while Kemper et al. [249] showed that human liver parenchyma behaves rate dependent with higher rates resulting in higher failure stresses and lower failure strains. These experiments provide novel data that can be useful to develop material models of liver tissue.

By now, several numerical models of the mechanical behaviour of liver tissue have been developed [72, 73, 150, 308, 390, 402, 404, 438, 508]. Raghunathan et al. [390] used a poro-visco-elastic model to model liver tissue as a biphasic fluid-filled porous medium. They simulated the mechanical response of porcine livers, resulting in accurate simulations of the stress relaxation behaviour for different strain rates. Roan et al. [404] developed a visco-hyperelas-tic constitutive model of bovine liver tissue. Their model was able to accurately describe the strain-rate dependent response. Marchesseau et al. [308] tried to combine both approaches in developing a porous visco-hyperelastic model of liver tissue aimed at performing real-time surgery simulations (Fig. 4.22). This study was conducted within the framework of the Passport project, an EU-FP7 project that stands for 'Patient-specific simulation and preoperative realistic training for liver surgery' (for more information: [12]). One of the project goals was to model the mechanical behaviour of liver tissue and its response to mechanical manipulations during surgery.

Elastography can be a useful tool to validate liver mechanics models and can be used in the clinical setting to assess *in vivo* mechanical properties of liver tissue (such as the stiffness as a measure of the stage of fibrosis) [310, 350]. Elastography techniques (ultrasound [32, 66, 101, 334, 353, 489, 490] and MRI [75, 215, 310, 421] based) seem to become a safe and reliable non-invasive alternative to liver biopsies [310].

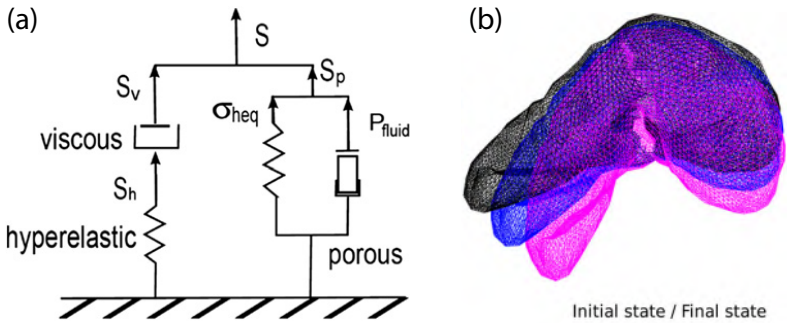

Figure 4.22: Constitutive models of liver tissue by Marchesseau et al. [308]: (a) constitutive model combining viscosity, hyperelasticity and porosity; (b) simulated deformation of a liver with black being the initial position, blue the deformation of a hyperelastic liver, and pink the deformation of a visco-hyperelastic liver.

4.3.2 Liver function

As shown in section 1.2, the liver plays a key role in maintaining the body homeostasis due to its multitude of hepatic functions. Different mathematical models of the hepatic metabolism have been developed to elucidate the ammonia metabolism [368], toxicological effects [120, 224, 247, 426, 499], liver regeneration [147, 198–200] etc. [160, 190, 229, 287, 376, 503].

Since the liver removes harmful chemicals from the body, it is important to study the long-term risk of environmental pollutants. Wambaugh et al. [499] and Shah et al. [426] used a graphical model with a discrete topology of the sinusoidal network to simulate the portal to centrilobular mass transfer of chemicals in hepatic lobules (Fig. 4.23). These virtual tissues were created within the context of the Virtual Liver Project (for more information: [1]) funded by the USA to simulate the impact of environmental chemical pollutants on the onset of chronic liver diseases with the focus on liver cancer. To this end, models are being developed to estimate the risk of liver injury and to reduce the dependence on animal testing by estimating dose-dependent toxicities [224, 247].

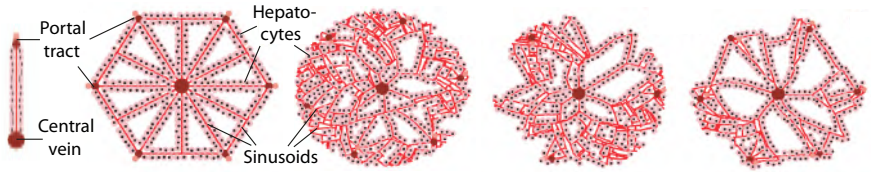

Figure 4.23: Lobule models by Wambaugh et al. [499] used to simulate mass transport of chemicals: five different morphologies were examined.

Additionally, attempts have been undertaken to develop models which are able to support diagnosing whether a patient has a liver disease and to determine the corresponding type of disease (e.g. a hybrid intelligent diagnostic model based on biomedical liver tests and a health/lifestyle survey [287], models to detect liver steatosis using electrical bioimpedance spectroscopy [190, 376], models to estimate the health status in patients with cirrhosis by using the 'Cirrhosis Relative Wellness Index' [157] etc.).

Liver regeneration (section 1.2.12) is a unique functionality of the liver that is exploited in the context of partial hepatectomy, e.g. for LDLT procedures. As the processes of regeneration are not well understood, some models have been developed to elucidate this phenomenon [147, 198–200]. Furchtgott et al. [147] developed a model of the network of interactions between cytokines and growth factors, active in the hyperplasia process of regeneration. Hoehme et al. [198–200] established a mathematical model of

liver regeneration after CCl_4 intoxication. The model showed pericentral cell death after CCl_4 intoxication, followed by the proliferation of hepatocytes to restore the macro-architecture (Fig. 4.24). Their models suggest that the orientation of hepatocytes may play an important role in the regeneration process. The work of Hoehme et al. [198–200] fits within the Virtual Liver Network (VLN; [15]), an ongoing German project on modelling human liver function [204].

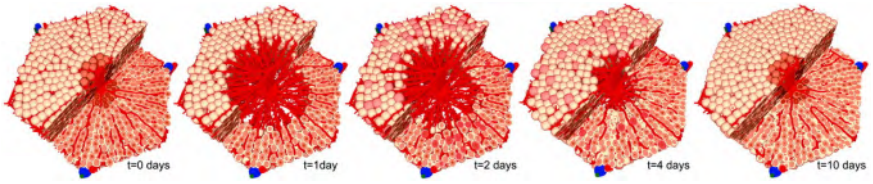

Figure 4.24: Model of liver regeneration after CCl_4 intoxication. CCl_4 intoxication first results in centrilobular damage (day 1) followed by liver regeneration during the following days. Source: [198].

Two

The hepatic macrocirculation: from experiments to electrical analog models

Chapter 5

Analysing the human liver vascular architecture by combining vascular corrosion casting and micro-CT scanning

The liver has a unique vascular architecture, which is not fully understood. Nevertheless, detailed data on the vasculature are necessary to model liver perfusion. Therefore, this chapter proposes a multiscale approach to further unravel the hepatic angioarchitecture at the level of the macro-, meso- and microcirculation.

This chapter is based on: *"Analyzing the human liver vascular architecture by combining vascular corrosion casting and micro-CT scanning: a feasibility study"*, submitted for publication [95].

5.1 Introduction

The liver is a fascinating but complex multifunctional organ, characterised by its intricate vascular architecture. Compared to other organs, the liver's vasculature is unique due to the dual blood inflow. Traditionally, the hepatic artery (HA) is regarded to supply the liver with oxygenated blood. The portal vein (PV) collects partially deoxygenated blood from the intestinal tract including spleen and pancreas. HA and PV blood mixes in the sinusoids, the hepatic microcirculation, often portrayed as a lattice of small vessels in between rows of hepatocytes, determining the smallest functional unit or liver

lobule. Blood subsequently leaves these liver lobules through central veins and eventually drains into the vena cava inferior (VCI) via the hepatic venous system (HV) [409]. All vascular trees as well as the microcirculation have their own morphological and functional characteristics. Together, they determine the hepatic haemodynamic behaviour, such as the hepatic arterial buffer response (HABR; [114]) or less physiologic phenomena such as flow competition between the HA and PV [342] (see chapter 1 for more information).

The clinical relevance to understand the exact hepatic vascular anatomy is illustrated by the disturbed vascular architecture in case of liver pathology, such as cirrhosis with fibrosis (overproduction of extracellular matrix), regenerative nodules, increased vascular resistance, neoangiogenesis and vascular remodelling leading to portal hypertension and intrahepatic shunt vessels [22, 69, 467] (see section 2.1). Moreover, the hepatic vasculature is subject to intraspecies anatomical differences, relevant in the context of transplantation (see section 1.1.3). Patient-specific analysis of the hepatic vascular topology through CT and MRI angiography may facilitate surgical planning and improve its outcome [356, 423, 514] (see section 4.1.1). Furthermore, topology information and geometrical characteristics may be fed to numerical models to simulate hepatic haemodynamics, useful to model surgical procedures or the performance of new preservation techniques for transplant livers (e.g. machine perfusion) etc. [43, 93, 98, 100, 393, 402].

Morphological analysis of vascular trees in different organs and species is not new (e.g. rodent pulmonary trees [166], mouse placental arteries [397], human coronary arteries [137], mouse kidneys [498]). However, to our knowledge, only a few papers were published on the liver's vasculature (see also chapter 4). Op Den Buijs et al. [52] classified the PV tree of the rat liver, but not the HA or HV tree. Selle et al. [423] focused on analysing the macrocirculation for surgical planning based on vascular territories. We previously performed studies on modelling liver perfusion based on the macrovessel architecture of the human [93] and rat liver [100, 142]. A larger number of studies has been published on liver microcirculation using microscopy, histological techniques etc. [118, 119, 169, 317, 318, 321, 324, 394, 465, 466], or by performing 3D reconstructions by registering 2D serial cryosections as done by Teutsch et al. [465] (see section 4.1.2).

Until now, the human liver vascular architecture has not been analysed yet in a systematic way on single liver samples. Therefore, the aim of this study was to analyse the human liver vascular architecture using a combination of vascular corrosion casting, micro-CT scanning and image processing. Hereby, a novel multiscale approach was applied to consecutively analyse the macro- and mesocirculation.

5.2 Materials and methods

In this study, a human liver was used after being discarded for transplantation due to failed reallocation. The protocol was conform to the ethical guidelines of the 1975 Declaration of Helsinki, and was approved by the Ethical Committee of the University Hospitals Leuven, Belgium, and by the Belgian Liver and Intestine Committee as foreseen by the initial protocol.

5.2.1 Vascular corrosion casting

After hepatectomy, the liver (weight ± 1.9 kg) was connected to a machine perfusion preservation device (LifePort Workstation, Organ Recovery Systems, Zaventem, Belgium; see also section 3.3.2.8) during a 24h period, and was continuously perfused at 4-6°C with pressure-control through the HA (25 mmHg; unlimited flow) and PV (7 mmHg; flow limitation of 300 ml/min). This allowed preserving the vasculature and parenchyma and keeping the blood vessels open whilst preparing the necessary logistics. Subsequently, the liver was prepared for the vascular corrosion casting procedure by cannulation of the HA, PV as well as the VCI. Casting resin was prepared by mixing Batson's #17 monomer solution, catalyst and promoter (Polysciences, Florida, USA) with monomeric methyl metacrylate (Merck, Darmstadt, Germany) and colour dyes (red and blue for the HA and PV, respectively). In addition, barium sulfate (50 mg/ml; Micropaque, Delpharm, France) was added to the HA injection to amplify the contrast between arterial and venous vessels on CT images, facilitating distinguishing different contributing vessels. The HA and PV were simultaneously and manually injected until the resin emerged sufficiently from the VCI. Afterwards, inlet and outlet vessels were clamped to avoid resin leakage during polymerisation of the injected mixture. Next, the liver was macerated in a potassium hydroxide bath.

5.2.2 Micro-CT imaging

5.2.2.1 Macrocirculation

The resulting human liver cast (Fig. 5.1a) was imaged in globo to acquire data of the first blood vessel generations, being a similar number of generations as obtained with traditional angiography techniques (macrocirculation; Fig. 5.1a). This was done using a state-of-the-art in-house developed high resolution micro-CT scanner (Fig. 5.2). Two thousand images were recorded during a 360° rotation of the cast. The image dataset (resolution of 102 µm) was reconstructed with Octopus software (Ghent University, Gent, Belgium) and converted to the DICOM format. More detailed information on the scanning procedure is available in section 6.2.1.2.

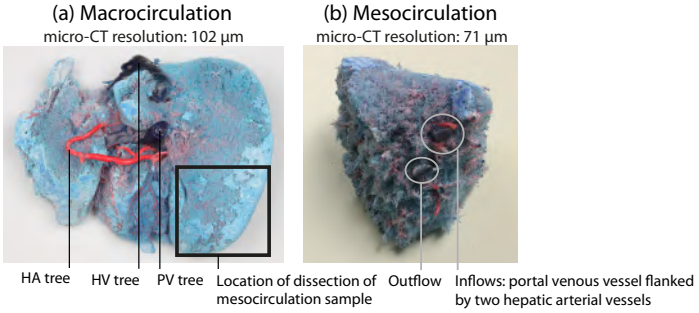

Figure 5.1: Human liver vascular corrosion cast: (a) total liver with indication of the dissection location of the mesocirculation sample; (b) mesocirculation sample.

5.2.2.2 Mesocirculation

A smaller sample (wedge-shaped; approximately 88 mm x 68 mm x 80 mm) was dissected from the inferior part of the right lobe (Fig. 5.1a-b) to investigate the morphology of vessel generations distal to the macrocirculation. This sample was imaged at a resolution of 71 µm.

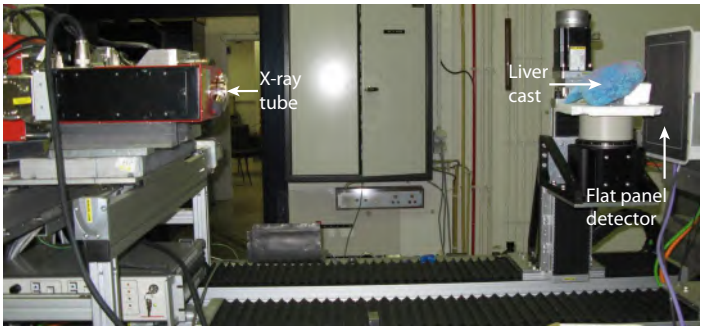

Figure 5.2: Micro-CT scanner. In contrast to traditional computer tomography (CT) scanners in clinics, the X-ray tube (closed-type with directional target; Hamamatsu Photonics KK, Shimokanzo, Japan) and flat panel detector (amorphous-Si; Varian Medical Systems, Inc., Palo Alto, California) of this setup are static, while the liver cast rotates to capture images during a 360°rotation.

5.2.3 Image processing and vascular architecture analysis

5.2.3.1 Macrocirculation

The resulting micro-CT dataset was processed using Mimics (Materialise, Leuven, Belgium). The vascular trees were segmented based on the grey

values of the images. Separating arterial from venous vessels was straightforward due to the arterial contrast agent. It was, however, challenging to segment the PV and HV trees (having similar grey values), which were manually separated at locations where they touched each other. Therefore, each vascular tree was followed starting at the first generation vessel going down to smaller vessels. When a touching vessel was detected, it was separated by removing the pixel(s) of the connection. After segmentation, a 3D reconstruction of each tree was calculated. After image processing, the vascular tree centrelines were calculated. Using the concept of blood vessel generations, the centrelines were used to determine the branching topology and geometrical features of all vascular trees. This was done by classifying vessels based on their branching pattern, being either n-furcations (parent vessels splitting in n similar daughter vessels (dichotomous bifurcations when n=2) or monopodial vessels (small side branches coming of parent vessels at an angle close to 90°) [167]. Hereby, the inlet vessel of each vascular tree is assigned to generation 1. Daughter vessels typically have higher generation numbers than their parent vessel. For instance, if a generation n vessel splits into two daughter vessels with a similar smaller diameter, the daughter vessels are assigned to generation n+1. In addition, each vessel was also assigned its radius (r; best fit radius) and length (l; centreline length). After data acquisition, exponential trend lines were fitted to the data (mean radius, mean length, number of vessels) as a function of the generation number (eq. 5.1 with y the geometrical feature, x the generation number; a and b the coefficients to be fitted).

$$y = a\, e^{-bx} \tag{5.1}$$

5.2.3.2 *Mesocirculation*

Again, segmentations and 3D reconstructions were performed. As this sample contains vessel generations distal to the macrocirculation, while the resolution is insufficient to capture the microvessels, it is labeled 'mesocirculation'. Vascular tree analysis of this sample was similar to that of the macrocirculation. However, for labour-intensity reasons, we did not analyse the total sample but selected four representative subsamples. To register the mesocirculatory dataset with the macrocirculatory dataset, the ingoing HA, PV and HV vessel of each mesocirculation subsample were identified by their corresponding vessel in the macrocirculatory dataset. Doing so, it was straightforward to assign generation numbers and geometrical feature measurements (radii and lengths) to the mesovessels. However, since we did not quantify the total liver mesovasculature, the number of vessels versus the generation number ($n_{meso,estimated}(x)$; x is the generation number) had to be estimated. This was done by multiplying the measured number of vessels

for each mesocirculation generation ($n_{meso}(x)$) by a factor. This factor is determined by dividing the number of macrocirculation vessels of the f^{th} generation ($n_{macro}(f)$; f is the number of the first mesocirculation generation included in all four subsamples) by the number of measured vessels of generation f in the mesocirculation ($n_{meso}(f)$) (eq. 5.2).

$$n_{meso,estimated}(x) = \frac{n_{macro}(f)}{n_{meso}(f)}\, n_{meso}(x) \tag{5.2}$$

5.3 Results

The casting procedure resulted in a replica of the human hepatic vascular system (Fig. 5.1a). HA vessels were red, while PV and HV were blue, due to the relatively high PV flow (75% of the outflow) compared to HA flow, resulting in dominantly blue HV flow.

5.3.1 Macrocirculation

Fig. 5.3 shows 3D reconstructions of the total liver micro-CT scan. The HA, PV and HV vascular beds were clearly distinguishable. Next to n-furcations (such as bifurcations and trifurcations), the trees count a high number of monopodial vessels, sprouting from parent vessels at angles close to 90° (Fig. 5.3b-d). After the first generations, HA vessels run parallel to PV vessels. In a few cases, one PV vessel is even flanked by two HA vessels. Moreover, HA vessels have predominantly circular cross-sections compared to elliptical cross-sections of PV and HV vessels. Each tree was classified according to its branching topology, resulting in 6, 6 and 5 generations for the HA, PV and HV tree, respectively. Mean HA radii drop from 3.45 mm to $5.92{\cdot}10^{-1}$ mm, PV radii from 7.34 mm to 1.08 mm and HV radii from 13.2 mm (VCI) to 1.13 mm (Fig. 5.4a-c). As anticipated, portal and hepatic venous vessels (PV and HV) have larger diameters compared to HA vessels. Exponential trend lines, fitted to radii measurements, have high determination coefficients ($R^2 \geq 0.97$). Mean lengths don't show a clear-cut decreasing trend in the first generations (especially for PV vessels), but decrease in higher generations (Fig. 5.4d-f). This is partially due to the first generation vessel of each tree being cut to resect the liver, implying an underestimated length. Therefore, the first generation length is not accounted for when calculating length trend lines. The PV length trend line has the lowest R^2 value (0.77). Length standard deviations are higher than those for radii. Numbers of vessels per generation clearly increase exponentially towards higher generation numbers: from 1 to 271, 1 to 216, and 1 to 76 vessels for the HA, PV, and HV tree, respectively (Fig. 5.5).

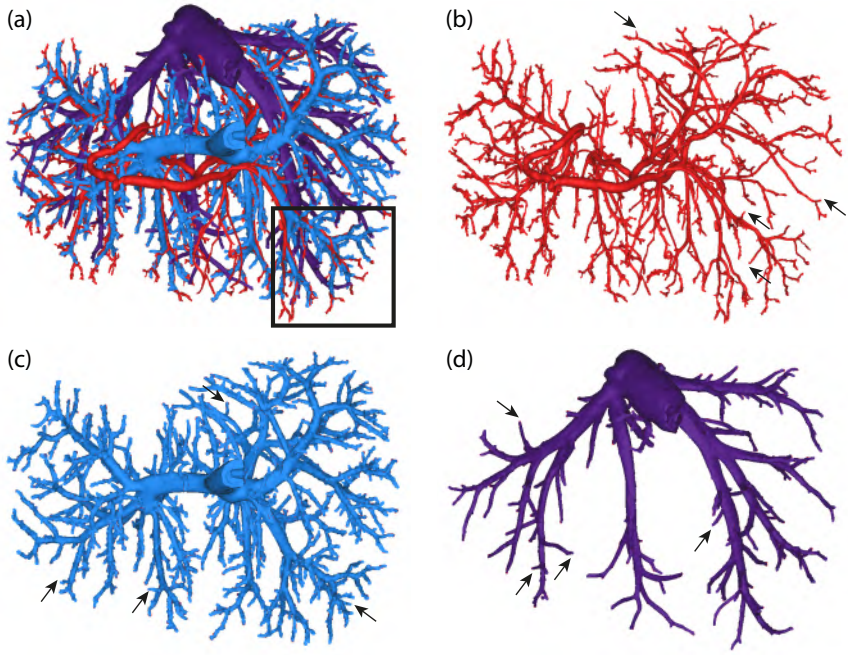

Figure 5.3: 3D reconstructions of the macrocirculation: (a) superposition of three vascular trees with indication of the dissection location of the mesocirculation sample; (b) hepatic arterial (HA), (c) portal venous (PV) and (d) hepatic venous (HV) trees. Arrows indicate examples of monopodial branches.

5.3.2 Mesocirculation

Segmentations of the mesocirculation subsample (Fig. 5.1b) were more challenging than the macrocirculation, because more vessels were touching each other (Fig. 5.6). Fig. 5.1b and 5.6a show that the PV inflow runs parallel to two HA vessels. Similar to the macrocirculation, this sample shows elliptical PV and HV vessels compared to circular HA vessels. Analysing four subsamples (brighter subsamples in Fig. 5.6b-d) resulted in the visualisation of higher generation vessels, going up to generation 13, 13 and 10 for the HA, PV and HV trees, respectively (Table 5.1, Figs. 5.4-5.5). Mean radii decrease to $8.00{\cdot}10^{-2}$, $1.23{\cdot}10^{-1}$ and $1.60{\cdot}10^{-1}$ mm for the HA, PV and HV trees, respectively (Fig. 5.4a-c). Radii trend lines were fitted to the pooled macro- and mesocirculation measurements ($R^2 \geq 0.98$). Mean lengths also decrease for all trees ($R^2 \geq 0.94$). The numbers of vessels per generation again increase exponentially, almost exactly following extrapolations of the macrocirculation trend lines. All trend lines fitted to the combination of macro- and mesocirculation measurements show equal or higher goodness of fit than those fitted to only the macrocirculation, except for the HA radii (Figs. 5.4-5.5).

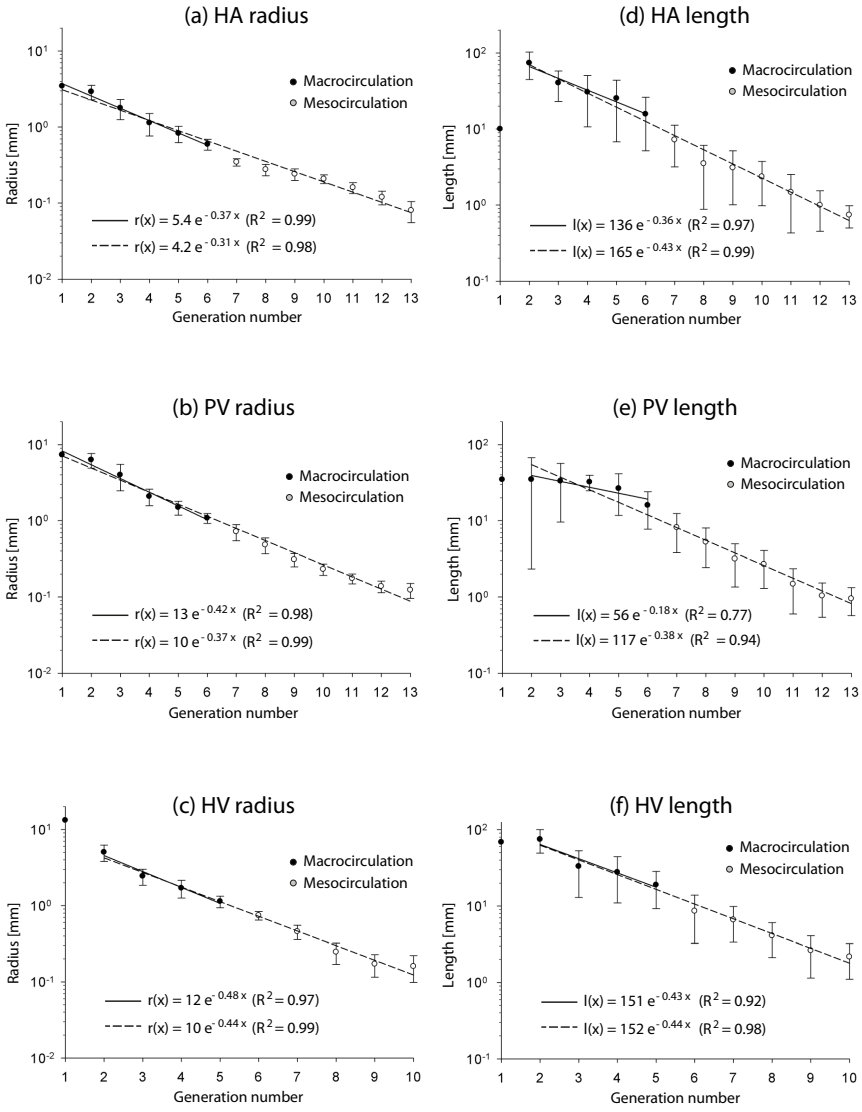

Figure 5.4: Results of the vascular tree analysis of the macro- and mesocirculation: radius (a-c) and length (d-f) with their standard deviations as a function of the generation number for the hepatic arterial (HA), portal venous (PV) and hepatic venous (HV) trees, respectively. Macro- and mesocirculation measurements are indicated by black and white markers, respectively. Exponential trend lines are depicted by full lines when fitted to macrocirculation data, and dashed lines when fitted to macro- and mesocirculation data. Equations and coefficients of determination (R^2) of the exponential functions are given. The first HV generation (vena cava inferior; VCI) was not taken into account when fitting the radius trend line, since the VCI has a much larger diameter and is not really part of the hepatic vasculature. Length trend lines did not incorporate the first generation, since these vessels were cut to resect the liver, resulting in an underestimated length.

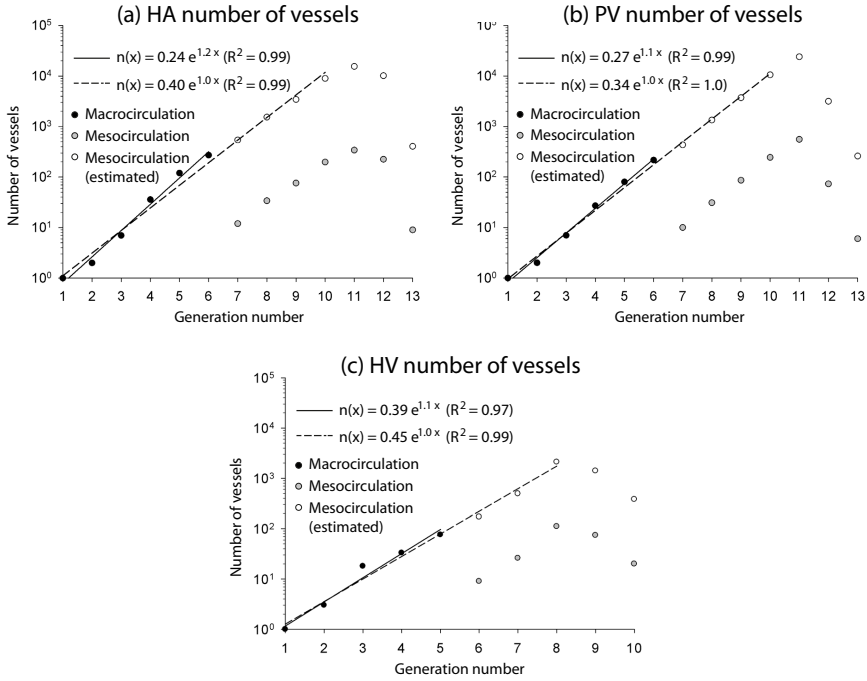

Figure 5.5: Results of the number of vessels per generation number of the macro- and mesocirculation for the hepatic arterial (HA), portal venous (PV) and hepatic venous (HV) trees, respectively. Macro- and mesocirculation measurements are indicated by black and grey markers, respectively. Estimated numbers of vessels for the mesocirculation (Table 5.1) are indicated by white dots. Exponential trend lines are depicted as full lines when fitted to the macrocirculation data, and dashed lines when fitted to the macro- and estimated mesocirculation data. Equations and coefficients of determination (R^2) of the exponential functions are given.

5.4 Discussion

For the first time, the (human) hepatic vasculature of one and the same liver is visualised and 3D reconstructed at different length scales (from the largest vessels down to the mesocirculation; see chapter 9 for the microcirculation). Therefore, this pilot study used a combination of state-of-the-art vascular corrosion casting and micro-CT scanning techniques with a novel image processing and analysis technique.

However, one has to be careful when generalising these findings based on a single liver. More livers should thus be similarly analysed to get a general overview of the human hepatic vascular architecture. As such, this pilot study should be interpreted as the vascular analysis of a specific liver. This human liver was offered to our lab after failed rescue allocation and there

Table 5.1: Overview of the HA, PV and HV measurements of the macro- and mesoscale. Results are reported as the generation number with its mean radius, mean length and number of vessels. (Estimated numbers of vessels of mesocirculation generations are calculated using eq. 5.2.)

	Generation number	Mean radius [mm]	Radius standard deviation [mm]	Mean length [mm]	Length standard deviation [mm]	Number of vessels	Estimated number of vessels
HA Macroscale	HA 1	3.45	0	10.0	0	1	
	HA 2	2.91	$6.33 \cdot 10^{-1}$	73.9	29.2	2	
	HA 3	1.78	$5.28 \cdot 10^{-1}$	40.4	17.5	7	
	HA 4	1.13	$3.71 \cdot 10^{-1}$	30.6	19.9	36	
	HA 5	$8.25 \cdot 10^{-1}$	$2.00 \cdot 10^{-1}$	25.3	18.5	120	
	HA 6	$5.92 \cdot 10^{-1}$	$9.61 \cdot 10^{-2}$	15.7	10.5	271	
HA Mesoscale	HA 5	$8.62 \cdot 10^{-1}$	$3.54 \cdot 10^{-3}$	54.4	25.4	2	
	HA 6	$5.21 \cdot 10^{-1}$	$1.54 \cdot 10^{-1}$	12.2	8.29	6	
	HA 7	$3.45 \cdot 10^{-1}$	$3.90 \cdot 10^{-2}$	7.22	4.04	12	542
	HA 8	$2.77 \cdot 10^{-1}$	$4.70 \cdot 10^{-2}$	3.51	2.62	34	1536
	HA 9	$2.41 \cdot 10^{-1}$	$4.19 \cdot 10^{-2}$	3.09	2.08	76	3433
	HA 10	$2.08 \cdot 10^{-1}$	$2.73 \cdot 10^{-2}$	2.36	1.38	198	8943
	HA 11	$1.60 \cdot 10^{-1}$	$2.62 \cdot 10^{-2}$	1.48	1.05	342	15447
	HA 12	$1.19 \cdot 10^{-1}$	$2.47 \cdot 10^{-2}$	1.00	$5.45 \cdot 10^{-1}$	225	10163
	HA 13	$8.00 \cdot 10^{-2}$	$2.46 \cdot 10^{-2}$	$7.41 \cdot 10^{-1}$	$2.40 \cdot 10^{-1}$	9	407
PV Macroscale	PV 1	7.34	0	34.7	0	1	
	PV 2	6.30	1.36	34.9	32.5	2	
	PV 3	4.00	1.52	33.2	23.6	7	
	PV 4	2.09	$5.17 \cdot 10^{-1}$	32.3	7.55	27	
	PV 5	1.49	$3.09 \cdot 10^{-1}$	26.5	14.8	80	
	PV 6	1.08	$1.60 \cdot 10^{-1}$	15.9	8.18	216	
PV Mesoscale	PV 5	1.41	0	19.9	0	1	
	PV 6	$8.86 \cdot 10^{-1}$	$2.25 \cdot 10^{-1}$	14.8	7.94	5	
	PV 7	$7.18 \cdot 10^{-1}$	$1.72 \cdot 10^{-1}$	8.14	4.33	10	432
	PV 8	$4.82 \cdot 10^{-1}$	$1.12 \cdot 10^{-1}$	5.24	2.80	31	1339
	PV 9	$3.09 \cdot 10^{-1}$	$6.16 \cdot 10^{-2}$	3.16	1.80	86	3715
	PV 10	$2.31 \cdot 10^{-1}$	$3.92 \cdot 10^{-2}$	2.68	1.39	244	10541
	PV 11	$1.75 \cdot 10^{-1}$	$2.61 \cdot 10^{-2}$	1.48	$8.75 \cdot 10^{-1}$	555	23976
	PV 12	$1.38 \cdot 10^{-1}$	$2.39 \cdot 10^{-2}$	1.03	$4.91 \cdot 10^{-1}$	73	3514
	PV 13	$1.23 \cdot 10^{-1}$	$2.71 \cdot 10^{-2}$	$9.50 \cdot 10^{-1}$	$3.79 \cdot 10^{-1}$	6	259
HV Macroscale	HV 1	13.2	0	68.4	0	1	
	HV 2	5.02	1.20	74.4	25.2	3	
	HV 3	2.43	$5.79 \cdot 10^{-1}$	33.0	20.1	18	
	HV 4	1.70	$4.45 \cdot 10^{-1}$	27.6	16.7	33	
	HV 5	1.13	$1.94 \cdot 10^{-1}$	18.8	9.60	76	
HV Mesoscale	HV 5	1.27	$4.42 \cdot 10^{-1}$	32.5	12.7	4	
	HV 6	$7.41 \cdot 10^{-1}$	$9.27 \cdot 10^{-2}$	8.56	5.30	9	171
	HV 7	$4.56 \cdot 10^{-1}$	$9.66 \cdot 10^{-2}$	6.59	3.23	26	494
	HV 8	$2.46 \cdot 10^{-1}$	$7.65 \cdot 10^{-2}$	4.09	1.97	111	2109
	HV 9	$1.71 \cdot 10^{-1}$	$5.59 \cdot 10^{-2}$	2.61	1.47	74	1406
	HV 10	$1.60 \cdot 10^{-1}$	$6.10 \cdot 10^{-2}$	2.17	1.06	20	380

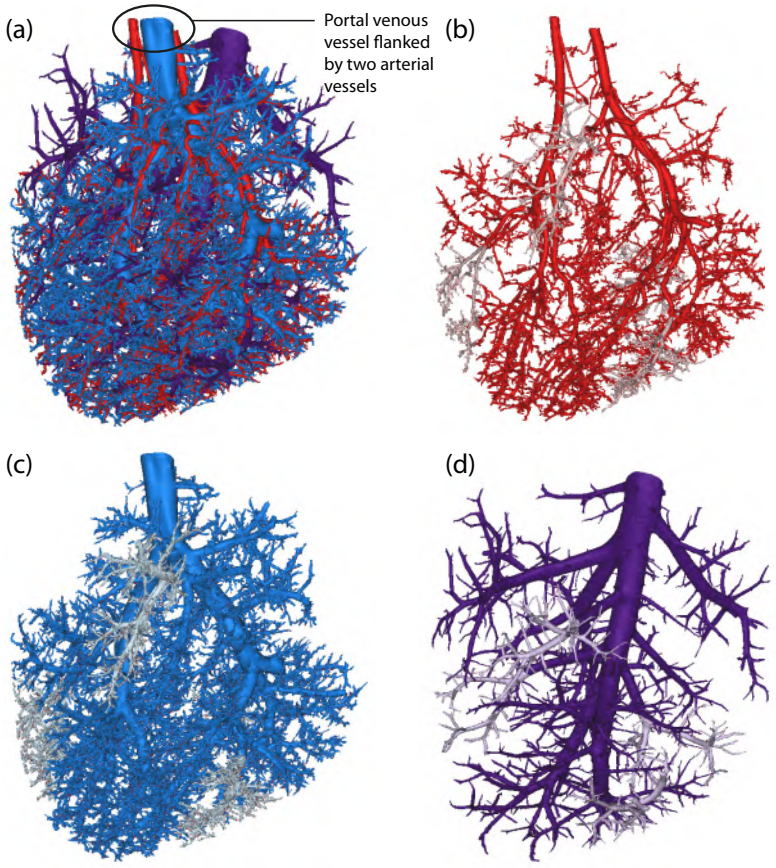

Figure 5.6: 3D reconstructions of the mesocirculation: (a) superposition of three vascular trees; (b) hepatic arterial (HA), (c) portal venous (PV) and (d) hepatic venous (HV) trees. The brighter parts of (b)-(d) show the four subsamples used to acquire geometrical data.

was no obvious macroscopic abnormality. The casting procedure was done by manual injection, having the advantage of sensing how the organ reacts while injecting. Also, it has been described that casting may lead to slight shrinkage of the resin, which would imply slightly smaller diameters [260]. However, our diameter measurements were comparable with literature data on the largest hepatic vessels [317, 496, 501]. Moreover, the casting procedure was performed according to standardised procedures by a team having many years of expertise [63, 93, 100].

Ideally, the complete cast should be scanned at once at a sufficiently high resolution to allow visualising all vessels down to the sinusoids. However, it was technically impossible to scan a total liver at a resolution of a few micrometers due to computational and software limitations to process datasets with an extremely large file size. Consequently, a multiscale approach was

used to consecutively study the macro- and mesocirculation (see chapter 9 for the microcirculation), allowing the quantification of 13 (HA and PV) and 10 (HV) blood vessel generations as well as the sinusoids. However, there is still a gap of a number of generations between the 10/13th generation and the sinusoids. Nonetheless, the total number of generations can be approximated by extrapolating the resulting exponential trend lines of the radius (Fig. 5.4) down to the level of radius values of the terminal vessels, resulting in an estimation of 19-20, 17-18 and 13-14 generations for the HA, PV and HV trees, respectively. Hereby, sinusoids are interpreted as being the connection between the terminal/last generation of the inflow trees (HA and PV) and outflow tree (HV).

Our data reveal a complex hepatic vascular topology covering the macro- down to the microcirculation, showing that hepatic trees do not solely branch according to a dichotomous bifurcating pattern, which is often assumed in vascular tree models. *N*-furcations as well as monopodial vessels were clearly visualised in the macro- and mesocirculation. Geometrical characteristics (Figs. 5.4-5.5) show exponential behaviour as a function of generation numbers. HA and PV trees show similar behaviour and exponential trends, resulting in equal numbers of generations for the macro- and mesocirculation. However, PV radii are larger than HA radii, and starting from generation 4, numbers of HA vessels are higher than those of PV vessels (Table 5.1), probably due to some PV vessels being flanked by two parallel HA vessels. The HV tree has the largest radii and typically counts less generations than the HA and PV tree.

The novel and detailed morphological data gathered in this study are useful to complement scientific insights into liver morphology and physiology. The new multiscale approach is also applicable in the context of liver pathophysiology, e.g. to investigate pathology-related vascular alterations in case of fibrosis and cirrhosis [69, 486], hepatocellular carcinoma [302], portal hypertension [140, 513] etc. Furthermore, this approach may generate input data for the development of numerical models of liver perfusion. These models can be applied to simulate the haemodynamic impact of (ab)normal situations such as isolated organ perfusion and surgical procedures, e.g. partial hepatectomy.

5.5 Conclusion

Combining vascular corrosion casting with state-of-the-art high resolution micro-CT scanning provides novel and unique data on the human hepatic vasculature from the macrocirculation and mesocirculation (see chapter 9 for the microcirculation). A new multiscale approach allows visualising the complex liver vasculature at different levels in 3D and performing a detailed

analysis of the topology and geometrical features. These data are useful to create numerical models of the hepatic blood circulation. This approach could also be applied to other organs, such as kidneys.

Chapter 6

From vascular corrosion cast to electrical analog model for the study of human liver haemodynamics and perfusion

This chapter is based on *"From vascular corrosion cast to electrical analog model for the study of human liver hemodynamics and perfusion"*, as published in IEEE Transactions on Biomedical Engineering, 58(1):25-35, 2011 [93]. In this chapter, the macrocirculation data obtained in chapter 5 are used.

6.1 Introduction

Liver transplantation is an effective therapy for patients with end-stage liver disease, but is being confronted with an increasing shortage of donor livers. In 2008, the Eurotransplant International Foundation (responsible for the mediation and allocation of organ donation in Austria, Belgium, Croatia, Germany, Luxemburg, the Netherlands and Slovenia) reported 2442 patients on the waiting list for liver transplantation, of whom 463 patients died [125]. A possible solution is to extend the donor pool to marginal or expanded criteria donors, including non-heart-beating donors [481]. Transplanting these suboptimal donor organs, however, requires better preservation methods than static cold storage (CS), where donor organs are not perfused,

but simply preserved on ice. Due to the limitations of CS, the organs lose viability, suffer from irreversible injury (e.g. cellular oedema, acute inflammation and reperfusion damage) and can only be preserved during a restricted period [326]. As a result, hypothermic machine perfusion (HMP) is experiencing a revival as an alternative organ preservation method. In HMP, the physiological perfusion within the body is imitated by continuous perfusion of the organ with a hypothermic (4 - 6°C) perfusion fluid. HMP thus combines the advantages of hypothermia, which substantially decreases the metabolic activity, and perfusion, which can supply nutrients, pharmaceuticals and oxygen to the organ, and remove waste products [340]. Although HMP is already commercially available and clinically widely applied for kidneys [338], this is not the case for livers. The liver has a more complex vascular architecture with two blood inlets, requiring a more complicated perfusion and the need for two supplying pumps (either pressure- or flow-driven). However, prototypes of perfusion machines for donor livers exist, but they still encounter several problems. Shear stresses, produced by the perfusion fluid flow, may damage the endothelial cells lining the sinusoids. Morphological changes of sinusoidal endothelial cells have been reported after HMP, as well as flow heterogeneity, elevated vascular resistances and possibly sinusoidal flow obstruction [227]. Furthermore, there is still no consensus on the optimal perfusion settings and on the composition of the most appropriate perfusion fluid for liver HMP. In addition, flow competition has been observed between the hepatic artery (HA) and the portal vein (PV) during HMP experiments, counteracting a well-balanced perfusion (see section 3.3.3) [191, 342]. Consequently, the challenge is to define optimal parameter settings for HMP to maintain sufficient perfusion without damaging liver tissue [488]. Within this context, it would be of specific interest to gain more insight into the liver vascular architecture and the distribution of pressure and flow throughout the organ during HMP.

The aim of the present study is to develop an electrical analog model of the blood flow through the human liver following a methodology previously applied to the dog liver. Since (electrical) models of the total human liver do not yet exist, we based our model on an electrical analogue of a dog liver [482] and adapted it to a human liver. Because detailed anatomical data of the human liver vasculature are required as input for the electrical model and since literature only provides few data of the main human liver branches, we first gathered detailed data of the human liver, using a novel data acquisition technique (including vascular corrosion casting, micro-CT imaging and image processing).

6.2 Materials and Methods

6.2.1 Anatomical data

The study was conducted on two human livers discarded for transplantation after failed reallocation. This was approved by the Ethical Committee of the University Hospitals Leuven (Belgium) and by the Belgian Liver and Intestine Committee as foreseen by the initial protocol. The procedure to obtain anatomical data consisted of four steps: vascular corrosion casting, micro-CT scanning, image processing and data acquisition.

6.2.1.1 HMP and vascular corrosion casting procedure

After the initial vascular flush and hepatectomy, the livers underwent HMP and were perfused for 24 hours with KPS-1 perfusion fluid (Organ Recovery Systems, Zaventem, Belgium) at 4-6°C in order to preserve the macrocirculation as well as the microcirculation. A liver HMP prototype (LifePort Workstation; Organ Recovery Systems, Zaventem, Belgium) allowed pressure-controlled (25 mmHg), flow-unlimited continuous perfusion for the HA and pressure-controlled (7 mmHg), flow-limited (300 ml/min) continuous perfusion through the PV. For the vascular corrosion casting procedure of the HA, PV and hepatic veins (HV), the livers were positioned with their diaphragmatic surface down into a bowl-shaped container, allowing the organ to preserve its normal anatomical shape as much as possible. Subsequently, each liver was simultaneously injected via the HA and the PV with a casting resin prepared just before the injection by mixing Batson's #17 monomer solution (100 parts), Batson's catalyst (15 parts) and Batson's promoter (1 part) (Polysciences, Florida, USA) with monomeric methyl metacrylate (20 parts) (Merck, Darmstadt, Germany). In addition to using two different colouring dyes to distinguish the arterial and venous trees (red for HA, blue for PV), a suspension of 25% barium sulfate (Micropaque, Delpharm, France) was mixed with the resin for the HA tree. The goal of adding this contrast agent was to allow a discrimination of the arterial blood vessels from the venous system on X-ray images. The PV and the HA were manually injected with a total volume of ± 200 ml and ± 100 ml casting solution, respectively. This volume proved to be sufficient, as the resin was emerging from the HV in sufficient quantities at the end of the injection. Next, all vessels were clamped and the injected fluid was allowed to polymerise for ± 2 hours. Manipulation of the liver was kept to a strict minimum during this period. Subsequently, the livers were macerated in a 25% potassium hydroxide solution for approximately two days. The remaining casts of the vascular trees were rinsed in tap water overnight, flushed with three liters of distilled water and dried under a vented hood.

6.2.1.2 Micro-CT imaging

The 3D geometry of the liver casts was acquired with an in-house developed high-resolution micro-CT scanner. In contrast to conventional CT scanners, this scanner has a different configuration: the sample rotates, while the X-ray tube and flat panel detector are static. As normally small samples with mm-dimensions are scanned, scanner setup adjustments were necessary to be able to scan liver casts with larger dimensions. The setup consisted of a closed-type X-ray tube with directional target (Hamamatsu Photonics KK Shimokanzo, Japan) and an amorphous-Si flat panel detector (Varian Medical Systems Inc., Palo Alto, California). The detector (0.127 µm pixel size) was tiled with a mechanical translation stage in order to obtain a detector field of 2800 x 1000 pixels (36 x 12 cm). Two thousand projection images were recorded while the cast was rotated over 360°. The tube operated at 90 keV and 250 µA, and the reconstruction was performed with Octopus-software (Ghent University, Gent, Belgium), resulting in a 2800 x 2800 x 1000 voxel dataset with a voxel pitch or resolution of 101.8 µm for cast 1 and 111.8 µm for cast 2. Because of computer performance restrictions, 3D datasets were binned. The datasets of cast 1 and 2 underwent binning 4 and 2, respectively, meaning that new datasets were obtained by calculating the mean grey values of all volumes built up of 4 x 4 x 4 and 2 x 2 x 2 voxels, respectively. The new image datasets with smaller file size were subsequently converted to DICOM format for image processing.

6.2.1.3 Image processing

Images were processed using Mimics software (Materialise, Leuven, Belgium). First, the datasets were segmented in three vascular trees based on their grey values. Segmentations of arterial (HA) and venous (PV and HV) vascular beds were relatively straightforward because of the arterially added barium sulfate. In contrast, PV and HV trees were not clearly distinguishable due to their similar range of grey values in the digital images. PV and HV segmentations were therefore completed by manually separating the segmentation masks on locations where PV and HV vessels touched each other. Secondly, 3D reconstructions of the vascular trees were calculated and visualised.

6.2.1.4 Data acquisition

Data acquisition was performed using the centreline algorithm in Mimics, which allowed calculating the centrelines of all vessel segments defined by the software. Afterwards, vessel segments were manually grouped to blood vessels. Vessel classification and data acquisition was performed based on the vascular tree centrelines. First, an inventory of the vascular trees was

obtained using the concept of blood vessel generations. In literature, classification of vascular trees is usually based on branching patterns concerning dichotomous (bifurcations) and monopodial (side branches) branching (see also section 4.1.1) [167]. In contrast, human livers do not only contain these patterns, but also more sophisticated patterns such as trifurcations. To determine to which generation a vessel belonged, we started by defining the mother vessel of each vascular tree (HA, PV and HV) as generation 1. When the mother vessel branched into two or more equal daughter vessels, these were defined as generation 2. In this way, all vessels (except the monopodial vessels) were classified. Since neglecting the monopodial vessels would have a significant influence on the number of vessels and the results of the electrical model, it was necessary to take them into account. Monopodial side branches were mostly classified as belonging to the generation following that of the mother vessel from which they originate (e.g. a side branch of a generation 3 vessel was usually classified as a generation 4 vessel). However, when its diameter was significantly smaller than that of the other branched-off dichotomous daughter vessels, the monopodial vessel was classified as a further generation branch corresponding to its diameter by comparison with the mean diameters of the following generations.

All vessels were given a name '*x.y*', in which *x* stands for the generation number and *y* represents a unique vessel number inside the generation. Additionally, vessel diameters and lengths were measured. Since vessel diameters are usually not perfectly circular, diameter measurements were based on 'best fit diameter' measurements, using an algorithm which minimises the average distance between the vessel circumference and the circle defined by the fitted diameter. Vessel lengths were measured by determining lengths of the vessel centrelines. Applying this approach, a quantitative analysis was performed to collect the anatomical vascular data of human livers.

6.2.2 Electrical analog model

6.2.2.1 Principle

The model is based on an electrical analogue of hepatic blood flow through a dog liver, obtained in a previous study by van der Plaats et al. (see also section 4.2.2.1.2) [482]. Like any electrical analog model, it is based on the analogy of the simplified Navier-Stokes equations describing flow through a cylindrical tube (representing a blood vessel), and the electrical equations describing current and voltage through an electrical circuit, in this case a π-filter (see dotted line in Fig. 6.1) [90, 91]. The filter contains four different components defined in eq. 6.1 to 6.4 as derived in section 4.2.2.1.2: serial resistance R_s, serial inductance L, parallel conductance C and parallel resistance R_p.

$$R_s = \frac{8\mu l}{\pi r^4}\left[\frac{Ns}{m^5}\right] \tag{6.1}$$

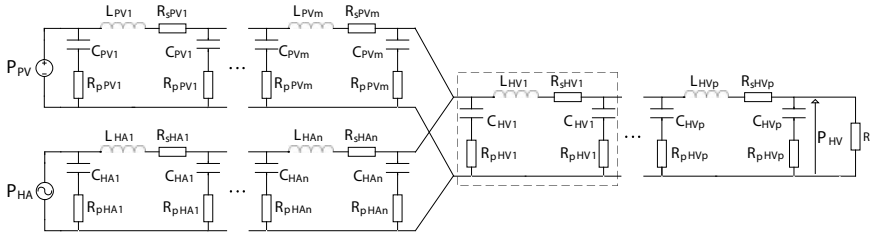

Figure 6.1: Electrical model of the liver. HA and PV inlet vascular trees are represented by hepatic arterial (HA) and portal venous (PV) voltage sources, each followed by a series of π-filters. These two vascular trees are connected at the level of the sinusoidal generation (dotted line). Subsequently, a third series of π-filters referring to the hepatic venous (HV) vascular tree ends in a vascular outflow resistance at the vena cava inferior (VCI).

$$L = \frac{1.33\rho l}{\pi r^2}\left[\frac{Ns^2}{m^5}\right] \tag{6.2}$$

$$C = \frac{l^2}{2{c_p}^2 L}\left[\frac{m^5}{N}\right] \tag{6.3}$$

$$R_p = \frac{2 \cdot 10^{-6}}{C}\left[\frac{Ns}{m^5}\right] \tag{6.4}$$

Variables are the dynamic viscosity ($\mu = 3.5 \cdot 10^{-3}$ Pa·s) and density ($\rho =$ 1050 kg/m^3) of the perfusion fluid (in this case of blood), the radius (r [m]) and length (r [m]) of the blood vessels and the pulse wave velocity (c_p [m/s]) as a measure of vessel stiffness. R_s represents the vascular resistance of the blood vessel, C the elasticity, R_p the visco-elasticity and L the inertia of the blood. Equations 6.1 to 6.4 refer to the components of a π-filter representing one blood vessel. Considering a blood vessel generation as a group of n parallel connected identical vessels, this corresponds to n parallel connected π-filters. Subsequently, this can be simplified to one π-filter by taking into account the number of parallel vessels (n). The component values of the π-filter are then found by dividing R_s, R_p and L by n and multiplying C by n. In this way, one generation of vessels is represented by one π-filter, the building block of the electrical analogue.

As the liver has three main vascular trees each comprising several generations, an electrical analogue of the liver with three π-filter branches was obtained (Fig. 6.1): two inlet branches representing the HA and PV tree, and one outlet branch representing the HV tree. The last generation of the HA and PV tree refers to the inlet arterioles and venules respectively, forming the portal triads at the corners of the lobules. These triads deliver blood to the sinusoids, modelled as the last HV generation where the HA and PV

blood is mixed (see dotted line in Fig. 6.1). Consequently, the second last HV generation stands for the central veins draining the blood coming from the sinusoids to the vena cava inferior (VCI). The output values of the model are the pressure and flow through all blood vessel generations. Based on these results, wall shear stresses (τ_{sin} [Pa]) at the level of the sinusoids, which are very prone to shear-related damage, can also be estimated using eq. 6.5, assuming Poiseuille flow and an equal flow in each of the sinusoids. Q_{HV} [m^3/s] represents the mean HV flow, n_{sin} refers to the number of vessels in the sinusoidal generation and r_{sin} [m] is the mean sinusoidal radius.

$$\tau_{sin} = \frac{4\mu Q_{HV}}{n_{sin}\pi {r_{sin}}^3}[Pa] \tag{6.5}$$

6.2.2.2 *From anatomical data to π-filter parameters*

Anatomical data (and hence input data for eq. 6.1-6.4) could be directly determined for the first 5 to 6 generations. For these generations, the measured data were used in the final model. However, it was not possible to obtain data for the smaller generations (generations 5 or 6 down to the sinusoids) from the scanned casts, so estimates had to be made. Since plots of diameter, lengths and numbers of vessels versus generation numbers showed exponential trend lines, extrapolations of these lines were used to estimate the lacking number of generations and their parameter values. To determine the number of generations, the trend line of the radius versus generation number was extrapolated up to the generation in which a radius value, being in accordance with literature values for diameters of liver sinusoids (7-15 μm) [309], was reached.

Results obtained with data based on simple extrapolations up to the last generation showed some differences in terms of model-predicted pressure and flow distributions in comparison with physiological values. For example, the sinusoidal pressure was higher than the PV pressure, which would result in backflow at the PV side. To solve this, the trend lines with the highest degree of uncertainty (the length and number of vessels per generation) were tuned in order to increase the physiological accuracy using, however, the original data where available (i.e. for the first 5 to 6 generations). By reverse engineering, starting from literature values of pressures and flows at the inlets (100 mmHg and 350 ml/min for the HA; 10 mmHg and 1100 ml/min for the PV) [309], sinusoids (5 mmHg and 1450 ml/min) [169] and outlet (3 mmHg and 1450 ml/min) [309] of the human liver, the presumed total vascular resistances R_s in each tree, necessary for truthfully simulating blood flow through the liver, were calculated. Three length and two number of vessels trend lines were optimised (by adjusting the coefficient and/or power of the exponential trend line) to approximately meet these resistance criteria. As such, trend lines for radii were not adjusted (Table 6.1).

Table 6.1: Equations of original and adjusted exponential trend lines. Only the length and two out of three number of vessels trend lines were adapted, original radius trend lines were maintained. Parameter x represents the generation number.

		HA	PV	HV
Radius[mm]	Original	$5.4e^{-0.37x}$	$13e^{-0.42x}$	$19e^{-0.6x}$
Length[mm]	Original	$136e^{-0.36x}$ if $(x > 1)$	$46e^{-0.14x}$	$113e^{-0.36x}$
	Adjusted	$680e^{-0.36x}$	$265e^{-0.36x}$	$161e^{-0.5x}$
Number of vessels	Original	$0.24e^{1.2x}$	$0.27e^{1.1x}$	$0.39e^{1.1x}$
	Adjusted	$0.27e^{x}$	/	$0.39e^{1.6x}$

To determine suitable values of the pulse wave velocity c_p, necessary to calculate the C-parameters (representing the elasticity), the Moens-Korteweg equation was used (eq. 6.6, in which h [m] refers to the vessel wall thickness and E_{wall} [Pa] to its Young's elasticity modulus).

$$c_p = \sqrt{\frac{h}{r}\frac{E_{wall}}{2\rho}}\left[\frac{m}{s}\right] \tag{6.6}$$

Since data for the Young's moduli and wall thickness of the hepatic vessels in humans were not collected in this study, c_p was estimated by finding its value for a typical large vessel and a typical small vessel: for a large vessel ($h/r \approx 0.1$; $E_{wall} \approx 400$ kPa) $c_p \approx 4$ m/s and for a small vessel ($h/r \approx 0.5$; $E_{wall} \approx 2000$ kPa) $c_p \approx 22$ m/s. These two values were used to estimate c_p in the first generation of the HV tree (the VCI, being the largest hepatic vessel) and in the sinusoids, respectively. For the intermediate generations of this tree, c_p was estimated by linear interpolation between these two values, depending on the generation number. For the HA and PV tree, an analogous interpolation was applied for the intermediate generations by using for the first generation $c_p \approx 5$ m/s at the PV (second largest hepatic vessel) and $c_p \approx 12$ m/s at the HA (significantly smaller than both the PV and HV).

To test the c_p sensitivity of the model, several scenarios of c_p variations were applied: multiplying or dividing all c_p values by 2, and using constant mean, minimum and maximum c_p values throughout the vascular trees. These variations only slightly influenced the amplitude and phase of the AC solution, suggesting that our linear c_p interpolations are acceptable.

6.2.2.3 Boundary conditions to model natural liver blood flow

For simulating natural liver blood flow, two voltage sources were used as input (analogous to the HA and PV perfusion pressure). The sinusoidal P_{HA} source was assumed to have a mean value of 100 mmHg, an amplitude of 20 mmHg and a frequency f of 1.2 Hz (heart rate of 70 bpm; eq. 6.7).

$$P_{HA} = 100 + 20\,cos(2\pi f t)\,[mmHg] \tag{6.7}$$

The P_{PV} source was given a constant value of 10 mmHg. At the VCI where the HV converge, the electrical circuit was closed by an outflow resistance R, which was estimated as $R = P_{HV}/Q_{HV}$ = 3 mmHg / (1450 ml/min) = $165 \cdot 10^5$ Ns/m^5. R represents the vascular resistance of the remaining blood vessels in the body, and P_{HV} refers to the pressure at the end of the HV. Though Q_{HV} is possibly influenced by right atrial pressure changes, this effect was not accounted for in our simulations. Since the outlet resistance R has only a minor influence on the final solution and the main interest of this study is HMP with free outflow, this assumption appears justified.

6.2.2.4 Solution method

The electrical superposition method was applied to solve the model. This means that the circuit was split into three partial networks: two direct current (DC) networks with only the PV source and the DC component of the HA source activated, respectively, and a third alternating current (AC) network with only the AC component of the HA source activated. The total solution of the model was the sum of the three partial network solutions. The methodology incorporated working in the frequency domain using complex numbers to facilitate calculations. In this way, it was possible to solve the model in steady state conditions of continuous or sinusoidal regimes (as well as more complex regimes in which the source signal is decomposed in its harmonics (Fourier analysis) to solve the AC part). The code was implemented in Matlab and was verified by using the same parameter values as applied by van der Plaats et al. [482], which were taken from data for dog livers [305]. Obtained results were identical.

6.2.2.5 Model application: HMP simulations

The model was used to simulate both natural human liver blood flow and HMP. As there is free HV outflow in HMP, P_{HV} = 0 and hence R = 0. Furthermore, the fluid viscosity μ had to be adapted to that of a perfusion fluid instead of blood. We used KPS-1 perfusion fluid with a viscosity of 4.5 mPa·s at the operating temperature (4-6°C). In contrast to periodic natural blood flow, liver HMP was assumed to be steady by applying continuous inlet pressures. To test the influence of the inlet pressures on the sinusoidal shear stress, a first HMP simulation was executed using the physiological inlet pressures. Secondly, we simulated the HMP settings applied to the organs prior to vascular corrosion casting (see methods section 6.2.1.1) using P_{HA} = 25 mmHg and P_{PV} = 2.5 mmHg. Additionally, a parameter study was conducted to determine viscosity and flow competition effects during HMP. Since other perfusion fluids than KPS-1 can be used, viscosity values were varied between 2 and 12 mPa·s, the typical range of perfusion fluid viscosities [384, 480]. Previous HMP experiments revealed that flow competition

occurred between the HA and PV when changing mean values of the inlet pressures [191, 342]. To study this competition phenomenon which disturbs homogeneous perfusion, the mean PV inlet pressure was varied between different runs from 1 to 7 mmHg.

6.3 Results

6.3.1 Anatomical data

Vascular corrosion casts of two human livers are shown in Fig. 6.2. The first liver was completely filled with the casting solution. In contrast, the second liver was only partially cast: the HV tree and half of the HA tree were missing, probably due to an obstruction in one or a few major vessels. Results of vascular measurements are therefore mainly based on the first liver cast. Red blood vessels represent HA vessels and blue refers to PV and HV vessels. These latter two were more difficult to distinguish, as HV flow is a mixture of approximately 75 % PV flow (blue) and 25 % HA flow (red), resulting in an HV flow with a dominating blue colour.

Image processing of cast 1 resulted in the geometries depicted in Fig. 6.3. Panel (a) shows the three vascular trees, panels (b) through (d) each depict one single tree. Internal branching patterns of all vascular trees could be visualised in this way.

Geometrical data could be determined for the first generations of every tree, i.e. up to six generations for the HA and PV tree of cast 1 (Fig. 6.4; Tables 6.2-6.4), and five for the HV tree. For cast 1, measured HA radii dropped from 3.5 mm to 0.59 mm (generation 6), PV radii from 7.3 mm to 1.1 mm

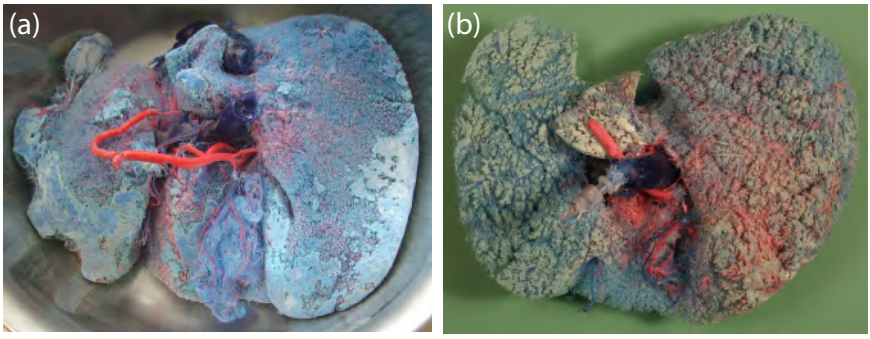

Figure 6.2: Liver casts: cast 1 (a) and cast 2 (b). Red blood vessels represent the arterial tree (HA), whereas blue vessels refer to venous vessels (portal venous (PV) and hepatic venous (HV) vascular trees).

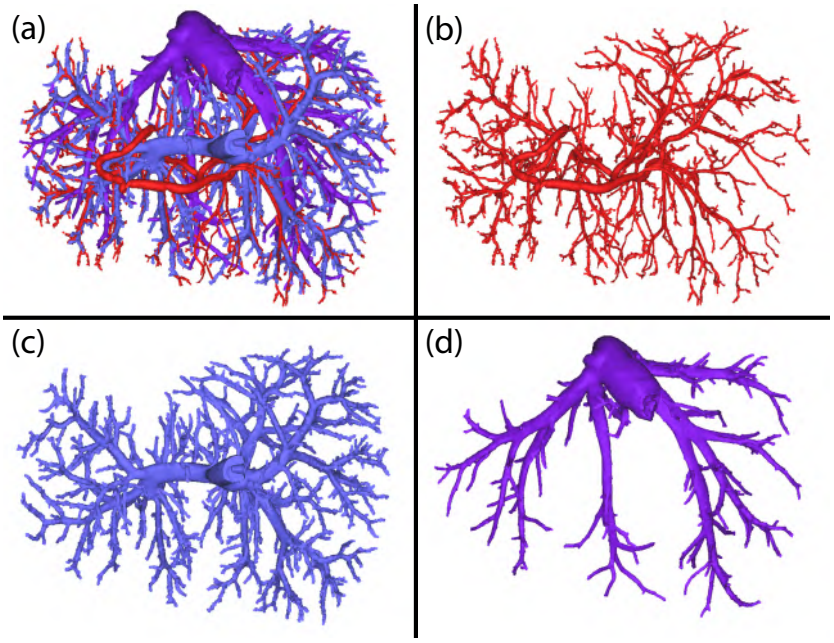

Figure 6.3: Segmentation and 3D reconstruction of the three vascular trees (a), and the hepatic arterial (HA) (b), portal venous (PV) (c) and hepatic venous (HV) (d) tree with 6, 6 and 5 generations visualised, respectively. Panel A depicts all blood vessels which have been measured to obtain the anatomical model.

(generation 6) and HV radii from 13 mm to 1.1 mm (generation 5). For a given generation, HV and PV radii were larger than HA radii. Numbers of vessels per generation rose from 1 to 271 (generation 6) for the HA tree, from 1 to 216 (generation 6) for the PV and from 1 to 76 (generation 5) for the HV tree. The variation of mean radii and numbers of vessels in function of generation numbers tended to be exponential. For each of the vascular beds, mean lengths dropped with rising generation numbers (not taking into account the first HA, PV and HV generation). Trends in lengths were less distinct: no exponential trend line could be determined for the PV lengths. Fig. 6.4 also shows a comparison of HA and PV radii of cast 1 and 2. The casts seem to have radii in the same range.

6.3.2 Electrical model

Using the anatomical measurements supplemented with estimations (Table 6.1) based on the trend line extrapolations, a total of 18 HA, 16 PV and 14 HV generations were obtained. A complete list of the data necessary to calculate the default model is given in Tables 6.2-6.4.

6.3.2.1 Pressure and flow: model of natural liver blood flow

Results of mean pressures and flows throughout the liver are given in Fig. 6.5a and d, respectively. Pressure smoothly decreased along the subsequent generations, resulting in pressures of approximately 5 mmHg at the level of the liver sinusoids. In the HV tree, pressures were further reduced until they reached 3 mmHg at the VCI outlet (where the HV converge). Mean flow displayed values of approximately 400 ml/min, 1100 ml/min and 1500 ml/min for the HA, PV and HV vascular tree, respectively. Next to the mean values, the pulsatile pressure and flow profiles versus time were also obtained (Fig. 6.6). The amplitude of pressure and flow profiles clearly decreased with increasing generation number through the HA tree from 20 mmHg and 236 ml/min respectively to 0.15 mmHg and 86 ml/min (Figs. 6.6a and b). In contrast, the PV tree displayed no pressure pulse at the inlet but a small pulse with an amplitude of 0.15 mmHg was developed towards the sinusoids (Fig. 6.6c). The outflow from the sinusoids to the HV and VCI again demonstrated a small drop in pressure amplitude from 0.15 mmHg to 0.10 mmHg (Fig. 6.6e). Pulsatile components of the PV and HV flow barely showed a change through the generations (Figs. 6.6d and f).

6.3.2.2 Pressure and flow: HMP simulations

Resulting pressure profiles throughout the liver in HMP conditions with physiological and low pressures are depicted in Figs. 6.5b and c, respectively, and were qualitatively very similar to natural blood flow (Fig. 6.5a). The only pressure difference between natural blood flow and HMP with physiological conditions were the slightly lower HV tree pressures caused by the zero outflow resistance in HMP conditions. HMP with low pressures, however, leads to overall lower pressures. Considering the flows (Fig. 6.5d), HMP with

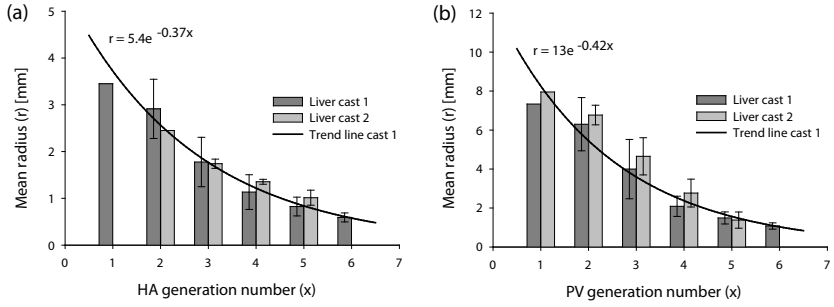

Figure 6.4: Comparison of hepatic arterial (HA) radii (a) and portal venous (PV) radii (b) between liver cast 1 and 2 in function of generation numbers. Both graphs show similar HA and PV radii for the two liver casts. The trend lines and accompanying equations fitted on the radii of liver cast 1 are also depicted and illustrate the exponential profiles. As the HA tree of liver cast 2 was only half cast, the radius of the first HA generation could not be determined.

Table 6.2: Anatomical data of the hepatic arterial (HA) tree.

	Generation	Number of vessels	Radius [mm]	Length [mm]
Measured generations	**HA 1**	1.0	3.5	10
	HA 2	2.0	2.9	74
	HA 3	7.0	1.8	40
	HA 4	36	1.1	31
	HA 5	$1.2 \cdot 10^{2}$	$8.3 \cdot 10^{-1}$	25
	HA 6	$2.7 \cdot 10^{2}$	$5.9 \cdot 10^{-1}$	16
Extrapolated generations	**HA 7**	$2.9 \cdot 10^{2}$	$4.0 \cdot 10^{-1}$	56
	HA 8	$8.0 \cdot 10^{2}$	$2.7 \cdot 10^{-1}$	39
	HA 9	$2.2 \cdot 10^{3}$	$1.9 \cdot 10^{-1}$	27
	HA 10	$5.9 \cdot 10^{3}$	$1.3 \cdot 10^{-1}$	19
	HA 11	$1.6 \cdot 10^{4}$	$9.0 \cdot 10^{-2}$	13
	HA 12	$4.4 \cdot 10^{4}$	$6.2 \cdot 10^{-2}$	9.4
	HA 13	$1.2 \cdot 10^{5}$	$4.2 \cdot 10^{-2}$	6.5
	HA 14	$3.2 \cdot 10^{5}$	$2.9 \cdot 10^{-2}$	4.6
	HA 15	$8.8 \cdot 10^{5}$	$2.0 \cdot 10^{-2}$	3.2
	HA 16	$2.4 \cdot 10^{6}$	$1.4 \cdot 10^{-2}$	2.2
	HA 17	$6.5 \cdot 10^{6}$	$9.6 \cdot 10^{-3}$	1.6
	HA 18	$1.8 \cdot 10^{7}$	$6.6 \cdot 10^{-3}$	1.1

physiological pressures resulted in a lower HA, a higher PV and a higher HV flow compared to natural blood flow, while HMP with low pressures overall resulted in much lower flows. These flows corresponded to estimated sinusoidal shear stress values of 1.04 Pa and 0.26 Pa in case of HMP with physiological and low pressures, respectively, compared to 0.77 Pa in case of natural blood flow.

Data obtained with variations of the PV inlet pressure are depicted in Fig. 6.7a-c. Increasing the PV pressure resulted in a manifest increase of the PV flow and a slightly decreasing HA flow, depicting a trade-off between HA and PV flows (Figs. 6.7a and b). HV flows, equaling the sum of the HA and PV flows, also increased (Fig. 6.7c). Rising PV pressures corresponded with higher sinusoidal pressures and wall shear stresses (Fig. 6.7d). These results were calculated using a fluid viscosity of 3.5 mPa·s, but the same results were obtained for all viscosity values as the higher viscosity was counteracted by a decrease in flow.

6.4 Discussion

In this study, an electrical model of the human liver blood circulation was built based on detailed anatomical data of the human liver vasculature. To

Table 6.3: Anatomical data of the portal venous (PV) tree.

	Generation	Number of vessels	Radius [mm]	Length [mm]
Measured generations	PV 1	1.0	7.3	35
	PV 2	2.0	6.3	35
	PV 3	7.0	4.0	33
	PV 4	27	2.1	32
	PV 5	80	1.5	27
	PV 6	$2.2 \cdot 10^{2}$	1.1	16
Extrapolated generations	PV 7	$7.0 \cdot 10^{2}$	$6.8 \cdot 10^{-1}$	22
	PV 8	$2.1 \cdot 10^{3}$	$4.5 \cdot 10^{-1}$	15
	PV 9	$6.6 \cdot 10^{3}$	$3.0 \cdot 10^{-1}$	11
	PV 10	$2.0 \cdot 10^{4}$	$2.0 \cdot 10^{-1}$	7.5
	PV 11	$6.2 \cdot 10^{4}$	$1.3 \cdot 10^{-1}$	5.2
	PV 12	$1.9 \cdot 10^{5}$	$8.5 \cdot 10^{-2}$	3.7
	PV 13	$5.9 \cdot 10^{5}$	$5.6 \cdot 10^{-2}$	2.6
	PV 14	$1.8 \cdot 10^{6}$	$3.7 \cdot 10^{-2}$	1.8
	PV 15	$5.5 \cdot 10^{6}$	$2.4 \cdot 10^{-2}$	1.3
	PV 16	$1.7 \cdot 10^{7}$	$1.6 \cdot 10^{-2}$	$8.8 \cdot 10^{-1}$

Table 6.4: Anatomical data of the hepatic venous (HV) tree.

	Generation	Number of vessels	Radius [mm]	Length [mm]
Measured generations	HV 1	1.0	13	68
	HV 2	3.0	5.0	74
	HV 3	18	2.4	33
	HV 4	33	1.7	28
	HV 5	76	1.1	19
Extrapolated generations	HV 6	$5.4 \cdot 10^{3}$	$5.2 \cdot 10^{-1}$	8.1
	HV 7	$2.6 \cdot 10^{4}$	$2.9 \cdot 10^{-1}$	4.9
	HV 8	$1.3 \cdot 10^{5}$	$1.6 \cdot 10^{-1}$	3.0
	HV 9	$6.3 \cdot 10^{5}$	$8.6 \cdot 10^{-2}$	1.8
	HV 10	$3.1 \cdot 10^{6}$	$4.8 \cdot 10^{-2}$	1.1
	HV 11	$1.5 \cdot 10^{7}$	$2.6 \cdot 10^{-2}$	$6.6 \cdot 10^{-1}$
	HV 12	$7.4 \cdot 10^{7}$	$1.4 \cdot 10^{-2}$	$4.0 \cdot 10^{-1}$
	HV 13	$3.7 \cdot 10^{8}$	$7.9 \cdot 10^{-3}$	$2.4 \cdot 10^{-1}$
	HV 14	$1.8 \cdot 10^{9}$	$4.3 \cdot 10^{-3}$	$1.5 \cdot 10^{-1}$

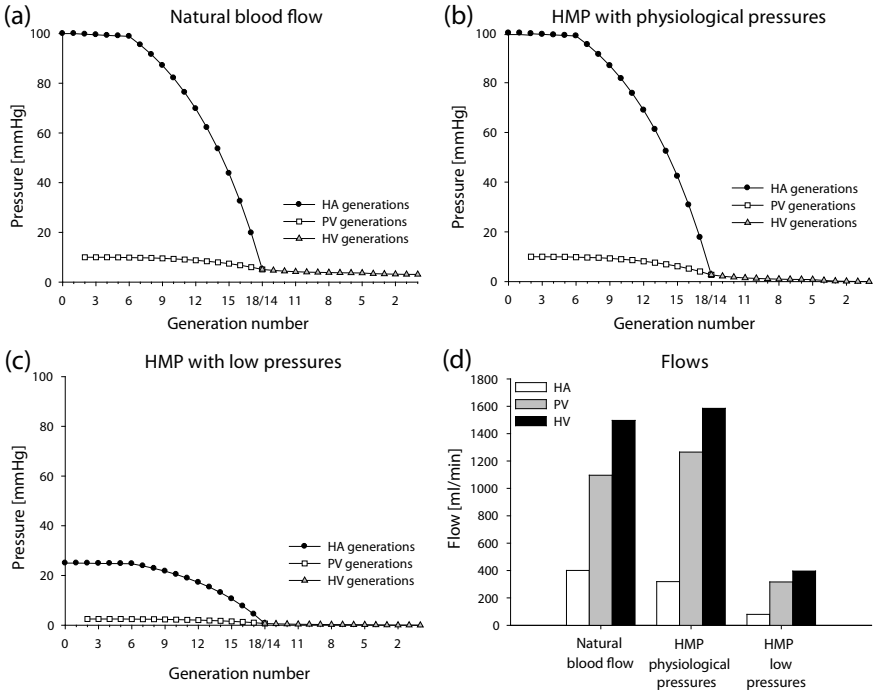

Figure 6.5: Mean pressure profiles before and after each blood vessel generation of the hepatic arterial (HA), portal venous (PV) and hepatic venous (HV) trees of liver cast 1 obtained from the electrical model for natural human liver blood flow (a), hypothermic machine perfusion (HMP) with physiological pressures (P_{HA} = 100 mmHg and P_{PV} = 10 mmHg) (b) and HMP with low pressures (P_{HA} = 25 mmHg and P_{PV} = 2.5 mmHg) (c). In the subsequent HA and PV generations, pressures decreased with the highest pressure drop before the sinusoids. Pressure profiles are qualitatively very similar, but absolute values are significant lower for HMP with low inlet pressures. Mean HA, PV and HV flows are depicted in (d) and clearly demonstrate that the HV flow is equal to the sum of the HA and PV flow. HMP with physiological pressures results in flow competition illustrated by a lower HA and a higher PV flow compared to natural blood flow. HMP with low pressures results in much lower flow in contrast to the other conditions.

the best of our knowledge, these human vascular data are unique. The model was used to generate pressure and flow distributions throughout the liver as a function of vessel generation, and was subsequently used to assess the haemodynamic impact of HMP perfusion. It was shown that the model could be tuned to simulate natural human hepatic blood flow, and that the results were in accordance with physiological literature values [169, 309]. Next, the model was applied to simulate liver HMP, resulting in more insight into the internal haemodynamic impact of HMP on human livers.

By extracting anatomical data from the digital 3D reconstructions of the vascular corrosion casts, it was possible to measure and classify the first 5 to

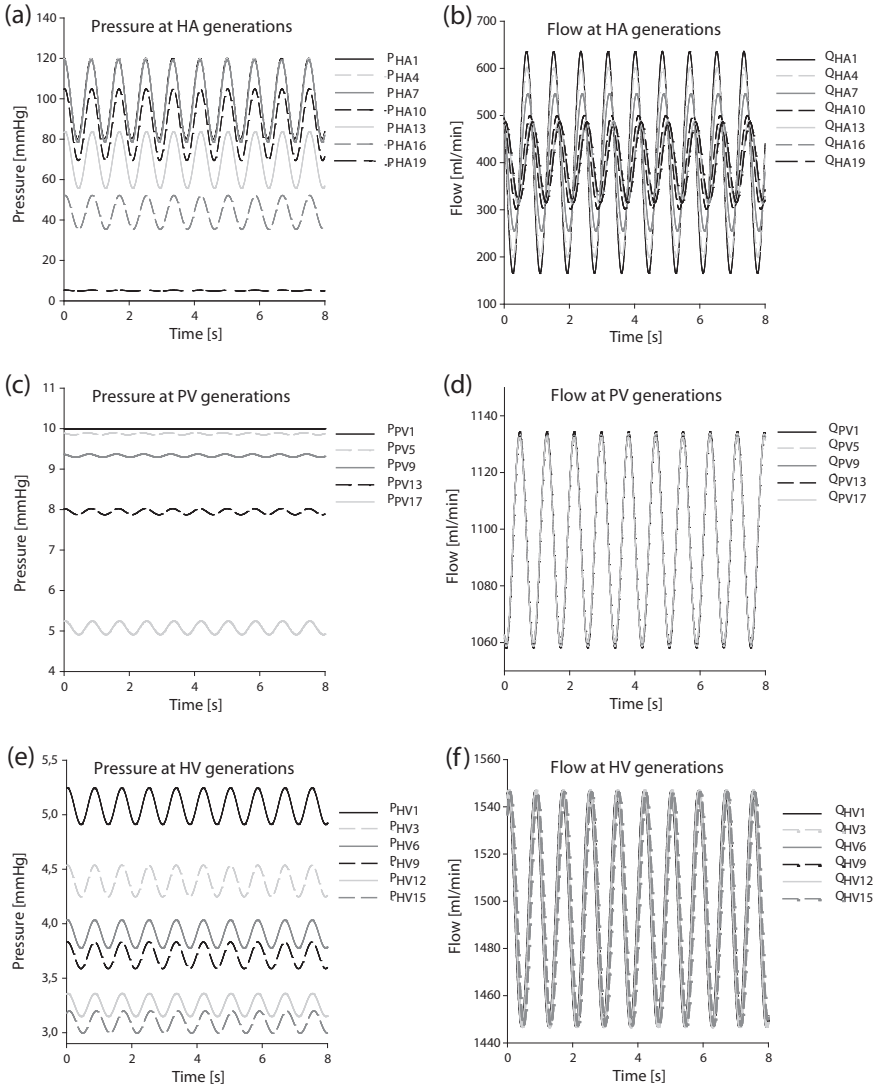

Figure 6.6: Time-dependent flow parameters calculated by the electrical liver model for natural human liver blood flow: sinusoidal pressures (a, c, e) and flows (b, d, f) of each blood vessel generation of the hepatic arterial (HA), portal venous (PV) and hepatic venous (HV) trees. The HA pressure and flow amplitudes clearly decrease with increasing generation numbers. Pressures in the PV tree were almost steady, except for a small pressure pulse developing towards the sinusoids. The HV tree demonstrated a small drop in pressure amplitude, whereas PV and HV flows showed almost no change in mean as well as pulsatile components.

6 generations of human liver vascular trees (see also the macrocirculation in chapter 5). Due to incomplete filling of one of the casts, complete data could only be obtained from one cast. Nevertheless, when comparing the

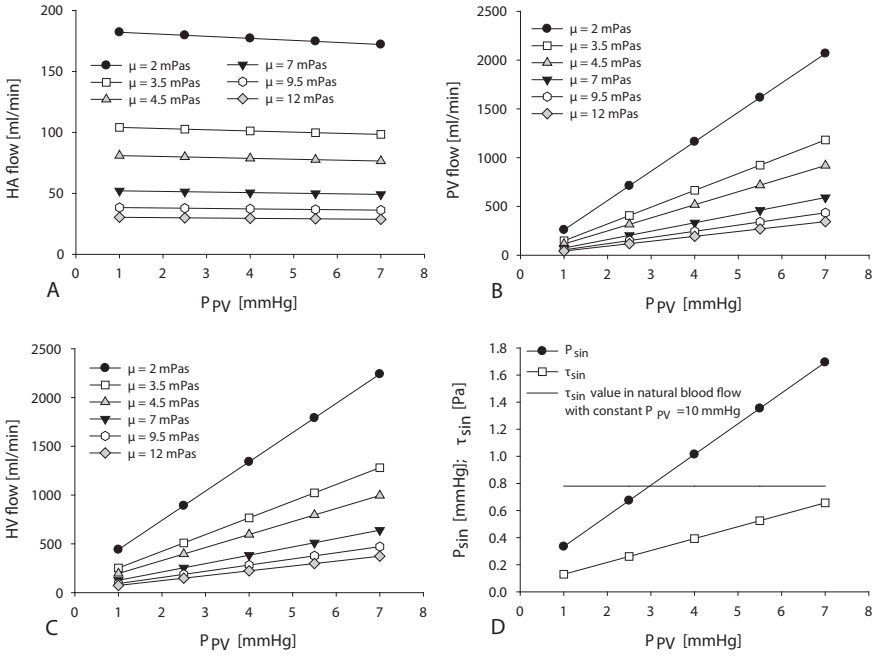

Figure 6.7: Results of the hypothermic machine perfusion (HMP) simulations investigated at several portal venous (PV) inlet pressures and fluid viscosities. Increasing the mean PV inlet pressure from 1 to 7 mmHg resulted in an increasing PV flow and a decreasing hepatic arterial (HA) flow, depicting the flow competition between HA and PV flows (a and b). Hepatic venous (HV) flows also increased (c). Increasing the viscosity (μ) lowered all liver flows. Variations of the PV inlet pressure also influenced the haemodynamic behaviour at the sinusoids (d). Rising PV pressures resulted for all viscosity values in higher sinusoidal pressures and wall shear stresses. To compare with natural liver flow in the body, a horizontal line is drawn at 0.77 Pa, referring to the sinusoidal shear stress level in natural blood flow (constant PV pressure of P_{PV} = 10 mmHg).

data from both liver casts wherever possible (PV and half of the HA tree), a reasonable resemblance was observed (Fig. 6.4). However, as the electrical model was based on data from a single liver cast, it is safe to consider these data as the basis of a model for that specific liver, rather than a generic model of human liver vasculature. Ideally, the complete cast should be scanned at a sufficient resolution to allow visualisation of the liver vasculature from the level of the large vessels down to the sinusoids, requiring a resolution of a few micrometers. It is, however, practically impossible to scan objects of the size of the human liver at this resolution due to computational limits (scanning an entire liver at 5 μm resolution would result in more than 7000 Gb of data). In addition, currently available software is unable to handle datasets of that magnitude. As such, data beyond the sixth generation used for the electrical

analogue were estimated based on extrapolations. For the complete cast, the evolution of vessel radii and lengths with the generation numbers is fairly well described by exponential trend lines. These trend lines allow estimations of parameters concerning the further generations, of which data could not be measured, to complete the electrical model. As a result, we obtained 18 HA, 16 PV and 14 HV generations. Knowing that ducts of the biliary tree run parallel with those of the HA and PV tree, our estimations are very similar to a previous study, which stated that there are 18 vessel generations in the biliary tree [272]. The direct extrapolations of the trend lines fitted on our geometrical measurements resulted in unphysiological pressures and flows, probably due to small measurement errors and thus slightly deviating exponential trend lines (or because the actual relation is not a true exponential). The problem was solved by adjusting the trend lines for the lengths and the number of vessels of the HA and HV tree. We feel this to be justified as the mean length and the number of vessels of the last measurable generation are probably underestimated because of the resolution and segmentation limits that are occurring at that level. This can be illustrated by the original extrapolation of the HV number of vessels trend line resulting in $2{\cdot}10^6$ sinusoids, while a larger value of $\pm 1.9 \cdot 10^9$ sinusoids is stated in literature [482]. After the modification, the final model results in $1.8 \cdot 10^9$ sinusoids. Trend lines for length showed lower R^2 values than the other trend lines, indicating a higher inaccuracy for these relations. We stress that we preserved the original fitted radii trend lines, so that the most determining and best measurable parameter to calculate the electrical components was not adjusted. To complete the model, simplifications were made regarding the structure of the liver microcirculation. We assumed that HA and PV vessels branch until they reach the eighteenth and sixteenth generation, respectively. Subsequently, blood is mixed at the sinusoids and drained via collecting HV. Thereby, sinusoids are modelled as a number of parallel vessels. Although liver microvasculature in reality is more complex due to a specific organisation of arterioles, venules and sinusoids in functional units, it is probably less important to incorporate this in our lumped parameter model, which represents a simplification of real liver blood flow. However, these assumptions possibly have an influence on the calculated wall shear stress at the level of the sinusoids. The hepatic microvascular structures would thus be of more concern in detailed microvascular flow models. Future research will include scans on higher resolutions to verify whether our estimated data based on adjusted extrapolations are in accordance with measurements on these scan datasets. Additionally, we also aim to develop a numerical model of the human liver microflow based on these detailed scan data (see chapter 9). Previously, Rani et al. [393] built a numerical model of the microcirculation in a single hepatic lobule, but this model was based on a simplified representation of a portal triad leading to two sinusoids draining into a central vein.

In addition to the considerations mentioned above, other issues should be taken into account when interpreting the data. First, the organs are recuperated from human donors discarded for transplantation. This, however, was based on strict medical criteria: liver 1 was discarded because of steatosis, and liver 2 because of a lung tumour in the donor body. Although discarded, the organs did not show significant differences in comparison with the anatomical vasculature of healthy subjects. A more complicated question arises from the procedure that was followed starting at the moment of harvesting the liver until the casting procedure was done, and more specifically how HMP and the casting procedure might have affected the measured vascular diameters. The livers were placed on HMP, which has the advantage that the microvasculature is kept open and intact, but the disadvantage is that high shear stresses may originate, caused by the hypothermic more viscous perfusion fluids that differ from natural blood, damaging the sinusoidal endothelial cells. Still, our simulation data seem to suggest that, with the applied HMP settings including low pressures (Fig. 6.5c), sinusoidal wall shear stress was probably not higher during HMP (± 0.26 Pa) than during normal perfusion in the body (± 0.77 Pa). However, when HMP would be executed using physiological pressures (Fig. 6.5b), the shear stress would be larger (± 1.04 Pa), probably resulting in organ damage. This is exactly why lower pressures are applied in HMP conditions. Following HMP, the casting procedure was done by manual injection, which does not provide an optimal control of the applied pressures. For instance, pressures may be elevated due to an obstruction, which could be the case for the incomplete casting of liver 2, with a risk of disrupting the internal vasculature. It has also been described that casting leads to slight vasoconstriction and shrinkage of the hardening Batson's, which implicates slightly smaller vessel diameters than *in vivo* [203, 260]. Nevertheless, the casting procedure was executed following standardised procedures and by a team with many years of expertise and knowledge in this field. As such, we are confident that the obtained casts represent the best possible achievable results using this technique.

Vascular pressure and flow parameters at the level of each liver generation could be calculated by the electrical model and were in accordance with physiological values for liver blood flow [169, 311]. Qualitatively, pressure profiles for all investigated conditions (Fig. 6.5a, b, and c) showed decreasing values starting at the HA and PV inlets with the highest pressure drop taking place proximal to the sinusoids between generations 7-18, and not over the sinusoids themselves. Distal to the sinusoids, only very slight pressure drops appeared through the HV tree until reaching the VCI. As expected, HV flow was equal to the sum of the HA and PV flow (Fig. 6.5d), and mean flow obviously remained constant over the generations of a specific vascular tree. A similar electrical model has previously been applied

to dog livers [482], but, to the authors' knowledge, this is the first time that an extended electrical model has been applied to blood flow in the total human liver. The dog liver model of van der Plaats et al. [482] was based on partially measured and estimated anatomical data collected by Mall [305]. Quantitatively, results of the dog and human liver model are different. For example, the dog liver described by Mall [305], only counts 8 HA, 7 PV and 8 HV generations [482]. Next, absolute flow values in the dog (e.g. Q_{HV} = 540 ml/min) are clearly lower than adult human values (e.g. Q_{HV} = 1500 ml/min). In contrast, pressure and flow profiles qualitatively correspond to each other. Both canine and human models give evidence of a similar development of pressure drops from HA and PV trees through the sinusoidal level down to the HV.

As well as to simulate blood flow in the natural liver, the model can also be used to simulate HMP. Assuming that the internal structure of the organ does not change, simulating HMP implies using a different set of boundary conditions and changing the fluid viscosity from blood to a perfusion fluid. In the context of the unknown optimal perfusion settings for liver HMP, this model may be useful to determine these settings without e.g. using animal experiments. The model enables calculation of the influence of various parameters on relevant outcomes such as the sinusoidal wall shear stress (Fig. 6.7). Varying the viscosity of the perfusion liquid from 2 to 12 mPa·s lowered the liver flows (as a consequence of the induction of higher vascular resistances), but did not influence the calculated pressure and shear stress at the level of the sinusoids. This is due to the pressure-driven HMP simulations, in which flows are adapted to obtain a certain imposed pressure [479]. It is expected that influences of fluid viscosity would be more pronounced when applying a flow-driven model, referring to the use of flow-driven HMP pumps, in which a specific flow is forced to enter the liver regardless of the pressure this implies. Such a flow-driven model would be obtained by substituting the voltage sources by current sources. This, however, suggests that pressure-driven HMP is the best mode of operation to avoid organ damage. *Ex vivo*, flow competition has been observed and monitored between HA and PV vascular trees during porcine liver HMP in a previous study [191]. We were able to mimic this phenomenon by comparing HA and PV flows of HMP under physiological pressures with natural blood flow (Fig. 6.5d). Additionally, flow competition could be provoked by changing the PV inlet pressures (Fig. 6.7). Elevating this pressure increased the flow through the corresponding PV vascular tree, but decreased the flow through the HA inlet tree slightly. Increasing the HA pressure, would inversely imply higher HA and lower PV flows, as well as a higher HV flow, sinusoidal pressure and wall shear stress. This flow competition is an important parameter influencing perfusion stability and homogeneity inside donor livers (see section 3.3.3).

Despite the fact that the model generates physiological data, it should be kept in mind that a lumped parameter model remains a drastic simplification of the complex anatomical reality. However, we feel that its use is justified for our current purpose, where we are mainly interested in relative differences (natural liver versus HMP) in overall haemodynamic parameters. Anyhow, future model refinements are advisable. First, more livers should be cast and investigated in order to provide a more generic dataset of the human liver. On the other hand, human livers are scarce and their availability depends on the moment that organs of a potential donor are discarded and permission is given to apply these organs for research purposes. Also, given the labour-intensity of the complete casting and data-acquisition procedure, it is expected that the final dataset on which a more generic model is to be based will still be fairly limited. Additionally, more exact data should be obtained on the higher order generations down to the sinusoids. These data can be obtained via dissections of small cast fragments and scanning them at higher resolutions (as was done for the meso- and microcirculation in chapters 5 and 9). Microvascular data could then be measured, and compared with the estimations of extrapolated data. Nevertheless, an important aspect will be the connectivity of the datasets and how to map this high-resolution scans of small samples onto the low-resolution scan of the complete liver. Next to refinements, future research should also address validation of the models. *Ex vivo* HMP experiments using isolated livers, combined with real time pressure and flow measurements (from which the impedance of the organ can be derived), would offer a good basis to test the corresponding results obtained via the electrical analogue (see chapter 7). A feasibility experiment using a porcine liver on HMP demonstrated good qualitative resemblance with our simulations when comparing input impedances of the experiment with those obtained using the electrical model (unpublished results). Moreover, the simulated results of the electrical model are in good qualitative agreement with the pressure measurements done in rabbit livers by Maass-Moreno et al. [295]. In addition, computational fluid dynamics (CFD) models could be applied for the first generations as well as to derive a microvascular model, in which flow parameters are calculated and visualised based on the original 3D geometries. Their results could subsequently be compared with results of the electrical model. This would in particular allow to assess to what extent the simple estimates of wall shear stress correspond to the actual values.

6.5 Conclusion

The combination of casting and high-resolution micro-CT scanning with image processing provides unique data on the human hepatic circulation.

This allows digital visualisation of the complex liver vasculature and the collection of high-resolution data for quantitative morphological analysis. The established electrical analog model of the human liver can predict flow parameters throughout the liver vasculature in accordance with physiological data. The model can be applied not only to natural blood flow, but also to HMP, simulations of certain pathologies and living donor liver transplantation, in which only a part of a living donor liver is removed to implant in a patient. In the case of HMP with low pressures, the model predicts lower sinusoidal shear stresses than in the case of natural blood flow, and hence no shear-related damage. However, there may be other factors that influence the impact on organ damage, e.g. transient effects when starting HMP or non-biomechanical parameters, such as biochemical influences evoked by using synthetic perfusion fluids instead of blood. Future research should focus on refinements of the model as well as on validation of the electrical model with *ex vivo* HMP experiments and numerical CFD models. Although further research and refinements are necessary, the first results seem to be promising.

Chapter 7

Validation and tuning of an electrical analog model of hepatic perfusion based on human liver HMP experiments

This chapter is based on: *"Validation and calibration of an electrical analog model of hepatic perfusion based on human liver hypothermic machine perfusion experiments"*, submitted for publication [94].

7.1 Introduction

In previous work (chapter 6), we developed an electrical analog model to gain more insight into the human hepatic perfusion, in particular during machine perfusion (MP). The electrical components of the model were calculated by using the geometrical vascular features as acquired in chapter 5 and the equations derived by de Pater [91] and van der Plaats [482]. Due to a number of unknown parameters (e.g. c_p values), however, some assumptions had to be made to fully define the model (section 6.2.2.2). At this point, it is unclear to which extent these assumptions are acceptable due to a lack of data to validate the model. Furthermore, the model was derived on data from a single liver. To tackle these limitations, additional data on human liver perfusion are required to test the model-predicted results against experimental measurements. Therefore, the aim of this study was

to (i) capture anatomical and functional data of human livers during hypothermic MP (HMP) experiments, (ii) to develop and test a procedure to fit the electrical model parameters to a specific liver, and (iii) to validate and possibly finetune the electrical model by comparing model predictions to experimental data. To achieve (ii) and (iii), we first fitted compact Windkessel (WK) models, containing only a few parameters, to the measurements, after which these lumped properties were 'smeared out' in a liver-specific extended electrical model.

7.2 Materials and methods

This study was conducted on two human livers, labelled HL2 and HL3 (different from the liver used in chapters 5 and 6 labelled HL1; see also Table 7.1), discarded for transplantation after failed reallocation, as approved by the Ethical Committee of the University Hospitals Leuven, Belgium, and by the Belgian Liver and Intestine Committee as foreseen by the initial protocol. The procedure to obtain experimental perfusion data and tune the electrical model consisted of several steps, as illustrated in the flowchart of Fig. 7.1. First, the livers were used for HMP experiments, after which their vasculature was cast and imaged. Data analysis of the HMP experiments and geometrical vascular features enabled generating compact WK models and further tuning an extended liver-specific electrical analog model.

Table 7.1: Characteristics of the human livers (HL). Dimensions were obtained during image processing (see also Fig. 7.6a). The weight of HL2 and HL3 was estimated as 2.5% of the body weight (see section 1.1.1.1). Additionally, it is illustrated which livers underwent hypothermic machine perfusion (HMP) experiments, casting and segmentation. (*) Since the body weight was unavailable for HL1, its weight was approximated as the volume of its image-based 3D envelope multiplied by the density of water.

Human liver	HL1	HL2	HL3
Width [cm]	26	23	19
Height [cm]	20	19	14
Depth [cm]	6	8	5
Weight [kg]	1.9 *	2.1	1.2
HMP experiment	(unavailable)	x	x
Casting	x	x	x
Segmentation	x	x	(unavailable)

7.2.1 HMP experiments

The goal of these experiments was to acquire simultaneous pressure and flow measurements at the inlet and outlet blood vessels of human livers during HMP (Fig. 7.2).

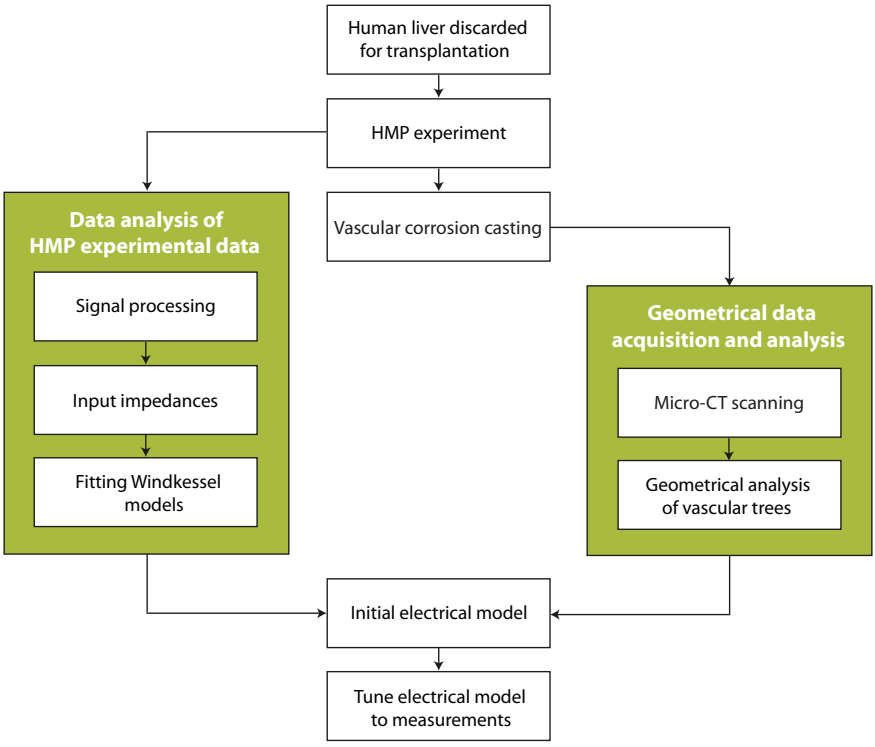

Figure 7.1: Methodological approach to obtain and to tune an extended liver-specific electrical model based on hypothermic machine perfusion (HMP) experiments and geometrical vascular analysis.

7.2.1.1 Liver benching

After an initial flush, the isolated livers were prepared for HMP by cannulation of the HA and PV with atraumatic straight-in cannulas (Fig. 7.2 and 7.3), while a larger cannula was positioned in the suprahepatic vena cava inferior (VCI). Two balloon catheters were retrogradely inserted into the hepatic venous (HV) system (Fig. 7.3). The infrahepatic VCI was closed by a watertight suture. Subsequently, the liver was placed in the organ cassette of the LifePort Workstation (Organ Recovery Systems, Zaventem, Belgium), being the HMP device that was used in this study (see section 3.3.2.8 for more detailed information on this prototype).

7.2.1.2 Experimental setup

While cannulating the graft, the HMP device and data acquisition (DAQ) equipment were prepared. The tub and organ cassette of the HMP device were filled with ice water and 2 litres of KPS-1 perfusion solution, respectively. An oxygenator (Minimax Plus Oxygenator; Medtronic, Minnesota,

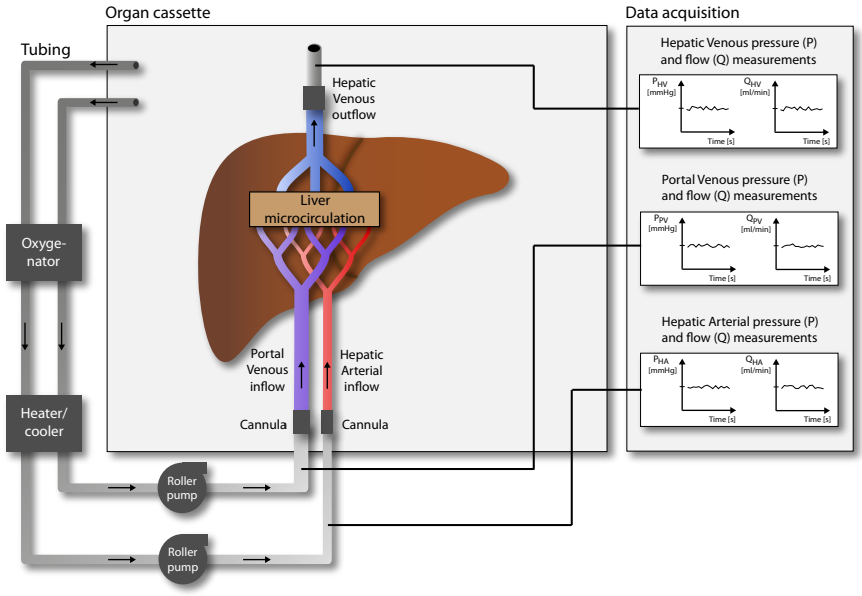

Figure 7.2: Schematic overview of the experimental hypothermic machine perfusion (HMP) setup. Two roller pumps provide the inflow into the hepatic artery (HA) and portal vein (PV) via the tubing and cannulas. After leaving the liver, the perfusion fluid is recirculated. Throughout HMP experiments, pressures and flows are measured at the HA and PV inflows and the hepatic venous (HV) outflow.

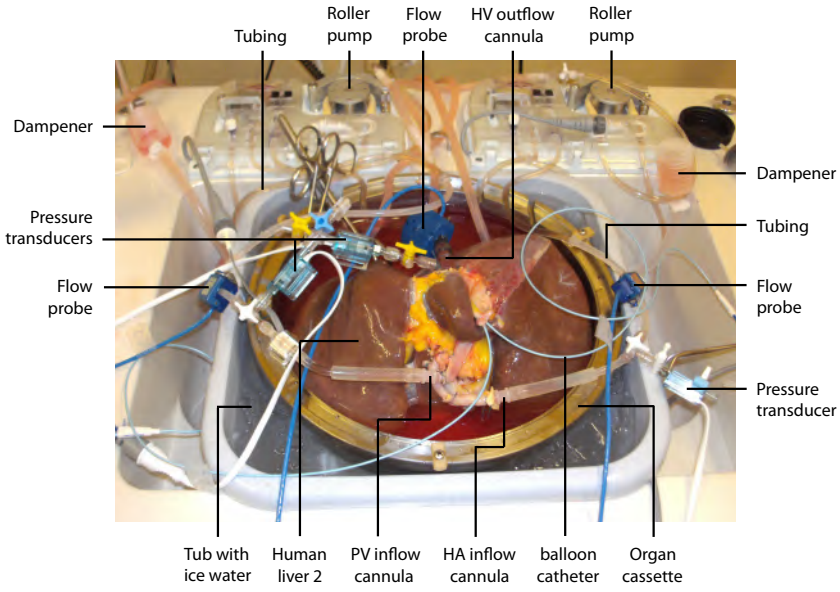

Figure 7.3: Experimental hypothermic machine perfusion (HMP) setup of human liver 2 (HL2) with indications of the measurement equipment and the hepatic in- and outflows.

USA) was included in the perfusion circuit to provide oxygenation of the perfusate (P_{O_2} of 150-300 mmHg) before entering the roller pumps (Fig. 7.2). Silicon tubes were used to connect the roller pumps to the HA and PV inlet cannulas (Fig. 7.3). A short tube was attached to the VCI cannula to guide the free fluid outflow into the organ cassette in order to be recirculated. Three pressure transducers (BD, New Jersey, USA) were connected to the tubing via three-way valves to perform pressure measurements as close as possible to the HA and PV inlet and the VCI outlet (Fig. 7.2 and 7.3). In addition, two pressure transducers were connected to the balloon catheters (inserted in the HV vessels; Fig. 7.3). The latter was done to estimate sinusoidal pressures, as the pressure difference between the sinusoids and HV system is known to be small. Before starting any measurements, the pressure transducers were zeroed to the ambient air pressure. Flow measurements were performed by using Transonic flow meters (T206 and HT109; Transonic Systems Inc., New York, USA) together with their corresponding flow probes. Tubing flow probes with a diameter of 5 mm, 5 mm and 9.5 mm were attached to the tubing of the HA, PV and VCI, respectively, as close as possible to the pressure transducers to minimise potential pressure-flow signal delays (Fig. 7.3). Both pressure transducers and flow meters were connected to an SC-2345 DAQ system (National Instruments Corporation (NI), Texas, USA) to simultaneously record all signals at a frequency of 200 Hz. A DAQ Card 6062E (NI) enabled reading all signals into a laptop using Labview software (NI). Throughout the HMP experiment, the temperature of the perfusate was measured by a thermometer (Ebro, Ingolstadt, Germany).

7.2.1.3 HMP measurement protocol

Perfusion settings of the HMP device were varied to investigate the liver's response. For every perfusion condition, stable perfusion was awaited (unless specified differently) and measurements were recorded for at least five minutes. Pressure-controlled pulsatile perfusion without a flow limit was used for the HA, while pressure-controlled continuous perfusion with an optional flow limit was used for the PV. The initial perfusion settings were a maximum HA perfusion pressure ($P_{HA,set}$) of 25 mmHg and a maximum PV pressure ($P_{PV,set}$) of 5 mmHg (lowest achievable pump pressure; see section 3.3.2.8) with an additional PV flow limit of ± 300 ml/min. Subsequently, these settings were repeated while varying certain perfusion parameters, such as increasing the $P_{HA,set}$ (to 35, 45, 55, 65, 85 and 99 mmHg), turning off the PV flow limit and increasing the $P_{PV,set}$ (to 7 and 9 mmHg). Furthermore, transient behaviour measurements were done to study the effect of starting and stopping perfusion, squeezing the HA, PV or VCI tubing, and perfusing only the HA or PV side.

7.2.2 Data analysis

After the HMP experiments, pressure and flow signals were processed to calculate the corresponding input impedances and tune compact Windkessel models to capture the hepatic perfusion behaviour. Data analysis was performed using Matlab (MathWorks, Massachusetts, USA).

7.2.2.1 Signal processing

Before analysing the acquired data, measured pressures and flow signals were calibrated and filtered. Flow measurements were calibrated by comparing the raw flow signals (voltage [V]) to volumetric flow values [m^3/s], acquired by physically collecting the perfusate volume per unit of time. For each flow signal (HA, PV and VCI), a linear fit was performed to all measurement points and allowed converting the raw signals [V] to calibrated flow signals [m^3/s]. Pressure signals were corrected for pressure losses between the blood vessel in-/outlet (HA, PV or VCI) and its pressure transducer according to Poiseuille's law (eq. 3.2) with a perfusate viscosity according to eq. 7.1 with T [°C] the perfusate temperature (based on previous viscosity measurements of KPS-1; data not shown). After calibration, pressure and flow signals were filtered to remove unwanted high frequency noise by a low pass third order Butterworth filter with a cut-off frequency of 15 Hz.

$$\mu_{KPS-1} = -1.19 \cdot 10^{-4} T + 5.51 \cdot 10^{-3} \tag{7.1}$$

7.2.2.2 Input impedances

After signal processing, HA and PV hydraulic input impedances were calculated to capture the hepatic perfusion behaviour. Hydraulic impedances are the hydraulic equivalent of electrical impedances and reflect the relation between pressure and flow as a function of frequency. Basically, the impedance of a system is, for every frequency (f [Hz]), represented by a complex number (Z [mmHg·min/ml] with a the real part and b the imaginary part) characterised by its modulus $|Z|$ [mmHg·min/ml] and phase angle ϕ [°] (eq. 7.2-7.4 with j the imaginary unit).

$$Z = a + bj = |Z|e^{j\phi} \tag{7.2}$$

$$|Z| = \sqrt{a^2 + b^2} \tag{7.3}$$

$$\phi = atan\left(\frac{b}{a}\right) \tag{7.4}$$

In order to calculate HA and PV input impedances, pressure and flow signals were converted from the time domain to the frequency domain by

means of the discrete Fourier transformation (DFT; eq. 7.5 with x an N points discrete time signal, X the DFT of x, l and k the indices of the time and frequency vector, respectively). This transformation represents a mathematical technique to rewrite (noisy) time signals as a sum of single frequency sinusoidal waves, which facilitates studying signal properties. The fast Fourier transform algorithm was used, and pressure and flow DFT calculations were based on a moving window method, implying that the resulting DFT was the average DFT of a series of time windows (30 s) with a 50% time overlap. Subsequently, HA and PV hydraulic impedances Z were calculated by dividing their pressure DFT (P_{DFT}) by their flow DFT (Q_{DFT}) (eq. 7.6).

$$X(k) = \sum_{l=0}^{N-1} x(l) e^{-j2\pi l \frac{k}{N}} \text{ with } k = 0, 1, \ldots, N-1 \tag{7.5}$$

$$Z = \frac{P_{DFT}}{Q_{DFT}} \tag{7.6}$$

In the next step, the magnitude-squared coherences between pressure and flow signals were calculated for both the HA and PV (eq. 7.7 with C_{xy} the coherence, G_{xy} the cross-spectral density between signals x and y, G_{xx} and G_{yy} the autospectral densities of x and y, respectively). This allows quantifying how well pressure and flow signals correspond to each other at each frequency, and to estimate the reliability of the corresponding Z spectra. Coherence values range between 0 (signals are not related) and 1 (signals are perfectly related). As noise is inherent to experimental measurements, noise may negatively affect the coherence values.

$$C_{xy} = \frac{|G_{xy}|^2}{G_{xx} G_{yy}} \tag{7.7}$$

7.2.2.3 Windkessel model fitting

Since it is not straightforward to directly tune an extended electrical model to MP-acquired data (due to a limited amount and non-homogeneous distribution of coherent points), the idea was to first determine the global parameters describing the hepatic perfusion behaviour by using more compact lumped parameter models (Windkessel models; WK). Subsequently, these WK models were used to 'smear out' the global properties over the extended electrical model. WK models are often used to model the haemodynamic properties of vascular systems (e.g. the arterial system) in a simplified way [39, 208, 264, 332, 372, 422, 428, 451, 471, 473, 491]. Ideally, the configuration

of the reduced model would equal the configuration of the previously developed extended electrical liver model in analogy with the findings of de Pater [91] and van der Plaats [482] (sections 4.2.2.1.2 and 6.2.2). Therefore, a π-element WK model (WKπ) was studied (Fig. 7.4; including a distal resistance R_d, an inductor L, a capacitor C and R_p representing the visco-elasticitity of the blood vessel walls). In addition, the performance of two other frequently used four-element WK models was studied with R_c (the characteristic impedance) and L either in series (WK4s) or in parallel (WK4p). Although three-element WK models (WK4s without L component) also have been used frequently in the past, we found that they are insufficient to describe the dynamic behaviour of the liver and are therefore not included in this study.

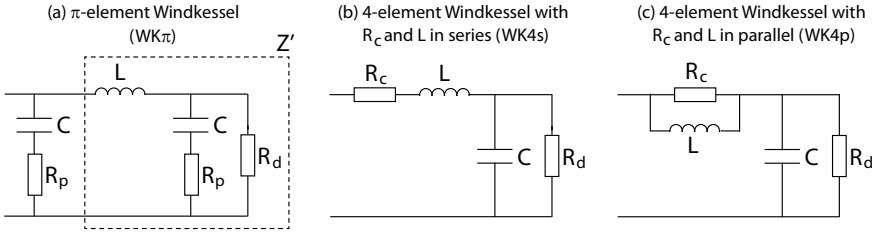

Figure 7.4: Overview of the Windkessel (WK) models that were tuned to the input impedances: a π-element model (a) and two four-element WK models with R_c and L either in series (b) or in parallel (c).

WK models were fitted for both the HA and PV by minimising the modulus difference between the WK impedances (Z_{WK}; eq. 7.8-7.11 with Z' as indicated in Fig. 7.4a) and the experimentally acquired impedances (Z).

$$Z_{WK4\pi} = \frac{1 + Z' + j2\pi f R_p C}{Z' + j2\pi f R_p C Z'} \tag{7.8}$$

$$\text{with } Z' = j2\pi f L + \frac{1 + R_d + j2\pi f R_p C}{R_d + j2\pi f R_p C R_d} \tag{7.9}$$

$$Z_{WK4s} = R_c + j2\pi f L + \frac{R_d}{1 + j2\pi R_d C} \tag{7.10}$$

$$Z_{WK4p} = \frac{j2\pi f R_c L}{R_c + j2\pi f L} + \frac{R_d}{1 + j2\pi f R_d C} \tag{7.11}$$

The tuning approach did not incorporate minimising the difference between phase angles, as this seemed to result in good fitting to the phase angles but not the moduli, or vice versa. Also, phase angles may be unreliable

to fit to as they are potentially affected by time delays resulting from pressure and corresponding flow measurements which could not be measured at the exact same location due to practical restrictions. Furthermore, only coherent impedance points (coherence ≥ 0.9) were taken into account and a weighting factor (w) was introduced to correct for the non-homogeneous distribution of coherent points along the frequency spectrum (see for example Fig. 7.11): the larger the frequency difference of a coherent point to its neighbouring coherent points, the higher its weight (eq. 7.12 with f [Hz] the frequency and k the index of the frequency vector of coherent points). (The non-homogeneous distribution of highly coherent points was also the reason why simply using coherence values as weighting factors was not sufficient.)

$$w_k = (f_k - f_{k-1}) + (f_{k+1} - f_k) = f_{k+1} - f_{k-1} \tag{7.12}$$

The weighting factor of the 0 Hz impedance was set to a very high value to make sure that the 0 Hz impedance modulus (vascular resistance) was fitted correctly. The resulting cost function (eq. 7.13) was minimised by means of unconstrained nonlinear optimisation using the *fminsearch* function in Matlab.

$$cost_{WK} = \sum w \cdot (|Z_{WK}| - |Z|)^2 \tag{7.13}$$

7.2.3 Fitting of the extended liver-specific electrical analog model

This section explains how a liver-specific electrical analog model can be developed and tuned to HMP experimental data.

7.2.3.1 Geometrical data acquisition

Similar to the methods described in sections 5.2 and 6.2 for HL1, vascular corrosion casting and micro-CT imaging of the global human liver grafts (HL2 and HL3) were performed (Fig. 7.5). Since the imaging results of HL3 were difficult to analyse due to a number of insufficiently cast regions (probably due to air bubbles), only data from HL2 was further processed.

The micro-CT scan of HL2 (resolution of 179 µm) enabled segmentation, 3D reconstructions (Fig. 7.6) and measurements of the vascular geometrical features (radii, length and numbers of vessels) up to the 4^{th} HA, PV and HV generation (Fig. 7.7 and 7.8). Data estimations for higher generations were based on the exponential trend lines resulting from the mesocirculation measurements of HL1 (see chapter 5; Fig. 5.4 and 5.5). For all vascular trees, the a coefficient of each HL1 exponential trend line (eq. 5.1) was recalculated to match to the r, l or n value of the 4^{th} generation of HL2. Doing

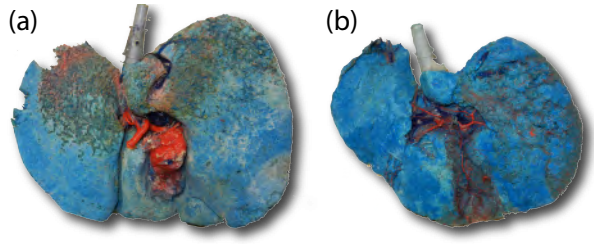

Figure 7.5: Vascular corrosion casts of human livers HL2 (a) and HL3 (b).

so, data were extrapolated up to generation 10, 10 and 8 for the HA, PV and HV tree, respectively (Fig. 7.7 and 7.8). Subsequently, new exponential trend lines were fitted to the combination of HL2 measured data (up to generation 4) and estimated mesodata. Analogous to the methods of chapter 6 (section 6.2.2.2), these trend lines were used to extrapolate the geometrical features up to the terminal HA, PV and HV level, and an additional HV generation was added to represent the sinusoids.

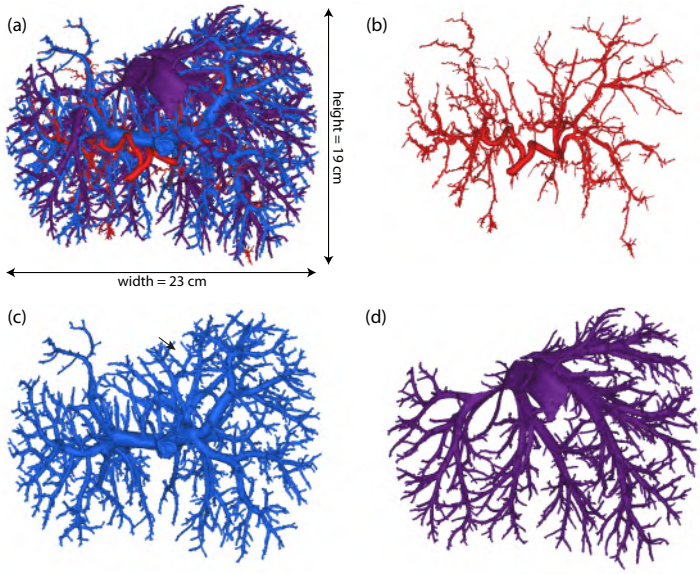

Figure 7.6: 3D reconstructions of the macrocirculation of human liver 2 (HL2): (a) superposition of the three vascular trees with indications of the height and width; (b) hepatic arterial (HA), (c) portal venous (PV) and (d) hepatic venous (HV) trees.

7.2.3.2 Initial extended electrical model of HL2

In addition to the geometrical features, c_p values (pulse wave velocity) had to be determined to define the electrical components of the initial extended

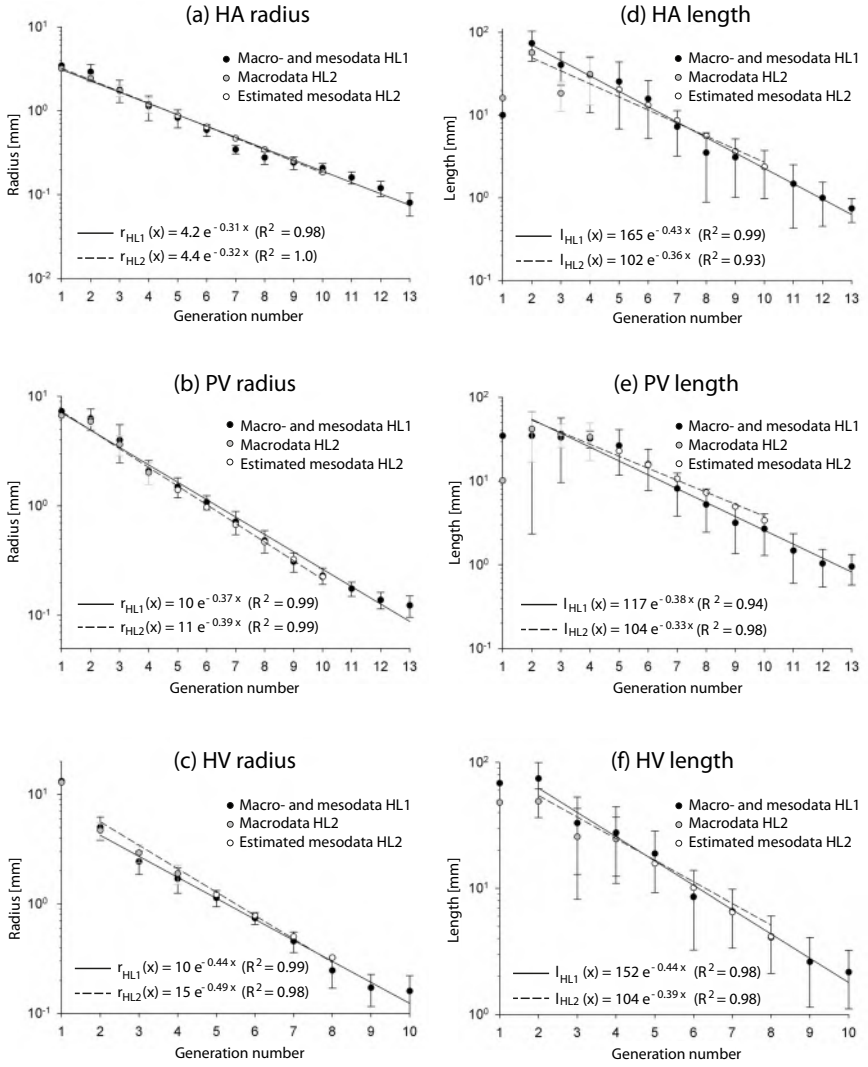

Figure 7.7: Results of the vascular tree analysis of human livers HL1 and HL2: radius (a-c) and length (d-f) with their standard deviations as a function of the generation number for the hepatic arterial (HA), portal venous (PV) and hepatic venous (HV) trees, respectively. Macro- and mesocirculation measurements are indicated by black markers for HL1. Macrocirculation measurements and mesocirculation estimations of HL2 are indicated by grey and white markers, respectively. Exponential trend lines are depicted by full and dashed lines when fitted to macro- and mesocirculation data of HL1 and HL2, respectively. Equations and coefficients of determination (R^2) of the exponential functions are given. The first HV generation (vena cava inferior; VCI) was not taken into account when fitting the radius trend line, since the VCI has a much larger diameter and is not really part of the hepatic vasculature. Length trend lines did not incorporate the first generation, since these vessels were cut to resect the liver, resulting in an underestimated length.

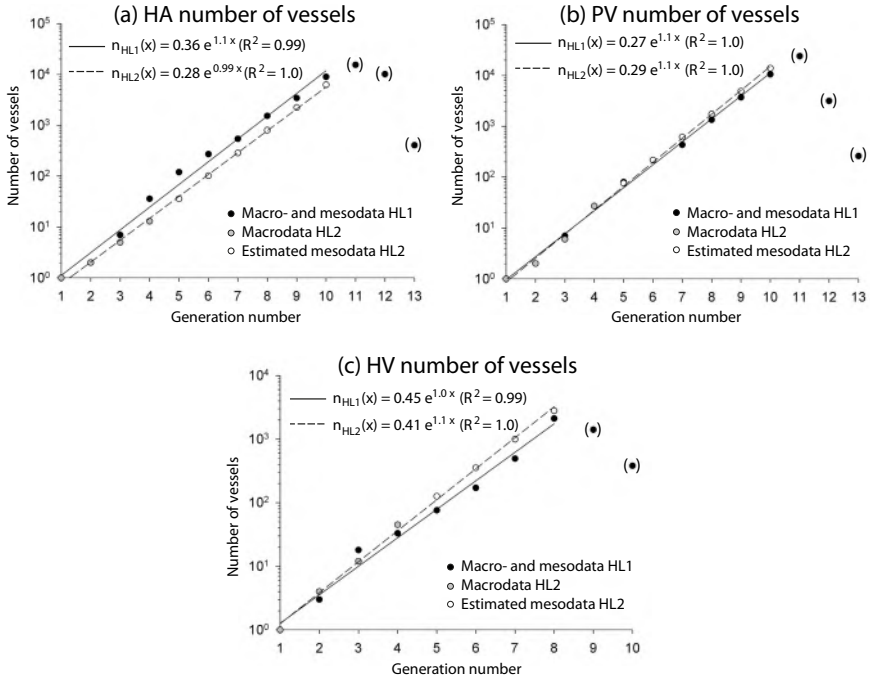

Figure 7.8: Results of the number of vessels per generation number of the macro- and mesocirculation for the hepatic arterial (HA), portal venous (PV) and hepatic venous (HV) trees of HL1 and HL2. Macro- and mesocirculation measurements are indicated by black markers for HL1. Macrocirculation measurements and mesocirculation estimations of HL2 are indicated by grey and white markers, respectively. Exponential trend lines are depicted by full and dashed lines when fitted to macro- and mesocirculation data of HL1 and HL2, respectively. Equations and coefficients of determination (R^2) of the exponential functions are given. Points between brackets indicate unreliable numbers of vessels, which were not used for the extrapolations.

electrical model. Similar to the methods described in section 6.2, c_p values were determined by interpolation between a maximum and minimum c_p value depending on the radius.

Next, R_s values (representing vascular resistance) were tuned such that the mean pressures and flows of the model match those measured during the experiments. Similar to section 6.2, the desired total vascular resistances were calculated for each vascular tree from the measurements. Subsequently, the exponential b coefficients of the length trend lines were tuned to correspond to literature values of terminal lengths, while the b coefficients of the number of vessels trend lines were adapted to yield the desired total vascular resistances. With this approach, only the trend lines with the highest degree of uncertainty are tuned (radii were not tuned), while the original data generated by measurements and meso-estimations were used where available.

Hereupon, all electrical components of the initial electrical liver model were calculated using eq. 6.1-6.4. HA and PV input impedances of the electrical model were calculated based on the electrical circuit of Fig. 6.1 by summing the impedances of all components (in series or parallel) up to the HA and PV inlet, respectively.

7.2.3.3 Finetuning the extended electrical model of HL2

After tuning the R_s values, additional tuning of the other electrical components (L, C and R_p) was required to match the input impedances of the extended electrical model (Z_{EM}) to those of the WK models (Z_{WK}; already tuned to represent the global properties of the liver-specific perfusion behaviour as described in section 7.2.2.3). Using unconstrained nonlinear optimisation (*fminsearch* function in Matlab), the optimal factors ($f_{L_{HA}}$, $f_{C_{HA}}$ and $f_{R_{p,HA}}$) were determined to multiply with the L, C and R_p values of the HA blood vessel generations in order to fit $|Z_{EM,HA}|$ to $|Z_{WK,HA}|$. Subsequently, the optimal PV factors ($f_{L_{PV}}$, $f_{C_{PV}}$ and $f_{R_{p,PV}}$) were similarly determined. The corresponding cost function that was minimised for both the HA and PV when tuning the extended liver-specific electrical model, is shown in eq. 7.14.

$$cost_{EM} = \sum \left(|Z_{EM}| - |Z_{WK}|\right)^2 \tag{7.14}$$

7.2.4 Sensitivity analysis

Finally, a parameter study was conducted on the tuned electrical model in order to investigate the sensitivity of the model to changes of its electrical components (all R_s, L, C and R_p components were divided and multiplied by 2).

Due to practical restrictions, pressure transducers and their corresponding flow probes could not be mounted at the exact same locations. As this may lead to time delays between pressure and flow signals, we investigated the effect of inducing time delays of -20 ms to 20 ms.

7.3 Results

Results are mainly focused on HL2 due to the image processing restrictions of HL3. The frequency domain of the reported impedances is restricted to 0-10 Hz as higher frequencies are physiologically of less importance.

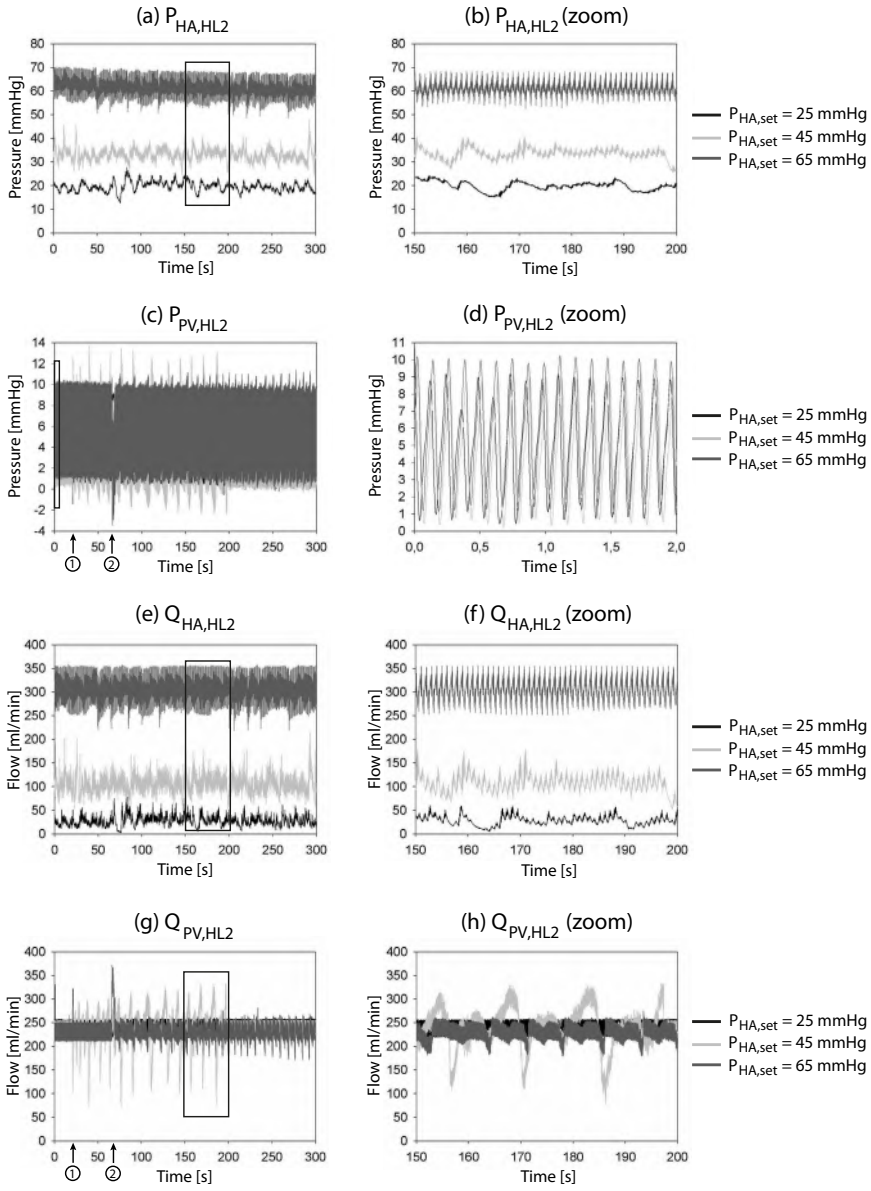

Figure 7.9: Hepatic arterial (HA) and portal venous (PV) pressure and flow measurements of the hypothermic machine perfusion (HMP) experiment on human liver HL2 for perfusion settings with a PV pressure ($P_{PV,set}$) of 5 mmHg, a PV flow limit of 300 ml/min and an HA pressure ($P_{HA,set}$) of 25, 45, 65 mmHg, respectively. Panels a, c, e, g and b, d, f, h present measurements during 300 s and during a shorter time window of 150-200 s as indicated by the boxes in panels a, c, e, g (except for the P_{PV} with a 2 s window to illustrate its inherent 8 Hz component). PV pressure (P_{PV}) and flow (Q_{PV}) signals gave evidence of unstable flow fluctuations starting at time stamp 1 (± 20 s) and 2 (± 70 s) for measurements with a $P_{HA,set}$ of 45 and 65 mmHg, respectively (panels c and g).

7.3.1 HMP experiments

7.3.1.1 Pressure and flow time signals

Pressure and flow signals are first visualised as a function of time (Fig. 7.9 for HL2). Time-averaged pressure, flow and vascular resistances ($Z(0\text{ Hz})$) of HL2 and HL3 are shown in Table 7.2 for a subset of measurements. Pulsatile P_{HA} and Q_{HA} signals showed repetitive fluctuations (± 1 Hz; Fig. 7.9 b and f). Due to MP protocol limitations, P_{PV} and Q_{PV} were more continuous, but the roller pump did induce some pulsatility with a sinusoidal component of ± 8 Hz (Fig. 7.9 d). An increasing $P_{HA,set}$ resulted in an increasing Q_{HA}, while the time-averaged P_{PV} also seemed to increase (especially for a $P_{HA,set}$ of 65 mmHg) in order to maintain Q_{PV} approximately constant (Fig. 7.9 and Table 7.2). P_{PV} and Q_{PV} signals gave evidence of unstable flow fluctuations starting at time stamp 1 (± 20 s) and 2 (± 70 s) for measurements with a $P_{HA,set}$ of 45 and 65 mmHg, respectively (Fig. 7.9). This instability may indicate the onset of flow competition (section 3.3.3). Interestingly, measured P_{HA} values did only sporadically reach $P_{HA,set}$ (Fig. 7.9; especially for a $P_{HA,set}$ of 25 and 45 mmHg), probably due to the HMP feedback system using P_{HA} measurements near the pump outlet, while we measured P_{HA} at the HA vessel inlet, imposing an additional pressure drop between both measurement points. $Z(0\text{ Hz})$ was found consistently higher in the HA compared to the PV. $Z_{HA}(0\text{ Hz})$ clearly decreased with increasing P_{HA} values, while $Z_{PV}(0\text{ Hz})$ tended to increase (especially for a $P_{HA,set}$ of 65 mmHg). HL3 showed consistently higher $Z_{HA}(0\text{ Hz})$ values (more than 2.5-fold) than HL2, while its $Z_{PV}(0\text{ Hz})$ values tended to be lower.

Table 7.2: Time-averaged pressure, flow and vascular resistance values of the hypothermic machine perfusion (HMP) experiments on human livers HL2 and HL3 for perfusion settings with a PV pressure ($P_{PV,set}$) of 5 mmHg, a PV flow limit of 300 ml/min and an HA pressure ($P_{HA,set}$) of 25, 45 and 65 mmHg, respectively.

$\mathbf{P_{HA,set}}$ **[mmHg]**	**25**		**45**		**65**	
Human liver	HL2	HL3	HL2	HL3	HL2	HL3
$\mathbf{P_{HA}}$ **[mmHg]**	19.7	19.5	33.0	38.2	60.5	54.1
$\mathbf{P_{PV}}$ **[mmHg]**	4.69	3.07	4.54	3.38	5.35	4.36
$\mathbf{Q_{HA}}$ **[ml/min]**	27.8	8.86	105	48.3	303	100
$\mathbf{Q_{PV}}$ **[ml/min]**	236	249	233	257	228	270
$\mathbf{Z_{HA}}(0\text{ Hz})$ **[mmHg · min/ml]**	$7.07{\cdot}10^{-1}$	2.20	$3.14{\cdot}10^{-1}$	$7.91{\cdot}10^{-1}$	$2.00{\cdot}10^{-1}$	$5.40{\cdot}10^{-1}$
$\mathbf{Z_{PV}}(0\text{ Hz})$ **[mmHg · min/ml]**	$1.99{\cdot}10^{-2}$	$1.24{\cdot}10^{-2}$	$1.95{\cdot}10^{-2}$	$1.32{\cdot}10^{-2}$	$2.35{\cdot}10^{-2}$	$1.61{\cdot}10^{-2}$

7.3.1.2 Input impedances

The resulting HA and PV input impedances for a $P_{HA,set}$ of 25, 45 and 65 mmHg are plotted in Fig. 7.10. While $|Z_{HA}|$ values at 0 Hz decreased with an increasing $P_{HA,set}$, $|Z_{HA}|$ seemed to align with each other at the higher end

of the studied frequency spectrum (± 7-10 Hz). For all three measurements, $|Z_{PV}|$ showed increasing values at low frequencies (± 0-5 Hz) and approximately constant values for higher frequencies (± 5-10 Hz). The HA phase angle (ϕ_{HA}) was mainly negative at low frequencies (± 0-4 Hz) and became positive for higher frequencies (± 4-10 Hz). ϕ_{PV} followed a similar trend as ϕ_{HA}.

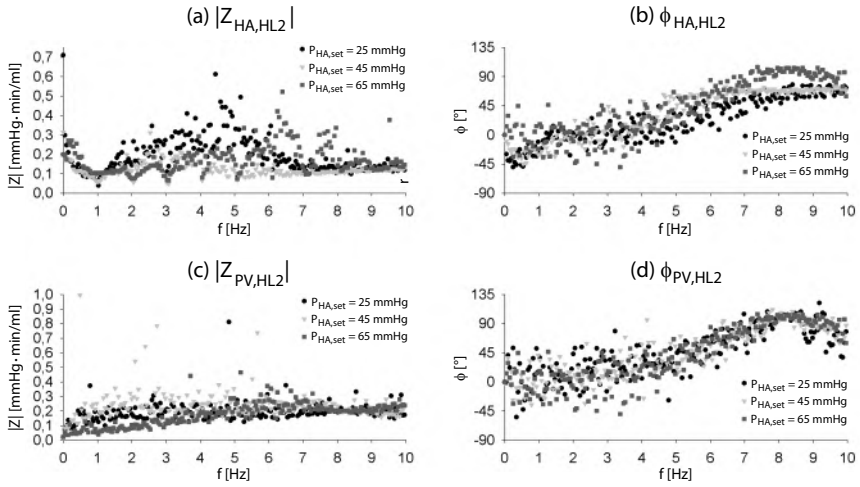

Figure 7.10: Hepatic arterial (HA) and portal venous (PV) input impedances of human liver HL2 for perfusion settings with a PV pressure ($P_{PV,set}$) of 5 mmHg, a PV flow limit of 300 ml/min and an HA pressure ($P_{HA,set}$) of 25, 45, 65 mmHg, respectively: HA and PV moduli (a, c) and phase angles (b, d).

Subsequently, coherence values were calculated as a measure of the reliability of the impedance spectra. HA and PV impedances for a $P_{HA,set}$ of 45 mmHg were replotted according to their coherence values (Fig. 7.11). HA coherence values were highest at the lower (0-1 Hz) and higher (6-10 Hz) end of the frequency spectrum, supplemented by a few intermediate points with relatively high coherences (near 2 and 3 Hz). This subset of coherent points shows that $|Z_{HA}|$ values seem to decline from 0-3 Hz, followed by a gradual and slow increase up to 10 Hz. PV impedances only showed coherent points between 0-2 Hz and near 8 Hz, implying little frequency content in the PV signals.

7.3.1.3 Windkessel models

HA and PV WK models were fitted to the coherent impedance points (Fig. 7.12), resulting in the parameter values reported in Table 7.3. For Z_{HA}, the WKπ and WK4s outperformed the WK4p model, while the WKπ and WK4p

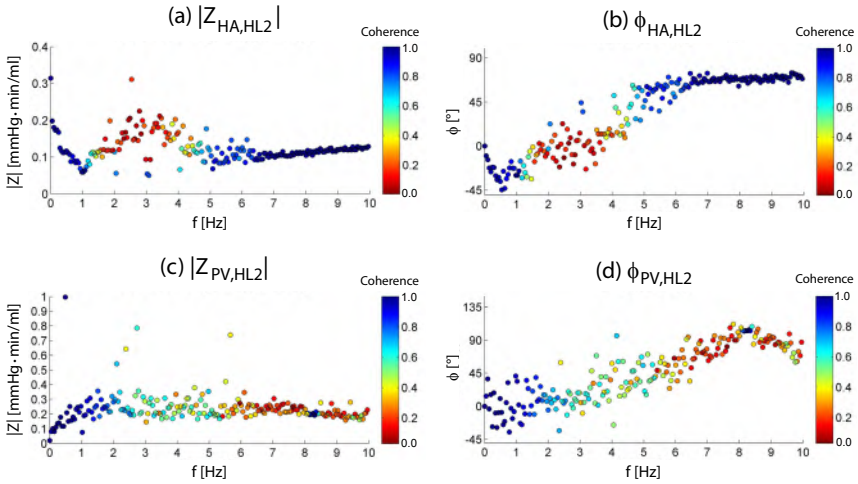

Figure 7.11: Hepatic arterial (HA) and portal venous (PV) input impedances of human liver HL2 colour-coded according to the coherence values for perfusion settings with a PV pressure ($P_{PV,set}$) of 5 mmHg, a PV flow limit of 300 ml/min and an HA pressure ($P_{HA,set}$) of 45 mmHg: HA and PV moduli (a, c) and phase angles (b, d).

models performed best for Z_{PV}. WK models were fitted based on the impedance moduli, and we found some discrepancies between fitted and measured phase angles. This might be due to time delays between the pressure and flow (see further in section 7.3.3). Furthermore, caution is warranted when analysing the PV WK models, as these were fitted to only a small number of coherent points. When comparing the WKπ components of the HA for measurements with an increasing $P_{HA,set}$, R_d, L and C values seemed to drop, while R_p values were rising. As WKπ models performed relatively well for both HA and PV, and as they are similar to the π-elements used for the electrical liver model (chapter 6), WKπ model parameters were further used to tune the extended electrical liver model (section 7.3.2.2).

7.3.2 Tuning of the extended liver-specific electrical model

Results for tuning the electrical liver model to HMP acquired data are focused on the measurement with a $P_{HA,set}$ of 45 mmHg (unless specified differently), since the results are similar for other measurements.

7.3.2.1 Initial extended liver-specific electrical model of HL2

Mean pressures and flows predicted by the initial extended electrical liver model throughout the blood vessel generations are shown in Fig. 7.13. Similar to the results in section 6.3.2, pressures decreased along subsequent generations resulting in a pressure of ± 0.51 mmHg at the sinusoids. Mean flows

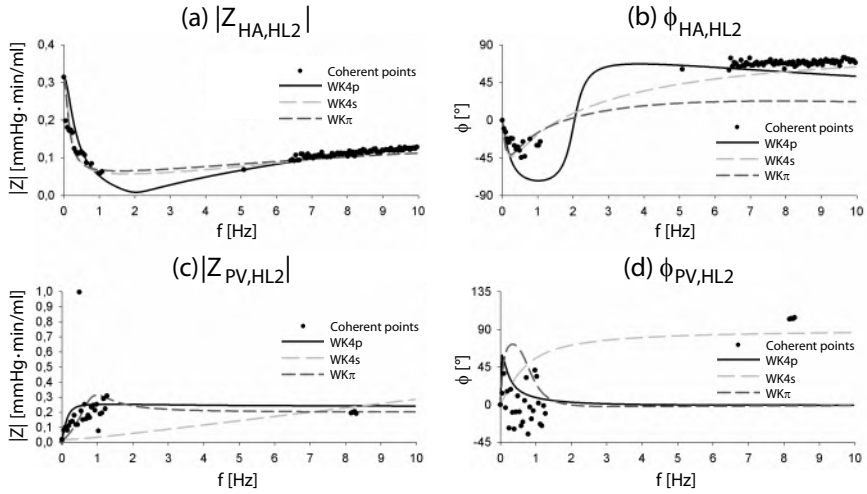

Figure 7.12: Hepatic arterial (HA) and portal venous (PV) input impedances of the Windkessel models tuned to the coherent impedance points of human liver HL2 for perfusion settings with a PV pressure ($P_{PV,set}$) of 5 mmHg, a PV flow limit of 300 ml/min and an HA pressure ($P_{HA,set}$) of 45 mmHg: HA and PV moduli (a, c) and phase angles (b, d).

Table 7.3: Electrical components of the Windkessel models (WKπ, WK4s and WK4p) fitted to the hepatic arterial (HA) and portal venous (PV) impedances of human liver HL2 for perfusion settings with a PV pressure ($P_{PV,set}$) of 5 mmHg, a PV flow limit of 300 ml/min and an HA pressure ($P_{HA,set}$) of 25, 45 and 65 mmHg (only 45 mmHg for the PV). Next to parameter values, the root mean square error (RMSE) is given for each WK fit.

	$P_{HA,set}$	WK model	$R_d[\frac{mmHg \cdot min}{ml}]$	$R_c[\frac{mmHg \cdot min}{ml}]$	$L[\frac{mmHg \cdot min^2}{ml}]$	$C[\frac{ml}{mmHg}]$	$R_p[\frac{mmHg \cdot min}{ml}]$	$RMSE[\frac{mmHg \cdot min}{ml}]$
HA	**25**	WKπ	$7.11 \cdot 10^{-1}$	/	$1.46 \cdot 10^{-4}$	$4.47 \cdot 10^{-1}$	$1.25 \cdot 10^{-1}$	$3.19 \cdot 10^{-2}$
		WK4p	$7.11 \cdot 10^{-1}$	$1.24 \cdot 10^{-1}$	$1.88 \cdot 10^{-4}$	$9.18 \cdot 10^{-2}$	/	$3.36 \cdot 10^{-2}$
		WK4s	$6.69 \cdot 10^{-1}$	$4.17 \cdot 10^{-2}$	$3.93 \cdot 10^{-5}$	$1.04 \cdot 10^{-1}$	/	$3.21 \cdot 10^{-2}$
HA	**45**	WKπ	$3.14 \cdot 10^{-1}$	/	$6.05 \cdot 10^{-5}$	$3.31 \cdot 10^{-2}$	$1.53 \cdot 10^{-1}$	$1.61 \cdot 10^{-2}$
		WK4p	$3.14 \cdot 10^{-1}$	$2.37 \cdot 10^{-1}$	$4.50 \cdot 10^{-5}$	$3.79 \cdot 10^{-2}$	/	$2.27 \cdot 10^{-2}$
		WK4s	$2.58 \cdot 10^{-1}$	$5.63 \cdot 10^{-2}$	$3.14 \cdot 10^{-5}$	$8.67 \cdot 10^{-2}$	/	$1.48 \cdot 10^{-2}$
HA	**65**	WKπ	$2.00 \cdot 10^{-1}$	/	$5.55 \cdot 10^{-5}$	$8.38 \cdot 10^{-3}$	$1.68 \cdot 10^{-1}$	$1.82 \cdot 10^{-2}$
		WK4p	$2.00 \cdot 10^{-1}$	$1.64 \cdot 10^{-1}$	$6.68 \cdot 10^{-5}$	$1.26 \cdot 10^{-2}$	/	$1.91 \cdot 10^{-2}$
		WK4s	$1.45 \cdot 10^{-1}$	$5.46 \cdot 10^{-2}$	$3.71 \cdot 10^{-5}$	$2.65 \cdot 10^{-2}$	/	$1.65 \cdot 10^{-2}$
PV	**45**	WKπ	$1.95 \cdot 10^{-2}$	/	$6.84 \cdot 10^{-4}$	$1.38 \cdot 10^{-2}$	$2.00 \cdot 10^{-1}$	$1.68 \cdot 10^{-1}$
		WK4p	$1.95 \cdot 10^{-2}$	$2.39 \cdot 10^{-1}$	$3.38 \cdot 10^{-3}$	$3.99 \cdot 10^{-2}$	/	$1.51 \cdot 10^{-1}$
		WK4s	$1.54 \cdot 10^{-2}$	$4.16 \cdot 10^{-3}$	$7.71 \cdot 10^{-5}$	$5.34 \cdot 10^{-3}$	/	$2.26 \cdot 10^{-1}$

were 105 ml/min, 233 ml/min and 338 ml/min for the HA, PV and HV vascular tree, respectively. Pulsatile pressure and flow curves as a function of time (Fig. 7.15 and 7.16) were calculated by applying boundary conditions as measured during the HMP experiment (see Table 7.2): a sinusoidal P_{HA} waveform with a mean value of 33 mmHg, a frequency of 1 Hz and an amplitude of 3 mmHg at the HA source and a continuous PV pressure source of 4.54 mmHg. Pressure amplitudes clearly decreased with increasing HA generation numbers, while the PV pressure was constant at the inlet, but

displayed a small pulse at its terminal generation. The HV outflow pressures again showed decreasing amplitudes along subsequent generations. Flow profiles throughout the vascular trees displayed only a very small change of amplitudes. HA and PV impedances of the initial electrical model substantially differed from those of the tuned WKπ models (Fig. 7.14). Impedance values did agree at 0 Hz, but not at higher frequencies, implying that additional parameter tuning was necessary.

7.3.2.2 *Tuning of the extended liver-specific electrical model of HL2*

The resulting HA and PV factors to be multiplied with the L, C and R_p components of the HA and PV tree, respectively, in order to tune the extended electrical model, are shown in Table 7.4 for perfusion settings with $P_{HA,set}$ values of 25, 45 and 65 mmHg. R_p components of the HA and PV tree as well as L components of the PV tree had to be multiplied by a remarkably high factor in the order of 10^4 and 80-300, respectively. Increasing $P_{HA,set}$ values were associated with decreasing f_C, while f_{R_p} increased when the $P_{HA,set}$ was set to 65 mmHg. No clear trend was observed for f_L. The impedance moduli of the tuned electrical model were in good agreement with the WKπ fitted impedances (Fig. 7.14). On the contrary, the HA and PV phase angles of the tuned model underestimated the phase angles of the coherent points.

Pulsatile pressure curves of the tuned electrical model were very similar to those of the initial model, but showed small amplitude differences and time shifts (Fig. 7.15; e.g. pressure amplitudes at the sinusoids were $1.43{\cdot}10^{-2}$

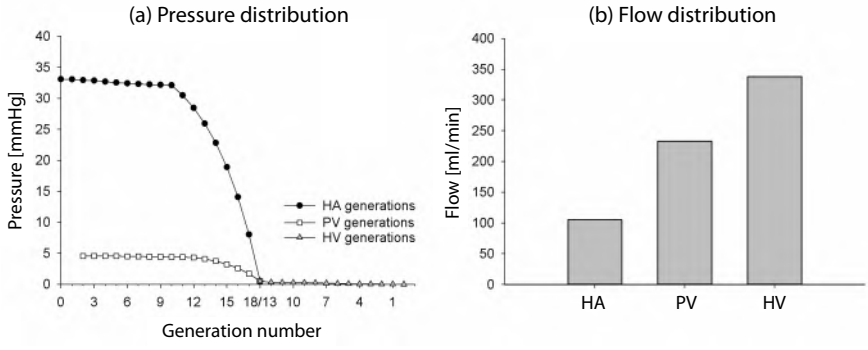

Figure 7.13: Time-averaged results of the initial and tuned electrical liver model of human liver HL2: (a) pressure profiles before and after each blood vessel generation of the hepatic arterial (HA), portal venous (PV) and hepatic venous (HV) trees; (b) time-averaged flows through the HA, PV and HV tree. Time-averaged values are equal for both the initial and tuned electrical model, as the initial model was already tuned to time-averaged pressures and flows.

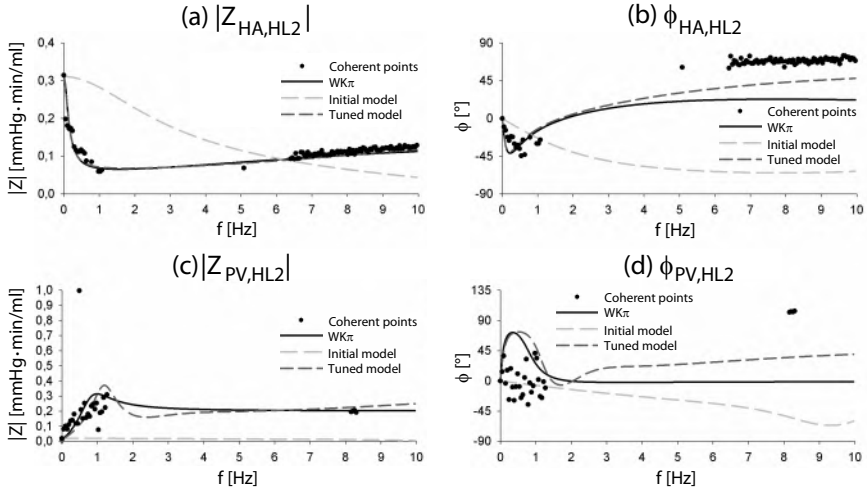

Figure 7.14: Hepatic arterial (HA) and portal venous (PV) input impedance of the initial and tuned electrical liver model of human liver HL2: HA and PV moduli (a, c) and phase angles (b, d). Coherent impedance points are also shown.

mmHg and $1.40{\cdot}10^{-2}$ mmHg for the initial and tuned model, respectively). In contrast, flow profiles of the tuned model displayed substantially larger Q_{HA} amplitudes (especially for the first HA generations), while Q_{PV} amplitudes were smaller and showed time shifts (Fig. 7.16). Q_{HV} were similar to those of the initial model with only very small amplitude differences (e.g. flow amplitudes at the sinusoids were 8.86 ml/min and 8.68 ml/min for the initial and tuned model, respectively).

Table 7.4: Results of tuning the electrical liver model for human liver HL2: f_L, f_C, f_{R_p} factors and root mean square error (RMSE) values for both the hepatic artery (HA) and portal vein (PV) tuned to the WKπ models corresponding to perfusion setting with a PV pressure ($P_{PV,set}$) of 5 mmHg, a PV flow limit of 300 ml/min and an HA pressure ($P_{HA,set}$) of 25, 45 and 65 mmHg, respectively.

$P_{HA,set}$ [mmHg]	$f_{L_{HA}}$	$f_{C_{HA}}$	$f_{R_{p,HA}}$	$RMSE_{HA}$ [mmHg · min/ml]	$f_{L_{PV}}$	$f_{C_{PV}}$	$f_{R_{p,PV}}$	$RMSE_{PV}$ [mmHg · min/ml]
25	4.03	26.0	$9.40{\cdot}10^{3}$	$9.2{\cdot}10^{-3}$	273	2.51	$1.36{\cdot}10^{4}$	$4.3{\cdot}10^{-2}$
45	3.51	17.4	$9.29{\cdot}10^{3}$	$2.3{\cdot}10^{-3}$	292	1.82	$1.33{\cdot}10^{4}$	$3.6{\cdot}10^{-2}$
65	3.65	4.15	$1.23{\cdot}10^{4}$	$2.2{\cdot}10^{-3}$	80.8	1.40	$2.82{\cdot}10^{4}$	$3.8{\cdot}10^{-3}$

7.3.3 Sensitivity analysis

A sensitivity study of the electrical components (illustrated for Z_{HA} in Fig. 7.17) showed that increasing R_s values lead to higher $|Z_{HA}|$ values at 0 Hz and generally lower $|\phi_{HA}|$. Variations in L mainly influenced the higher end

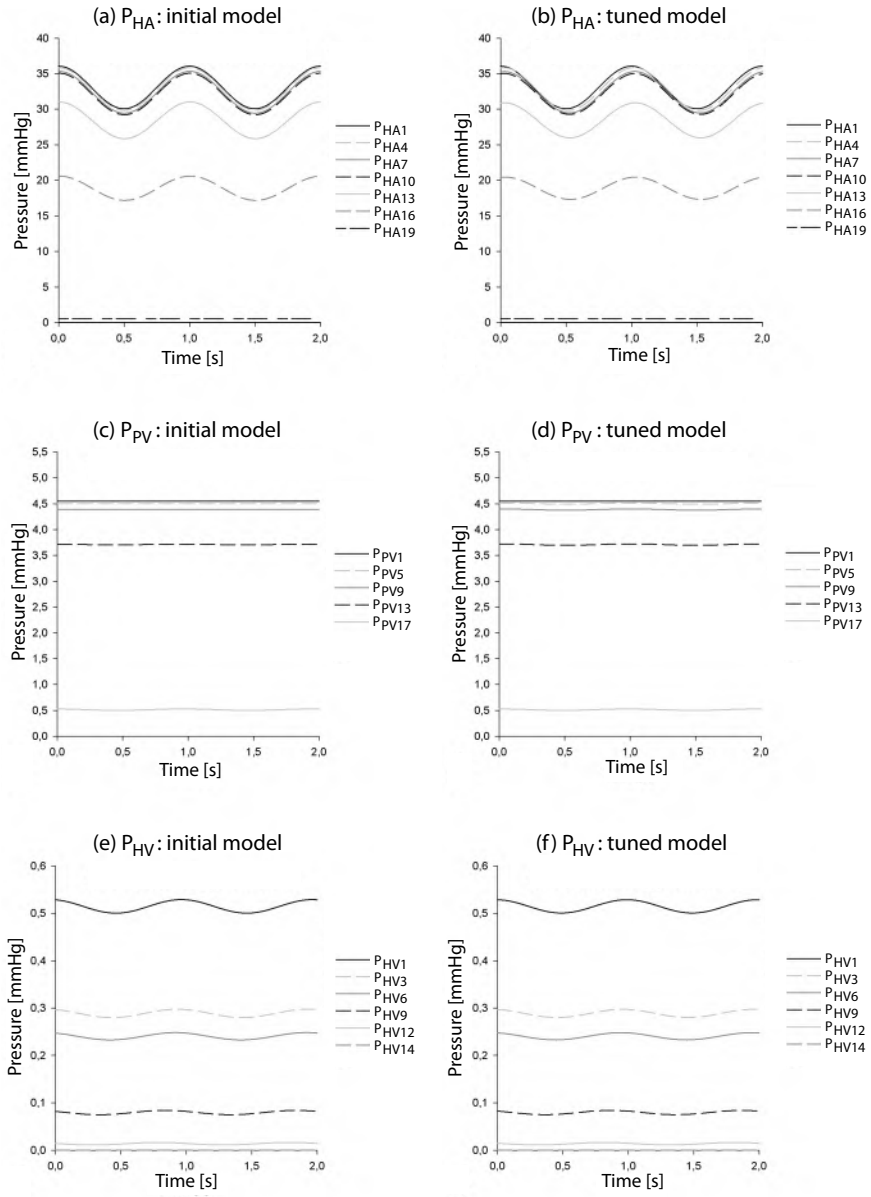

Figure 7.15: Time-dependent pressures calculated by the initial and tuned electrical liver model of human liver HL2: sinusoidal pressures of each blood vessel generation of the hepatic arterial (HA), portal venous (PV) and hepatic venous (HV) trees for the initial (a, c, e) and tuned (b, d, f) electrical liver model.

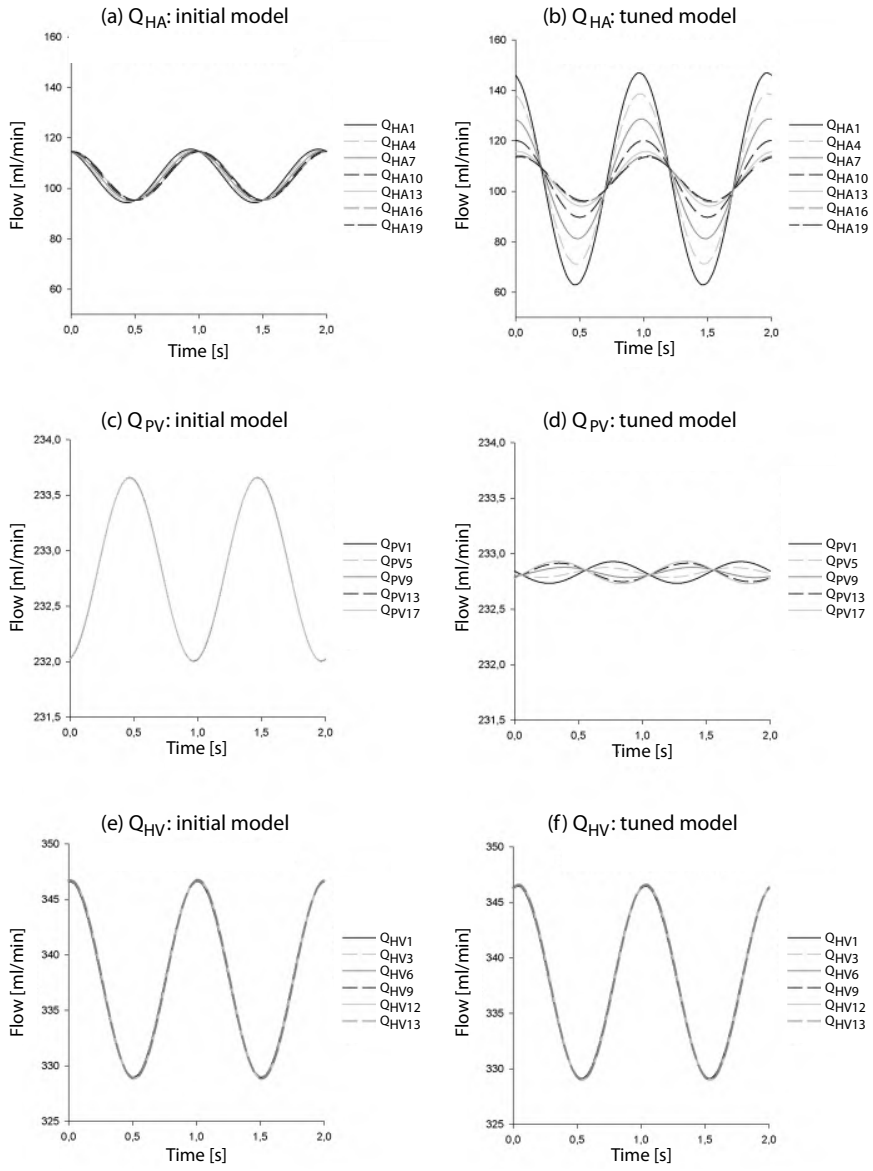

Figure 7.16: Time-dependent flows calculated by the initial and tuned electrical liver model of human liver HL2: sinusoidal flows of each blood vessel generation of the hepatic arterial (HA), portal venous (PV) and hepatic venous (HV) trees for the initial (a, c, e) and tuned (b, d, f) electrical liver model.

of the frequency spectrum with higher $|Z_{HA}|$ and $|\phi_{HA}|$ for higher L values. When increasing the value of the C components, $|Z_{HA}|$ and $|\phi_{HA}|$ spectra seemed to be shifted to the left, resulting in lower $|Z_{HA}|$ at low frequencies and higher $|\phi_{HA}|$ for the major part of the frequency spectrum. Rising R_p values gave evidence of mainly lower $|Z_{HA}|$ and smaller differences between the minimum and maximum $|\phi_{HA}|$.

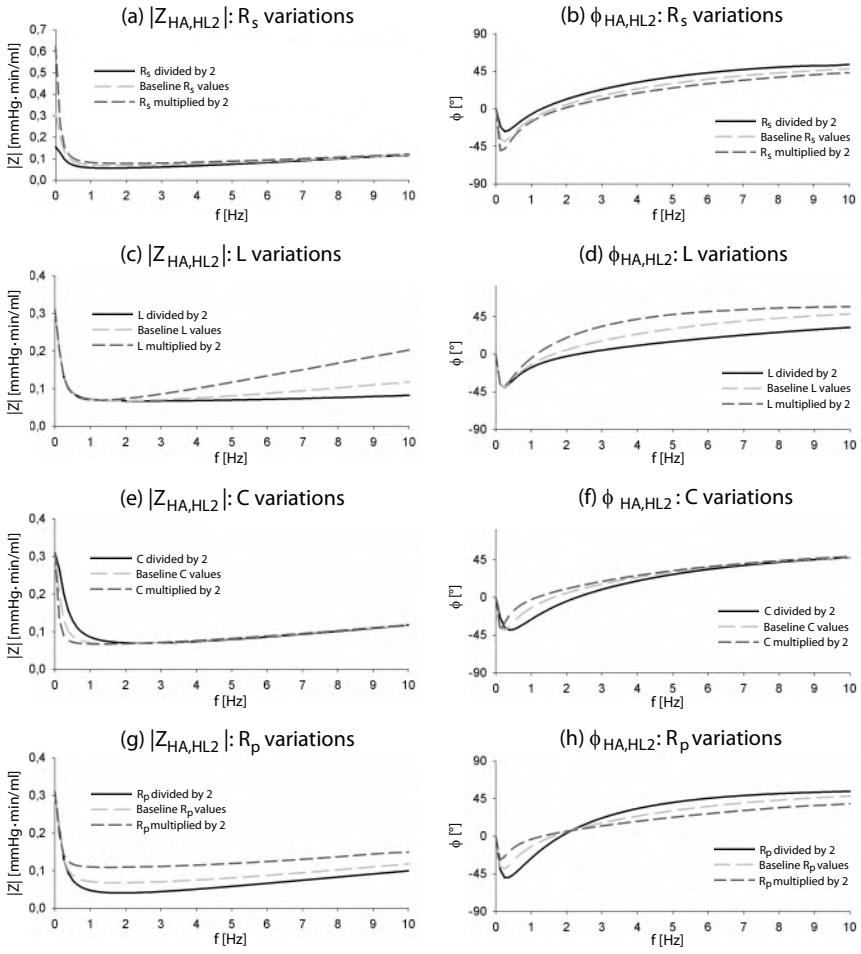

Figure 7.17: Results of the sensitivity analysis of the tuned electrical model: hepatic arterial (HA) impedance moduli (a, c, e, g) and phase angles (b, d, f, h) when varying R_s, L, C and R_p components, respectively.

Fig. 7.18 illustrates that a time delay between pressure and flow signals mainly influenced the phase angles, while impedance moduli did not change, except for a slight increase at high frequencies. Hence, time delays may explain the phase discrepancy between the tuned extended electrical model

and the coherent points. For example, a time delay of approximately −10 ms would make the $|\phi_{HA}|$ of the extended model and coherent points collide with each other.

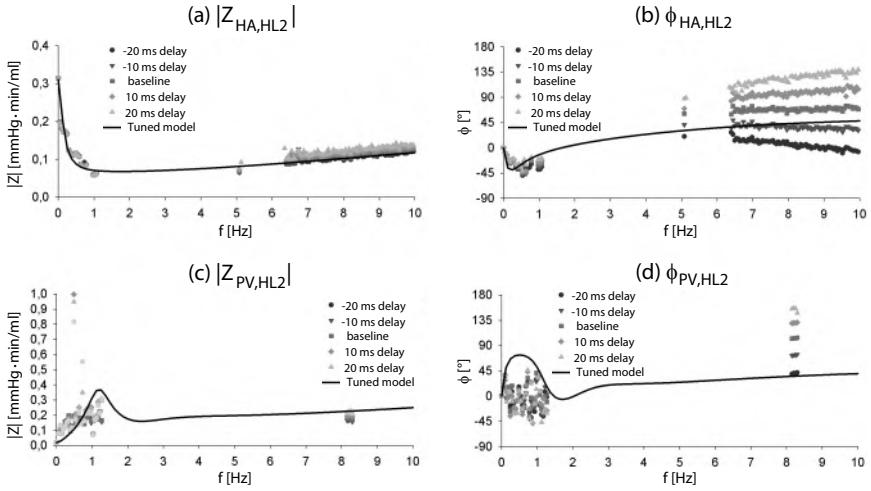

Figure 7.18: Impedance results when inducing a time delay between pressure and flow signals: hepatic arterial (HA) and portal venous (PV) impedance moduli (a, c) and phase angles (b, d) of the originally tuned model and coherent points with a time delay.

7.4 Discussion

7.4.1 Interpretation of the results

In this study, we developed a methodology to validate and tune an extended electrical analog model of hepatic perfusion based on anatomical and functional data of one and the same human liver graft. First, compact WK models were fitted to experimentally acquired input impedances in order to represent the global HA and PV perfusion behaviour. Subsequently, the WK impedances were 'smeared out' over an extended electrical analog model, resulting in a liver-specific model.

WKπ models (and impedance data) demonstrated that increasing $P_{HA,set}$ values clearly altered the perfusion properties with a lower resistance to flow (decreasing R_d), lower inertial forces of the blood flow (decreasing L), a lower elasticity of the blood vessels (decreasing C) and a more outspoken visco-elastic behaviour of the vessel walls (increasing R_p).

When comparing the results of the initial extended electrical model with those of the tuned extended model, substantial differences are observed in

both the impedance spectra (Fig. 7.14) and damping of flow curves throughout the livers (Fig. 7.15 and 7.16). As such, the tuned model resulted in higher Q_{HA} and lower Q_{PV} amplitudes, showing that tuning clearly influences flows - as well as the corresponding wall shear stress fluctuations - which may play a role in potential hepatic endothelial damage. However, the effect at the level of the sinusoids was rather limited (mean wall shear stress of $1.35{\cdot}10^{-1}$ Pa with an amplitude of $3.57{\cdot}10^{-3}$ Pa and $3.51{\cdot}10^{-3}$ Pa for the initial and the tuned extended model, respectively). Sudhamshu et al. [455] reported Doppler velocity measurements of the HA in 30 healthy patients, resulting in an estimated mean Q_{HA} of 398 ml/min and a maximum Q_{HA} of 816 ml/min (± 105% higher than its mean Q_{HA}). When changing the boundary conditions of the initial and tuned electrical analog model (based on a $P_{HA,set}$ of 45 mmHg) to physiological *in vivo* values (a $P_{HA,set}$ with a mean value of 100 mmHg and an amplitude of 20 mmHg, a $P_{PV,set}$ of 10 mmHg), the tuned extended model corresponds better to the measurements by Sudhamshu et al. as it predicts higher Q_{HA} amplitudes (280 ml/min; ± 89% of its mean Q_{HA} value of 314 ml/min) compared to the initial extended model (70.4 ml/min; ± 22% of its mean Q_{HA} value of 314 ml/min). However, absolute values between the measurements of Sudhamshu et al. and the tuned model still differed, which might have to do with the differences between individual livers and perfusion settings (*in vivo* measurements versus models based on *ex vivo* isolated organ HMP). Table 7.4 demonstrates that L, C and especially R_p values were underestimated by the initial extended model. Fig. 7.17 illustrates that changing these components substantially affects the impedance moduli and phase angles. Furthermore, changes in electrical components can be related to changes in the radius, length, number of vessels and pulse wave velocity values of the blood vessel generations (eq. 6.1-6.4). For example, changing the c_p values directly influences the C values, as can be illustrated for the HA by dividing all HA c_p values by 4 (e.g. from 17.7 m/s and 22.0 m/s to 4.41 m/s and 5.50 m/s for the first and terminal HA generation, respectively), which results in the C values being multiplied by a factor of approximately $f_{C_{HA}}$ to obtain the tuned extended model (Table 7.4; eq. 6.3). Hence, these lower c_p values indicate that the initial model overestimated the stiffness.

Since large f_{R_p} values were needed to tune the extended electrical model for both HA and PV, a closer look into the R_p component is advisable. The initial extended model was based on the work of de Pater [91] and van der Plaats [482], which resulted in an electrical analog model for blood vessels and the dog liver, respectively (section 4.2.2.1.2). Visco-elasticity of the vessel wall was introduced by de Pater by using the Kelvin-Voigt model (eq. 7.15 with σ the stress, E_{wall} the Young's elasticity modulus of the wall, ε the strain, μ_{wall} the viscosity of the visco-elastic wall material and t time).

$$\sigma = E_{wall}\varepsilon + \mu_{wall}\frac{\partial \varepsilon}{\partial t} \tag{7.15}$$

After deriving the differential equations for the electrical analog model from the Navier-Stokes equations, de Pater captured the visco-elastic behaviour of the vessel wall in eq. 7.16 with R_p and C defined as in eq. 7.17 and 7.18, p the pressure, q the flow, r the radius, h_{wall} the wall thickness (see also section 4.2.2.1.2). Hereupon, de Pater stated that the influence of R_p is unimportant, certainly for low frequencies, and that R_p can be considered constant and can be calculated from eq. 7.19.

$$-\frac{\partial q}{\partial z} = \frac{3\pi r^3}{2E_{wall}h}\frac{\partial p}{\partial t} + \frac{\mu_{wall}}{E_{wall}}\frac{\partial^2 q}{\partial z \partial t} = C_1\frac{\partial p}{\partial t} + C_1 R_{p1}\frac{\partial^2 q}{\partial z \partial t} \tag{7.16}$$

$$R_p = R_{p1}\frac{2}{l} = \frac{2\mu_{wall}}{3\pi r^3}\frac{h}{l}\frac{2}{l} \tag{7.17}$$

$$C = C_1\frac{l}{2} = \frac{3\pi r^3}{2E_{wall}h}\frac{l}{2} \tag{7.18}$$

$$R_{p1}C_1 = R_pC = 2 \cdot 10^{-6}s \tag{7.19}$$

Van der Plaats et al. [482] used the electrical analog blood vessel model of de Pater to develop an electrical analog model of the liver, hereby extrapolating the visco-elastic behaviour of a vessel to the whole liver. However, we speculate that the visco-elastic behaviour of the liver vasculature might not only depend on the wall material of the blood vessels, but also on the material properties of the surrounding liver tissue. Contradicting the assumption that R_p can be considered constant, our sensitivity study gave evidence of substantial moduli and phase differences when changing R_p values, even for low frequencies (Fig. 7.17 g and h). Moreover, the results for HL2 (Table 7.4) seem to indicate that eq. 7.19, used in the initial model, leads to R_p values that are approximately a factor 10^4 too small. To test this more elaborately, we compared the findings of de Pater with the WKπ models of HL2 and HL3, as well as a WKπ model fitted to *in vivo* $|Z_{HA}|$ values of a single patient, whose liver is called HL4 hereafter, obtained by Basciano et al. [30] (Table 7.5 and Fig. 7.19a). As we verified that no reliable frequency content higher than 5 Hz was present in the pressure and flow curves of HL4 due to filtering [30], the frequency spectrum, used to fit the WKπ model, was limited to 0-5 Hz. To the authors' knowledge, additional literature values on hepatic input impedances are non-existent. Despite the quite drastic differences in conditions, overall patterns agree well with our data (Fig. 7.19a). The R_pC values of all three human livers (Table 7.5) show substantial differences

with the value predicted by de Pater and presumed by van der Plaats for the liver ($R_pC = 2 \cdot 10^{-6}$ s = $3.33 \cdot 10^{-8}$ min; [91]). Additionally, Fig. 7.19b illustrates the large discrepancy between the R_p versus $1/C$ relation as proposed by de Pater (and used by van der Plaats) and the actual human liver results acquired in this study. We speculate that this discordance may be due to the effects of surrounding liver tissue.

Table 7.5: WKπ models fitted to the hepatic artetial (HA) impedance modulus ($|Z_{HA}|$) values of human livers HL2, HL3 and HL4. HL2 and HL3 Windkessel (WK) models were fitted to the hypothermic machine perfusion (HMP) acquired $|Z_{HA}|$ values for perfusion settings with a PV pressure ($P_{PV,set}$) of 5 mmHg, a PV flow limit of 300 ml/min and an HA pressure ($P_{HA,set}$) of 45 mmHg. The WKπ model of HL4 was fitted to the patient-specific values obtained by Basciano et al. [30]. As we verified that no reliable high frequency content was present in the pressure and flow curves of HL4, the frequency spectrum, used to fit the WKπ model, was limited to 0-5 Hz. The fitted parameters as well as the root mean square error ($RSME$) and R_pC values are given. (*) The L value of HL4 is unreliable as L mainly affects the high frequency response and no reliable high frequency data were available for fitting.

Human liver	$\mathbf{R_d}[\frac{mmHg \cdot min}{ml}]$	$\mathbf{L}[\frac{mmHg \cdot min^2}{ml}]$	$\mathbf{C}[\frac{ml}{mmHg}]$	$\mathbf{R_p}[\frac{mmHg \cdot min}{ml}]$	$\mathbf{RMSE}[\frac{mmHg \cdot min}{ml}]$	$\mathbf{R_p \cdot C}[min]$
HL2	$3.14 \cdot 10^{-1}$	$6.05 \cdot 10^{-5}$	$3.31 \cdot 10^{-2}$	$1.53 \cdot 10^{-1}$	$1.61 \cdot 10^{-2}$	$5.06 \cdot 10^{-3}$
HL3	$7.92 \cdot 10^{-1}$	$4.09 \cdot 10^{-5}$	$2.93 \cdot 10^{-3}$	$4.20 \cdot 10^{-1}$	$5.48 \cdot 10^{-2}$	$1.23 \cdot 10^{-3}$
HL4	$5.75 \cdot 10^{-1}$	$2.16 \cdot 10^{-10}$ *	$3.78 \cdot 10^{-3}$	$6.36 \cdot 10^{-1}$	$1.04 \cdot 10^{-2}$	$2.40 \cdot 10^{-3}$

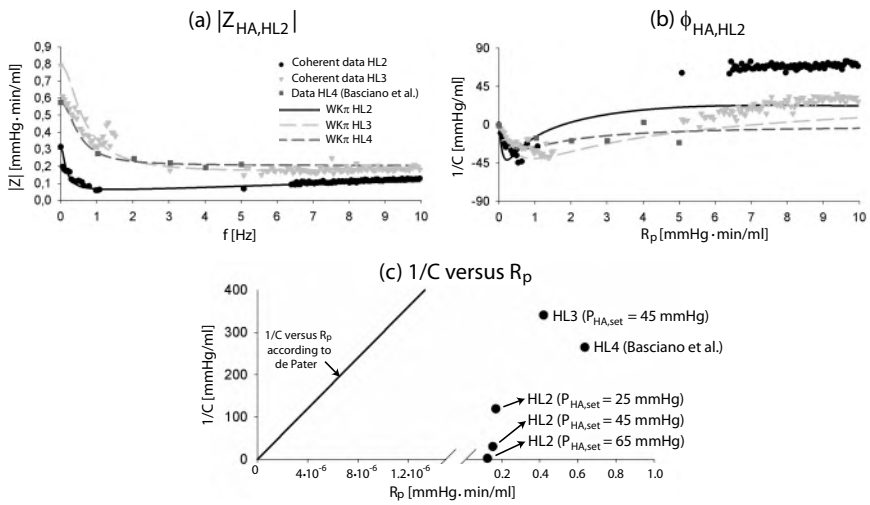

Figure 7.19: Comparison of the results of human livers HL2, HL3 and HL4: (a) hepatic artetial (HA) impedance modulus ($|Z_{HA}|$) values of the (coherent) data points and WKπ models with HL4 data taken from [30]; (b) comparison of the relation between R_p and C as assumed by de Pater [91] and as calculated from our WKπ data for Z_{HA}.

HA and PV input impedances may not only be powerful tools to tune hepatic perfusion models, but also to assess the liver response to perfusion,

which may be related to graft properties and viability. Contrary to vascular resistances (time-averaged pressure divided by time-averaged flow), impedances may include information on the elasticity of blood vessels, the inertia of the blood flow, and the visco-elastic behaviour of the walls and possibly also the surrounding liver tissue.

The human liver grafts used in this study were discarded for transplantation because of tumourous tissue in the kidneys (HL2) and because no suitable recipient was found (HL3). The livers showed no signs of abnormalities and, hence, were perfectly suitable for our study. The experimental procedure, starting from the hepatectomy and ending after vascular corrosion casting, was completed within 24 h for both livers. HMP results indicated that HL3 overall had a higher HA vascular resistance than HL2 (Table 7.2; possibly due to the smaller size of HL3), while its PV resistance was lower.

Comparison of the HL1 and HL2 measured geometrical data up to the 4^{th} generation (Fig. 7.7 and Fig. 7.8) demonstrates that HA, PV and HV radii were very similar for both livers, while lengths were less related. The numbers of vessels per generation also showed similar trends with the largest deviations for the HA tree.

7.4.2 Limitations

As we focused mainly on HL2 due to image processing limitations with HL3, care should be taken when generalising the results. Ideally, this study should be repeated on more livers in order to clearly demonstrate perfusion behaviour similarities and differences between livers. The procedure to obtain experimental data and build models (especially the image processing and data acquisition), however, is labour-intensive. Moreover, human liver grafts are scarce and their availability depends on the moment that a donor organ is discarded after failed reallocation.

The acquired PV impedances only showed a relatively small amount of highly coherent points (Fig. 7.11). Consequently, caution is recommended when interpreting the PV results. Changing the perfusion settings by inducing perturbations (such as transient phenomena, e.g. starting or stopping the pumps) or adjusting the HMP control circuit may enable generating PV data with more frequency content. HV outlet impedances were not studied, as these were not relevant due to the free outflow conditions.

Ideally, pressure and flow measurements at the sinusoids should be included to fully define the hepatic perfusion behaviour. We attempted to measure sinusoidal pressures using balloon catheters which were inserted in the HV system, but measurements were inaccurate and could not be used.

7.4.3 Future perspective

An obvious extension is to confirm our findings in a higher number of human liver grafts in order to generate a larger dataset. Furthermore, the pre-

sented experiments and models may also be applied to pathological organs to gain more insight into the vascular alterations affecting haemodynamics (e.g. in cirrhosis). Since data of only the first 4 generations of blood vessels were used to generate the electrical model, this could also be done using conventional CT-scanners in clinics. This may enable generating patient-specific liver models, which might be helpful in the context of surgical planning.

7.5 Conclusion

HMP experiments were used to capture the perfusion behaviour of human liver grafts, a.o. by calculating the liver-specific HA and PV hydraulic input impedances. Impedances were used to tune extended liver-specific electrical analog models of the hepatic perfusion. Future research may focus on broadening the applications of this approach from modelling HMP and natural blood flow to investigating hepatic pathologies and surgical procedures. Furthermore, the acquired impedances may be useful as boundary conditions for numerical models of e.g. the descending aorta, the splanchnic circulation or the portal circulation.

Chapter 8

Modelling the impact of partial hepatectomy on the hepatic haemodynamics using a rat model

This chapter is based on *"Modeling the impact of partial hepatectomy on the hepatic hemodynamics using a rat model"*, as published in IEEE Transactions on Biomedical Engineering, 59(12):3293-3303, 2012 [100].

8.1 Introduction

During the last decades, the number of patients on the waiting list for liver transplantation increased enormously (e.g. from 229 (1991) to 2695 (2010) in the Eurotransplant region [126]). As the number of available grafts did not grow accordingly, this results in a substantial shortage of donor livers. A lot of research therefore aims to enlarge the donor pool, such as the use of sub-optimal grafts, donation after circulatory death donor organs etc. [345]. In addition to total donor organs, the usage of split liver transplantation [205] is being investigated as well as living donor liver transplantation (LDLT) [152].

In the LDLT procedure, a healthy donor undergoes a partial hepatectomy, resulting in a part of his liver being transplanted into a patient with severe liver failure. During a post-transplant period of a few months, both donor and recipient usually regain a normal liver mass due to liver regeneration. However, LDLT-induced complications (such as cholestasis, ascites, gastrointestinal bleeding, renal impairment etc.) may occur in the donor as

well as the recipient [65]. If the remaining liver mass is too small compared to the total body mass, LDLT can lead to the small-for-size syndrome (SFSS; see also section 3.2.3.2) and tremendously hamper survival chances of both donor and recipient [140, 151, 153, 163, 218, 462, 513]. A typical complication of SFSS is portal hypertension, caused by a higher vascular resistance of the hepatectomised liver in comparison with the total liver before resection. Moreover, the portal venous (PV) inflow per gram of liver tissue is higher in the remnant liver than in the total liver before resection [431]. This is typically associated with higher intravascular shear stress [86, 114], which is necessary to trigger liver regeneration after hepatectomy [415, 513]. Nevertheless, excessive hyperperfusion and shear stress effects may irreversibly damage endothelial cells of the microvascular sinusoids and lead to graft dysfunction [65, 140]. In addition to LDLT, other procedures involving partial hepatectomy (e.g. split liver transplantation, liver resection due to hepatocellular carcinoma etc.) may also lead to similar complications.

Previous studies concerning the haemodynamic impact of liver hepatectomy mainly focused on an experimental approach, often using lab animals such as rodents (rats) or pigs [86, 106, 114, 131, 140, 145, 242, 280, 284, 298, 313, 314, 348]. Some other studies focused on virtual planning and modelling of LDLT procedures [423, 514]. Yamanaka et al. [514] developed software to virtually predict graft volumes and corresponding drainage volumes based on CT images. Similarly, Selle et al. [423] presented methods to plan surgical interventions based on vascular territories determined by a geometrical and structural analysis of the vascular trees. Although some other studies provide insights into how to possibly overcome hepatectomy-related complications using e.g. portocaval shunts, splenectomy etc. [114, 314, 472, 512], there is no consensus on how to prevent or treat the complications in the best way, and how to predict the optimal resection volumes and locations in the liver [151].

The aim of this study was to gain more insight into the influence of a partial hepatectomy on the liver haemodynamics. Detailed anatomical data of rat livers were obtained using a vascular corrosion casting technique. Afterwards, these data were applied to build an electrical analogue to model the blood circulation before and after partial hepatectomy (total liver versus resected liver) using different sets of boundary conditions. Hereby, we aim to model the moment immediately after hepatectomy, a haemodynamic snapshot which might set the trigger for an evolution towards either liver regeneration (recovery) or liver failure (due to SFSS complications).

8.2 Materials and Methods

8.2.1 Vascular corrosion casting of rat livers

Two female Wistar rats (albino, age of 10 weeks) with a body weight of 200-225 g (Harlan Laboratories Inc., Indianapolis, US) were used. Both rats were euthanised by an intraperitoneal injection of 1 ml of a solution containing 0.2 ml Xylazine Hydrochloride (Xyl-M 2%; V.M.D., Arendonk, Belgium) and 0.8 ml Ketamine Hydrochloride (Anesketin 10%; Eurovet, Bladel, the Netherlands). Subsequently, the abdomen was opened. The first rat was cast via a cannula inserted in the abdominal aorta with a resin (Batson's #17; Polysciences, Florida, USA) including a red colouring dye and a contrast agent (barium sulfate; Micropaque, Delpharm, France). Simultaneously, the ileocolic vein was injected with a blue coloured resin without contrast agent. As such, the rat liver was cast through resin entering the hepatic artery (HA) and PV, respectively. Subsequently, the injected resins polymerised (approximately two hours) and the tissue was macerated in a 25% potassium hydroxide solution during a few days (as more elaborately explained in [93]). Since there were some problems (likely caused by the particle size of the contrast agent) to gather data based on the HA vascular tree of this rat, a second rat was cast exclusively through the arterial side without contrast agent.

Vascular corrosion casting resulted in replicas of the HA, PV and hepatic venous (HV) vascular trees (Fig. 8.1). In both rats, the livers were dissected from the cast specimens to allow more detailed imaging of the liver vasculature by micro-CT scanning.

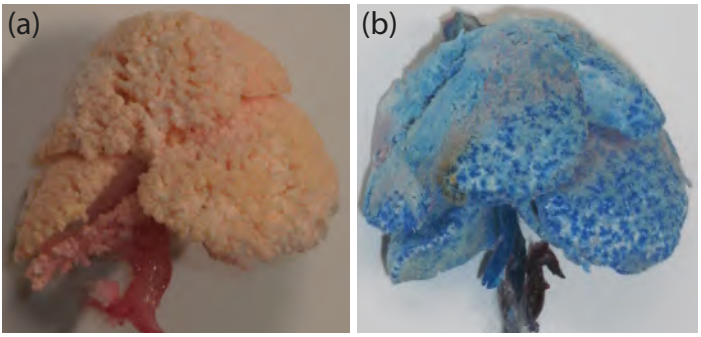

Figure 8.1: (a) Rat liver cast used to study the hepatic arterial (HA) vascular tree; (b) rat liver cast used to study the portal venous (PV) and hepatic venous (HV) vascular trees.

8.2.2 Micro-CT imaging and data acquisition

The liver casts were scanned using a high-resolution micro-CT scanner developed in-house [93] at a resolution of 46.6 µm (Fig. 8.1a) and 50.3 µm (Fig. 8.1b), respectively. The resulting digital datasets were processed using the

software package Mimics (Materialise, Leuven, Belgium). One rat liver cast was used to segment the HA vascular tree (Fig. 8.1a), while the other liver cast enabled studying the PV and HV vascular trees (Fig. 8.1b). As illustrated in Fig. 8.2, the rat liver typically contains 4 major liver lobes (of which 3 are subdivided in 2 sublobes), each corresponding to a certain percentage of the liver weight. The median lobe accounts for 38% of the liver tissue and is divided by a fissure in the right (RML) and left median lobe (LML). The superior (cranial) right lobe (SRL; 12%) and the inferior (caudal) right lobe (IRL; 10%) form the right lobe. In addition, there is the left lateral lobe (LLL; 30%) and the caudate lobe which consists of the anterior (ventral) caudate lobe (AC; 4%), posterior (dorsal) caudate lobe (PC; 4%) and a small paracaval portion called the caudate process (2%, not shown in Fig. 8.2) [312]. Segmentations of the HA, PV, HV vascular trees allowed for the calculation of 3D reconstructions and the separation of the rat liver lobes based on the vasculature (Fig. 8.3).

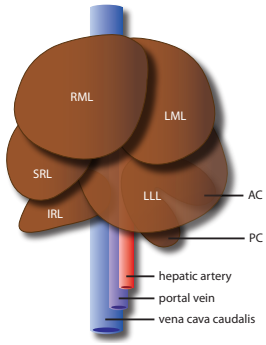

Figure 8.2: Schematic overview of the rat liver with 4 major lobes of which 3 are subdivided in 2 sublobes (with RML the right and LML the left median lobe, SRL and IRL the superior (cranial) and inferior (caudal) right lobe, LLL the left lateral lobe, AC the anterior (ventral) and PC the posterior (dorsal) caudate lobe) and its afferent (hepatic artery and portal vein) and efferent (vena cave caudalis) blood vessels.

After image processing, Mimics was used to calculate the centrelines of the vascular trees (HA, PV and HV) in all liver lobes separately (except for the caudate process which is very small and has no major vessels). Based on these centrelines, the branching topology of all trees (bifurcations, trifurcations and monopodial branches [93, 167]) was analysed and blood vessels were classified into generations. A similar study was performed by Op Den Buijs et al. [52] to classify the rat PV tree. However, they only studied the rat PV vascular tree, while data on the HA and HV trees were also required for our study. Furthermore, classification was performed assuming a purely bifurcating branching topology, while trifurcations and monopodial vessels are also taken into account in our study.

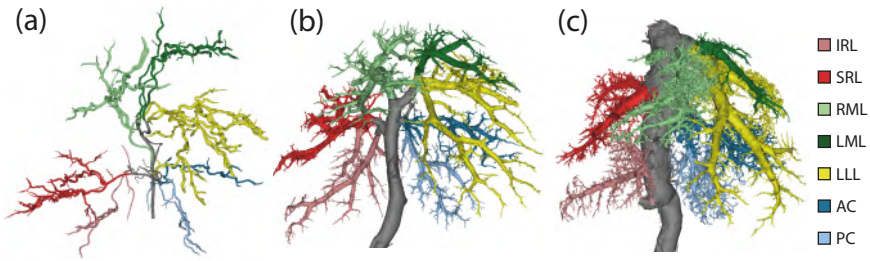

Figure 8.3: 3D reconstructions of the (a) hepatic arterial (HA), (b) portal venous (PV) and (c) hepatic venous (HV) vascular tree. Different colours were used to separate the lobes as explained in the legend with RML the right and LML the left median lobe, SRL and IRL the superior (cranial) and inferior (caudal) right lobe, LLL the left lateral lobe, AC the anterior (ventral) and PC the posterior (dorsal) caudate lobe.

Since rat liver lobes clearly differ in size (Fig. 8.2 and 8.3) and are imaged with a finite spatial resolution, the number of blood vessel generations measured was not equal for all lobes. In the two rat liver casts, the minimum and maximum generation number reached within one lobe was 5, 7, 6 and 6, 10, 7 for the HA, PV and HV tree, respectively. Subsequently, the radii and lengths of all vessels were measured [93]. Geometrical classification allowed for the calculation of the mean radius and length per blood vessel generation of the HA, PV and HV vascular tree, as well as the number of vessels per generation as listed in Table 8.1 (with HA 1, PV 1, HV 1 being the hepatic artery, portal vein and vena cava caudalis, respectively, n the number of vessels per generation, r [mm] the mean radius, l [mm] the mean length, and $\sigma(r)$ and $\sigma(l)$ the corresponding standard deviations). Moreover, data allowed analysing geometrical features on a lobe-specific basis (as illustrated for the PV and HV radii in Fig. 8.4).

Due to the finite spatial imaging resolution, a limited number of vessel generations could be measured. However, data of all generations were necessary to build the electrical model, and hence, extrapolations of the measured data were used to estimate the geometrical properties of lacking generations. Since measured data as a function of generation numbers (Fig. 8.4) clearly showed an exponential-like behaviour (similar to the human data in [93]), an exponential fitting algorithm was implemented in Matlab (Mathworks, Massachusetts, USA). This allowed acquiring lobe-specific exponential trend lines of the geometrical data, as defined in eq. 8.1 with y the geometrical measure (being r, l or n) and j the generation number.

$$y = ae^{b \cdot j} \tag{8.1}$$

Table 8.1: Summary of measurements averaged over the total liver.

Generation	n	r [mm]	$\sigma(\mathbf{r})$ [mm]	l [mm]	$\sigma(\mathbf{l})$ [mm]
HA 1	1	0.27	0	12	0
HA 2	5	0.11	$1.3 \cdot 10^{-2}$	6.3	4.2
HA 3	13	0.11	$2.0 \cdot 10^{-2}$	6.6	3.2
HA 4	32	$9.6 \cdot 10^{-2}$	$1.6 \cdot 10^{-2}$	4.2	2.3
HA 5	30	$7.7 \cdot 10^{-2}$	$1.5 \cdot 10^{-2}$	2.9	1.9
HA 6	8	$6.5 \cdot 10^{-2}$	$5.4 \cdot 10^{-3}$	1.8	0.73
PV 1	1	2.2	0	24	0
PV 2	4	0.71	0.13	3.9	3.4
PV 3	9	0.47	$6.9 \cdot 10^{-2}$	6.6	5.3
PV 4	23	0.36	$7.2 \cdot 10^{-2}$	4.7	2.2
PV 5	49	0.25	$7.2 \cdot 10^{-2}$	3.7	2.6
PV 6	114	0.17	$6.2 \cdot 10^{-2}$	2.1	1.4
PV 7	159	0.11	$2.9 \cdot 10^{-2}$	1.2	0.72
PV 8	136	$7.8 \cdot 10^{-2}$	$2.1 \cdot 10^{-2}$	1.0	0.58
PV 9	101	$7.0 \cdot 10^{-2}$	$7.5 \cdot 10^{-3}$	0.82	0.52
PV 10	204	$4.8 \cdot 10^{-2}$	$7.4 \cdot 10^{-3}$	0.66	0.31
HV 1	1	5.3	0	43	0
HV 2	6	0.87	0.24	14	5.3
HV 3	16	0.43	0.17	5.3	4.8
HV 4	53	0.27	0.13	2.6	1.6
HV 5	122	0.16	$6.9 \cdot 10^{-2}$	1.8	1.1
HV 6	191	0.12	$2.8 \cdot 10^{-2}$	1.3	0.64
HV 7	110	$8.5 \cdot 10^{-2}$	$1.6 \cdot 10^{-2}$	0.95	0.42

Since rat liver lobes substantially differ in dimensions (Fig. 8.1, 8.2 and 8.3), a lobe-specific fitting algorithm was applied. Accordingly, a cost function was minimised to find the optimal a and b values to determine the exponential functions. We use the same value of b for all lobes of the liver, because it was assumed that the exponential power of all lobes is similar and that they mathematically only differ in the initial starting value determined by the a value. The cost function c (eq. 8.2) was based on the least squares

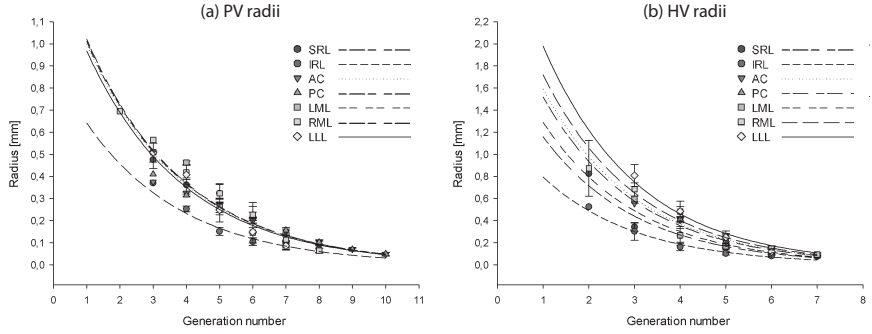

Figure 8.4: Lobe-specific mean radii and corresponding lobe-specific exponential trend lines for the portal venous (PV) and the hepatic venous (HV) vascular tree.

method. In (8.2), i is the lobe number, p the total number of (sub)lobes (being 7 in our study: RML, LML, LLL, SRL, IRL, AC and PC), j the generation number, n_i the number of generations in lobe i, a_i the a value for lobe i, and y_{ij} the average of the geometrical measure for the j^{th} generation of lobe i.

$$c = \sum_{i=1}^{p} \left(\sum_{j=1}^{n_i} (ln(a_i) + b \cdot j - ln(y_{ij}))^2 \right) \tag{8.2}$$

To determine the number of blood vessel generations in every vascular tree of all lobes, the exponential trend lines were extrapolated up to the generation number, for which a radius value corresponding to literature values of terminal vessels, was reached (10 µm for HA arterioles [315], 15 µm for PV venules [315], and 5 µm for the terminal HV generation modelled as being the sinusoids [358]).

8.2.3 Total liver electrical analog models

The total liver model was based on the model of a human liver as described in [93]. Since the rat liver (high variations in lobe size) substantially differs from the human liver concerning the anatomy [312], the model was adapted to be lobe-specific. Consequently, all blood vessel generations of every lobe-specific vascular tree (HA, PV and HV) were modelled using a vascular resistance R_s (eq. 8.3 with μ [$3.5 \cdot 10^{-3} Pa \cdot s$] the dynamic blood viscosity, l [m] the mean length of the generation, n the number of vessels, and r [m] the mean radius). The vascular resistances were calculated using eq. 8.3 based on the measured data and extrapolations of the geometrical data as described in section 8.2.2.

$$R_s = \frac{8\mu l}{n\pi r^4} \left[\frac{Ns}{m^5} \right] \tag{8.3}$$

This resulted in the network of Fig. 8.5a depicting the electrical model of one liver lobe. The serial HA and PV generations, each represented by a resistance, cluster after their terminal generations and run into the HV tree starting with the sinusoids. The sinusoids further drain the blood into the HV tree, which clusters until it reaches the lobe HV outflow. The total rat liver model is separated in HA, PV and HV blocks as schematically illustrated in Fig. 8.5b, based on the topology of the vessels supplying each liver lobe.

The analysis of the model was implemented in Matlab based on the electrical network theory. This allowed analysing the haemodynamics at every lobe-specific generation by calculating pressure drops and flows throughout the total liver.

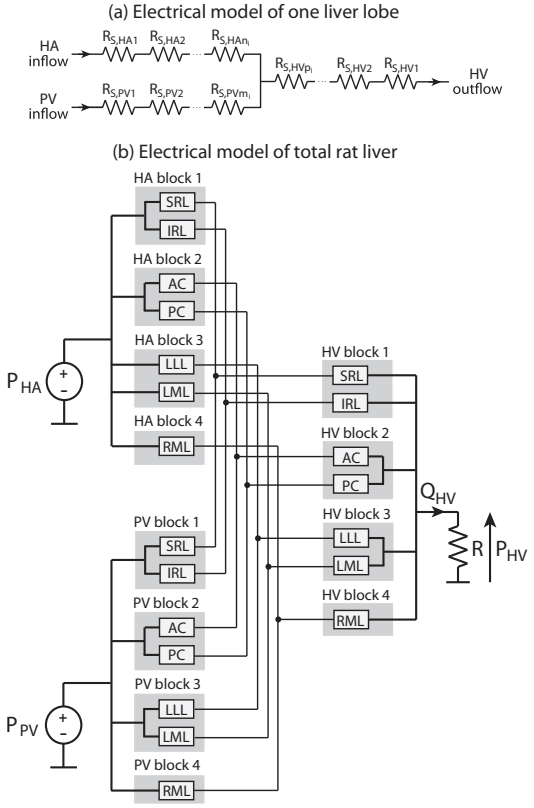

Figure 8.5: (a) Schematic representation of the electrical model of a liver lobe. The lobe model consists of vascular resistances each representing one generation of the hepatic arterial (HA), portal venous (PV) or hepatic venous (HV) vascular tree of the lobe. The blood in the last generation of the HA and PV tree (R_{s,HAn_i} and R_{s,PVm_i}, respectively) flows into the sinusoids depicted by the terminal HV generation (R_{s,HVp_i}), until it reaches the lobe outflow vessel ($R_{s,HV1}$). (b) The block diagram shows a schematic representation of the pressure-controlled total rat liver model. The model is divided in HA, PV and HV blocks based on the branching topology of the blood vessels supplying each liver lobe.

8.2.4 Boundary conditions for the total liver model

Two sets of boundary conditions were used to develop two models of the blood flow through the total liver: a pressure- and a flow-controlled model. A subset of the boundary conditions was defined by using results of *in vivo* rat hepatectomy experiments by Fan et al. according to the surgical procedure as described in [131, 485]. During these experiments, the PV pressure (P_{PV}) and total PV flow ($Q_{PV,total}$) as well as the HA flow ($Q_{HA,total}$) were measured before and after 70%, 80% and 90% hepatectomy (Table 8.2). The other boundary conditions (HA pressure P_{HA} and outlet resistance R) were defined using literature values as described below.

Table 8.2: Haemodynamic measurements of Fan et al. during *in vivo* rat experiments [131] at baseline and immediately after 70%, 80%, 90% hepatectomy.

		P_{PV} [mmHg]	$Q_{PV,total}$ [ml/min]	$Q_{HA,total}$ [ml/min]
Before hepatectomy	**0%**	5.85	7.35	3.17
Immediately after hepatectomy	**70%**	8.18	8.52	0.96
	80%	9.88	6.13	0.62
	90%	10.92	5.78	0.50

8.2.4.1 Pressure-driven model

Fig. 8.5b represents the pressure-driven total liver model, as pressure sources were used at the HA and PV inlets. The applied pressures were P_{HA} = 103 mmHg at the HA [3, 145, 412] and P_{PV} = 5.9 mmHg at the PV inlet (Table 8.2). Moreover, an output resistance R is used at the liver outflow (vena cava caudalis; Fig. 8.2 and 8.5) to represent the vascular resistance of the blood circulation distal from the liver (eq. 8.4 with P_{HV} = 0.90 mmHg the outlet pressure [84] and $Q_{HV,total}$ = 11 ml/min the total outflow, estimated as being the sum of $Q_{HA,total}$ and $Q_{PV,total}$ before resection (Table 8.2)).

$$R = \frac{P_{HV}}{Q_{HV,total}} = 6.1 \cdot 10^{8} \frac{Ns}{m^5} \tag{8.4}$$

8.2.4.2 Flow-driven model

In addition to the pressure-driven model, an adjusted model was developed to obtain flow-control at the PV side. This was done by changing the PV pressure source into a PV flow source $Q_{PV,total}$ of 7.4 ml/min (Table 8.2), while preserving the other boundary conditions as defined above.

8.2.5 Tuning of the total liver model

Both the pressure- and flow-driven model were initially solved and, subsequently, tuned to be in accordance with the pressure and flow measurements performed by Fan et al. [131] for a healthy total rat liver (Table 8.2).

Since results of the initial model showed some differences between model-predicted haemodynamics and those measured by Fan et al. [131] before hepatectomy, the exponential trend lines with the highest degree of uncertainty (mainly due to the finite spatial scanning resolution) were adjusted as in chapter 6 [93] in order to improve the physiological accuracy of the model. This resulted in the a and b values of Table 8.3. First, the HA radius power was adjusted from $b = -1.1 \cdot 10^{-1}$ to $b = -3.3 \cdot 10^{-1}$, and lobe-specific HA a values were also optimised. In addition, powers of the PV and HV number of vessels and the HV lengths exponential trend lines were adjusted from $b = 7.4 \cdot 10^{-1}$ to $b = 8.6 \cdot 10^{-1}$, from $b = 7.3 \cdot 10^{-1}$ to $b = 1.2$, and from $b = -5.9 \cdot 10^{-1}$ to $b = -5.1 \cdot 10^{-1}$, respectively. In the end, the tuned model

counted 11-12, 11-12 and 10-12 generations for the lobe-specific HA, PV and HV vascular trees, respectively. As such, a slightly different number of generations per lobe was possible, since data extrapolations were lobe-specific.

Table 8.3: Lobe-specific *a* and *b* values of the exponential trend lines after model tuning. Bold values were optimised.

Parameter	b	a_{SRL}	a_{IRL}	a_{AC}	a_{PC}	a_{LML}	a_{RML}	a_{LLL}
r_{HA}	**−0.33**	**0.36**	**0.26**	**0.36**	**0.36**	**0.36**	**0.36**	**0.36**
l_{HA}	−0.33	23	29	29	18	23	13	26
n_{HA}	0.91	$8.2 \cdot 10^{-2}$	$7.1 \cdot 10^{-2}$	$5.8 \cdot 10^{-2}$	0.12	0.15	0.21	0.13
r_{PV}	−0.34	1.4	0.90	1.4	1.4	1.4	1.4	1.4
l_{PV}	−0.31	14	14	12	12	16	12	22
n_{PV}	**0.86**	0.16	0.17	$6.8 \cdot 10^{-2}$	$7.9 \cdot 10^{-2}$	0.11	0.12	0.20
r_{HV}	−0.49	1.9	1.3	2.6	2.5	2.1	2.8	3.2
l_{HV}	**−0.51**	23	15	34	33	31	28	39
n_{HV}	**1.2**	0.11	0.19	$4.2 \cdot 10^{-2}$	$3.8 \cdot 10^{-2}$	$3.6 \cdot 10^{-2}$	0.12	$9.1 \cdot 10^{-2}$

8.2.6 Resected liver electrical analog models

In literature, different techniques are described to perform *in vivo* partial rat liver hepatectomy. For instance, Vanheule et al. [485] and Fan et al. [131] resected the LML, RML, LLL, IRL, AC and PC to do a 90% resection, while in contrast, Dahmen et al. [86] removed the LML, RML, LLL, SRL and IRL (Fig. 8.2). In this study, the resection method of Fan et al. [131] was applied virtually to the 3D reconstructions of the vascular trees. Consequently, a resection of 70% corresponds with the removal of the LML, RML and LLL (Fig. 8.2). A 80% resection corresponds with the additional removal of the IRL, and in the case of a 90% resection, the AC and PC lobes are also removed. Additionally, the 90% hepatectomy method of Dahmen et al. [86] was also simulated to compare with the results of Fan et al. [131].

Boundary conditions were adapted (as defined below) and the vascular resistances R_s of resected liver lobes were set to infinity. The latter resulted in a zero flux through the resected lobes.

8.2.6.1 Pressure-driven models

For the pressure-driven LDLT model, only the P_{PV} was changed to be equal to the P_{PV} measurements immediately after hepatectomy by Fan et al. [131], being 8.2 mmHg, 9.9 mmHg and 11 mmHg for the 70%, 80% and 90% partial hepatectomy simulations, respectively (Table 8.2).

8.2.6.2 Flow-driven models

The boundary conditions for the flow-driven resected liver model were equal to those of the flow-driven total liver model. In this way, the $Q_{PV,total}$ of the resected liver was set equal to the $Q_{PV,total}$ measured before resection, being 7.4 ml/min.

8.3 Results

8.3.1 Total liver model

Results of the total liver model are equal for the pressure- and the flow-controlled model (Fig. 8.6), since they are both tuned to correspond to the experimental measurements before hepatectomy performed by Fan et al. [131] (Table 8.2).

Pressure profiles (Fig. 8.6a) show similar trends for the different rat liver lobes. The pressure drop is hereby largest in the HA tree before the sinusoids (from 103 mmHg to a mean value of 3.2 mmHg). In parallel, the pressure drops from 5.9 mmHg to a mean value of 3.2 mmHg in the PV tree. The pressure after the last HA and PV generation of every individual lobe is thus equal. At this location, the blood enters the sinusoids which cluster until they reach the HV and the vena cava caudalis at a pressure of 0.90 mmHg. When looking closer to the sinusoidal pressure in the lobes (Fig. 8.6a), there is a pressure range of 2.0 mmHg (LLL) to 4.8 mmHg (LML) at the entrance of the sinusoids and 1.8 mmHg (LLL) to 3.9 mmHg (LML) at the outlet of the sinusoids.

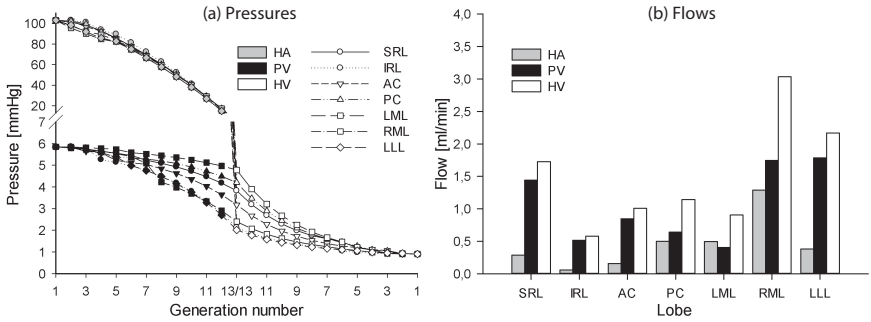

Figure 8.6: Results of the total rat liver model: (a) lobe-specific pressure profiles as a function of the hepatic arterial (HA), portal venous (PV) and hepatic venous (HV) generation numbers; (b) lobe-specific HA, PV and HV flows ($Q_{HA,lobe}$, $Q_{PV,lobe}$, $Q_{HV,lobe}$).

There is a $Q_{HA,total}$ into the liver of 3.2 ml/min and a $Q_{PV,total}$ of 7.4 ml/min. This results in a $Q_{HV,total}$ of 11 ml/min, which is the sum of $Q_{HA,total}$ and $Q_{PV,total}$. In contrast to the overall pressure profiles, there is a clear difference in the lobe-specific flows (Q_{lobe}; Fig. 8.6b). This seems to be logical, since smaller liver lobes have a higher vascular resistance, resulting in a smaller inflow when experiencing similar pressure drops. Q_{lobe} varies between $6.0 \cdot 10^{-2}$ ml/min (IRL) and 1.3 ml/min (RML) for the HA tree, between 0.41 ml/min (LML) and 1.8 ml/min (LLL) for the PV tree, and between 0.58 ml/min (IRL) and 3.0 ml/min (RML) for the HV tree.

8.3.2 Resected liver models

Virtual resections lead to 3D reconstructions of the vascular trees after a 70%, 80% or 90% hepatectomy, as demonstrated in Fig. 8.7 for the PV tree. Results of the resected liver electrical models are depicted in Fig. 8.8 for the pressure-controlled models and Fig. 8.9 for the flow-controlled models.

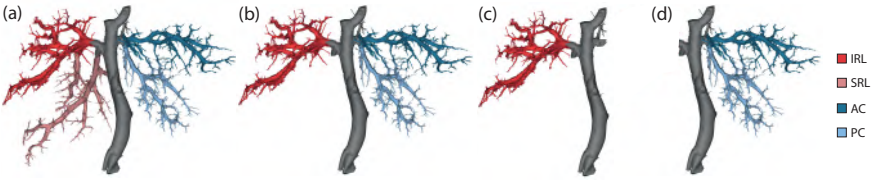

Figure 8.7: Illustration of the virtual resections with the portal venous (PV) vascular tree for a (a) 70%, (b) 80% and (c) 90% hepatectomy as performed by Fan et al. [131], and a (d) 90% hepatectomy as performed by Dahmen et al. [86] (with SRL and IRL the superior (cranial) and inferior (caudal) right lobe, AC the anterior (ventral) and PC the posterior (dorsal) caudate lobe).

8.3.2.1 Pressure-controlled models

The pressure-driven model results in increased pressures throughout the PV vascular tree (Fig. 8.8a-c) compared to the total liver model (Fig. 8.6a). As such, the PV pressure drops from 8.2 mmHg, 9.9 mmHg, 11 mmHg at the PV inlet to a mean value of 4.1 mmHg, 5.4 mmHg, 6.3 mmHg at the entrance of the sinusoids for a 70%, 80% and 90% resection, respectively. Consequently, the lobe-specific pressure at the entrance of the sinusoids increases to a range of 2.4-5.3 mmHg, 4.7-6.2 mmHg and 6.3 mmHg for a 70%, 80% and 90% hepatectomy, respectively, compared to the lower range before surgery (see 8.3.1).

On the other hand, $Q_{HV,total}$ was smaller after hepatectomy than before, and is almost equal for the 70% and 80% resection (6.6 ml/min and 6.9 ml/min, respectively), but clearly smaller for the 90% resection (3.6 ml/min). This trend was also noticed for $Q_{PV,total}$: 5.6 ml/min, 6.0 ml/min and 3.3 ml/min for a 70%, 80% and 90% partial hepatectomy, respectively. $Q_{HA,total}$ decreased in successive resections (1.0 ml/min, 0.93 ml/min and 0.28 ml/min for a 70%, 80% and 90% resection, respectively). When looking at Q_{lobe} (Fig. 8.8d-f), it becomes clear that $Q_{PV,lobe}$ and $Q_{HV,lobe}$ in all remaining lobes are increasing when performing resections of more liver mass. As such, $Q_{PV,lobe}$ was 0.80-2.3 ml/min, 1.4-2.9 ml/min and 3.3 ml/min after a 70%, 80% and 90% partial hepatectomy, respectively, while $Q_{HV,lobe}$ ranged between 0.86-2.6 ml/min, 1.8-3.1 ml/min and 3.6 ml/min. In contrast, $Q_{HA,lobe}$ was almost equal before and after hepatectomy (with only a very small decrease).

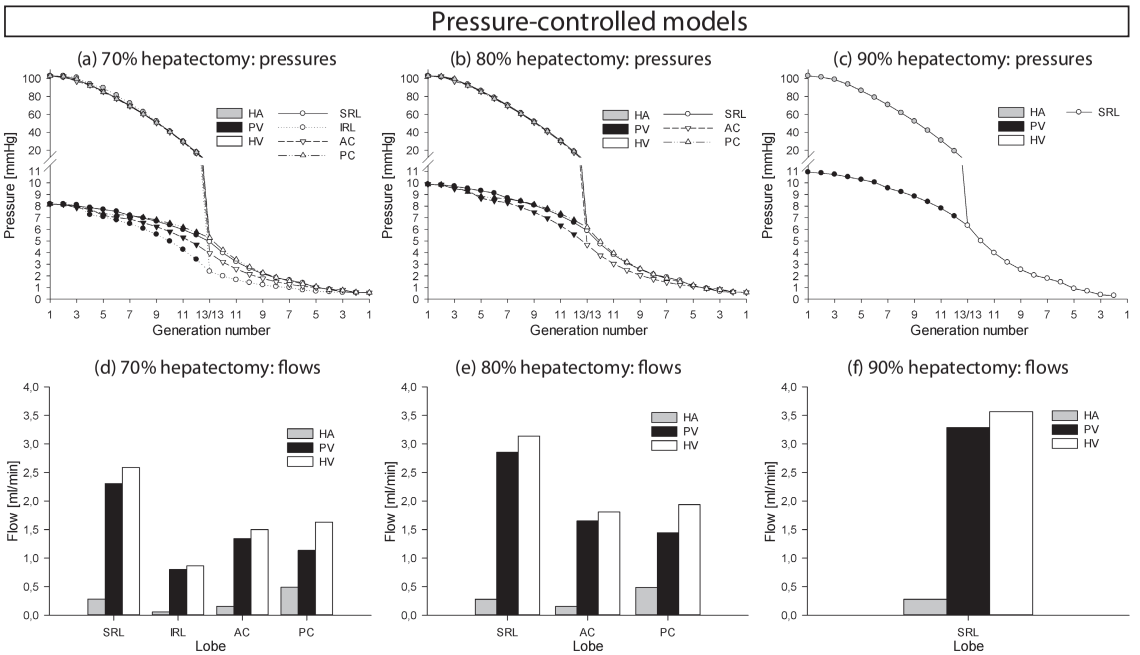

Figure 8.8: Results of the pressure-controlled resected liver models: pressure profiles for a (a) 70%, (b) 80% and (c) 90% hepatectomy as performed by Fan et al. [131]; hepatic arterial flow ($Q_{HA,lobe}$), portal venous flow ($Q_{PV,lobe}$) and hepatic venous flow ($Q_{HV,lobe}$) through the remaining liver lobes separately in case of a (d) 70%, (e) 80% and (f) 90% hepatectomy.

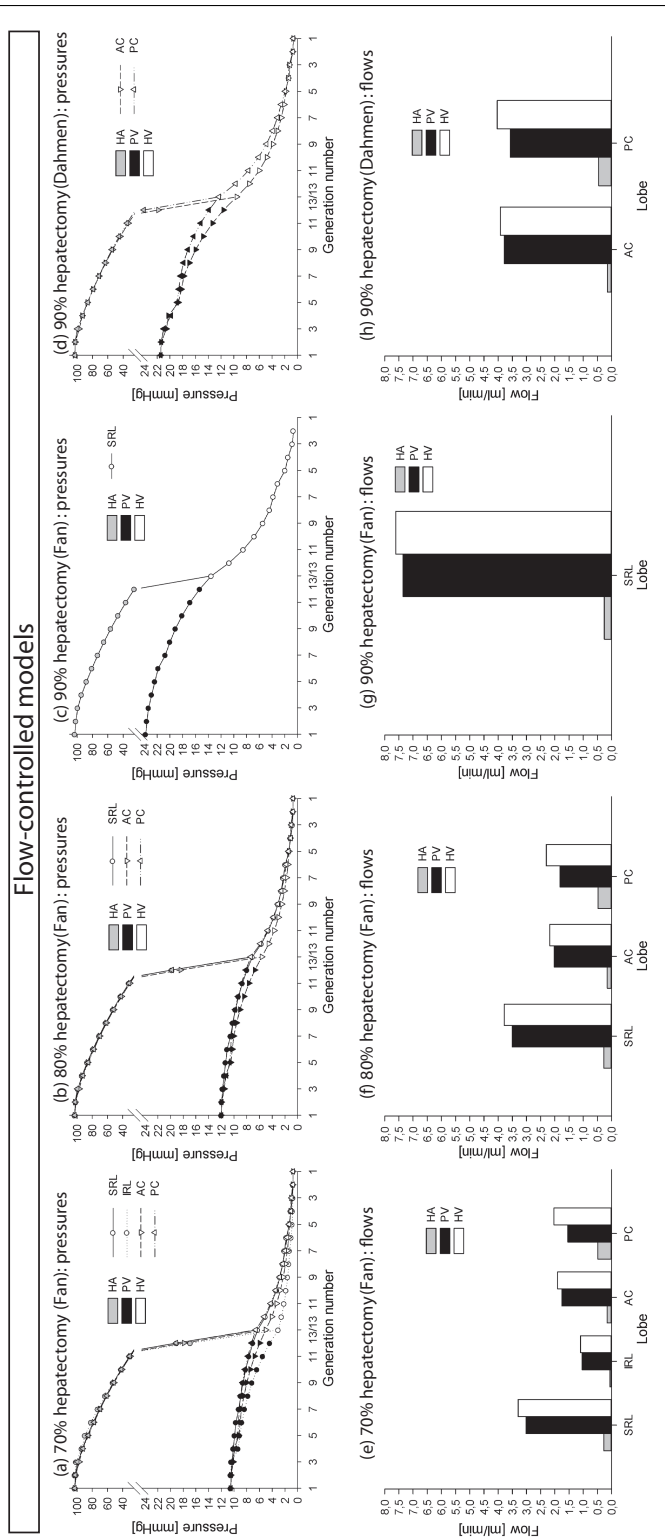

Figure 8.9: Results of the flow-controlled resected liver models: pressure profiles for a (a) 70%, (b) 80%, (c) 90% hepatectomy as performed by Fan et al. [131], and for a (d) 90% hepatectomy as performed by Dahmen et al. [86]; hepatic arterial flow ($Q_{HA,lobe}$), portal venous flow ($Q_{PV,lobe}$) and hepatic venous flow ($Q_{HV,lobe}$) through the remaining liver lobes separately in case of a (e) 70%, (f) 80% and (g) 90% hepatectomy as performed by Fan et al. [131], and for a (h) 90% hepatectomy as performed by Dahmen et al. [86].

8.3.2.2 Flow-controlled models

The flow-controlled model results in a more distinct rise of the PV pressure (Fig. 8.9a-c) in comparison with the pressure-controlled model. PV pressure ranges from 11 mmHg, 12 mmHg, 23.8 mmHg at the PV inlet to a mean pressure of 5.2 mmHg, 6.7 mmHg, 14 mmHg at the entrance of the sinusoids for a 70%, 80% and 90% resection, respectively. Sinusoidal pressure elevations are more pronounced with 3.0-6.6 mmHg, 5.6-7.4 mmHg, and 14 mmHg for a 70%, 80% and 90% resection, respectively.

Concerning the flows (Fig. 8.9e-g), $Q_{HA,total}$ seemed to decrease again in case of resections of more liver mass to 0.98 ml/min, 0.92 ml/min and 0.26 ml/min for a 70%, 80% and 90% resection, respectively. $Q_{PV,total}$, however, is determined by the PV boundary conditions (7.4 ml/min for all cases). $Q_{HV,total}$ was 8.3 ml/min, 8.3 ml/min and 7.6 ml/min after 70%, 80% and 90% hepatectomy, respectively. $Q_{HA,lobe}$ ranges were $6.0{\cdot}10^{-2}$ – 0.49 ml/min, 0.16 – 0.48 ml/min and 0.26 ml/min for a 70%, 80% and 90% hepatectomy, respectively. In contrast, $Q_{PV,lobe}$ was clearly increasing to 1.0 – 3.0 ml/min, 1.8 – 3.5 ml/min and 7.4 ml/min for a 70%, 80% and 90% hepatectomy, respectively. $Q_{HV,lobe}$ was also increasing: 1.1 – 3.3 ml/min, 2.2 – 3.8 ml/min, 7.6 ml/min for a 70%, 80% and 90% hepatectomy, respectively.

In addition, the flow-controlled model was used to simulate the haemodynamic effects of a 90% resection as performed by Dahmen et al. [86]. Fig. 8.9d and h depict the results of the remaining AC and PC lobe. In comparison with the results of the 90% resection method of Fan et al. [131] (Fig. 8.9 and 8.10), this approach results in slightly lower P_{PV} (21 mmHg) and sinusoidal pressures (9.5 mmHg and 12 mmHg), but an almost threefold $Q_{HA,total}$ (0.61 ml/min). $Q_{PV,total}$ and $Q_{HV,total}$ were 7.4 ml/min and 8.0 ml/min, respectively. $Q_{HA,lobe}$, $Q_{PV,lobe}$ and $Q_{HV,lobe}$ were 0.15 – 0.46 ml/min, 3.6 – 3.8 ml/min and 3.9 – 4.0 ml/min, respectively.

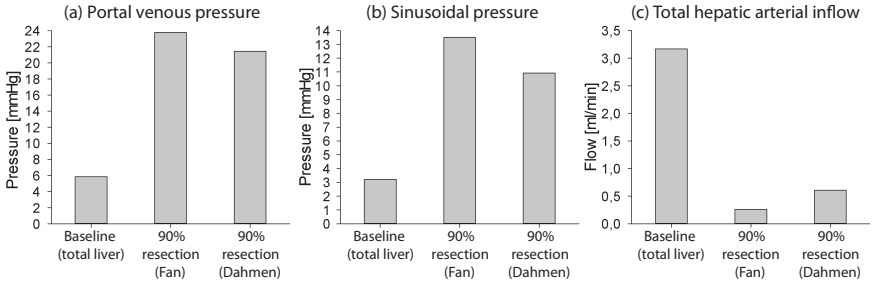

Figure 8.10: Comparison of simulation results for baseline conditions and 90% resection as performed by Fan et al. [131] and Dahmen et al. [86]: (a) portal venous pressure (P_{PV}) and (b) mean sinusoidal pressure, (c) hepatic arterial flow ($Q_{HA,total}$).

8.4 Discussion

8.4.1 Interpretation of the results

In this study, detailed anatomical data of the rat liver vasculature were obtained by a combination of vascular corrosion casting and high resolution micro-CT scanning. Geometrical data (up to 10 generations) showed exponential relations with the generation number, and accordingly, enabled extrapolating the measurements. Subsequently, the blood flow through the rat liver was simulated and tuned using a lobe-specific pressure- as well as flow-controlled electrical analog model. Virtual resections of 70%, 80% and 90% liver mass were performed and modelled to compare normal liver haemodynamics with those of resected livers.

When comparing results of the pressure- and flow-driven models (Fig. 8.8 and 8.9), it is clear that haemodynamic LDLT effects (hyperperfusion resulting in portal hypertension and SFSS complications) are more pronounced in the flow-controlled model. Flow-driven resection models resulted in P_{PV} and sinusoidal pressures up to 24 mmHg and 14 mmHg, respectively, while the pressure-driven model resulted in more moderate LDLT effects (P_{PV} and sinusoidal pressures up to 11 mmHg and 6.3 mmHg, respectively). Furthermore, $Q_{PV,lobe}$ and $Q_{HV,lobe}$ only moderately increased in case of pressure-control (Fig. 8.8), while a more severe rise, as described in literature [114, 145, 242, 280], was observed with flow-control (Fig. 8.9).

An advantage of flow-control is that the PV boundary condition (7.4 ml/min) is equal for every case (total liver versus resection). Practically, this means that an equal $Q_{PV,total}$ is imposed into the liver before and after hepatectomy, as was also found in [145, 280].

In the end, the flow-driven model seems to correspond more closely with the clinically observed hyperperfusion and SFSS effects (e.g. an increased PV flow relative to the remnant liver weight), and is therefore preferred over the pressure-controlled model to predict the impact of LDLT on the hepatic haemodynamics.

More extensive liver partial hepatectomy results in more severe LDLT effects as can be seen in Fig. 8.8 and 8.9. When focussing on the flow-controlled models (Fig. 8.9), a 70%, 80%, 90% hepatectomy increases the baseline P_{PV} by 4.7 mmHg, 6.2 mmHg, 18 mmHg and the sinusoidal pressure by 2.0 mmHg, 3.5 mmHg, 10 mmHg, respectively. In addition to elevated pressures, 70%, 80% and 90% hepatectomy increases $Q_{HV,lobe}$, e.g. for the SRL lobe by 1.6 ml/min, 2.1 ml/min, 5.9 ml/min, respectively. As such, a 70% and 80% hepatectomy results in an approximately two-fold increase of the P_{PV} as well as the $Q_{PV,SRL}$ and $Q_{HV,SRL}$ in comparison with the total liver. A 90% resection results in more severe elevations of these parameters approximately by a factor 4. This is in good agreement with Eipel et al. [114]

who observed an approximately fourfold increase of the PV flow relative to liver weight in the case of a 90% resection during *in vivo* rat experiments.

Since sinusoids are very prone to higher flows and the thereby induced higher shear stresses, one of the key issues in LDLT complications is damage at the endothelial lining of the sinusoids by hyperperfusion [86, 114, 415]. Yagi et al. [513] performed a human follow up study on 32 adult recipients who underwent LDLT, and reported that PV pressures higher than 20 mmHg (as is the case in the 90% resection model) were associated with poor survival. In the context of these findings and based on our results, we hypothesise that a 90% hepatectomy induces very severe hyperperfusion effects, damaging the microcirculation. In contrast, 70% and 80% resection might also induce SFSS effects, but are less explicit. This also corresponds to the findings of Fan et al. [131], who stated that 90% resections were most of the time lethal in case of their experiments, but resections of 70% and 80% were not. Other studies also report low survival rates when performing 90% hepatectomy: 31% [145] and 27% [114]. Interestingly, Dahmen et al. [86] mentioned that 95% resection showed 50% survival and 97 % hepatectomy was lethal, and hence, a 90% hepatectomy was not lethal in their approach. Simulation of the 90% resection technique of Dahmen et al. [86] resulted in slightly lower PV and sinusoidal pressures than for Fan et al. [131] (Fig. 8.9 and 8.10): sinusoidal pressures of 9.5 mmHg (AC) and 12 mmHg (PC) instead of 14 mmHg (SRL). Moreover, the simulated $Q_{HA,total}$ (0.61 ml/min) was approximately the threefold of the simulated $Q_{HA,total}$ (0.26 ml/min) using the method of Fan et al. [131], resulting in more oxygen-enriched blood flowing into the liver. Consequently, the difference in survival outcome between the results of Fan et al. [131] and Dahmen et al. [86] could be as a result of the choice of lobes resected by Dahmen et al., rather than the surgical techniques employed.

8.4.2 Comparison of results with literature

In literature, several studies have been published concerning rat liver hepatectomy experiments [86, 106, 114, 131, 145, 242, 280, 284, 298, 313, 314, 348]. Pressure and flow measurements at baseline, 67-70% and 90% hepatectomy conditions of the most relevant studies are summarised in Table 8.4. Flows, reported in other units than ml/min, were converted to ml/min by assuming a rat body weight of 200 g and a total rat liver weight of 10 g at baseline conditions (liver weight is approximately equal to 5% of the rat body weight [312]). For a 67%, 70% and 90% resection, rat liver weight was assumed to be 3.3 g, 3 g and 1 g, respectively. Note the wide range of data: at baseline for instance, $Q_{PV,total}$ ranges from 4.7 ml/min [145] to 16 ml/min [114]. Hence, the studies show no clear consensus concerning haemodynamic parameters.

Table 8.4: Comparison of the results of the flow-controlled model with several partial hepatectomy studies on rat livers for baseline conditions, 67-70% and 90% resection. Flows, reported in other units than ml/min, were converted to ml/min (‡) and their originally reported values were put in brackets.

	Parameter	Flow-control model	Fan [131]	Lee [280]	Karran [242]	Morsiani [348]	Dahmen [86]	Fukuchi [145]	Eipel [114]
Baseline	$Q_{PV,total}$ [ml/min]	7.35	7.35	15.7 ± 3.2* (1.57 ± 0.32 /g liver)			15	4.66 ± 0.32* (23.3 ± 1.6 /kg body weight)	16 ± 1* (1.6 ± 0.1 /g liver)
	$Q_{HA,total}$ [ml/min]	3.17	3.17					0.74 ± 0.16* (3.7 ± 0.8 /kg body weight)	2.1 ± 0.1* (0.21 ± 0.01 /g liver)
	$Q_{HV,total}$ [ml/min]	10.52			25.1 ± 1.7			5.4 ± 0.34* (27.0 ± 1.7 /kg body weight)	±19* (±1.9 /g liver)
	P_{PV} [mmHg]	5.85	5.85	7.5 ± 1.1		±9.2	7	7.7 ± 1	
	P_{HA} [mmHg]	103					±110	103 ± 11	
	P_{HV} [mmHg]	0.90				±2.8	0.7 – 1.2		
67-70% hepatectomy	$Q_{PV,total}$ [ml/min]	7.35	8.52	11.48 ± 3.43* (3.48 ± 1.04 /g liver)			±9		±10.5* (±3.5 /g liver)
	$Q_{HA,total}$ [ml/min]	0.98	1.00						±0.60* (±0.20 /g liver)
	$Q_{HV,total}$ [ml/min]	8.33			22.5 ± 2.2				±12* (±4.0 /g liver)
	P_{PV} [mmHg]	10.53	8.18	11.1 ± 1.2		±12.9	±10.5		
	P_{HA} [mmHg]	103					±90		
	P_{HV} [mmHg]	0.71				±0.96	0.7 – 1.2		
90% hepatectomy	$Q_{PV,total}$ [ml/min]	7.35	5.78				±7	4.74 ± 0.42* (24.7 ± 2.2 /kg body weight)	±6.0* (±6.0 /g liver)
	$Q_{HA,total}$ [ml/min]	0.26	0.50					0.46 ± 0.19* (2.4 ± 1.0 /kg body weight)	±0.15* (±0.15 /g liver)
	$Q_{HV,total}$ [ml/min]	7.61						4.58 ± 0.23* (24.0 ± 1.2 /kg body weight)	6.0 ± 1.0* (6.0 ± 1.0 /g liver)
	P_{PV} [mmHg]	23.79	10.92				12.5	11.1 ± 1.5	
	P_{HA} [mmHg]	103					±75	100 ± 10	
	P_{HV} [mmHg]	0.65					0.7 – 1.2		

It is however important to keep in mind that differences in the experimental setups (rat breed, age, gender, weight, hepatectomy techniques such as stepwise resections versus one resection per animal, etc.) probably have a non-negligible impact on the reported measurements.

Results after partial hepatectomy agree on a significant increase of the PV and HV flow per g liver mass, but a slight decrease of HA flows (Table 8.4) as is also the case in our LDLT model for the lobe-specific flows. Concerning $Q_{PV,total}$, some studies state a decreasing $Q_{PV,total}$ when performing resections, while Fukuchi et al. [145] and Lee et al. [280] report an approximately equal $Q_{PV,total}$ before and after hepatectomy (as is also assumed in our LDLT model). In contrast, there is consensus on the fact that $Q_{HA,total}$ and $Q_{HV,total}$ (slightly) decrease when resecting liver tissue.

Concerning pressures, Fukuchi et al. [145] showed approximately constant P_{HA} before and after LDLT (as was also stated in [114] and assumed in the model), while Dahmen et al. [86] observed significant P_{HA} pressure drops when performing stepwise resections. P_{HV} seem to be in the same order of magnitude between studies. However, P_{PV} range from 8.2 mmHg to 12.9 mmHg and from 10.9 mmHg to 12.5 mmHg for a 70% and a 90% hepatectomy, respectively.

The flow-controlled model shows relatively good accordance with the reported values for a 70% and 90% hepatectomy, except for an overestimation of the P_{PV} (23.8 mmHg) for a 90% hepatectomy. This may be due to the sinusoidal dilatation effect evoked by hyperperfusion [86, 145] resulting in an increased permeability of the sinusoidal endothelium [348]. As such, Dahmen et al. [86] reported a significant increase in sinusoidal diameter when performing stepwise hepatectomy, most explicitly after 90% hepatectomy. As a result, 23.8 mmHg may be an overestimated P_{PV} for a 90% resection, since the sinusoidal dilatation effect is not incorporated into the model. However, the model hereby clearly illustrates the severe haemodynamic impact of 90% hepatectomy with harmful hyperperfusion effects leading to critical small-for-size complications. Consequently, we can interpret the flow-controlled model as the 'worst case scenario' simulation when performing a partial hepatectomy. In addition, it illustrates that a 90% partial hepatectomy rather than a 70% or 80% hepatectomy should be considered as a proper (experimental) model for SFSS in rats.

8.4.3 Limitations

Though the liver vasculature was studied in detail, there were some limitations. Since the HA tree typically had the smallest vessel radii, this led to some difficulties to segment and quantify HA vessels with the initial dual-cast rat liver. This was probably caused by the particle size of the contrast agent, getting trapped in the smaller HA generations. Eventually, the dual

cast was used to study the PV and HV tree. In addition, a new HA cast was obtained by injecting a second rat liver only through the arterial side without contrast agent, and the HA tree could be segmented. However, HA were small compared to the finite resolution and radius measurements of subsequent HA generations were close to each other. This resulted in an extrapolation to 19 HA generations, which is a high number compared to the 12 PV generations, especially knowing that the HA and PV trees approximately run parallel and count a similar number of generations. Subsequently, the HA exponential trend lines were corrected to correspond with 12 HA generations. In addition, the last measured PV and HV generations were also at the resolution limits. To overcome these problems (as also described in [93]), n_{PV}, n_{HV} and l_{HV} exponential equations were tuned (section 8.3.1; Table 8.3).

As this study was based on data coming from only one HA, PV and HV vascular tree, it is important to keep in mind that the findings in this study are indicative. For instance, anatomical variations are possible within the same rat breed, which implies that this may have an influence on the results as is also illustrated in the literature overview of section 8.4.2. Using more rat livers may thus result in more accurate predictions using the models.

In this study, an electrical analog model is used solely based on vascular resistances. Though this is a simplification of the original model (which includes elasticity and inertia effects [93]), it was justified in this case because our main interest was to analyse the DC model to obtain mean pressure and flow profiles throughout the liver generations. Since signal amplitudes (AC component) caused by the heart frequency are almost absent at the microcirculatory level due to dampening througout the HA tree, DC components of pressure and flow profiles were sufficient to quantify hyperperfusion effects at the level of the microvasculature which are prone to elevated flow and shear stress [93].

The presented hepatectomy model does not include any adaptation and is to be seen as providing a snapshot of the liver's haemodynamic conditions at the moment immediately after partial hepatectomy. This moment is likely to trigger a cascade of both acute and chronic adaptive events determining the evolution of the liver towards either regeneration or failure, which are not included in the model. As such, a potential extension of the model might be to incorporate liver adaptation and remodelling as a function of time.

8.4.4 Future perspective

These models may be tuned for the human liver by repeating the presented modelling approach in the human setting. As such, models may be helpful in predicting patient outcomes in the case of a partial hepatectomy. Moreover, the models could also be applied in other contexts, for which liver resections

are required: split liver transplantation, liver resections due to hepatocellular carcinoma etc.

8.5 Conclusion

In conclusion, our model indicates that a 90% hepatectomy leads to an approximately fourfold rise of $Q_{PV,lobe}$ and $Q_{HV,lobe}$, which may damage the microvasculature. The model may be applicable in the human context and help to optimise surgical planning for partial hepatectomy procedures.

Three

The hepatic microcirculation: from imaging the sinusoidal geometry to microscale CFD models

Chapter 9

Perfusion characteristics of the human hepatic microcirculation based on 3D reconstructions and CFD analysis

This chapter is based on *"Perfusion characteristics of the human hepatic microcirculation based on three-dimensional reconstructions and computational fluid dynamic analysis"*, as published in Journal of Biomechanical Engineering, 134(1), 2012 [98].

9.1 Introduction

The blood flow through the liver is known to be unique and complex, especially at the level of the microcirculation due to the fact that the liver receives blood from the hepatic artery (HA) and the portal vein (PV) (see chapter 1) [303, 317, 318, 321, 324, 409]. The HA and PV vascular trees branch until they reach the microcirculation at the level of the so-called hepatic functional units, typically considered as hexagonal lobules [311, 465, 466]. In this conceptual model, each lobule receives blood from its periphery through the hepatic arterioles and portal venules located in each of the portal triads (Fig. 9.1). At the level of the lobules, HA and PV blood is mixed in the sinusoids (hepatic-specific capillaries) where the metabolic activity and exchange of nutrients, oxygen etc. with the hepatocytes takes place. Subsequently, the blood is drained radially towards the central veins. These veins cluster

until they reach the outflow hepatic veins (HV) and the vena cava inferior [311, 409].

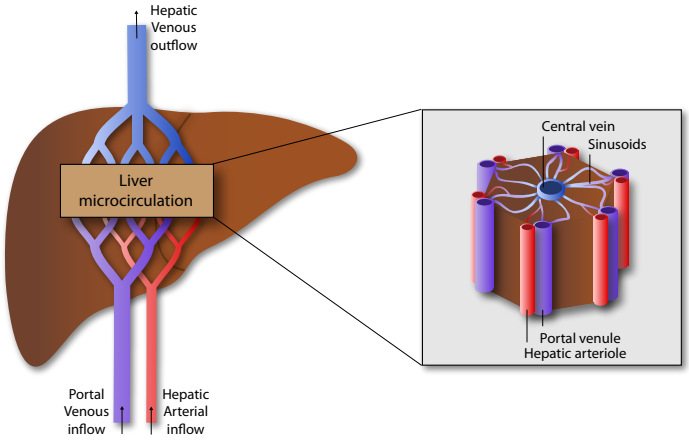

Figure 9.1: The human liver macrocirculation (left) and microcirculation (right). The liver receives blood from the hepatic artery (HA) and portal vein (PV). The HA and PV branch until they reach the level of the microcirculation at the typical hexagonal lobules (right panel). Every lobule receives blood from its periphery through the hepatic arterioles and portal venules. These are located in the portal triads at each corner of the lobule. Consequently, HA and PV blood is mixed in the sinusoids and drained radially towards the central vein. On their turn, the central veins cluster towards the outflow hepatic veins (HV) and vena cava inferior.

Despite the fact that this conceptual model of liver functional units is widely used, liver perfusion is still relatively poorly understood. This has implications for several liver-related research areas. In liver transplantation research, the optimal conditions to preserve and perfuse donor livers, when livers are subjected to (hypothermic) machine perfusion, are still poorly defined [110, 146, 227, 340–342, 389, 458]. Moreover, the haemodynamic influence of complications such as portal hypertension and the small-for-size syndrome induced by living donor liver transplantation is being investigated [140, 151, 462]. In addition, similar questions arise in the case of liver pathologies (cirrhosis, steatosis etc.) influencing the liver perfusion, ablation treatments for hepatocellular tumours, diagnosis etc. [444, 527].

Numerical models may be an important tool to study liver perfusion on different scales (macrocirculation versus microcirculation), and lead to a better understanding of the organ's haemodynamics. Existing liver circulation models, however, mainly focus on the liver macrovasculature, representing the branching of the HA, PV and HV vessels [93, 250, 328, 482, 516]. In contrast, only a few studies have been performed on the liver microcirculation, i.e. the sinusoids between the portal tracts and the central veins

within the lobules (Fig. 9.1). These studies were usually based on idealised geometries and the conceptual hexagonal liver lobule model. Rani et al. [393] studied the hepatic microcirculation using finite volume blood flow simulations in an idealised 3D segment of a hepatic lobule including a terminal HA, PV, HV and fenestrated sinusoidal space. Ricken et al. [402] developed an idealised 2D model of the blood flow through a longitudinal transection of liver lobules using a transverse isotropic permeability in the direction of the central vein. Furthermore, a 2D porous model of the blood flow through a hexagonal lobule transection was developed by Bonfiglio et al. [43], assuming an isotropic permeability and porosity for their first model, and an anisotropic permeability (radial versus circumferential) but isotropic porosity for a second model. Wambaugh et al. [499] and Shah et al. [426] used a graphical model with a discrete topology of the sinusoidal network to simulate the portal to centrilobular mass transfer of chemicals in a virtual tissue representing a hepatic lobule.

The sinusoidal microvasculature is thus often modelled as a porous medium with an isotropic permeability and/or porosity, an assumption which, to our knowledge, has never been validated. In addition, (human) liver microvascular flow has so far only been studied based on idealised geometries. The aim of the present study is to numerically model the blood flow in the human hepatic sinusoidal microcirculation based on micro-CT images of real 3D sinusoidal geometries of a human liver, using computational fluid dynamic methods. Moreover, we investigated whether modelling the hepatic sinusoidal microvasculature as a homogeneous isotropic material is a valid approach by calculating the sinusoidal porosity as well as the permeability tensor of the tissue.

9.2 Materials and methods

This study was executed using a human liver discarded for transplantation after failed rescue allocation by Eurotransplant (Leiden, The Netherlands). As part of research related to machine perfusion preservation of the liver, this study was approved by the Ethical Committee of the University Hospitals Leuven (Belgium) and by the Belgian Liver and Intestine Committee. To obtain the numerical microcirculation model and the corresponding results, several steps were taken as described below: (1) vascular corrosion casting and micro-CT imaging to acquire the sinusoidal geometry; (2) image processing to calculate the 3D morphology; (3) the generation of the meshes for the computational fluid dynamics calculations; (4) defining the boundary conditions for the simulations and post-processing of the data; (5) calculation of the permeability tensor.

9.2.1 Vascular corrosion casting and micro-CT imaging

The human liver used for this study was recuperated from a human donor discarded for transplantation based on strict medical criteria (in this case because of steatosis). Although discarded, the liver showed no evidence of relevant anatomical or vascular differences compared to healthy livers. After resection of the liver from the donor body, the liver was preserved using hypothermic machine perfusion (HMP) as described in [93] and chapter 6. Even though the advantage of HMP is that the microvasculature is kept open and intact, the combination of HMP and casting might have had an effect on the microcirculation. Nevertheless, the dimensions of the sinusoids were in good agreement with the sinusoidal dimensions found in literature [169, 324, 409].

The goal of the vascular corrosion casting procedure was to obtain a replica of the vascular trees of a human liver. A human liver with a normal macroscopic appearance was simultaneously injected with a polymer through the HA and the PV. The injection fluid contained Batson's #17 monomer solution (100 parts), Batson's catalyst (15 parts), Batson's promoter (1 part) (Polysciences, Florida, USA) and monomeric methyl methacrylate (20 parts) (Merck, Darmstadt, Germany). The liver was injected until sufficient quantities of resin were emerging from the HV. Subsequently, all vessels were clamped and the injected fluid polymerised during a period of approximately 2 hours. Afterwards, the liver tissue was macerated in potassium hydroxide (25% KOH) to generate the polymerised vascular replica. More elaborate details about the vascular corrosion casting procedure can be found in [93].

A small volume sample (approximately 2.0 mm x 1.5 mm x 1.7 mm), was dissected from the superior part of the right lobe to study the smallest vessels of the liver. To assure that the sinusoids were sufficiently filled during casting, this sample was imaged by scanning electron microscopy (SEM; JEOL JSM 5600 LV, Jeol, Zaventem, Belgium). This resulted in the SEM image of the geometry shown in Fig. 9.2a. The intertwined and interconnected liver sinusoids are clearly visible, giving evidence of a liver cast of which the microcirculation was clearly filled with the injected polymer. The sample was subsequently imaged with an in-house developed high-resolution micro-CT scanner to obtain the 3D geometry with a resolution of 2.6 μm (see [93] and chapter 6 for more information).

9.2.2 Image processing

The digital micro-CT datasets were processed using the software package Mimics (Materialise, Leuven, Belgium). The dataset was segmented based on its grey values to extract the features of the liver lobules and sinusoids, and a 3D reconstruction was calculated, leading to the visualisation of three

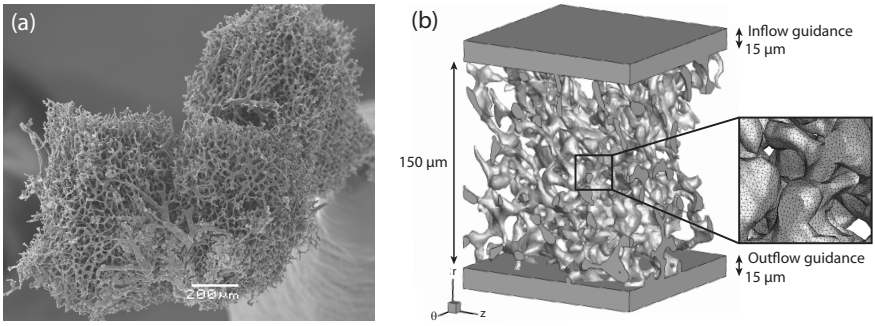

Figure 9.2: (a) Scanning electron microscopic image of the sample that was dissected out of the human liver cast. The intertwined and interconnected liver sinusoids are clearly visible in this cast sample representing three liver lobules. (b) 3D reconstruction of the simulation geometry of the case in which a pressure difference is established in the *r* direction. The origin (0,0,0) is located at the centre of the sample. The inflow and outflow guidances are clearly visible, as well as an illustration of the surface mesh density. The meshes existed of approximately 1 million triangular surface elements and 9 million tetrahedral volume elements capturing the sinusoidal geometrical features.

liver lobules (see Fig. 9.2a) or three primary modules according to Teutsch [465]. Consequently, this dataset was used to investigate the hepatic vascular microstructure and its dimensions by measuring lobule and sinusoid diameters. Because of the total dataset size and computer performance restrictions as well as computational costs, a sample was virtually dissected (Fig. 9.2b and 9.3) by calculating the intersection between a cube with predefined dimensions (0.15 x 0.15 x 0.15 mm^3) and a lobule by using Magics (Materialise, Leuven, Belgium). As such, the fluid domain for the computational fluid dynamics model was created. However, it was not straightforward to identify the individual classical liver lobules in the dataset (hexagonal prism-like structures; Fig. 9.1 and 9.3), since it was difficult to localise the portal triads (consisting of the terminal branches of the HA and PV as well as the intrahepatic bile ductules) at the boundaries of the lobules in a human liver (lobules are clearer delineated by connective tissue in other species such as rat and porcine livers). The final segmentation was based on the identification of the vascular septa in between lobules which appeared brighter on the micro-CT images. This was due to contrast agent particles added to the HA casting injectate. These particles were probably captured before entering the sinusoids because of their particle size and, hence, delineated the lobule boundaries. As illustrated in Fig. 9.3, the dissected cube was oriented such that the origin (0,0,0) was at the centre of the sample and its *z* axis was approximately parallel to the direction of the central vein (i.e. longitudinally according to the liver lobule schematic with a hexagonal prism-like

geometry). In addition, its transections perpendicular to the z axis were located in the area which we considered to be in between the central vein and the HA and PV at the portal triads. This resulted in the r and θ axis being oriented along the radial and circumferential directions, respectively, according to the hexagonal transection of the lobule (Fig. 9.3).

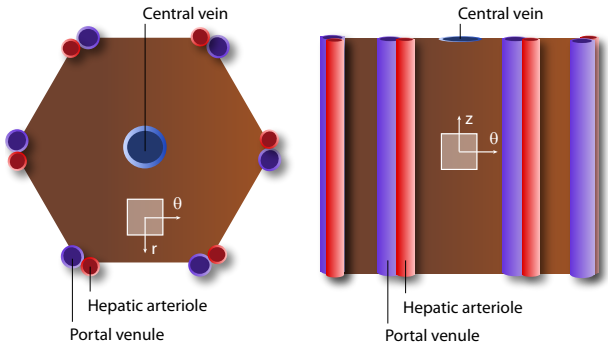

Figure 9.3: Dissection of the sample used for the numerical simulations: transectional (left) and longitudinal side (right) views of a hexagonal lobule with indications of the location of the dissected sample. A cube with dimensions (0.15 x 0.15 x 0.15 mm^3) was dissected of a liver lobule. The dissected cube was oriented in such a way that its z axis was approximately parallel to the direction of the central vein (longitudinal according to the liver lobule). In addition, the r and θ axis were approximately oriented along the radial and circumferential directions, respectively, according to the hexagonal transection of the lobule.

9.2.3 Mesh generation

As we wish to assess the complete permeability tensor of the sample (see also 9.2.5), three computational fluid dynamics cases (and meshes) were developed corresponding to a simulation of flow in the r, θ and z directions, respectively. For each of the setups, a dedicated simulation geometry needed to be created. An inflow and outflow box was added (height being 10% of the sample height) as a flow guidance proximal to the inlet and distal to the outlet, respectively (Fig. 9.2b). This was done to avoid convergence problems caused by too many inlets and outlets, as well as to avoid forcing a predefined flow through the inlet sinusoids [299].

The obtained surface geometries were processed using 3-Matic (Materialise, Leuven, Belgium) to provide good quality surface meshes of the fluid domain. First, noise shells were removed (e.g. a part of a bisected sinusoid which is not attached to the rest of the sinusoidal fluid domain). Subsequently, the meshes were improved by removing double or intersecting triangles and filling small holes which may originate from mesh manipulations. Next, the geometries were remeshed with a maximum triangle edge length of 1.2 µm to capture the morphological features of the geometries

studied, followed by a quality preserving reduction of triangles. To this purpose, some channels with a very small diameter had to be refined because they would otherwise collapse during the remeshing procedure. In a last step, the surface meshes were further manually improved to result in a surface mesh of which all triangles had a skewness less than 0.6. The resulting surface meshes were then exported to TGrid (Ansys, Pennsylvania, USA) to generate volume meshes. The volume meshes consisted of tetrahedral cells with a maximal skewness less than 0.95. The resulting meshes existed of approximately 1 million triangular surface elements and 9 million tetrahedral volume elements clearly capturing the sinusoidal geometrical features (Fig. 9.2b).

9.2.4 Computational fluid dynamics simulations & post-processing

The steady and laminar computational fluid dynamics models were solved using Fluent (Ansys, Pennsylvania, USA). The inlet boundary condition consisted of a flat velocity profile at the top plane of the inflow guidance (plane defined by a r, θ, z coordinate equal to 90 µm for the r, θ, z flow simulation, respectively; see Fig. 9.2). Since there are, to the authors' knowledge, no literature data available on the flow velocities in three orthogonal directions for the human hepatic microcirculation, the applied velocity was estimated by scaling down the total liver blood flow to the flow through the sample studied (eq. 9.1). This was done by using literature values of the average human liver blood flow Q_{liver} (1450 ml/min), the average liver mass m_{liver} (1.4 kg) [311], density ρ (1000 kg/m^3 equal to water) and the dimensions of the sample studied (volume $V_{sample} = 0.15^3$ mm^3; area of inflow plane $A_{sample} = 0.15^2$ mm^2). Using eq. 9.2, this resulted in a velocity inlet v of $2.59{\cdot}10^{-6}$ m/s.

$$Q_{sample} = Q_{liver}\frac{\rho \cdot V_{sample}}{m_{liver}} \tag{9.1}$$

$$v = \frac{Q_{sample}}{A_{sample}} \tag{9.2}$$

As outlet boundary condition, a pressure outlet of 0 Pa was used at the bottom (plane defined by a r, θ, z coordinate equal to -90 µm for the r, θ, z flow simulation, respectively; Fig. 9.2b). The lateral boundaries existing of transected sinusoids were set to symmetry boundary conditions implying no flux perpendicular to these planes. The sinusoidal lumen was modelled as a closed wall (no slip). Blood was modelled as an incompressible Newtonian fluid with a density of 1050 kg/m^3 and a dynamic viscosity μ of $3.5{\cdot}10^{-3}$ Pa·s [482]. Tecplot (Tecplot Inc., Washington, USA) was used to process, calculate and visualise the haemodynamic parameters of interest such as pressure difference, flow velocity, wall shear stress, flow trajectories, etc.

9.2.5 Calculation of the permeability tensor

Subsequently, the permeability tensor K (eq. 9.3; [286]) was assessed to quantify the permeable behaviour of the sinusoidal perfusion in different directions for the dissected sample (Fig. 9.3). The permeability tensor defines the permeability of the tissue in the r, θ or z direction caused by the pressure difference in the r, θ or z direction. For instance, $k_{r\theta}$ specifies the permeability along the r direction due to the pressure difference in the θ direction [286].

$$K = \begin{bmatrix} k_{rr} & k_{r\theta} & k_{rz} \\ k_{\theta r} & k_{\theta\theta} & k_{\theta z} \\ k_{zr} & k_{z\theta} & k_{zz} \end{bmatrix} \tag{9.3}$$

The permeability tensor is calculated based on Darcy's law, which describes the fluid flow through a porous medium (eq. 9.4 with P the pressure [Pa], μ the dynamic viscosity [Pa·s], k the permeability [m²] and v the velocity [m/s]).

$$\vec{v} = -\frac{k}{\mu}\nabla P \tag{9.4}$$

Darcy's law can be rewritten for every pressure difference direction separately inducing fluid flow in the r, θ and z direction. This is illustrated in eq. 9.5-9.7 for a pressure difference in the r direction with L [m] the characteristic length of the sample studied.

$$\frac{\Delta P_r}{L_r} = -\frac{\mu}{k_{rr}} v_r \tag{9.5}$$

$$\frac{\Delta P_r}{L_r} = -\frac{\mu}{k_{\theta r}} v_\theta \tag{9.6}$$

$$\frac{\Delta P_r}{L_r} = -\frac{\mu}{k_{zr}} v_z \tag{9.7}$$

The velocity magnitude in eq. 9.5-9.7 can be calculated as the corresponding flow Q [m³/s] divided by the area A [m²]. This is illustrated in eq. 9.8-9.10 in which Darcy's law is rearranged to calculate the corresponding permeability coefficients for the pressure difference in the r direction.

$$k_{rr} = -\mu \frac{L_r}{\Delta P_r} \frac{Q_r}{A_r} \tag{9.8}$$

$$k_{\theta r} = -\mu \frac{L_r}{\Delta P_r} \frac{Q_\theta}{A_\theta} \tag{9.9}$$

$$k_{zr} = -\mu \frac{L_r}{\Delta P_r} \frac{Q_z}{A_z} \tag{9.10}$$

For each of the 3 computational fluid dynamics cases (simulation of flow in the r, θ and z direction), fifteen cubic samples with a characteristic length of 50 µm were studied to determine the permeability tensor to allow for some statistical sampling of the simulated specimen. The cubes were defined by the coordinates as shown in Table 9.1. They were positioned such that they did not include the boundary regions, since the flow behaviour in those regions is influenced by the prescribed lateral boundary conditions (symmetry; no flux). For every cubic sample, all permeability coefficients were calculated based on eq. 9.8-9.10. The pressure differences ΔP were calculated by subtracting the mean pressure of the inflow plane of the studied cubic sample from the mean pressure of the outflow plane (eq. 9.11 for the r direction).

$$\Delta P_r = P_{r,inflow} - P_{r,outflow} \tag{9.11}$$

The characteristic lengths L (50 µm) and areas A ($2.5{\cdot}10^{-3}$ mm^2) were equal for all cubes since they had the same dimensions. The flow Q in eq. 9.8-9.10 was calculated as the average flow of the volumetric flows through 5 parallel planes equally distributed over the length of the cube and perpendicular to the permeability direction studied. This was implemented in Fluent by writing journal files to obtain the necessary bounded planes.

Table 9.1: Coordinates of the cubes (characteristic length 50 µm) dissected from the simulation geometry (characteristic length 0.15 mm; Fig. 9.2b). These cubes were used to calculate the permeability tensor. The boundaries of the cubes are given by specifying the upper and lower limits of the r, θ and z coordinates, respectively. The origin (0, 0, 0) is located at the centre of the sample dissected from the dataset (see also Fig. 9.3).

Cube	r_{min} [µm]	r_{max} [µm]	θ_{min} [µm]	θ_{max} [µm]	z_{min} [µm]	z_{max} [µm]
1	-25	25	-25	25	-25	25
2	-50	0	0	50	0	50
3	0	50	0	50	0	50
4	-50	0	-50	0	0	50
5	0	50	-50	0	0	50
6	-50	0	0	50	-50	0
7	0	50	0	50	-50	0
8	-50	0	-50	0	-50	0
9	0	50	-50	0	-50	0
10	-25	25	-25	25	0	50
11	-25	25	-25	25	-50	0
12	-25	25	-50	0	-25	25
13	-25	25	0	50	-25	25
14	0	50	-25	25	-25	25
15	-50	0	-25	25	-25	25

After calculating the permeability tensor for every separate cube, the mean, standard deviation and median values of all permeability coefficients were determined. The normality of the distribution of the permeability coefficients was verified by means of a Shapiro-Wilk test using SPSS (IBM, New York, United States). Additionally, the principal axes (defined by the eigenvectors) as well as the permeability values in the principal directions were calculated from the permeability tensor K (see Appendix A for the linear algebraic equations). This allows quantifying the angles between the original coordinate system axes and the principal axes of the permeability tensor. Finally, the 3D sinusoidal porosity was also determined (using Magics software) for every cube (as defined by the coordinates in Table 9.1) by dividing the volume occupied by the sinusoids by the volume of the cube studied (eq. 9.12).

$$\varepsilon = \frac{V_{sinusoids}}{V_{cube}} \tag{9.12}$$

9.3 Results

9.3.1 Image processing and geometrical analysis of the liver microcirculation

Scanning electron microscopy of the microcirculation sample shows that casting resin was observed in the sinusoids (Fig. 9.2). The sample represents a complex network of interconnected and tortuous sinusoids (Fig. 9.4c-d). Measurements of one hundred sinusoids resulted in a mean diameter of 13.23 ± 2.36 μm.

9.3.2 Calculation of the permeability tensor

The computational fluid dynamics simulation results are represented in Figs. 9.5-9.8. Fig. 9.5 illustrates the static pressure visualisation on the boundaries of the 3 cases. The pressure differences over the cube along the r and θ flow directions are very similar (approximately ranging from 0 to 170 Pa and 0 to 180 Pa, respectively). In contrast, the pressure difference for the simulation of blood flow in the z-direction is clearly smaller (0-100 Pa), while applying the same boundary conditions as in the r and θ flow simulations (velocity inlet of $2.59{\cdot}10^{-6}$ m/s at the top and zero pressure outlet at the bottom).

As visualised in Fig. 9.5, the pressure drops significantly through certain sinusoids and stays almost constant throughout others. This corresponds to the typical presence of preferential pathways in the sinusoidal geometry along tracks with relevant pressure drops. Fig. 9.6 depicts some of these preferential streamlines coloured by their velocity magnitude. The preferential

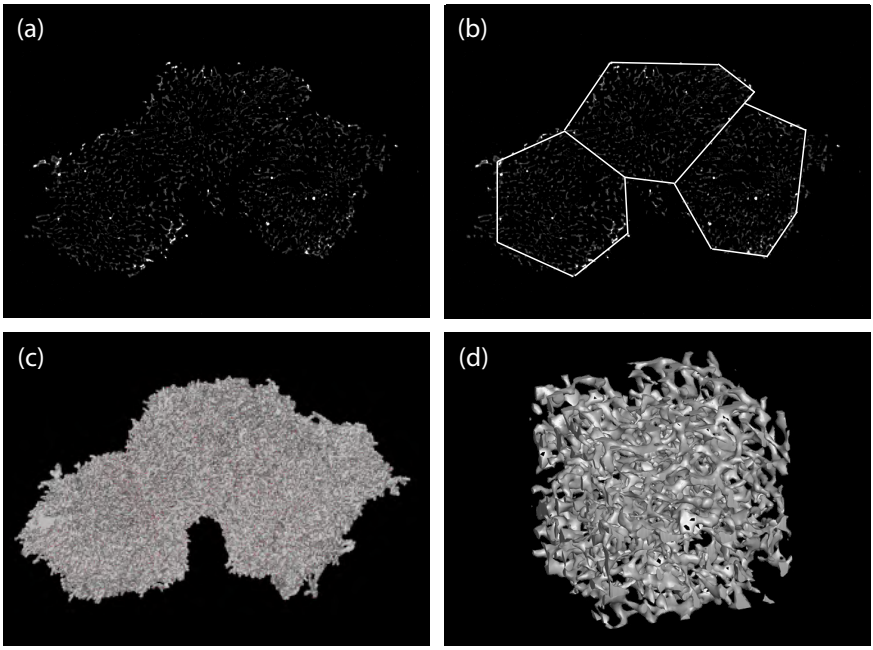

Figure 9.4: Liver microcirculation. (a) Single micro-CT slice showing bright spots (probably contrast agent particles); (b) indication of the most likely lobule borders; (c) 3D reconstruction of the microcirculation sample and (d) of a virtually dissected cubic subsample.

paths seem to be mainly concentrated in the middle region of the geometry, and not at locations near to the transected sinusoids delineating the lateral boundaries. This is obviously a consequence of the symmetry boundary condition applied at the sides. The velocity magnitude approximately ranges from 0 to $1.4{\cdot}10^{-3}$ m/s, 0 to $2.6{\cdot}10^{-3}$ m/s, 0 to $1.1{\cdot}10^{-3}$ m/s for the case of a pressure difference in the r, θ , z directions, respectively. The mean velocity in all of these cases is typically at the lower end of these ranges as can be deducted from the streamlines in Fig. 9.6.

Since the boundary conditions are likely to influence the solution, data of a smaller central cube of 50 µm (cube 1 as defined in Table 9.1) are further analysed to minimise the boundary induced effects. The velocity magnitude in the smaller cube has a mean value of $1.0{\cdot}10^{-4}$ m/s, $7.3{\cdot}10^{-5}$ m/s, $7.7{\cdot}10^{-5}$ m/s for the r, θ, z flow simulations, respectively.

Figure 9.5: Static pressure visualisation on the boundaries of the 3 computational fluid dynamics models. The flow direction is from top to bottom (along the r, θ and z axis, respectively). The top plane was set to a velocity inlet, and the bottom plane to a pressure outlet. The pressure difference for the r and θ simulations are similar within a range of approximately 0 - 170 and 0 - 180 Pa, respectively. The z simulation pressure difference is typically smaller, ranging approximately from 0 to 100 Pa.

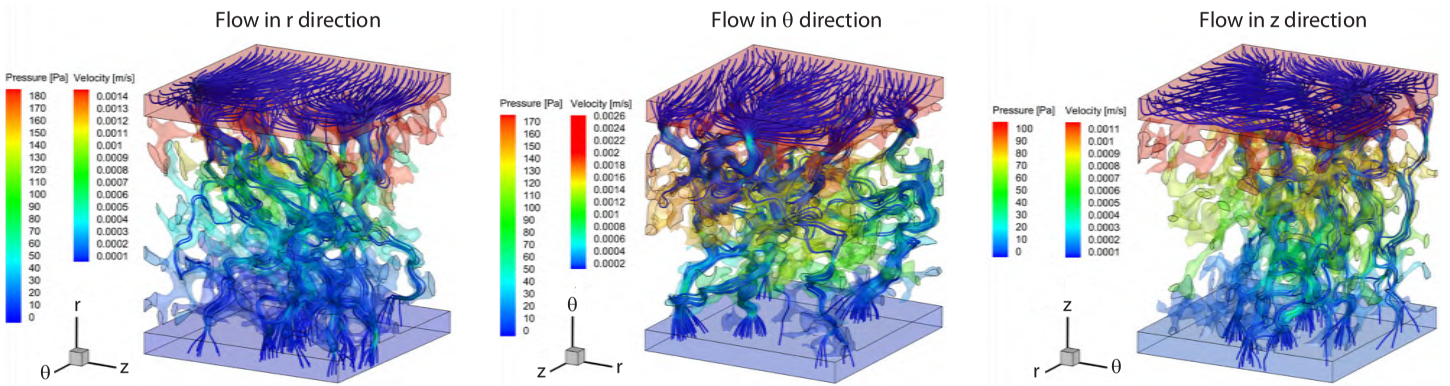

Figure 9.6: Visualisation of the streamlines (colour coded according to the velocity scale) in combination with the translucent pressure contours. The streamlines clearly indicate the preferential pathways followed by the fluid flow. In addition, the figures clearly illustrate higher velocities at locations where the sinusoids are narrow.

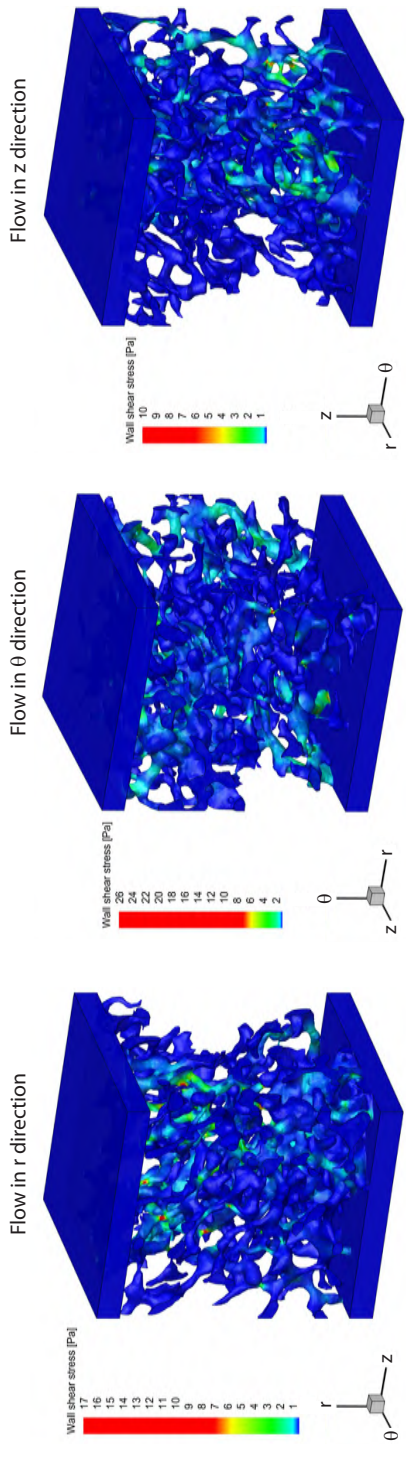

Figure 9.7: Wall shear stress distribution colour map visualised on the boundaries of the 3 computational fluid dynamics models. The flow direction is from top to bottom (along the r, θ and z axis, respectively). Wall shear stresses were typically very low in the major part of all simulation geometries. At the level of narrow channels, wall shear stress increased to higher values.

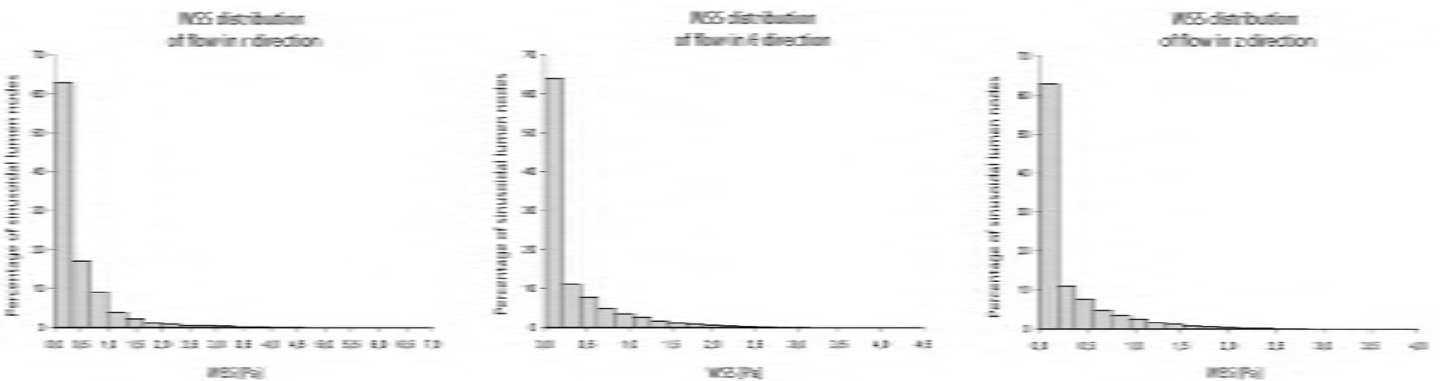

Figure 9.8: Histograms of the wall shear stress distribution on the walls of a cube centrally located in the simulation geometry for each of the three models (flow in the r, θ and z directions). This corresponds to cube 1 as defined in Table 9.1. In all cases, wall shear stress was typically in the range of 0 to 1 Pa for the major part of the geometry.

For the major part of the model boundaries, wall shear stress remains below 1 Pa for each of the simulations (Fig. 9.7). At narrow channel locations, however, higher values are found. Histograms of the wall shear stress distribution for the central cube (cube 1 in Table 9.1) are depicted in Fig. 9.8. Overall, very low wall shear stresses cover the major part of the sinusoidal lumen surface. The mean wall shear stress in the central cube for the r, θ and z simulation was 0.42 Pa, 0.31 Pa, and 0.28 Pa, respectively. The corresponding local maximum wall shear stress was 6.62 Pa, 4.19 Pa, and 3.80 Pa, respectively.

9.3.3 Porosity and permeability tensor

The sinusoidal porosity was calculated for every cube as defined by the coordinates in Table 9.1, and values are depicted in the last column of Table 9.2. The resulting mean porosity was 14.3% ± 2.8%. The components of the permeability tensor for each of the 15 subsampled cubes are given in Table 9.2. As the Shapiro-Wilk test indicated that the distribution of the resulting permeability coefficients was not normal for 4 out of 9 coefficients (significance level of 0.1; see Table 9.2), the overall permeability tensor for the sample is best based on the median values (as shown in eq. 9.13 and 9.14) to avoid a large influence of outlier values.

$$K = \begin{bmatrix} k_{rr} & k_{r\theta} & k_{rz} \\ k_{\theta r} & k_{\theta\theta} & k_{\theta z} \\ k_{zr} & k_{z\theta} & k_{zz} \end{bmatrix} \tag{9.13}$$

$$= \begin{bmatrix} 1.78 \cdot 10^{-14} & -1.29 \cdot 10^{-15} & -7.20 \cdot 10^{-15} \\ 1.07 \cdot 10^{-15} & 1.76 \cdot 10^{-14} & -1.06 \cdot 10^{-15} \\ -5.45 \cdot 10^{-15} & 2.73 \cdot 10^{-15} & 3.43 \cdot 10^{-14} \end{bmatrix} \tag{9.14}$$

Calculating the eigenvectors of the permeability tensor as illustrated in Appendix A, resulted in the principal axes determined by the eigenvectors ($\vec{e}_1$,$\vec{e}_2$,$\vec{e}_3$) in matrix V (eq. 9.15) and the corresponding diagonal matrix K_d with the permeability values along the principal axes (eq. 9.16 and 9.17).

$$V = \begin{bmatrix} \vec{e}_1 & \vec{e}_2 & \vec{e}_3 \end{bmatrix} = \begin{bmatrix} 0.943 & 0.0924 & -0.320 \\ -0.0827 & 0.996 & 0.0438 \\ 0.323 & -0.0148 & 0.946 \end{bmatrix} \tag{9.15}$$

Table 9.2: Results of the permeability tensor and 3D porosity calculations. For each of the fifteen cubes as defined in Table 9.1, the permeability tensor K as well as the porosity ε were studied. For every permeability coefficient and the porosity, the mean value, standard deviation, p-value resulting from the Shapiro-Wilk test and median were calculated. The 3D porosity is distributed around a mean value of 14.3%.

Cube	k_{rr} [m²]	$k_{\theta r}$ [m²]	k_{zr}[m²]	$k_{r\theta}$[m²]	$k_{\theta\theta}$[m²]	$k_{z\theta}$[m²]	k_{rz}[m²]	$k_{\theta z}$ [m²]	k_{zz}[m²]	ε
1	$3.80{\cdot}10^{-14}$	$1.11{\cdot}10^{-14}$	$-1.31{\cdot}10^{-14}$	$-8.27{\cdot}10^{-15}$	$1.88{\cdot}10^{-14}$	$4.96{\cdot}10^{-15}$	$-2.22{\cdot}10^{-14}$	$-5.77{\cdot}10^{-15}$	$3.66{\cdot}10^{-14}$	$1.58{\cdot}10^{-1}$
2	$2.06{\cdot}10^{-14}$	$1.47{\cdot}10^{-15}$	$-1.21{\cdot}10^{-14}$	$2.35{\cdot}10^{-15}$	$2.65{\cdot}10^{-14}$	$2.42{\cdot}10^{-14}$	$-2.99{\cdot}10^{-15}$	$6.77{\cdot}10^{-15}$	$7.14{\cdot}10^{-14}$	$1.74{\cdot}10^{-1}$
3	$3.57{\cdot}10^{-14}$	$-6.39{\cdot}10^{-15}$	$1.32{\cdot}10^{-14}$	$3.86{\cdot}10^{-15}$	$2.48{\cdot}10^{-14}$	$1.12{\cdot}10^{-15}$	$1.40{\cdot}10^{-15}$	$2.08{\cdot}10^{-15}$	$1.03{\cdot}10^{-14}$	$1.82{\cdot}10^{-1}$
4	$7.93{\cdot}10^{-15}$	$3.13{\cdot}10^{-15}$	$-3.76{\cdot}10^{-15}$	$7.11{\cdot}10^{-15}$	$1.76{\cdot}10^{-14}$	$-6.14{\cdot}10^{-15}$	$-5.27{\cdot}10^{-15}$	$-8.93{\cdot}10^{-15}$	$3.68{\cdot}10^{-14}$	$1.26{\cdot}10^{-1}$
5	$1.94{\cdot}10^{-15}$	$1.11{\cdot}10^{-16}$	$-1.23{\cdot}10^{-15}$	$1.45{\cdot}10^{-15}$	$2.87{\cdot}10^{-15}$	$1.03{\cdot}10^{-15}$	$-1.68{\cdot}10^{-15}$	$1.88{\cdot}10^{-15}$	$3.14{\cdot}10^{-15}$	$1.10{\cdot}10^{-1}$
6	$1.78{\cdot}10^{-14}$	$-5.34{\cdot}10^{-15}$	$-7.63{\cdot}10^{-15}$	$-8.17{\cdot}10^{-15}$	$1.17{\cdot}10^{-14}$	$3.05{\cdot}10^{-15}$	$-1.63{\cdot}10^{-14}$	$-3.11{\cdot}10^{-16}$	$4.09{\cdot}10^{-14}$	$1.35{\cdot}10^{-1}$
7	$6.95{\cdot}10^{-15}$	$1.07{\cdot}10^{-15}$	$-7.59{\cdot}10^{-15}$	$-1.76{\cdot}10^{-15}$	$3.95{\cdot}10^{-15}$	$2.73{\cdot}10^{-15}$	$-9.78{\cdot}10^{-15}$	$2.38{\cdot}10^{-15}$	$1.57{\cdot}10^{-14}$	$1.23{\cdot}10^{-1}$
8	$5.25{\cdot}10^{-15}$	$-7.04{\cdot}10^{-16}$	$-1.34{\cdot}10^{-15}$	$-9.26{\cdot}10^{-16}$	$4.78{\cdot}10^{-15}$	$-4.02{\cdot}10^{-16}$	$-6.16{\cdot}10^{-16}$	$1.61{\cdot}10^{-15}$	$9.67{\cdot}10^{-15}$	$1.36{\cdot}10^{-1}$
9	$3.11{\cdot}10^{-15}$	$-1.23{\cdot}10^{-15}$	$-2.21{\cdot}10^{-15}$	$-6.28{\cdot}10^{-15}$	$3.21{\cdot}10^{-15}$	$1.22{\cdot}10^{-15}$	$-1.61{\cdot}10^{-15}$	$-1.50{\cdot}10^{-15}$	$4.30{\cdot}10^{-15}$	$8.60{\cdot}10^{-2}$
10	$2.51{\cdot}10^{-14}$	$5.64{\cdot}10^{-16}$	$7.57{\cdot}10^{-15}$	$1.14{\cdot}10^{-15}$	$2.38{\cdot}10^{-14}$	$1.01{\cdot}10^{-15}$	$-7.20{\cdot}10^{-15}$	$-2.21{\cdot}10^{-15}$	$3.43{\cdot}10^{-14}$	$1.64{\cdot}10^{-1}$
11	$1.53{\cdot}10^{-14}$	$-3.45{\cdot}10^{-15}$	$-1.05{\cdot}10^{-14}$	$-6.57{\cdot}10^{-14}$	$6.93{\cdot}10^{-14}$	$2.50{\cdot}10^{-14}$	$-1.89{\cdot}10^{-14}$	$2.32{\cdot}10^{-15}$	$4.75{\cdot}10^{-14}$	$1.80{\cdot}10^{-1}$
12	$1.24{\cdot}10^{-14}$	$1.15{\cdot}10^{-14}$	$-4.86{\cdot}10^{-15}$	$2.02{\cdot}10^{-15}$	$2.32{\cdot}10^{-14}$	$-7.07{\cdot}10^{-15}$	$-2.46{\cdot}10^{-15}$	$-8.81{\cdot}10^{-15}$	$1.04{\cdot}10^{-14}$	$1.34{\cdot}10^{-1}$
13	$3.09{\cdot}10^{-14}$	$5.17{\cdot}10^{-15}$	$-5.45{\cdot}10^{-15}$	$-4.88{\cdot}10^{-15}$	$7.52{\cdot}10^{-15}$	$3.48{\cdot}10^{-15}$	$-2.46{\cdot}10^{-14}$	$-3.27{\cdot}10^{-15}$	$4.61{\cdot}10^{-14}$	$1.63{\cdot}10^{-1}$
14	$1.82{\cdot}10^{-14}$	$2.77{\cdot}10^{-15}$	$-1.27{\cdot}10^{-14}$	$-1.30{\cdot}10^{-15}$	$2.62{\cdot}10^{-15}$	$3.62{\cdot}10^{-15}$	$-9.13{\cdot}10^{-15}$	$-1.06{\cdot}10^{-15}$	$1.03{\cdot}10^{-14}$	$1.18{\cdot}10^{-1}$
15	$3.69{\cdot}10^{-14}$	$7.76{\cdot}10^{-15}$	$-1.67{\cdot}10^{-14}$	$-4.68{\cdot}10^{-15}$	$1.78{\cdot}10^{-14}$	$5.56{\cdot}10^{-15}$	$-1.31{\cdot}10^{-14}$	$-4.65{\cdot}10^{-15}$	$4.11{\cdot}10^{-14}$	$1.57{\cdot}10^{-1}$
Mean	$1.84{\cdot}10^{-14}$	$1.84{\cdot}10^{-15}$	$-5.22{\cdot}10^{-15}$	$-5.60{\cdot}10^{-15}$	$1.72{\cdot}10^{-14}$	$4.23{\cdot}10^{-15}$	$-8.95{\cdot}10^{-15}$	$-1.30{\cdot}10^{-15}$	$2.79{\cdot}10^{-14}$	$1.43{\cdot}10^{-1}$
Stdev	$1.25{\cdot}10^{-14}$	$5.33{\cdot}10^{-15}$	$7.93{\cdot}10^{-15}$	$1.72{\cdot}10^{-14}$	$1.69{\cdot}10^{-14}$	$9.00{\cdot}10^{-15}$	$8.31{\cdot}10^{-15}$	$4.42{\cdot}10^{-15}$	$2.02{\cdot}10^{-14}$	$2.80{\cdot}10^{-2}$
***p*-value**	$2.11{\cdot}10^{-1}$	$5.82{\cdot}10^{-1}$	$3.16{\cdot}10^{-1}$	$6.73{\cdot}10^{-6}$	$1.04{\cdot}10^{-3}$	$1.31{\cdot}10^{-3}$	$1.67{\cdot}10^{-1}$	$5.98{\cdot}10^{-1}$	$8.81{\cdot}10^{-2}$	$6.15{\cdot}10^{-1}$
Median	$1.78{\cdot}10^{-14}$	$1.07{\cdot}10^{-15}$	$-5.45{\cdot}10^{-15}$	$-1.29{\cdot}10^{-15}$	$1.76{\cdot}10^{-14}$	$2.73{\cdot}10^{-15}$	$-7.20{\cdot}10^{-15}$	$-1.06{\cdot}10^{-15}$	$3.43{\cdot}10^{-14}$	$1.36{\cdot}10^{-1}$

$$K_d = \begin{bmatrix} k_{d,11} & 0 & 0 \\ 0 & k_{d,22} & 0 \\ 0 & 0 & k_{d,33} \end{bmatrix} \tag{9.16}$$

$$= \begin{bmatrix} 1.56 \cdot 10^{-14} & 0 & 0 \\ 0 & 1.75 \cdot 10^{-14} & 0 \\ 0 & 0 & 3.64 \cdot 10^{-14} \end{bmatrix} \tag{9.17}$$

Using these results, the angles between the original coordinate system axes and the principal axes were 19.5°, 5.4° and 18.9° for the r, θ and z axes, respectively. The principal axes coordinate system would thus be obtained by rotating the original orthogonal coordinate system approximately -19° around the θ axis. In addition, the permeability coefficients in the principal directions (diagonal coefficients of K_d) show that the permeability in the central vein direction ($k_{d,33}$ = 3.64·10^{-14} m²) is higher than the corresponding permeabilities in the radial and circumferential directions ($k_{d,11}$ = 1.56·10^{-14} m² and $k_{d,22}$ = 1.75·10^{-14} m², respectively) which are almost equal.

9.4 Discussion

In this paper, a numerical model of the human liver microcirculation has been developed based on a 3D image-based geometry of the liver sinusoids, and was used to study the fluid mechanical characteristics of perfusion at the sinusoidal level. The model presented in this study is, to the best of our knowledge, unique in its kind and provides a further step towards a more quantitative assessment of the perfusion properties of the liver microcirculation.

In contrast to the larger hepatic vessels (see chapter 5), the microcirculation gives evidence of a completely different type of organisation compared to vascular trees. Tortuous sinusoids form an interconnected and intertwined network embedded in a matrix of liver cells. Consequently, the exponential behaviour of the HA, PV and HV trees probably stops at the level of the terminal microcirculation (where blood is drained from the terminal hepatic arterioles and portal venules into the sinusoids). From our data, macro- and mesovessels may be interpreted as 'distributing' vessels (see chapter 5), ensuring that blood reaches all liver lobules, and the sinusoids may be interpreted as 'functional' vessels, ensuring that blood solutes are able to penetrate through sinusoidal fenestrations into the space of Disse and reach the microvilli of hepatocytes for metabolic exchange. The microvascular sample clearly shows sinusoidal structures (Fig. 9.2; meaning that the casting resin was able to fill the sinusoids) and is thought to include

three liver lobules. Hereby, the vascular septa of lobules seem to be highlighted by contrast agent particles (bright dots in Fig. 9.4a). These particles are probably not able to penetrate into the sinusoids because of their size, leaving them trapped at the vascular septa, (partially) delineating the lobule borders (Fig. 9.4b). Accordingly, the sample represents three liver lobules (Fig. 9.4a-b) and based on these contours, lobule diameters were in the order of 700-800 μm. As illustrated, it is not obvious to distinguish between neighbouring lobules. This might be due to the fact that the human liver microcirculation is characterised by less connective tissue delineating its lobule borders in comparison with pig or rodent livers, often used as animal liver models. Furthermore, lobules can have more irregular shapes than the traditionally hexagonal prism-shaped lobules. Concerning this, literature gives evidence of an ongoing discussion on the most appropriate functional unit to represent the liver microcirculation (e.g. hexagonal lobule, primary lobule, liver acinus etc.) [409].

The sample that formed the basis of the model was obtained from a cast of the human liver, and oriented such that - bearing in mind the functional liver lobule unit - the z-axis was approximately aligned parallel to the central vein. Our data indicate that the pressure difference in the z direction is typically smaller than those in the r and θ directions. Since the pressure difference can be interpreted as a degree of resistance to flow (given the same boundary conditions in all 3 cases), the resistance to flow is smallest in the z direction. This corresponds with the resulting diagonal permeability tensor K_d in which $k_{d,33}$ is clearly larger than $k_{d,11}$ and $k_{d,22}$ (which are approximately equal), implying highest permeability of the liver lobule parallel to the direction of the central vein ($k_{d,33}$). Radial ($k_{d,11}$) and circumferential ($k_{d,22}$) permeabilities, as seen in the plane of a hexagonal transection of a lobule, are of a similar magnitude (Fig. 9.3). Since rotating the original coordinate system -19° around the θ axes approximately equals the principal axes determined by the eigenvectors, this suggests that the orientation and corresponding coordinate system as applied in this study, are reasonably well aligned along the principal directions of permeability. The immediate result of these findings is that the sinusoidal circulation is clearly anisotropic. Consequently, the assumption of a homogeneous isotropic tissue seems insufficient to describe the porous behaviour of the sinusoidal microvasculature.

Given the fact that the study is based on one sample from one human liver cast, results should be interpreted as indicative and one should be reluctant to generalise our findings. More samples might allow a better estimation of these characteristics and identify potential regional heterogeneities in tissue properties of the liver under study, but imply a very labour-intensive procedure to acquire good geometries and meshes. Consequently, only one sample was studied, of which, however, subsamples were used to characterise the permeability of liver tissue. Care was taken to make sure that the

sinusoidal heterogeneity was sufficiently covered when selecting the sample to study. A cube with dimensions of 0.15 x 0.15 x 0.15 mm^3 seemed to be sufficient to capture the heterogeneity of tortuous and interconnected sinusoids.

In the process of developing the computational fluid dynamics model geometry, it was inevitable to make compromises and take decisions that have an impact (which we tried to minimise) on the simulation results. Some sinusoids, for instance, were cut when dissecting the cubic sample. As a consequence, these transection planes of bisected sinusoids had to be defined as a boundary condition. Symmetry conditions were applied resulting in no flux through the boundary sections. However, in reality these sinusoids are continuous and flux is possible. To minimise the influence of these boundary induced effects on the results, we limited the quantitative analyses to cubes at a certain minimal distance (25 µm which is equal to 16.6% of the characteristic length of 0.15 mm) from these boundaries (Table 9.1).

In this study, blood is modelled as an incompressible and Newtonian fluid with a constant density and dynamic viscosity. It is, however, known that the haemodynamic behaviour of blood at the microcirculation level is different from the behaviour at the macrocirculation level (non-Newtonian fluid, Fahraeus-Lindqvist effect [28]). However, the assumption of an incompressible and Newtonian fluid is justified for this study, since the Fahraeus-Lindqvist effect at sinusoidal diameters (±10 μm) indicates viscosities near that of blood plasma, which is close to a Newtonian fluid. When assuming a Newtonian fluid and geometrically similar structures, the permeability tensor is independent of the fluid studied and is a purely geometrically determined parameter. The reported shear stress levels, on the other hand, might not fully reflect the haemodynamic stress exerted by the blood *in vivo*. Note, however, that they might be indicative of shear stress exerted by blood-mimicking liquids upon machine perfusion of isolated organs for transplantation.

Our model and results can be compared with some studies based on idealised microcirculation models, in particular the 2D models of Ricken et al. [402] and Bonfiglio et al. [43]. However, both 2D models lack one dimension which has a non-negligible influence on the resulting flow behaviour. The model of Ricken et al. [402] does take into account longitudinal sections of idealised lobules with the central veins and hepatic arterioles, while modelling the liver microcirculation using a biphasic approach. On the contrary, the model of Bonfiglio et al. [43] focuses on the hexagonal transection of a liver lobule to build a porous medium model of the liver microcirculation. In this study, a porosity estimate (ε = 12%) based on brain tissue imaging, was used to calculate the corresponding sinusoidal permeability. This value is somewhat lower than the porosity acquired in our study (14.3% ± 2.8%).

The results of our study can lead to new, improved models using porous media to simulate the behaviour of the liver microcirculation taking

into account the anisotropy. Moreover, these models could also be applied to liver perfusion settings other than the natural blood flow, such as the haemodynamic conditions experienced by the microcirculation in the case of liver pathologies, treatments and transplantation procedures such as machine perfusion preservation, ischaemia reperfusion etc.

9.5 Conclusion

Vascular corrosion casting and micro-CT scanning allowed to generate microcirculation morphological data. These data enable gaining more insight into structural-related characteristics (porosity, permeability tensor), which allow capturing and modelling the microcirculation behaviour (especially relevant when studying microvascular alterations caused by e.g. cirrhosis). A 3D numerical microcirculation model of a human liver was constructed and the resulting data indicate that the human hepatic microcirculation clearly displays anisotropic behaviour in terms of permeability, which was quantified by means of a permeability tensor. In particular, a higher permeability was demonstrated along the direction of the central vein, and about two times lower but approximately equal permeabilities along the radial and circumferential directions of the liver lobule. Since the permeability coefficients depend on the flow direction, liver microcirculation models should take into account sinusoidal anisotropy.

CHAPTER 10

A 3D porous media liver lobule model: the importance of vascular septa and anisotropic permeability for homogeneous perfusion

This chapter is based on *"A 3D porous media liver lobule model: the importance of vascular septa and anisotropic permeability for homogeneous perfusion"*, Computer Methods in Biomechanics and Biomedical Engineering, 2012 [99].

10.1 Introduction

The perfusion of the liver is complex and distinct from that of other organs, mainly due to its dual blood supply from both the hepatic artery and the portal vein [93, 311, 342, 409]. In particular, the microcirculation on the scale of the liver lobules and sinusoids displays complicated haemodynamics [118, 169, 311, 317, 318, 409, 466].

In the literature, microperfusion of the liver is often schematically represented in terms of classical lobules, each having the shape of a hexagonal prism (Fig. 10.1) [311, 409]. Liver lobules are assumed to be configured in a tessellating pattern, similar to the organisation of hexagonal wax cells in the honeycombs of bees. Blood enters a lobule via the portal tracts (PTs), located at the corners. Each PT contains a hepatic arteriole (supplying the liver with oxygenated blood), a portal venule (providing nutrient-rich blood

from the intestines), and a bile duct. The latter drains the bile produced in the lobule in the opposite direction from the blood flow in the PTs. A fraction of the blood from the PTs enters the vascular septa (VS), which are the vascular surfaces between neighbouring lobules, bordered at opposite edges by two PTs (Fig. 10.1). As such, the VS foresee the blood supply of the tissue between PTs by a number of microvessels branching off the PTs. Blood flows from the PTs and VS into the interconnected network of tortuous sinusoids, which are the hepatic-specific capillaries and are lined by a fenestrated endothelial cell layer. Blood solutes can flow through the fenestrations into the space of Disse, which is the space between the endothelial cells and the hepatocytes. Here, the metabolic exchange (e.g. oxygen or nutrient uptake) takes place with the neighbouring hepatocytes. The blood is further drained from the sinusoids into the central vein (CV), and from there into the hepatic veins and vena cava inferior [311, 409]. Due to the liver's microvascular organisation and its metabolic functions, liver lobules are characterised by metabolic zonation [409, 532]. For example, the cell zone closest to the PTs will receive blood that is rich in nutrients and oxygen, while the zone close to the CV receives blood that is poorer in nutrients and oxygen. Although the liver lobule is the most frequently used functional liver unit, a number of other units has been proposed in the past, such as the hepatic acinus [394] (dotted line in Fig. 10.1b) and the primary lobule [317, 318]. Nevertheless, the actual real 3D structure of the liver microcirculation seems to be more complicated, as was illustrated in one of our previous papers ([98]; chapter 9), on the basis of a high resolution 3D micro-CT dataset of the human liver microcirculation, and liver lobules are not always perfect prisms. Additionally, variations are frequently observed in the number of PTs per lobule (polyhedral lobules with four, five or seven corners instead of six).

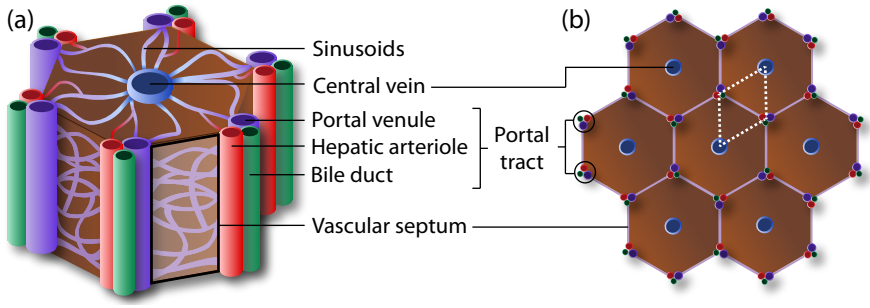

Figure 10.1: Schematic representation of the hepatic microcirculation. (a) Liver lobule with the shape of a hexagonal prism and its vascular network; (b) Spatial organisation of the liver lobules. A liver acinus is indicated by the white dotted line.

Until now, our knowledge of the liver microcirculation is mainly based on schematic concepts, and its haemodynamic behaviour is still not fully understood. Especially in the case of abnormal liver conditions, the liver microcirculation plays a crucial role: when impaired or damaged (for instance due to disease), this can result in a loss of liver function due to the tight coupling between liver microperfusion and its metabolic function. Consequently, it is necessary to gain more insight into liver microvascular haemodynamics to also have a deeper understanding of function. Previously, numerical models have been used successfully to better understand the microcirculation. These models (or modelling techniques) might be helpful to understand microhaemodynamics in a healthy liver as well as in liver pathology. Knowing that the microcirculation operates within relatively narrow ranges of haemodynamic conditions, microcirculation alterations might lead to biomechanical stressors (high shear stresses, high wall stresses). As such, these numerical models are applicable to investigate transplant-related phenomena (for which the preservation of the hepatic microcirculation is crucial for the viability of the liver graft [340, 341]), pathology-related microvascular alterations (e.g. in the case of fibrosis, cirrhosis [69, 486], hepatocellular carcinoma [302], steatosis [408], portal hypertension [140, 513]), as well as surgery-induced effects (e.g. small-for-size liver syndrome [163, 218, 462] after partial hepatectomy). For example, cirrhosis is known to alter and deteriorate the liver's microvessel structure leading to higher vascular resistances, which could be modelled by changing structure-related parameters such as the permeability. Next to these applications, reduced order versions of these models may also be implemented in larger scale models (e.g. [93]) to capture the total liver haemodynamics, incorporating the macro- as well as the meso- and microcirculation and the interaction of the liver with other organs in whole system models.

However, only a few models on the topic of liver microhaemodynamics have been published, which might be due to the complexity of the liver microcirculation and the difficulties associated with the acquisition of the required anatomical and functional data at sufficient resolution. A few studies focused on modelling the lobule haemodynamics based on porous medium approaches, in which the sinusoids are represented as pores imbedded in a parenchymal matrix. One such, Ricken et al. [402] developed a 2D biphasic model of the blood flow in a longitudinal cross-section of the liver lobules using a permeability that is isotropic over the cross-section. Bonfiglio et al. [43] studied the flow patterns in a 2D hexagonal cross-section in a porous lobule model, assuming both isotropic permeability as well as 2D anisotropic permeability (radial versus circumferential). Both of these models neglected the existence of VS [43, 402], leading to predictions of poor perfusion of the regions midway between neighbouring PTs in the paper of Bonfiglio et al.

[43]. Given the need to perfuse every hepatocyte well, this is unlikely to occur *in vivo*. Consequently, Siggers et al. [433] used a 2D symmetric triangular porous medium model (representing one sixth of a hexagonal cross-section of a lobule), which they solved analytically to investigate the effect of VS. The PT inflows, VS inflows and central outflows were approximated as point sources, line sources and point sinks, respectively.

Although the porous medium models described above are useful to capture the overall haemodynamics, they are based on a number of key assumptions. The flow is assumed to be planar (2D), while it is known that the real liver microcirculation has a complex 3D structure [98]. In all but one section of the paper by Bonfiglio et al. [43], the permeability is assumed to be isotropic. Furthermore, VS were either neglected [43, 402] or modelled as a line source, implying a constant inflow into the sinusoids along the length of the VS [433]. However, in reality, the inflow from the VS is likely to be smaller further away from the PTs (due to a lower pressure within the VS there). Since these assumptions were not validated before, 3D models may be helpful to clarify this. Rani et al. [393] previously developed a finite volume blood flow model in a 3D geometry incorporating a terminal hepatic arteriole, portal venule and CV, as well as two fenestrated sinusoids using non-Newtonian blood properties. Though the modelling approach was sophisticated, an idealised 3D geometry was used to locally represent the blood flow from the portal tract passing through two sinusoids into the central vein. More complex tortuous and interconnected sinusoids as well as the VS were not taken into account here, while these are relevant for the haemodynamics at this level. In recent work, we developed a 3D numerical model of the liver terminal circulation based on high resolution micro-CT data [98]. We demonstrated that the three-dimensional permeability tensor of a sinusoidal network displays significant anisotropy, which is in contrast with the isotropic permeability conditions assumed in the 2D porous models mentioned above [43, 402, 433]. Working in a cylindrical coordinate system with the z-axis along the central vein of a lobule (Fig. 10.2), we found the permeability tensor to be approximately diagonal with an axial component roughly two times that of the radial and azimuthal components, which were themselves approximately equal.

Combining the strengths of the previous models and extending them could lead to a more accurate model and a better understanding of the hepatic microhaemodynamics. Therefore, the aim of this study was to develop a 3D porous medium model of the perfusion of a liver lobule, accounting for anisotropy in the permeability of the sinusoidal network and incorporating the VS as a separate volume zone within the model. In addition, we performed a parameter sensitivity analysis of the newly proposed model.

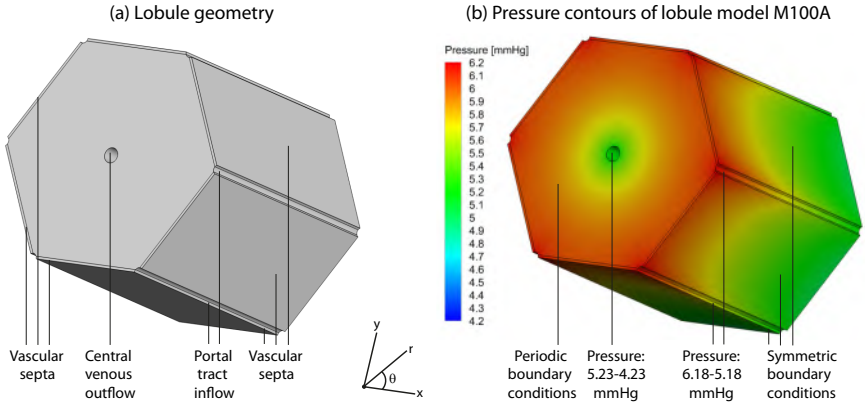

Figure 10.2: (a) Simulation geometry of a liver lobule; (b) pressure contours (in mmHg) obtained in model M100A (see also Table 10.1). The z-axis of the cylindrical coordinate system is located along the longitudinal axis of the lobule and its origin is at the centre of the simulation geometry.

10.2 Materials and methods

10.2.1 Simulation geometry and mesh generation

A geometry, representing a liver lobule with VS, was studied using a cylindrical coordinate system (r,θ,z) with its z-axis along the CV and its origin at the centre of the simulation geometry (Fig. 10.2a).

The lobule geometry (Fig. 10.2a) was assumed to be a hexagonal prism with cross-section defined by a circumscribing cylinder of diameter 1 mm [309, 409], resulting in a hexagonal edge length of 0.5 mm. Lobules are reported to have lengths of up to several millimetres [309], and in this study we used a length of 1 mm as a representative value. Reported measurements of the diameter of the CV and portal venule (corresponding to the major PT inflow) vary substantially in the literature [295, 358, 409, 465, 466], and in our model we chose representative values. As such, the CV was modelled as a cylinder of diameter 60 µm parallel to the z-axis, and the PTs along the six parallel edges as cylinders, each of diameter 40 µm. VS zones were defined as the outermost 10 µm depth on the six faces of the prism that delineate the borders with the neighbouring lobules (Fig. 10.2a).

The simulation geometry was meshed with Gambit (Ansys, Pennsylvania, USA). A mesh sensitivity study was performed by creating four meshes using the Cooper scheme with the linked surface meshes of the top and bottom plane of the geometry as sources, and applying an interval size of 24, 12, 6 and 5 µm resulting in $4.6{\cdot}10^4$, $3.8{\cdot}10^5$, $3.1{\cdot}10^6$ and $5.1{\cdot}10^6$ hexahedral volume elements, respectively. The mesh sensitivity analysis showed approximately

constant results for models having $3.1{\cdot}10^6$ or more elements. Consequently, the mesh with a 6 μm interval size corresponding to $3.1{\cdot}10^6$ elements was used.

10.2.2 Cell zone conditions and fluid properties

The volume of the lobule, representing the sinusoids, was characterised as a porous medium, with fluid flow given by Darcy's law:

$$\vec{v}_{porous} = -\frac{1}{\mu} K \nabla p \tag{10.1}$$

where p [Pa] is the sinusoidal blood pressure, μ [Pa·s] the dynamic viscosity of blood, K [m²] the second order permeability tensor and $\vec{v}_{porous}$ [m/s] the Darcy velocity) [286]. The permeability tensor K (consisting of permeability coefficients k [m²]; eq. 10.2) is represented by a diagonal matrix in the cylindrical coordinate system (r,θ,z):

$$K = \begin{bmatrix} k_{rr} & k_{r\theta} & k_{rz} \\ k_{\theta r} & k_{\theta\theta} & k_{\theta z} \\ k_{zr} & k_{z\theta} & k_{zz} \end{bmatrix} = \begin{bmatrix} k_{rr} & 0 & 0 \\ 0 & k_{\theta\theta} & 0 \\ 0 & 0 & k_{zz} \end{bmatrix} \tag{10.2}$$

In this study, two different permeability tensors were used: an isotropic and an anisotropic tensor. The anisotropic tensor was defined by the permeability coefficients found in chapter 9 [98], giving $k_{zz} = 3.64{\cdot}10^{-14}$ m², $k_{rr} = 1.56{\cdot}10^{-14}$ m² and $k_{\theta\theta} = 1.75{\cdot}10^{-14}$ m². Isotropic permeability conditions were defined by assuming that the isotropic permeability equals the anisotropic radial permeability coefficient, $k_{rr} = k_{\theta\theta} = k_{zz} = 1.56 \cdot 10^{-14}$ m². This choice was based on the observation that the radial permeability coefficient has the biggest impact on the resulting lobule outflow (CV).

The porosity of the lobule, ε , equals the fraction of the volume occupied by the blood ($V_{sinusoids}$) divided by the total volume V_{total} (eq. 10.3), and we fixed its value at 0.143, as found in chapter 9 [98]. It also equals the ratio of the magnitude of the Darcy velocity (the volume-averaged flux per unit area; $\vec{v}_{porous}$ [m/s]) to the magnitude of the cross-sectionally averaged physical velocity in the sinusoids ($\vec{v}_{physical}$ [m/s]):

$$\varepsilon = \frac{V_{sinusoids}}{V_{total}} = \frac{\left\|\vec{v}_{porous}\right\|}{\left\|\vec{v}_{physical}\right\|} \tag{10.3}$$

In the following, all reported velocities are Darcy velocities and we will denote $\vec{v}_{porous}$ simply by $\vec{v}$. In order to estimate the typical physical velocities within the sinusoids, the Darcy velocity should thus be divided by the porosity ε (eq. 10.3).

For the model without VS, the VS zones were defined using the same permeability coefficients as for the lobule zone of the sinusoids. In the case of models with VS, VS were treated as porous media with a higher circumferential permeability due to the circumferential orientation of the vessels within the VS. As such, we used in the VS the lobular value of $k_{\theta\theta}$ multiplied by a factor of either 10 or 100, but keeping the values of the radial and longitudinal coefficients, k_{rr} and k_{zz}, the same as their values in the sinusoids. Note that, ideally, we would have altered the component of the permeability tensor in the exact direction of the VS (rather than $k_{\theta\theta}$ in the circumferential direction, which is approximately in the same direction), but in this paper we considered this slightly simpler case.

In total, six cases were simulated to investigate the influence of including VS and the usage of (an)isotropy. We denote these models as M0I, M0A, M10I, M10A, M100I, M100A, where '0' refers to no VS, '10' to VS with $k_{\theta\theta}$ 10 times that in the lobule interior and '100' to VS with $k_{\theta\theta}$ 100 times that in the lobule interior, and 'I' refers to isotropic permeability and 'A' to anisotropic permeability (Table 10.1). Blood was assumed to be an incompressible Newtonian fluid with a dynamic viscosity of 3.5 mPa·s [482].

10.2.3 Boundary conditions and computational fluid dynamics

For all models, the top and bottom hexagonal planes were characterised by a translational periodic boundary condition (Fig. 10.2b), and we assumed 1 mmHg/mm to be the z-component of the pressure gradient. The pressure was defined to drop from 6.18 mmHg to 5.18 mmHg along the PT inflow and from 5.23 mmHg to 4.23 mmHg along the CV outflow (corresponding to mean pressures of 5.68 mmHg at the PTs and 4.73 mmHg at the CV, as found in [295]). At the planes of interface between the lobule and VS, continuity of pressure and flux was applied. Since we assumed a repeating honeycomb pattern (Fig. 10.1b), we used symmetry boundary conditions at the surfaces delineating the lobule borders. The steady computational fluid dynamic models were solved using Fluent (Ansys, Pennsylvania, USA). Tecplot (Tecplot Inc., Washington, USA) was used to process, calculate and visualise the haemodynamic parameters of interest.

10.2.4 Parameter sensitivity study

Since some assumptions were made concerning the boundary conditions and simulation geometry, with some degree of variability in values reported in literature, we performed a parameter sensitivity analysis of the model. The M100A model was used as the baseline model to perform parameter variations of the pressure boundary conditions as well as geometry-related parameters (see also Table 10.1).

Table 10.1: Overview of all simulations with the corresponding vascular septa (VS) and permeability conditions, as well as the longitudinal pressure gradient, the lobule circumferential diameter, the pressure drop between the portal tracts (PTs) and central vein (CV), the VS thickness, and the PT and CV diameters.

Model	VS conditions ($k_{\theta\theta}$ scaling factor)	Permeability conditions	Pressure gradient [mmHg/mm]	Lobule diameter [mm]	PT-CV pressure difference [mmHg]	VS thickness [µm]	PT diameter [µm]	CV diameter [µm]
M0I	1	Isotropic	1	1	0.95	10	40	60
M0A	1	Anisotropic	1	1	0.95	10	40	60
M10I	10	Isotropic	1	1	0.95	10	40	60
M10A	10	Anisotropic	1	1	0.95	10	40	60
M100I	100	Isotropic	1	1	0.95	10	40	60
M100A	100	Anisotropic	1	1	0.95	10	40	60
M100A_1	100	Anisotropic	0	1	0.95	10	40	60
M100A_2	100	Anisotropic	0.5	1	0.95	10	40	60
M100A_3	100	Anisotropic	2	1	0.95	10	40	60
M100A_4	100	Anisotropic	1	1	1.45	10	40	60
M100A_5	100	Anisotropic	1	1	1.95	10	40	60
M100A_6	100	Anisotropic	1	1	0.95	5	40	60
M100A_7	100	Anisotropic	1	1	0.95	10	60	60
M100A_8	100	Anisotropic	1	1	0.95	10	40	90
M100A_9	100	Anisotropic	1	0.5	0.95	10	40	60
M100A_10	100	Anisotropic	1	0.5	1.45	10	40	60
M100A_11	100	Anisotropic	1	0.5	1.95	10	40	60

As such, the longitudinal pressure gradient was changed from the default value of 1 mmHg/mm to 0 mmHg/mm (M100A_1), 0.5 mmHg/mm (M100A_2) and 2 mmHg/mm (M100A_3). The pressure drop between the PTs and CV was changed by increasing the default PT pressure, defined to drop from 6.18 mmHg to 5.18 mmHg along the PT inflow, by 0.5 mmHg (M100A_4) and 1 mmHg (M100A_5).

The thickness of the VS was changed to 5 μm (M100A_6) instead of 10 μm, and the PT (M100A_7) and CV diameters (M100A_8) were increased by 50% of their original value. Additionally, the effect of the lobule circumferential diameter was investigated by scaling down the lobule. Note that if we would consider a scaled model in which we change all length scales (lobule circumferential diameter, and the radii of the CV and PTs) in the same way, the flux would remain unchanged, since the velocity scale is inversely proportional to the length scale. Consequently, we considered a lobule circumferential diameter of 0.5 mm instead of 1 mm, but kept the radii of the PTs and CV the same (M100A_9). A summary of all simulated cases and the corresponding parameters is shown in Table 10.1.

10.3 Results

We first compare the haemodynamics of the models with and without VS (Section 10.3.1), followed by a comparison of the isotropic and anisotropic permeability cases (Section 10.3.2). The results of the parameter sensitivity analysis are reported in section 10.3.3.

10.3.1 Comparison of the models with and without vascular septa

Since the impact of VS on the results for the isotropic and anisotropic models are qualitatively similar (Figs. 10.3-10.7), we only describe here the results for the anisotropic models in detail.

10.3.1.1 Flow in the hexagonal cross-sectional plane in the middle of the lobule (z=0)

In model M0A, over the hexagonal cross-section z=0, the pressure drops from 5.68 mmHg at the PTs to 5.40 mmHg at the points midway between neighbouring PTs to 4.73 mmHg at the CV (Fig. 10.3a, 10.4b). The projection of the velocity into the cross-section, $\|\vec{v}_{r\theta}\|$, has a relatively high magnitude at the entry from the PTs (Fig. 10.3b). From there the blood flows to the CV, either directly, or first towards the regions midway between neighbouring PTs and then towards the CV. Along each pathway, the cross-sectional velocity decreases away from the PTs, reaching a streamline-specific minimum (with the lowest value being a zero velocity, which is attained at the stagnation points at the outer lobule borders midway between neighbouring PTs; Fig. 10.3c) before rising to its highest value at the CV outlet (Fig. 10.3d).

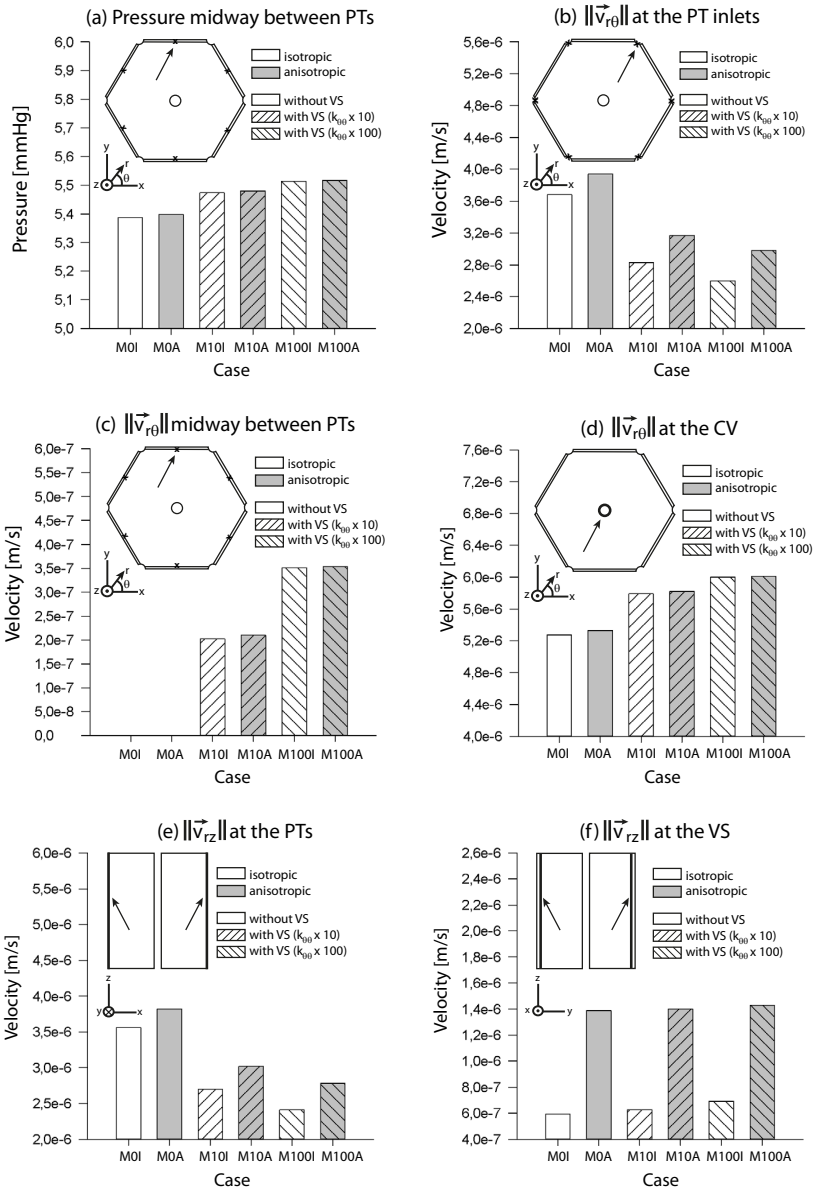

Figure 10.3: Comparison of the pressures and velocities at particular locations in the lobule for the models M0I, M0A, M10I, M10A, M100I and M100A: (a) pressure at the points midway between neighbouring portal tracts (PTs); (b-d) magnitudes of the cross-sectional projection of the velocity ($\|\vec{v}_{r\theta}\|$): (b) at PT inlets (mean value over the PT inlet), (c) at the midpoints of the border lines of the sinusoidal volume connecting neighbouring PTs, and (d) at the central venous (CV) outlet (mean value over the CV outlet); (e-f) magnitude of the velocity projected into a longitudinal cross-section ($\|\vec{v}_{rz}\|$): (e) at PT inlets (longitudinal section through the PTs, θ = 0°, 180°), and (f) at the vascular septal (VS) inflow into the lobule (longitudinal section through the midpoints of the VS, $\theta = \pm$ 90°).

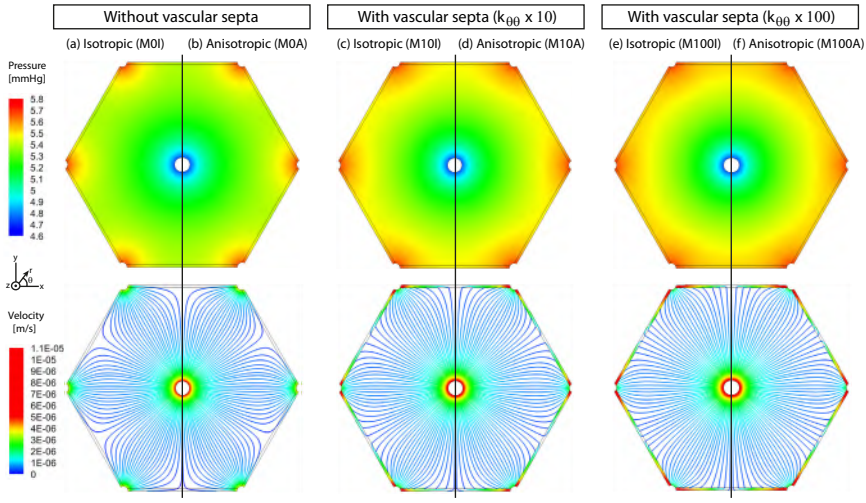

Figure 10.4: Pressures (top) and streamlines (bottom, coloured according to the magnitude of the projection of the velocity into the plane ($\|\vec{v}_{r\theta}\|$) obtained on the middle cross-section (z=0) of the lobule models: (a) M0I, (b) M0A, (c) M10I, (d) M10A, (e) M100I, (f) M100A.

As can be seen in Figs. 10.4d, f, the model demonstrates different haemodynamics when VS are present. The pressure drop from the PTs to the VS is smaller in M10A and M100A than in the case without VS (Fig. 10.3a), and the pressure drop from the centre of the VS to the CV is larger. There are two flow pathways: those pathways on which fluid enters the sinusoids directly from the PTs; and those on which fluid travels through the VS before entering the sinusoids. Within the VS, the flow is predominantly circumferential, and the cross-sectional velocities at the PT-VS interface are high. At the CV outflow the velocities are approximately spatially uniform (Fig. 10.3d, Fig. 10.4 d, f). On leaving the PTs, the flow pathways that go directly from the PTs into the sinusoids have lower velocities than those that first enter the VS and also than those leaving the PTs in model M0A (see Fig. 10.3b). The streamlines in models M10A and M100A are predominantly radial, and the regions midway between neighbouring PTs are better perfused, leading to a more uniform distribution of blood throughout the tissue than in M0A (Fig. 10.4). This effect is more pronounced for higher circumferential permeability in the VS, i.e. more in M100A than in M10A. Moreover, as shown in Table 10.2, the volumetric flow rate at the outflow of the lobule (Q_{lobule}) is higher when including VS ($6.58{\cdot}10^{-5}$ ml/min and $6.78{\cdot}10^{-5}$ ml/min for M10A and M100A, respectively) than when neglecting VS ($6.02{\cdot}10^{-5}$ ml/min for M0A).

Table 10.2: Overview of results for the simulated cases: the lobule and estimated total liver flow (Q) and resistance (R; see Appendix B for details), as well as the percentage of difference of the lobule and total liver outflow relative to the baseline model M100A (calculated as $(Q_{Mx} - Q_{M100A})/Q_{M100A}$).

Model	Q_{lobule} [ml/min]	Q_{liver} [ml/min]	R_{lobule} [mmHg·min/ml]	R_{liver} [mmHg·min/ml]	Percentual difference of Q_{lobule}	Percentual difference of Q_{liver}
M0I	$5.95{\cdot}10^{-5}$	$1.37{\cdot}10^{2}$	$1.60{\cdot}10^{4}$	$6.91{\cdot}10^{-3}$	-12.2 %	-12.2 %
M0A	$6.02{\cdot}10^{-5}$	$1.39{\cdot}10^{2}$	$1.58{\cdot}10^{4}$	$6.83{\cdot}10^{-3}$	-11.2 %	-11.2 %
M10I	$6.54{\cdot}10^{-5}$	$1.51{\cdot}10^{2}$	$1.45{\cdot}10^{4}$	$6.29{\cdot}10^{-3}$	-3.6 %	-3.6 %
M10A	$6.58{\cdot}10^{-5}$	$1.52{\cdot}10^{2}$	$1.44{\cdot}10^{4}$	$6.26{\cdot}10^{-3}$	-3.0 %	-3.0 %
M100I	$6.77{\cdot}10^{-5}$	$1.57{\cdot}10^{2}$	$1.40{\cdot}10^{4}$	$6.08{\cdot}10^{-3}$	-0.1 %	-0.1 %
M100A	$6.78{\cdot}10^{-5}$	$1.57{\cdot}10^{2}$	$1.40{\cdot}10^{4}$	$6.07{\cdot}10^{-3}$	0.0 % (baseline)	0.0 % (baseline)
M100A_1	$6.78{\cdot}10^{-5}$	$1.57{\cdot}10^{2}$	$1.40{\cdot}10^{4}$	$6.07{\cdot}10^{-3}$	0.0 %	0.0 %
M100A_2	$6.78{\cdot}10^{-5}$	$1.57{\cdot}10^{2}$	$1.40{\cdot}10^{4}$	$6.07{\cdot}10^{-3}$	0.0 %	0.0 %
M100A_3	$6.78{\cdot}10^{-5}$	$1.57{\cdot}10^{2}$	$1.40{\cdot}10^{4}$	$6.07{\cdot}10^{-3}$	0.0 %	0.0 %
M100A_4	$1.03{\cdot}10^{-4}$	$2.39{\cdot}10^{2}$	$1.40{\cdot}10^{4}$	$6.07{\cdot}10^{-3}$	52.6 %	52.6 %
M100A_5	$1.39{\cdot}10^{-4}$	$3.21{\cdot}10^{2}$	$1.40{\cdot}10^{4}$	$6.07{\cdot}10^{-3}$	105.2 %	105.2 %
M100A_6	$6.51{\cdot}10^{-5}$	$1.50{\cdot}10^{2}$	$1.46{\cdot}10^{4}$	$6.32{\cdot}10^{-3}$	-4.0 %	-4.0 %
M100A_7	$7.01{\cdot}10^{-5}$	$1.62{\cdot}10^{2}$	$1.35{\cdot}10^{4}$	$5.87{\cdot}10^{-3}$	3.4 %	3.4 %
M100A_8	$7.80{\cdot}10^{-5}$	$1.80{\cdot}10^{2}$	$1.22{\cdot}10^{4}$	$5.27{\cdot}10^{-3}$	15.1 %	15.1 %
M100A_9	$9.74{\cdot}10^{-5}$	$9.00{\cdot}10^{2}$	$9.75{\cdot}10^{3}$	$1.06{\cdot}10^{-3}$	43.7 %	474.8 %
M100A_10	$1.49{\cdot}10^{-4}$	$1.37{\cdot}10^{3}$	$9.75{\cdot}10^{3}$	$1.06{\cdot}10^{-3}$	119.3 %	777.4 %
M100A_11	$2.00{\cdot}10^{-4}$	$1.85{\cdot}10^{3}$	$9.75{\cdot}10^{3}$	$1.06{\cdot}10^{-3}$	195.0 %	1079.9 %

10.3.1.2 *Flow in the longitudinal cross-section through opposite PTs (θ=0°, 180°)*

Fig. 10.5b shows the pressure and streamlines in M0A in a longitudinal plane of cross-section containing the axis of the lobule and two PTs. The flow follows a diagonally downward pathway, due to the combined effects of the imposed z-component of the pressure gradient and of the radial pressure gradient. The velocity is high at the inflow (Fig. 10.3e), lower midway between the PTs and the CV, and then higher near the CV outflow.

Similar flow patterns are found in M10A and M100A (Figs. 10.5d, f); however, these models have lower velocities at the PT inflow (Fig. 10.3e), and higher velocities at the CV outflow.

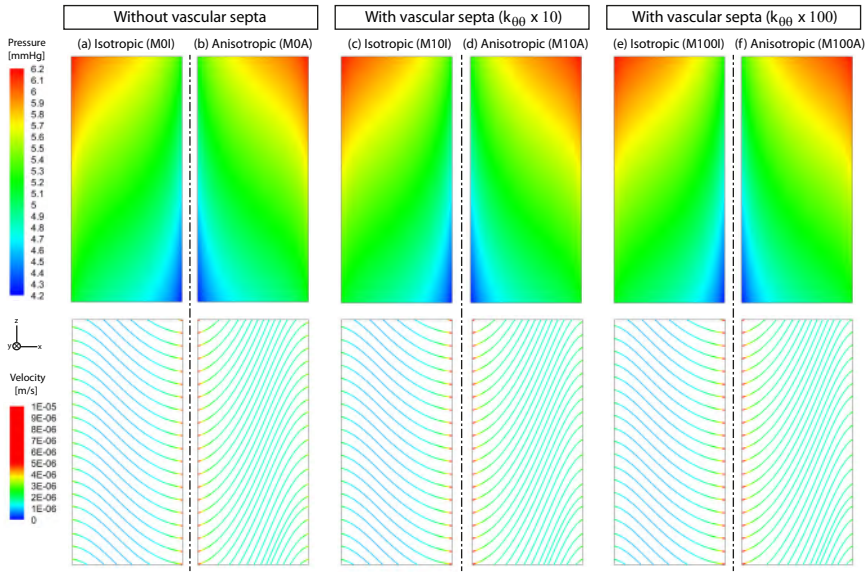

Figure 10.5: Pressures (top) and streamlines (bottom, coloured according to the magnitude of the projection of the velocity into the plane ($\|\vec{v}_{rz}\|$)) obtained on a longitudinal cross-section passing through two portal tracts (θ = 0°, 180°) of the lobule models: (a) M0I, (b) M0A, (c) M10I, (d) M10A, (e) M100I, (f) M100A.

10.3.1.3 *Flow in the longitudinal cross-section through the centrelines of opposite VS (θ=±90°)*

Fig. 10.6b shows the pressure in M0A in a longitudinal plane of cross-section containing the axis of the lobule and passing through the midpoints of two VS. The pressure decreases from the outer boundary to the CV outflow. Flow velocities in this plane are generally smaller than the velocities in the plane

passing through the PTs, especially near the peripheral boundaries, where there is a stagnation line with a zero velocity midway between two PTs along the outer lobule borders. Comparing the models with and without VS, we find that the pressures in M10A and M100A are generally higher than those in M0A, see Fig. 10.6b, d, f. The planar velocity magnitudes at the VS-lobule interfaces are $1.40 \cdot 10^{-6}$ m/s and $1.43 \cdot 10^{-6}$ m/s for M10A and M100A, respectively (see Fig. 10.3f). However, velocities at the CV outflow are higher.

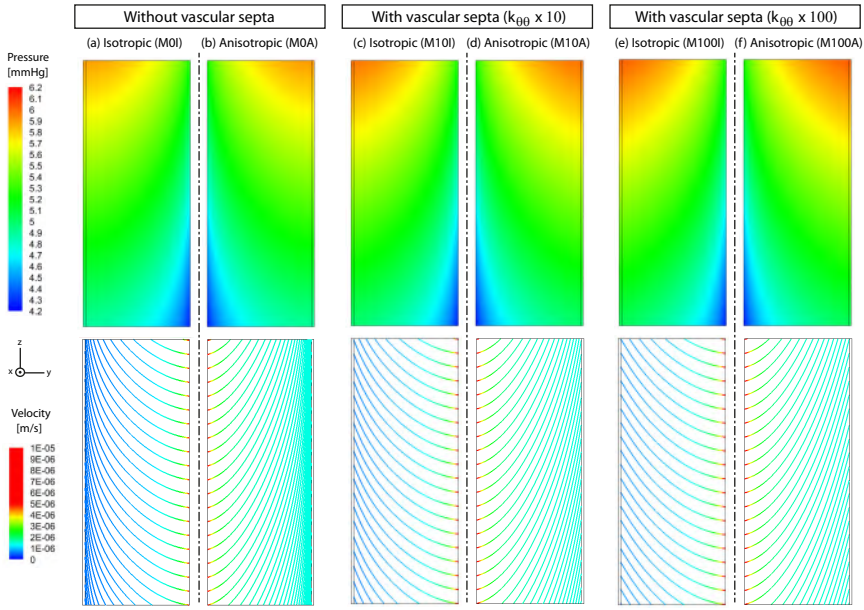

Figure 10.6: Pressures (top) and streamlines (bottom, coloured according to the magnitude of the projection of the velocity into the plane) obtained on a longitudinal cross-section passing through the centre of two opposite vascular septa ($\theta = \pm 90°$) of the lobule models: (a) M0I, (b) M0A, (c) M10I, (d) M10A, (e) M100I, (f) M100A.

In the end, the models without VS show low magnitudes of velocity and thus poor perfusion of the zones lying between neighbouring PTs (Figs. 10.4a-b, 10.7a-b). In contrast, the models with VS predict a better perfusion of these zones and a more uniform velocity distribution (Figs. 10.4c-f, 10.7a-b). Figs. 10.7c-d show, respectively, the in-plane and the total (3D) magnitudes of the velocity as a function of the angle on a circle around the CV (r = 0.3 mm), in order to investigate the homogeneity of the perfusion. The flow is more homogeneous when VS are included, with the amplitude of the velocity magnitude fluctuations clearly being smaller when including VS.

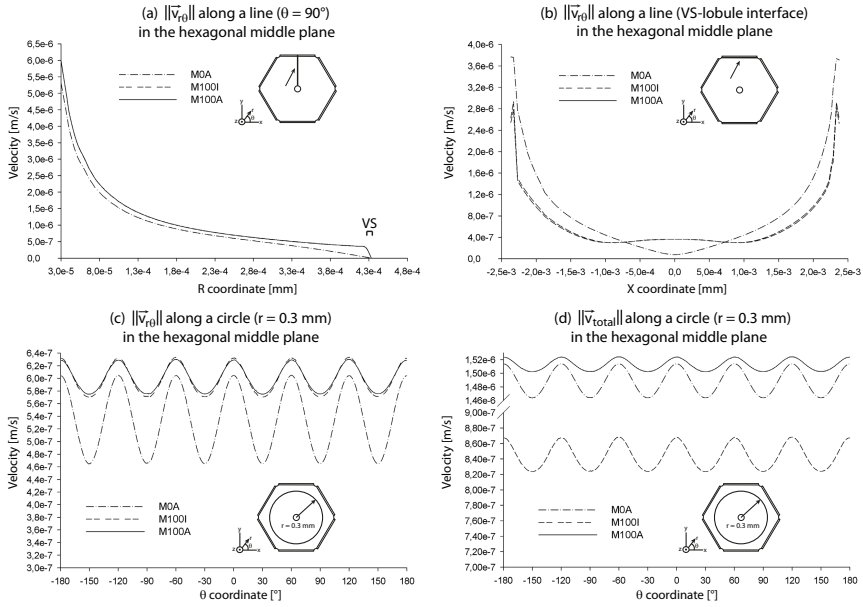

Figure 10.7: Comparison of the velocities at various locations for models M0A, M100I and M100A. (a-c) Magnitudes of the projection of the velocity in the cross-section ($\|\vec{v}_{r\theta}\|$): (a) along a line connecting the central vein (CV) to the middle of a vascular septum (θ=90°) (the range of r is 0.030 mm < r < 0.433 mm), (b) along a line connecting two portal tracts, and (c) around the circle centred on the CV with radius 0.3 mm, plotted against the angle. (d) Magnitudes of the 3D velocity vector around the same circle as shown in (c).

10.3.2 Comparison of isotropic versus anisotropic permeability

In this section we discuss isotropic versus anisotropic conditions, focussing on models M100I and M100A.

In the hexagonal cross-section z=0, the pressure contours and directions of the flow trajectories are similar in the isotropic and the anisotropic models (Fig. 10.4e-f). The in-plane magnitudes of the velocity as well as the total flow rate through the lobule are almost equal (slightly higher in the anisotropic cases): $6.77{\cdot}10^{-5}$ ml/min in M100I and $6.79{\cdot}10^{-6}$ ml/min in M100A (Table 10.2). Figs. 10.5e-f and 10.6e-f show that the flow is similar for the corresponding cases of isotropic and anisotropic permeability, although it is closer to vertical in the anisotropic case. As such, anisotropic permeability leads to a larger longitudinal z-component of the velocity, due to the larger longitudinal permeability in the z-direction. Similar effects are observed in the other models: M0I, M0A, M10I and M10A.

Fig. 10.7c shows that the planar velocity along a circle around the CV in the hexagonal cross-section is approximately equal for both the anisotropic

and isotropic cases, with isotropic conditions resulting in only a slightly higher variation of the predicted velocity. However, the spatially averaged magnitude of the total (3D) velocity is significantly higher and also shows a smaller spatial variance in the anisotropic case, owing to the higher z-component of the velocity (Fig. 10.7d).

10.3.3 Parameter sensitivity study

Boundary conditions as well as geometrical features were varied to investigate the sensitivity of the lobule fluid dynamics to the choice of such parameters.

10.3.3.1 Impact of changes in imposed boundary conditions

Comparing Fig. 10.5f with Fig. 10.8 illustrates how changes of the pressure gradient in the z-direction affect the solution. Increasing the longitudinal pressure gradient leads, as expected, to a larger z-component of the velocity. In contrast, the lobule and total liver outflow and resistance do not change in comparison with the baseline model M100A (Table 10.1 and 10.2). Obviously, the radial and circumferential components of the velocity do not depend on the longitudinal pressure gradient, whereas the z-component of the velocity is directly proportional to $\partial p/\partial z$. As the total flux through the lobule only depends on the radial and circumferential velocity components, it is also independent of $\partial p/\partial z$.

Secondly, the PT-CV pressure drop was increased by increasing the PT pressure by 0.5 mmHg and 1 mmHg (Fig. 10.9). This resulted in higher velocities and lobule flows ($1.03{\cdot}10^{-4}$ ml/min and $1.39{\cdot}10^{-4}$ ml/min for a 0.5 mmHg and 1 mmHg increase of the PT pressure, respectively), because the flow is given by dividing the pressure difference by the resistance (see also Appendix B for details). The lobule resistance remained equal, since the simulation geometry did not change (Table 10.1 and 10.2). Lobule and total liver flow increases were linearly proportional to the increase of the PT-CV pressure drop (Table 10.2). Note that this dependence of the results on the PT-CV pressure difference is predictable, owing to the linearity of the governing equations: the radial and circumferential components of the velocity (and consequently also the flux through the lobule) are directly proportional to the PT-CV pressure drop, while such difference does not affect the z-component of the velocity. Doubling the PT-CV pressure drop, for instance, thus implies doubling the flux through the lobule.

10.3.3.2 Impact of geometry-related parameter variations

Reducing the VS thickness to 5 μm (instead of 10 μm) results in a decrease of the fraction of the PT inflow that drains into the VS (Fig. 10.10). This led to an increase in the lobule resistance ($1.46{\cdot}10^{4}$ mmHg·min/ml) and a decrease

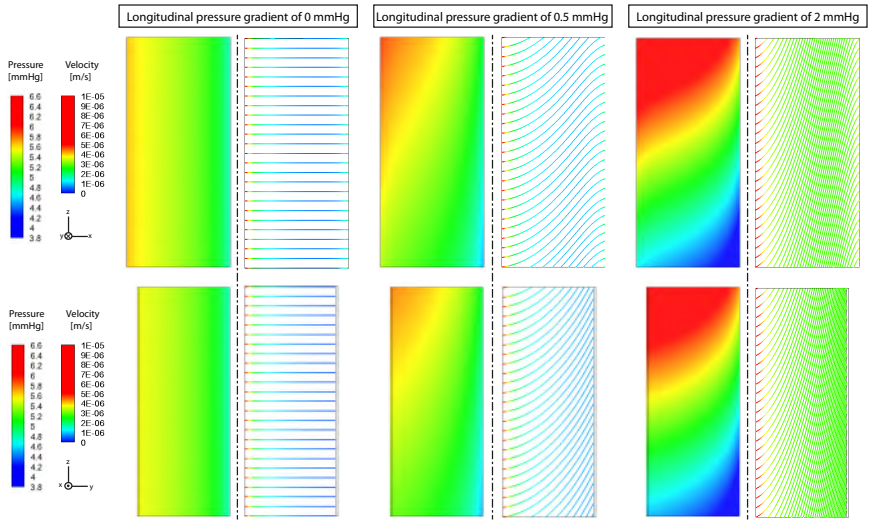

Figure 10.8: Pressures and streamlines (coloured according to the magnitude of the projection of the velocity into the plane $\|\vec{v}_{rz}\|$) obtained on a longitudinal cross-section passing through two portal tracts (top; θ=0°, 180 °) and on a longitudinal cross-section passing through the centre of two opposite vascular septa (bottom; θ=± 90°) for variations of the pressure gradient along the longitudinal z direction (0, 0.5 and 2 mmHg corresponding to models M100A_1, M100A_2 and M100A_3, respectively) compared to the baseline model.

of the lobule flow ($6.51{\cdot}10^{-5}$ ml/min). As such, decreasing the VS thickness by 50% resulted in a lobule and total liver outflow decrease of 4.0% (Table 10.2).

Increasing the PT diameter from 40 to 60 µm results in a decrease of the lobule resistance ($1.35{\cdot}10^{4}$ mmHg·min/ml). Consequently, the lobule outflow increased ($7.01{\cdot}10^{-5}$ ml/min). Pressures and velocities changed accordingly, as illustrated in Fig. 10.10 (lower PT inflow velocity but a larger PT inflow front, higher CV outflow velocity). A 50% increase of the PT diameter thus resulted in a 3.4% increase of the lobule and total liver outflow (Table 10.2). When increasing the CV diameter to 90 µm (instead of 60 µm; Fig. 10.10), the lobule outflow increases ($7.80{\cdot}10^{-5}$ ml/min) while the lobule resistance decreases due to a larger CV outflow front ($1.22{\cdot}10^{4}$ mmHg·min/ ml). As such, a 50% CV diameter increase results in a 15.1% increase of the lobule and total liver outflow (Table 10.2).

Furthermore, when reducing the lobule circumferential diameter to 0.5 mm (Fig. 10.10), the result is a significant increase in the lobule flow ($9.74{\cdot}10^{-5}$ ml/min), implying a smaller lobule resistance to flow ($9.75{\cdot}10^{3}$ mmHg·min/ ml). In addition, a smaller lobule results in a larger number of lobules in a liver of a given size, and leads in this case to a total estimated liver flow of

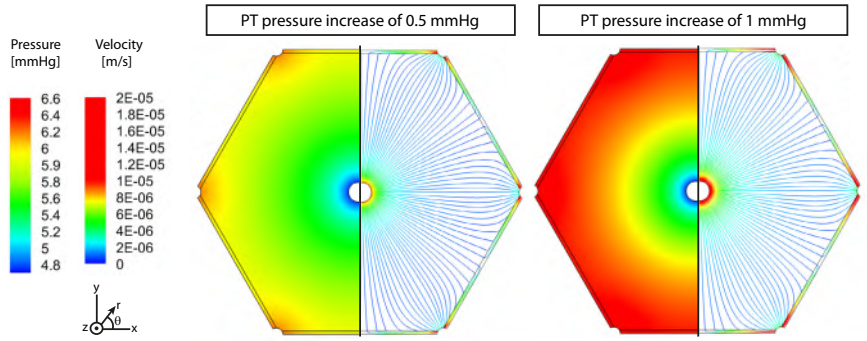

Figure 10.9: Pressures and streamlines (coloured according to the magnitude of the projection of the velocity into the plane $\|\vec{v}_{r\theta}\|$) obtained on the middle cross-section (z=0) using a 0.5 mmHg and 1 mmHg increase of the portal tract pressure (corresponding to models M100A_4 and M100A_5, respectively) compared to the baseline model.

900 ml/min. Consequently, a 50% decrease of the lobule circumferential diameter leads to a 43.7% increase of the lobule outflow and a 474.8% increase of the total liver outflow (Table 10.2).

In summary, amongst the model parameters studied, the lobule circumferential diameter is the most sensitive parameter when looking at the total liver outflow, followed by the pressure drop between the PTs and the CV.

10.4 Discussion

In this study, a 3D computational fluid dynamics model of a liver lobule was developed to study the hepatic microcirculation in order to investigate the effect of vascular septa and anisotropic permeability properties. Additionally, a parameter sensitivity analysis was performed to study the influence of the choice of geometrical and physical parameters on the lobule fluid dynamics.

The models with VS clearly show better perfusion of the zones lying between neighbouring PTs compared to the models without VS, and the flow patterns are more homogeneous when VS are included. The physiological needs of the hepatocytes, and, in particular the requirement of a sufficient supply of oxygen and nutrients for every cell, make the models that include VS seem more physiologically plausible than those without. This is particularly the case for the cells midway between neighbouring PTs whose supply of oxygen is dramatically increased by the existence of VS.

Models with anisotropic permeability show a more spatially homogeneous magnitude of the velocity field compared to those having isotropy (Fig.

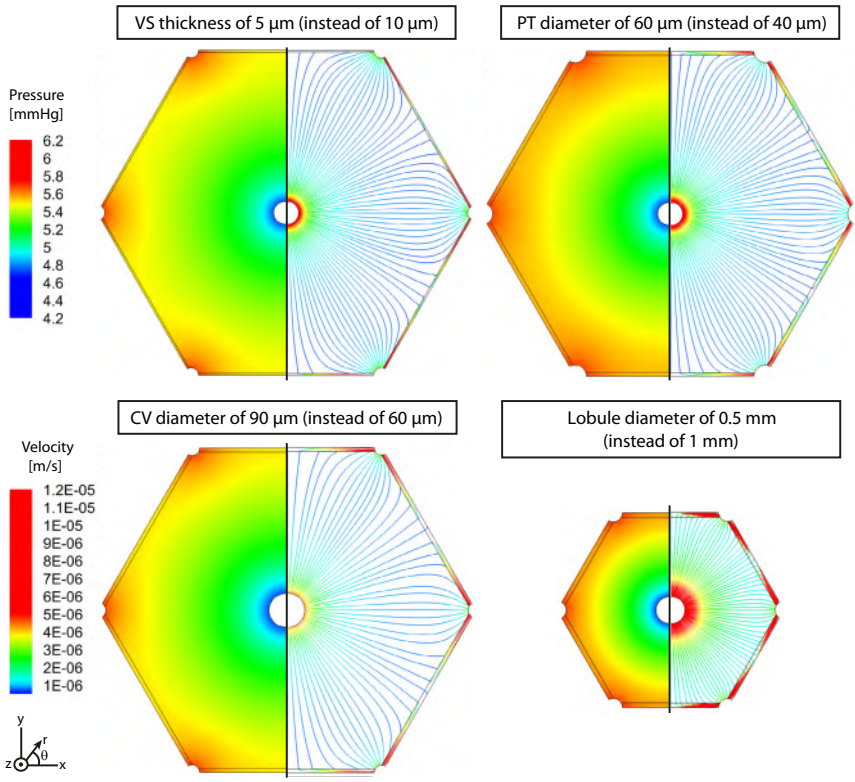

Figure 10.10: Pressures and streamlines (coloured according to the magnitude of the projection of the velocity into the plane $\|\vec{v}_{r\theta}\|$) obtained on the middle cross-section (z=0) using variations of the geometrical features compared to the baseline model: vascular septal thickness of 5 µm (M100A_6), portal tract diameter of 60 µm (M100A_7), central venous diameter of 90 µm (M100A_8) and a lobule circumferential diameter of 0.5 mm (M100A_9).

10.7). Again, this is especially relevant for the relatively poorly perfused zone midway between neighbouring PTs. However, one has to be cautious with this interpretation, since the influence of anisotropy depends on the applied boundary conditions, in particular on the longitudinal pressure gradient. To the authors' knowledge, there are no data available in literature on the longitudinal pressure gradient over a lobule (defined in our model as 1 mmHg per mm; see section 10.2.2). Therefore, we performed a parameter study in which variations of the longitudinal pressure gradient showed as expected differences in the z-components of the velocities, but the lobule and total liver flow did not change (Table 10.1 and 10.2).

In addition, the sensitivity of other parameters was analysed (Table 10.1 and 10.2), showing that the total liver outflow was most sensitive to changes

in the lobule cross-sectional size (determined by the lobule circumferential diameter) and the PT-CV pressure drop. In contrast, the total liver outflow was not or only slightly sensitive to some other parameters (such as the longitudinal pressure gradient in the z-direction and the PT diameter). Estimations of the flow rate and resistance of both a single lobule and the liver as a whole for M100A resulted in $Q_{lobule} = 6.79{\cdot}10^{-5}$ ml/min, $Q_{liver} = 157$ ml/min, $R_{lobule} = 1.40{\cdot}10^{4}$ mmHg·min/ml and $R_{liver} = 6.06{\cdot}10^{-3}$ mmHg·min /ml, respectively (Table 10.2). However, physiological values of Q_{liver} are around 1500 ml/min, which our baseline model underestimates. This is due to the assumptions we made in our modelling, which is not surprising since there are significant variations of certain parameters reported in the literature (PT and CV pressures and diameters, lobule dimensions, liver weight and flow rate etc.). We anticipate that, as better estimates of these parameters become available, the model will become more realistic and can be tuned based on these parameters so that it effectively leads to realistic whole-liver flow characteristics. For example, with a lobule diameter of 0.5 mm and a pressure in the PTs of 0.5 mmHg or 1 mmHg above the default values, the flow rate through the whole liver is 1380 ml/min (M100A_10) or 1850 ml/min (M100A_11), respectively, and these values are within the physiological range (Table 10.2). It is important to stress that we did not perform a direct validation of the proposed models, which would require measurements of pressures or flows at the liver microcirculation level, which is very challenging. However, our results correspond to values that have been described in the literature, and we expect the qualitative predictions of our model to be valid. The demonstrated differences in the flow patterns, especially in the presence of VS, are independent of the assumed sets of boundary conditions. As such, our models incorporating VS and anisotropic permeabilities are probably more accurate since they result in more homogeneous flow patterns compared to previous models.

When comparing the outcomes of our models to literature, the highest magnitudes of velocity were found near the inflow from the PTs and near the CV, which agrees with the findings of Bonfiglio et al. and Ricken et al. [43, 402]. Cohen et al. [76] also stated that the velocity near the CV is higher, resulting in a region of hepatocytes near the CV that have a much higher flux of blood passing them, as compared with hepatocytes that are located nearer the periphery. The flow patterns in the longitudinal sections through the PTs shown in Fig. 10.5 are also similar to those reported earlier by Ricken et al. [402]. However, in their study, the streamlines are closer to those we obtained in our isotropic models, and they are orientated further from the axis than the streamlines we obtained in our anisotropic models. This seems to be a logical consequence of the fact that Ricken et al. [402] used a permeability that is isotropic over the longitudinal cross-section in his 2D model. The

flow patterns in the hexagonal cross-sectional plane of the models without VS (shown in Fig. 10.4 a, b), are also qualitatively similar to those obtained by Bonfiglio et al. [43]. Furthermore, the results obtained by Siggers et al. [433] in their 2D model including VS were comparable with our models including VS (projection into the hexagonal cross-sectional plane). Note that the 3D lobule model obtained in this study could also be interpreted and solved as a combination of a 2D porous model [43, 433] with a superimposed pressure gradient in the z direction and the corresponding z-component of the velocity, since our model uses a prescribed longitudinal pressure drop. Comparing our model with the 3D model of Rani et al. [393], some major differences exist regarding the modelling approach. Rani et al. [393] based the fluid domain of their model on the 3D structure of a liver acinus, while in this study we used the classic schematic hexagonal lobule to represent the functional unit of the liver microcirculation (Fig. 10.1). Which model is most appropriate to represent the functional unit of the liver (e.g. the classic lobule, primary lobule, liver acinus, choleohepaton etc.) is still a matter of debate [117–119, 409, 465, 466]. Furthermore, the model of Rani et al. [393] included a terminal HA, PV and CV as well as two sinusoids having a 23.5 μm radius and fenestrations. These sinusoidal diameter values seem to be high, since sinusoidal diameters are typically reported as being in the order of magnitude of 10 μm (which we also observed in a previous study [98]; see also chapter 9). Larger sinusoids will result in lower vascular resistances and higher permeability compared to our model geometry. Another difference is that Rani et al. [393] used non-Newtonian fluid properties, while we modelled blood as an incompressible Newtonian fluid. Non-Newtonian effects (such as the Fahraeus-Lindqvist effect [28] and the shear thinning effect [393]) are important on the scale of the microscopic sinusoids. Nevertheless, Bonfiglio et al. [43] reported pressure differences of less than 4% when comparing the results of a Newtonian model with those of a shear thinning model. This seems to suggest that non-Newtonian effects are of minor importance for our models. As for the boundary conditions, Rani et al. [393] applied a pressure drop from 95 mmHg to 20 mmHg along the terminal HA and from 25 mmHg to 15 mmHg along the terminal PV, which seems quite high (a PV pressure of 15-25 mmHg is considered indicating portal hypertension). Thus, combining higher pressure(s) (drops) with lower vascular resistances (due to higher sinusoidal diameters) leads to significant differences in the order of magnitude of the predicted velocities with our data. Furthermore, the model of Rani et al. [393] explicitly accounts neither for the effect of more than two tortuous sinusoids, nor for the presence of VS.

10.5 Conclusion

In this study, we developed a 3D mathematical model of a liver lobule, using a porous medium approach, incorporating the effect of vascular septa and anisotropic permeability. The inclusion of vascular septa leads to better perfusion of the zones lying between portal tracts as well as a more spatially homogeneous perfusion of the lobule. The inclusion of anisotropic permeability results in clearly different flow patterns, with streamlines that are oriented closer to the lobule axes. A parameter study revealed that the lobule and total liver flow is most sensitive to variations of the lobule circumferential diameter and the radial pressure drop. In conclusion, the findings suggest that especially the presence of vascular septa results in a more physiologically realistic model of the hepatic microcirculation, and that the model can be tuned to correspond with physiological flows and pressures. Future work should aim at direct validation of the model and to explore applications for a better understanding of liver pathophysiology as well as improved diagnosis and treatment of liver disease.

Four

Conclusions

CHAPTER 11

Conclusions and future perspectives

This chapter recapitulates the most important conclusions of this manuscript.

11.1 Where are we now?

In the introduction of this dissertation, three specific research goals were formulated. We strived to meet these goals with the original research of this PhD work. Below, the key findings are summarised according to each research goal, as well as the innovation of this work, some methodological considerations and future perspectives.

11.1.1 Key findings

Goal 1. *Development of a methodology for the quantitative analysis of the human liver vasculature from the macro- down to the microscopic level.*

The combination of vascular corrosion casting and high-resolution micro-CT scanning with image processing provided novel and unique data on the human hepatic vasculature of the macro-, meso- and microcirculation of one and the same liver (see chapters 5 and 9). This new multilevel approach allows (digitally) visualising the complex liver vasculature at different length scales in 3D and performing a detailed quantitative analysis of the topology and geometrical features, such as vessel radii and lengths. The generated

datasets formed the basis of the computer models of liver perfusion as discussed below (chapters 6 and 9).

Goal 2. *Development of computer models to study the intrahepatic haemodynamics and quantify biomechanical stressors on the macro- and microscale level.*

Based on the quantitative morphological analysis of the hepatic macrovasculature, an initial electrical analog model of the human liver was established (chapter 6). The model is able to predict pressure and flow parameters throughout the liver vasculature while perfusion is in regime (steady state). It is applicable not only to natural blood flow, but also to machine perfusion (MP). In the case of pressure-controlled hypothermic MP (HMP) with low pressures, the model predicts lower sinusoidal shear stresses than in the case of natural blood flow, and hence no shear-related endothelial damage (during regime perfusion). However, there may be other non-biomechanical factors that contribute to endothelial damage, such as biochemical influences evoked by using synthetic perfusion fluids instead of blood. Though the results of the initial electrical models are promising, additional experimental research was necessary to validate and tune the electrical liver model (see Goal 3).

Image processing of the micro-CT datasets of human liver microvascular samples provided more insight into structural-related perfusion characteristics (e.g. porosity) of the microcirculation. A 3D numerical microcirculation model of a sample from a human liver was constructed (chapter 9). The resulting data indicate that the human hepatic microcirculation clearly displays anisotropic behaviour in terms of permeability, which was quantified by means of a permeability tensor. In particular, a higher permeability was demonstrated along the direction of the central vein, and about two times lower but approximately equal permeabilities along the radial and circumferential directions of the liver lobule. Since the permeability coefficients depend on the flow direction, liver microcirculation models should thus take into account sinusoidal anisotropy.

With these new insights, we developed a 3D porous medium model of a liver lobule, incorporating anisotropic permeability as well as vascular septa (chapter 10). The inclusion of vascular septa leads to better perfusion of the zones lying between portal tracts as well as a more spatially homogeneous perfusion of the lobule. The inclusion of anisotropic permeability results in clearly different flow patterns, with streamlines that are oriented closer to the lobule axes. In conclusion, our findings suggest that especially the presence of vascular septa results in a more physiologically plausible model of the hepatic microcirculation, and that the model can be tuned to correspond with physiological flows and pressures.

Goal 3. *Validation and application of the acquired models.*

To test the electrical analog model against experimental data, we presented a methodology to validate and tune the initial electrical analog model of hepatic perfusion (developed in chapter 6) to a specific liver (to one liver in particular in chapter 7). To do so, HMP experiments were used to capture the perfusion behaviour of two human liver grafts by simultaneously measuring pressures and flows at the hepatic in- and outlet vessels. Experimentally acquired HA and PV input impedances were used to fit compact Windkessel (WK) models in order to mathematically capture the global hepatic perfusion behaviour. Subsequently, the WK properties were distributed over the extended liver-specific electrical analog model.

In chapter 8, we used the electrical analog liver model to assess the haemodynamic effects of partial hepatectomy procedures (e.g. in the case of living donor liver transplantation). The model was tuned to the rat liver to allow for comparison with existing experimental data. Results gave evidence of hyperperfusion effects such as portal hypertension and elevated lobe-specific portal venous flows. For example, the model predicts that a 90% partial hepatectomy leads to an approximately fourfold increase in portal pressure and a fourfold rise of the lobe-specific portal venous and hepatic venous flow, which may severely damage the microvasculature.

11.1.2 Methodological considerations

One of the major limitations of this dissertation is the limited number of human livers that were used. Consequently, one has to be careful when generalising findings and results should rather be interpreted as those of a specific liver. This inevitably has to do with the fact that human livers, available for research, are extremely scarce and their availability depends on the moment that a donor liver is discarded after failed reallocation. It is important to stress that, although discarded, the organs did not show any macroscopic abnormalities compared to healthy subjects. It remains, however, important to do this kind of research in human livers because of well-known limitations of animal models (e.g. anatomical differences). In the end, more livers should thus be investigated in order to provide a more generic dataset of the human liver vascular architecture and perfusion characteristics. At the same time, however, many processing steps are laborious and extremely time demanding, limiting the feasibility of extended research.

As vascular geometrical data are the input for our hepatic computer models, it is important to address how HMP and vascular corrosion casting might affect the vasculature. While HMP has the advantage of keeping the microvasculature open and intact, the disadvantage is that high shear stresses may arise and damage endothelial cells (although this is contradicted by our results when performing pressure-controlled HMP at low pressures). Moreover, vascular corrosion casting may lead to slight shrinkage of

the resin. Nevertheless, the casting procedure was executed according to standardised procedures by a team having many years of expertise and our diameter measurements were comparable with literature data.

Ideally, complete liver casts should be scanned *at once* at a sufficient resolution to allow visualising all vessels down to the sinusoids. However, this is practically impossible due to computational and software limitations. Consequently, a multilevel approach had to be used to consecutively study the macro-, meso- and microcirculation. As there is still a gap of a few blood vessel generations between the meso- and microcirculation, additional data on these missing generations may be helpful to describe the full spectrum of the hepatic vasculature. However, image processing becomes extremely complicated at this level due to an exponential increase of the number of (touching) vessels when moving towards higher generation numbers.

The developed electrical analog model is a lumped parameter model, meaning that it is a concise model to analyse complicated vascular networks based on a simplification of the actual anatomical reality. However, we regarded its use justified to model the overall hepatic haemodynamic parameters, as we are mainly interested in relative differences (e.g. natural liver versus HMP), and as it is practically impossible - at this moment - to develop models taking into account all anatomical features of the complete liver vasculature due to computational and software limitations. Nonetheless, further refinements may be relevant, especially at the level of the microcirculation. This is why we focused on modelling the perfusion behaviour of the hepatic microcirculation in chapters 9 and 10. Furthermore, the electrical model simulates steady state hepatic perfusion, while transient phenomena (for instance when starting up perfusion) may induce different biomechanical stressors in the vasculature compared to steady state perfusion, possibly leading to endothelial damage.

The PV hydraulic input impedances, acquired in chapter 7, showed a relatively low frequency content due to a small amount of coherent points between pressure and flow signals. Caution is thus recommended when interpreting the PV results. Ideally, more frequency content should be acquired to more accurately fit Windkessel models and extended electrical models to PV impedance data. This might be achieved by inducing analysing perfusion perturbations (such as transient phenomena, e.g. starting or stopping the pumps as was done during the experiments of chapter 7) or adjusting the HMP control circuit.

The electrical analog rat liver model of chapter 8 was solely based on vascular resistances (simplification of the original model in chapter 6), not taking into account (visco-)elasticity and inertial effects. Since pulsatility is heavily damped when reaching the hepatic microcirculation, our main interest was analysing the DC model to obtain time-averaged pressures and

flows, as we believed this to be sufficient to quantify overall hyperperfusion effects at the level of the microvasculature.

The microcirculatory perfusion characteristics were acquired based on one microvascular sample of a human liver (chapter 9). Again, results should be interpreted as indicative. More samples might allow a better estimation of these characteristics, but imply a labour-intensive procedure to acquire good geometries and meshes. Consequently, only one sample was studied, of which subsamples were used to characterise the permeability of liver tissue. Care was taken to make sure that the sinusoidal heterogeneity was sufficiently covered when selecting the studied sample. Furthermore, it was difficult to define accurate boundary conditions, especially for the lobule model of chapter 10, as literature data on the microvasculature (dimensions, pressures etc.) are scarce and vary substantially (e.g. for the diameter of central veins). Due to a lack of accurate measurement techniques to acquire pressures and flow data at the microcirculation level, the obtained micromodels were not (yet) validated. However, we showed that our lobule model (chapter 10) can be tuned to predict physiological liver flows and pressures.

As this PhD work focused on modelling the hepatic vasculature and blood perfusion, other vessel systems (the biliary system and the lymphatics) as well as mass transport (e.g. between the vascular compartment and the space of Disse) were not taken into account. We believe that these phenomena only slightly affect hepatic perfusion (e.g. approximately 0.5 ml lymph production for every litre of blood flow; section 1.2.2). However, these systems as well as other factors (such as biological and metabolic factors) play an important role in the homeostasis of the organ and may be involved in the process of (endothelial) damage.

11.1.3 Innovation

This PhD thesis is innovative both at the level of liver morphology research as well as at the level of hemodynamic modelling of hepatic blood flow.

11.1.3.1 Morphology-related novelties

We applied an innovative combination of state of-the-art techniques (vascular corrosion casting, micro-CT imaging, image processing and vascular architecture analysis) to generate detailed and unique morphological data on the vasculature of human livers. Both the combination and integration of these techniques, as well as the use of human liver samples, was unprecedented. Most other studies are indeed based on animal models (rat livers, porcine livers etc.). Furthermore, we analysed the geometrical features of the three hepatic vascular trees (the hepatic arterial, portal venous and hepatic venous tree) simultaneously, spanning the micro-, meso- and the microvasculature for one and the same liver, where previous work often addressed

only one (or two) vascular trees and focused on only one length scale. The acquired data are thus truly unique.

11.1.3.2 Modelling-related novelties

While the modelling techniques (lumped parameter modelling and computational fluid dynamics) as such are not novel, the applications and the level of detail of implementation are (fairly) new. We are the first to generate the data to develop a liver-specific extended electrical analog model for human livers. A previous model was based on dog liver data. More important, we also validated and calibrated the electrical liver model by performing human liver HMP experiments. These experiments revealed that literature values of one of the critical model parameters is actually a few orders of magnitude off, with important consequences for computed (pulsatile) hemodynamic variables. We also applied an extended lobe-specific version of the model to assess the hemodynamic effects immediately after partial hepatectomy.

In addition to the electrical model, the perfusion characteristics of the human liver microcirculation were studied using a computational fluid dynamics micromodel based on effective 3D imaging data of the human hepatic microcirculation instead of an idealised geometry as in existing literature. This allowed us to convincingly demonstrate the anisotropic nature of the microcirculation, and to provide quantitative values for the anisotropic permeability tensor which can be used in future research. We used this information to construct a 3D porous media liver lobule model. Besides the extension to 3D, other novelties over existing models were the inclusion of the anisotropic permeability tensor as well as vascular septa.

11.2 Where to go from here?

Future research may focus on optimising and extending the methodologies and models developed in this dissertation. Although the original research of this PhD work is mainly fundamental, future research may also include (new) applications.

First of all, it would be relevant to enlarge the data pool by repeating the presented methodology for more livers. In addition, developing an algorithm to (semi-)automate the geometrical data acquisition of the hepatic vasculature may significantly speed up this procedure (for some preliminary results: see [96, 97]).

The electrical analog model of the hepatic perfusion may be extended from modelling steady state perfusion to transient behaviour, and the microcirculation models may be coupled to the electrical model. The (tuned) electrical model may be useful to test and compare different MP settings before performing animal or human liver MP experiments, as well as to predict

- in the longer term - liver-specific optimal perfusion settings. Furthermore, the monitoring system of MP devices may potentially benefit from incorporating real-time calculations of input impedances and Windkessel models, giving the user information on the perfusion properties of the organ (such as its vascular resistance and stiffness).

The models, developed within this PhD, may also be useful in other domains of hepatology, in which liver perfusion plays an important role (e.g. liver cirrhosis with pulmonary hypertension, the prediction of the outcome of transjugular intrahepatic portosystemic shunt procedures etc.).

In the longer term, surgery may benefit from more detailed models of hepatic perfusion as they allow taking the haemodynamics of functional liver tissue into account during surgical planning besides information on the anatomy of the macro- and microcirculation. As such, these models may be helpful to predict patient-specific outcomes after e.g. a partial hepatectomy due to living donor liver transplantation, split liver transplantation, a resection due to hepatocellular carcinoma, the placement of a transjugular intrahepatic portosystemic shunt and the prediction of its potential failure etc. Another possible model application in surgery is to simulate the effect of the paediatric Fontan procedure (which may result in severe hepatic complications in the longer term) on the liver haemodynamics. As a matter of fact, H. Ho et al. recently used a simplified version of our electrical model to simulate the effect of a right lobectomy [195] and transjugular intrahepatic portosystemic shunts [197], as well as to enlighten the hepatic arterial buffer response effect [196].

In several liver pathologies, alterations in the vasculature and hepatic haemodynamics seem to be important markers of disease progression (e.g. for cirrhosis, hepatocellular carcinoma etc.) and complications (e.g. portal hypertension, collateral formation etc.). This field is largely unexplored. Our methodologies can thus also be applied to diseased organs (e.g. liver cirrhosis) in order to compare them to normal organs and to enlighten the underlying disease processes. Liver cirrhosis is characterised by liver fibrosis and the formation of regenerative nodules, which severely alters the hepatic microarchitecture by inducing a step-by-step loss of normal lobular structure with abnormal branching patterns, the capillarisation of sinusoids, the formation of shunt vessels etc. (see also section 2.1.4). We are actually planning a study on the development of cirrhotic liver disease by means of a rat model and by applying our methodologies. At certain time steps, rats will be sacrificed to image and model their hepatic perfusion.

The detailed hepatic angioarchitectural data, obtained in this work, may also be of interest to anatomists and morphologists, e.g. to better understand the topographical hepatic vascular anatomy and function. In this respect, it may be interesting to also take into account the anatomical segmental subdivision when analysing the hepatic vasculature of new human liver casts.

Furthermore, the generated 3D visualisations of the liver vasculature at different scales may be applicable for educational purposes (and potentially for surgical training).

Our approach of quantifying and modelling the hepatic vasculature and perfusion, may analogously be applied to the biliary tree and bile flow, or to other organs (e.g. kidneys). Furthermore, our approach offers the possibility to compare the hepatic vasculature of different species (e.g. human versus rat livers).

These applications thus illustrate that this PhD resulted in a number of methodologies, forming the building blocks for different future research directions.

11.3 Take home message

The take home message of this work is that a multi-level framework of models was developed to simulate hepatic perfusion at different scales. This versatile framework was applied in the context of liver transplantation and resulted in unique 3D morphological and geometrical data on human and rat livers, as well as novel models and insights into the haemodynamic impact of machine perfusion preservation of donor livers, partial hepatectomy procedures (such as living donor liver transplantation), and into the perfusion characteristics of the liver microcirculation. Doing so, we were able to find some missing pieces of the puzzle on liver perfusion. However, further research is necessary to reveal the complete picture…

Appendices

APPENDIX A

Calculation of the principal axes of the permeability tensor

To determine the principal axes and principal permeabilities of tensor K, the eigenvalues as well as the eigenvectors had to be calculated. As illustrated in Liakopoulos et al. [286], a permeability tensor has to be a symmetric matrix. Accordingly, a real symmetric matrix has real eigenvalues and real eigenvectors corresponding to an orthogonal coordinate system representing the principal axes [33]. As such, the symmetric part of K was defined by calculating the mean values of the off-diagonal coefficients as illustrated for $k_{r\theta}$ and $k_{\theta r}$ in eq. A.1. This operation resulted in a symmetric matrix K_{symm} as defined in eq. A.2.

$$k_{symm,r\theta} = \frac{k_{r\theta} + k_{\theta r}}{2} \tag{A.1}$$

$$K_{symm} = \begin{bmatrix} k_{rr} & k_{symm,r\theta} & k_{symm,rz} \\ k_{symm,r\theta} & k_{\theta\theta} & k_{symm,\theta z} \\ k_{symm,rz} & k_{symm,\theta z} & k_{zz} \end{bmatrix} \tag{A.2}$$

Subsequently, the eigenvalues (λ_1, λ_2, λ_3) were calculated by solving the characteristic polynomial of K_{symm} (eq. A.3), and accordingly, the eigenvectors ($\vec{e_1}$, $\vec{e_2}$, $\vec{e_3}$), being the directions of the principal axes belonging to K_{symm}, were determined (eq. A.4).

$$det(K_{symm} - \lambda I) = \begin{bmatrix} k_{rr} - \lambda & k_{symm,r\theta} & k_{symm,rz} \\ k_{symm,r\theta} & k_{\theta\theta} - \lambda & k_{symm,\theta z} \\ k_{symm,rz} & k_{symm,\theta z} & k_{zz} - \lambda \end{bmatrix} = 0 \tag{A.3}$$

$$(K_{symm} - \lambda I) \cdot \vec{e} = 0 \tag{A.4}$$

Using the eigenvectors (columns of matrix V; eq. A.5), K_{symm} was diagonalised resulting in the diagonal matrix K_d (eq. A.6). This matrix represents the principal permeabilities belonging to the principal axes defined by the eigenvectors.

$$K_d = V^T K_{symm} V = \begin{bmatrix} \vec{e}_1 \\ \vec{e}_2 \\ \vec{e}_3 \end{bmatrix} K_{symm} \begin{bmatrix} \vec{e}_1 & \vec{e}_2 & \vec{e}_3 \end{bmatrix} \tag{A.5}$$

$$= \begin{bmatrix} k_{d,11} & 0 & 0 \\ 0 & k_{d,22} & 0 \\ 0 & 0 & k_{d,33} \end{bmatrix} \tag{A.6}$$

Knowing the eigenvectors and accompanying diagonal matrix, we were able to calculate the angles between the predefined coordinate system (r, θ, z) and the resulting principal axes (defined by the eigenvectors). This is illustrated in eq. A.7 for the angle α between the r axis and $\vec{e}_1$.

$$\alpha = acos\left(\frac{\vec{r} \cdot \vec{e}_1}{\|\vec{r}\| \, \|\vec{e}_1\|}\right) \tag{A.7}$$

APPENDIX B

Estimation of the lobe-specific and total liver flow and resistance

Based on the simulation results, the flow rate in a single lobule, Q_{lobule} [m³/s], can be estimated by multiplying the surface area of the CV by a typical normal velocity component of the flux entering the CV:

$$Q_{lobule} = \|\vec{v}_{CV}\| \cdot A_{CV} = \|\vec{v}_{CV}\| \cdot 2\pi r_{CV} \cdot l_{lobule} \tag{B.1}$$

where $\vec{v}_{CV}$ [m/s] is the radial velocity at the CV outflow, A_{CV} [m²] is the surface area of the CV lumen, r_{CV} [3·10^{-5} m] is the CV radius, and l_{lobule} [10^{-3} m] the lobule length. The total liver flow, Q_{liver} [m³/s], is calculated by multiplying Q_{lobule} by the number of lobules, n, which is estimated by dividing a typical volume of the liver by the volume of a lobule (hexagonal prism volume):

$$Q_{liver} = Q_{lobule} \cdot n \tag{B.2}$$

$$n = \frac{V_{liver}}{V_{lobule}} = \frac{\frac{m_{liver}}{\rho_{liver}}}{3r_{lobule}\frac{\sqrt{3}r_{lobule}}{2}l_{lobule}} \tag{B.3}$$

where V_{liver} [m³] is the liver volume, V_{lobule} [m³] is the lobule volume, m_{liver} [1.5 kg] is the mass of the liver [311], ρ_{liver} [10³ kg/m³; equal to water] the liver density and r_{lobule} is the length of a side of the lobule hexagonal

cross-section. The lobule-specific hydraulic resistance, R_{lobule} [Pa·s/m^3], is estimated by dividing the pressure difference between the inflow and outflow (along the streamlines running from PT to CV) by the lobule-specific flow:

$$R_{lobule} = \frac{\Delta P_{lobule}}{Q_{lobule}} \tag{B.4}$$

Since the lobules are arranged in parallel with respect to the blood flow, the total hydraulic resistance of the microvasculature of the liver is calculated as the lobule resistance divided by the estimated number of lobules n:

$$R_{liver} = \frac{R_{lobule}}{n} \tag{B.5}$$

Bibliography

[1] epa.gov/ncct/virtual_liver.

[2] histologyatlas.wisc.edu.

[3] web.williams.edu/biology/Faculty_Staff/sswoap/site/ratmousepic.

[4] www.adamimages.com.

[5] www.arizonatransplant.com/healthtopics/liver.

[6] www.eltr.org/spip.php?article161.

[7] www.eurotransplant.org.

[8] www.fresenius.com/586.htm.

[9] www.gambro.com/en/global/Products/Acute-Care/Acute-Monitors/MARS.

[10] www.nlm.nih.gov/frankenstein/preface.html.

[11] www.organ-assist.nl.

[12] www.passport-liver.eu.

[13] www.scientificamerican.com/slideshow.cfm?id=placenta-capturing-inner-beauty.

[14] www.transplantliverindia.com/node/13.

[15] www.virtual-liver.de.

[16] M. Abdolrazaghi, M. Navidbakhsh, and K. Hassani. Mathematical modelling and electrical analog equivalent of the human cardiovascular system. *Cardiovascular Engineering*, 10(2):45–51, 2010.

[17] P. Abt, M. Crawford, N. Desai, J. Markmann, K. Olthoff, and A. Shaked. Liver transplantation from controlled non-heart-beating donors: An increased incidence of biliary complications. *Transplantation*, 75(10):1659–1663, 2003.

[18] S. Aharinejad, W. Schreiner, and F. Neumann. Morphometry of human coronary arterial trees. *The Anatomical Record*, 251(1):50–59, 1998.

[19] M.A. Aller, L. Lorente, I. Prieto, L.M. Moquillaza, and J. Arias. Hepatectomies in the rat: A look at the caudate process through microsurgery. *Digestive and Liver Disease*, 41(10):695–699, 2009.

[20] G. Almeida-Porada, E.D. Zanjani, and C.D. Porada. Bone marrow stem cells and liver regeneration. *Experimental Hematology*, 38(7):574–580, 2010.

[21] R. Anaya-Prado and J.A. Delgado-Vazquez. Scientific basis of organ preservation. *Current Opinion in Organ Transplantation*, 13(2):129–134, 2008.

[22] P.P. Anthony, K.G. Ishak, N.C. Nayak, H.E. Poulsen, P.J. Scheuer, and L.H. Sobin. Morphology of cirrhosis. *Journal of Clinical Pathology*, 31(5):395–414, 1978.

[23] M.M. Augustine, I.R. Kamel, and T.M. Pawlik. Morphometric imaging techniques and the functional liver remnant. In D.C. Madoff, M. Makuuchi, M. Nagino, and J.-N. Vauthey, editors, *Venous embolization of the liver*, chapter 11, pages 95–105. Springer, London, 2011.

[24] R. Avritscher, K.C. Wright, S. Javadi, R. Uthamanthil, S. Gupta, M. Gagea, R.L. Bassett, R. Murthy, M.J. Wallace, and D.C. Madoff. Development of a large animal model of cirrhosis and portal hypertension using hepatic transarterial embolization: A study in swine. *Journal of Vascular and Interventional Radiology*, 22(9):1329–1334, 2011.

[25] C. Bae, S.D. Henry, and J.V. Guarrera. Is extracorporeal hypothermic machine perfusion of the liver better than the 'good old icebox'? *Current Opinion in Organ Transplantation*, 17(2):137–142, 2012.

[26] D. Balfoussia, D. Yerrakalva, K. Hamaoui, and V. Papalois. Advances in machine perfusion graft viability assessment in kidney, liver, pancreas, lung, and heart transplant. *Experimental and Clinical Transplantation*, 10(2):87–100, 2012.

[27] R. Banares, F. Nevens, F.S. Larsen, R. Jalan, A. Albillos, M. Dollinger, F. Saliba, T. Sauerbruch, S. Klammt, J. Ockenga, A. Pares, J. Wendon, T. Brunnler, L. Kramer, P. Mathurin, M. de la Mata, A. Gasbarrini, B. Mullhaupt, A. Wilmer, W. Laleman, M. Eefsen, S. Sen, A. Zipprich, T. Tenorio, M. Pavesi, H.H. Schmidt, S. Mitzner, R. Williams, and V. Arroyo. Extracorporeal albumin dialysis with the molecular adsorbent recirculating system in acute-on-chronic liver failure: The RELIEF trial. *Hepatology*, 57(3):1153–1162, 2013.

[28] J.H. Barbee and G.R. Cokelet. The Fahraeus effect. *Microvascular Research*, 3(1):6–16, 1971.

[29] A. Baretta, C. Corsini, W. Yang, I.E. Vignon-Clementel, A.L. Marsden, J.A. Feinstein, T.Y. Hsia, G. Dubini, F. Migliavacca, and G. Pennati. Virtual surgeries in patients with congenital heart disease: A multi-scale modelling test case. *Philosophical Transactions of the Royal Society A: Mathematical, Physical & Engineering Sciences*, 369(1954):4316–4330, 2011.

[30] C.A. Basciano. *Computational particle-hemodynamics analysis applied to an abdominal aortic aneurysm with thrombus and microsphere-targeting of liver tumors*. PhD thesis, North Carolina State University, 2010.

[31] C.A. Basciano, C. Kleinstreuer, A.S. Kennedy, W.A. Dezarn, and E. Childress. Computer modeling of controlled microsphere release and targeting in a representative hepatic artery system. *Annals of Biomedical Engineering*, 38(5):1862–1879, 2010.

[32] E. Bavu, J.-L. Gennisson, M. Couade, J. Bercoff, V. Mallet, M. Fink, A. Badel, A. Vallet-Pichard, B. Nalpas, M. Tanter, and S. Pol. Noninvasive in vivo liver fibrosis evaluation using supersonic shear imaging: A clinical study on 113 hepatitis C virus patients. *Ultrasound in Medicine and Biology*, 37(9):1361–1373, 2011.

[33] R.A. Beezer. *A first course in linear algebra*. University of Puget Sound, Tacoma, Washington, USA, 2010.

[34] S. Beloucif, N. Brienza, K. Andreoni, T. Ayuse, M. Takata, C.P. Odonnell, and J.L. Robotham. Distinct behavior of portal venous and arterial vascular waterfalls in porcine liver. *Journal of Critical Care*, 10(3):104–114, 1995.

[35] M. Bessems, B.M. Doorschodt, J.L.P. Kolkert, R.L. Vetelainen, A.K. van Vliet, H. Vreeling, J. van Marle, and T.M. van Gulik. Preservation of steatotic livers: A comparison between cold storage and machine perfusion preservation. *Liver Transplantation*, 13(4):497–504, 2007.

[36] M. Bessems, B.M. Doorschodt, A.K. van Vliet, and T.M. van Gulik. Improved rat liver preservation by hypothermic continuous machine perfusion using Polysol, a new, enriched preservation solution. *Liver Transplantation*, 11(5):539–546, 2005.

[37] J. Bézy-Wendling, M. Kretowski, and Y. Rolland. Hepatic tumor enhancement in computed tomography: Combined models of liver perfusion and dynamic imaging. *Computers in Biology and Medicine*, 33(1):77–89, 2003.

[38] H. Bismuth. Surgical anatomy and anatomical surgery of the liver. *World Journal of Surgery*, 6(1):3–9, 1982.

[39] P.J. Blanco and R.A. Feijoo. A dimensionally-heterogeneous closed-loop model for the cardiovascular system and its applications. *Medical Engineering & Physics*, 2012.

[40] E. Bloch. The termination of hepatic arterioles and the functional unit of the liver as determined by microscopy of the living organ. *Annals of the New York Academy of Sciences*, 170:78–87, 1970.

[41] I. Bockx. *Neurohepatology: The role of the vagus nerve in liver disease*. PhD thesis, Katholieke Universiteit Leuven, 2010.

[42] H.G. Bohlen, R. Maass-Moreno, and C.F. Rothe. Hepatic venular pressures of rats, dogs, and rabbits. *American Journal of Physiology*, 261(3):G539–G547, 1991.

[43] A. Bonfiglio, K. Leungchavaphongse, R. Repetto, and J.H. Siggers. Mathematical modeling of the circulation in the liver lobule. *Journal of Biomechanical Engineering*, 132(11):111011, 2010.

[44] C. Booth, T. Soker, P. Baptista, C.L. Ross, S. Soker, U. Farooq, R.J. Stratta, and G. Orlando. Liver bioengineering: Current status and future perspectives. *World Journal of Gastroenterology*, 18(47):6926–34, 2012.

[45] H. Bourquain, A. Schenk, and H.O. Peitgen. Computer-assisted planning and decision-making in living-donor liver transplantation. In Kaihara S I.Y. Tanaka K, editor, *Living-donor liver transplantation - surgical techniques and innovations*, pages 23–28. Prous Science, Barcelona, 2003.

[46] E.M. Boyle and E.D. Verrier. Rheologic considerations in organ preservation. *Annals of Thoracic Surgery*, 69(1):12–13, 2000.

[47] D.J. Breen, E.E. Rutherford, B. Stedman, C. Lee-Elliott, and C.N. Hacking. Intrahepatic arterioportal shunting and anomalous venous drainage: Understanding the CT features in the liver. *European Radiology*, 14(12):2249–2260, 2004.

[48] L. Brettschneider, J. Kolff, G.V. Smith, A.J. Martin, P. Taylor, and T.E. Starzl. An evaluation of perfusion constituents in liver preservation. *Surgical Forum*, 19:354–356, 1968.

[49] J. Brockmann, S. Reddy, C. Coussios, D. Pigott, D. Guirriero, D. Hughes, A. Morovat, D. Roy, L. Winter, and P.J. Friend. Normothermic perfusion A new paradigm for organ preservation. *Annals of Surgery*, 250(1):1–6, 2009.

[50] J.G. Brockmann, A. Vaidya, S. Reddy, and P.J. Friend. Retrieval of abdominal organs for transplantation. *British Journal of Surgery*, 93(2):133–146, 2006.

[51] A. Brunon, K. Bruyere-Garnier, and M. Coret. Mechanical characterization of liver capsule through uniaxial quasi-static tensile tests until failure. *Journal of Biomechanics*, 43(11):2221–2227, 2010.

[52] J. Op Den Buijs, Z. Bajzer, and E.L. Ritman. Branching morphology of the rat hepatic portal vein tree: A micro-CT study. *Annals of Biomedical Engineering*, 34(9):1420–1428, 2006.

[53] W.E. Burkel. The fine structure of the terminal branches of the hepatic arterial system of the rat. *Anatomical Record*, 167(3):329–349, 1970.

[54] P. Burra and R. Freeman. Trends in liver transplantation 2011. *Journal of Hepatology*, 56:S101–S111, 2012.

[55] A.K. Burroughs. The hepatic artery, portal venous system and portal hypertension: The hepatic veins and liver in circulatory failure. In *Sherlock's diseases of the liver and biliary system*, pages 152–209. Wiley-Blackwell, 2011.

[56] A.J. Butler, M.A. Rees, D.G.D. Wight, N.D. Casey, G. Alexander, D.J.G. White, and P.J. Friend. Successful extracorporeal porcine liver perfusion for 72 hr. *Transplantation*, 73(8):1212–1218, 2002.

[57] F. Ariza Cadena, L.F. Carmona Serna, I.F. Quintero C, L.A. Caicedo, C.A. Vidal Perdomo, and L.F. González. Sistemas de soporte hepático extracorpóreo. *Revista Colombiana de Anestesiología*, 39:528–543, 2011.

[58] R.Y. Calne, K. Rolles, D.J. White, S. Thiru, D.B. Evans, P. McMaster, D.C. Dunn, G.N. Craddock, R.G. Henderson, S. Aziz, and P. Lewis. Cyclosporin A initially as the only immunosuppressant in 34 recipients of cadaveric organs: 32 kidneys, 2 pancreases, and 2 livers. *Lancet*, 2(8151):1033–1036, 1979.

[59] E.M. Carlisle and G. Testa. Adult to adult living related liver transplantation: Where do we currently stand? *World Journal of Gastroenterology*, 18(46):6729–6736, 2012.

[60] J.C. Carr, A.A. Nemcek, M. Abecassis, A. Blei, L. Clarke, F.S. Pereles, R. McCarthy, and J.P. Finn. Preoperative evaluation of the entire hepatic vasculature in living liver donors with use of contrast-enhanced MR angiography and true fast imaging with steady-state precession. *Journal of Vascular and Interventional Radiology*, 14(4):441–449, 2003.

[61] A. Carrel and C.A. Lindbergh. The culture of whole organs. *Science*, 81(2112):621–623, 1935.

[62] C. Casteleyn. *Vascular anatomy of the mouse visualized by the corrosion casting technique*. master thesis, Ghent University, 2008.

[63] C. Casteleyn, B. Trachet, D. Van Loo, D.G.H. Devos, W. Van den Broeck, P. Simoens, and P. Cornillie. Validation of the murine aortic arch as a model to study human vascular diseases. *Journal of Anatomy*, 216(5):563–571, 2010.

[64] S.C. Chan, C.M. Lo, and S.T. Fan. Simplifying living donor liver transplantation. *Hepatobiliary & Pancreatic Diseases International*, 9(1):9–14, 2010.

[65] S.C. Chan, C.M. Lo, K.K.C. Ng, I.O.L. Ng, B.H. Yong, and S.T. Fan. Portal inflow and pressure changes in right liver living donor liver transplantation including the middle hepatic vein. *Liver Transplantation*, 17(2):115–121, 2011.

[66] S. Chatelin, J. Oudry, N. Perichon, L. Sandrin, P. Allemann, L. Soler, and R. Willinger. In vivo liver tissue mechanical properties by transient elastography: Comparison with dynamic mechanical analysis. *Biorheology*, 48(2):75–88, 2011.

[67] C.Y. Chen, S.C. Shiesh, M.C. Wu, and X.Z. Lin. The effects of bile duct obstruction on the biliary secretion of ciprofloxacin in piglets. *American Journal of Gastroenterology*, 94(9):2408–2411, 1999.

[68] H. Chen, Y. Zhang, L. Zhou, H.-Y. Xie, and S.-S. Zheng. Role of basic studies in expanding the donor pool for liver transplantation. *Hepatobiliary & Pancreatic Diseases International*, 7(6):571–580, 2008.

[69] M.L. Chen, Q.Y. Zeng, J.W. Huo, X.M. Yin, B.P. Li, and J.X. Liu. Assessment of the hepatic microvascular changes in liver cirrhosis by perfusion computed tomography. *World Journal of Gastroenterology*, 15(28):3532–3537, 2009.

[70] Z. Chen, L. Yan, B. Li, Y. Zeng, T. Wen, J. Zhao, W. Wang, M. Xu, and J. Yang. Prevent small-for-size syndrome using dual grafts in living donor liver transplantation. *Journal of Surgical Research*, 155(2):261–267, 2009.

[71] T.M. Chu and N.P. Reddy. A lumped parameter mathematical model of the splanchnic circulation. *Journal of Biomechanical Engineering - Transactions of the ASME*, 114(2):222–226, 1992.

[72] C. Chui, E. Kobayashi, X. Chen, T. Hisada, and I. Sakuma. Combined compression and elongation experiments and non-linear modelling of liver tissue for surgical simulation. *Medical & Biological Engineering & Computing*, 42(6):787–798, 2004.

[73] C. Chui, E. Kobayashi, X. Chen, T. Hisada, and I. Sakuma. Transversely isotropic properties of porcine liver tissue: Experiments and constitutive modelling. *Medical & Biological Engineering & Computing*, 45(1):99–106, 2007.

[74] R. Ciria, J. Briceno, S. Rufian, A. Luque, and P. Lopez-Cillero. Donation after cardiac death: Where, when, and how? *Transplantation Proceedings*, 44(6):1470–1474, 2012.

[75] E.C. Clarke, S. Cheng, M. Green, R. Sinkus, and L.E. Bilston. Using static preload with magnetic resonance elastography to estimate large strain viscoelastic properties of bovine liver. *Journal of Biomechanics*, 44(13):2461–2465, 2011.

[76] R.D. Cohen, C.L. Brown, C. Nickols, P. Levey, B.J. Boucher, S.E. Greenwald, and W. Wang. Inbuilt mechanisms for overcoming functional problems inherent in hepatic microlobular structure. *Computational and Mathematical Methods in Medicine*, 2011:185845, 2011.

[77] P. Cornillie, W. Van den Broeck, and P. Simoens. Origin of the infrarenal part of the caudal vena cava in the pig. *Anatomia Histologia Embryologia*, 37(5):387–393, 2008.

[78] C. Couinaud. *Le foie: Études anatomiques et chirurgicales*. Masson et Cie, 1957.

[79] C. Couinaud. Liver anatomy: Portal (and suprahepatic) or biliary segmentation. *Digestive Surgery*, 16(6):459–467, 1999.

[80] F.G. Court, S.A. Wemyss-Holden, C.P. Morrison, B.D. Teague, P.F. Laws, J. Kew, A.R. Dennison, and G.J. Maddern. Segmental nature of the porcine liver and its potential as a model for experimental partial hepatectomy. *British Journal of Surgery*, 90(4):440–444, 2003.

[81] A.R. Crawford, X.Z. Lin, and J.M. Crawford. The normal adult human liver biopsy: a quantitative reference standard. *Hepatology*, 28(2):323–331, 1997.

[82] J.M. Crawford. Development of the intrahepatic biliary tree. *Seminars in Liver Disease*, 22(3):213–226, 2002.

[83] J.M. Crawford. Vascular disorders of the liver. *Clinical Liver Disease*, 14(4):635–650, 2010.

[84] S. Cui, T. Shibamoto, W. Zhang, H. Takano, and Y. Kurata. Venous resistance increases during rat anaphylactic shock. *Shock*, 29(6):733–739, 2008.

[85] M.H. Dahlke, H. Aselmann, D. Ceylan, T. Bellin, P. Flemming, P.N. Meier, K. Oldhafer, J. Klempnauer, H.J. Schlitt, and P. Piso. Effectiveness of peripheral hepatogastrostomy versus hepatojejunostomy in the treatment of obstructive cholestasis: Results of an experimental model. *Surgery Today*, 34(4):349–353, 2004.

[86] U. Dahmen, C.A. Hall, N. Madrahimov, V. Milekhin, and O. Dirsch. Regulation of hepatic microcirculation in stepwise liver resection. *Acta Gastro-Enterologica Belgica*, 70(4):345–351, 2007.

[87] U. Dahmen, N. Madrahimov, F. Madrahimova, Y. Ji, A. Schenk, and O. Dirsch. Small-for-size syndrome in the rat: Does size or technique matter? *Journal of Surgical Research*, 149(1):15–26, 2008.

[88] U. Dahmen, A. Radtke, T. Schroeder, H. Chi, N. Madrahimov, M. Lu, A. Schenk, K.H. Peitgen, and O. Dirsch. Median liver lobe of woodchuck as a model to study hepatic outflow obstruction: A pilot study. *Liver International*, 28(9):1236–1244, 2008.

[89] C. Rodriguez de Lope, S. Tremosini, A. Forner, M. Reig, and J. Bruix. Management of HCC. *Journal of Hepatology*, 56:S75–S87, 2012.

[90] L. de Pater. An electrical analogue of the entire human circulatory system. *Medical electronics and biological engineering*, 2:161–166, 1964.

[91] L. de Pater. *An electrical analogue of the human circulatory system*. PhD thesis, University of Groningen, 1966.

[92] O. de Rougemont, S. Breitenstein, B. Leskosek, A. Weber, R. Graf, P.A. Clavien, and P. Dutkowski. One hour hypothermic oxygenated perfusion (hope) protects nonviable liver allografts donated after cardiac death. *Annals of Surgery*, 250(5):674–683, 2009.

[93] C. Debbaut, D. Monbaliu, C. Casteleyn, P. Cornillie, D. Van Loo, B. Masschaele, J. Pirenne, P. Simoens, L. Van Hoorebeke, and P. Segers. From vascular corrosion cast to electrical analog model for the study of human liver hemodynamics and perfusion. *IEEE Transactions on Biomedical Engineering*, 58(1):25–35, 2011.

[94] C. Debbaut, D. Monbaliu, and P. Segers. Validation and calibration of an electrical analog model of hepatic perfusion based on human liver hypothermic machine perfusion experiments. *Submitted for publication*.

[95] C. Debbaut, P. Segers, P. Cornillie, C. Casteleyn, M. Dierick, W. Laleman, and D. Monbaliu. Analyzing the human liver vascular architecture by combining vascular corrosion casting and micro-CT scanning: a feasibility study. *Submitted for publication*.

[96] C. Debbaut, J.G. Sled, D. Monbaliu, and P. Segers. Semi-automatic morphological analysis of vascular trees: Application to the human liver. *11th Belgian National Day on Biomedical Engineering*, 2012.

[97] C. Debbaut, J.G. Sled, D. Monbaliu, and P. Segers. Semi-automatic analysis of the branching topology and geometrical characteristics of hepatic vascular trees. *The International Liver Congress (EASL), Journal of Hepatology*, 58:S230, 2013.

[98] C. Debbaut, J. Vierendeels, C. Casteleyn, P. Cornillie, D. Van Loo, P. Simoens, L. Van Hoorebeke, D. Monbaliu, and P. Segers. Perfusion characteristics of the human hepatic microcirculation based on three-dimensional reconstructions and computational fluid dynamic analysis. *Journal of Biomechanical Engineering*, 134(1):011003, 2012.

[99] C. Debbaut, J. Vierendeels, J. Siggers, R. Repetto, D. Monbaliu, and P. Segers. A 3D porous media liver lobule model : the importance of vascular septa and anisotropic permeability for homogeneous perfusion. *Computer Methods in Biomechanics and Biomedical Engineering*, e-publication ahead of print, 2012.

[100] C. Debbaut, D. De Wilde, C. Casteleyn, P. Cornillie, D. Van Loo, L. Van Hoorebeke, D. Monbaliu, Y.-D. Fan, and P. Segers. Modeling the impact of partial hepatectomy on the hepatic hemodynamics using a rat model. *IEEE Transactions on Biomedical Engineering*, 59(12):3293–3303, 2012.

[101] T. Deffieux, G. Montaldo, M. Tanter, and M. Fink. Shear wave spectroscopy for in vivo quantification of human soft tissues visco-elasticity. *IEEE Transactions on Medical Imaging*, 28(3):313–322, 2009.

[102] K. Derveaux, D. Monbaliu, T. Crabbe, D. Schein, J. Brassil, D. Kravitz, J. Fevery, L. Jacobbi, T. Roskams, and J. Pirenne. Does ex vivo vascular resistance reflect viability of non-heart-beating donor livers? *Transplantation Proceedings*, 37(1):338–339, 2005.

[103] V.J. Desmet. The amazing universe of hepatic microstructure. *Hepatology*, 50(2):333–344, 2009.

[104] V.J. Desmet. Ductal plates in hepatic ductular reactions. Hypothesis and implications. II. Ontogenic liver growth in childhood. *Virchows Archiv*, 458(3):261–270, 2011.

[105] O. Dirsch, J. Li, Q. He, Y. Ji, Y.L. Gu, and U. Dahmen. Induction of rejection after small-for-size liver transplantation: Size matters. *Journal of Investigative Surgery*, 21(5):288–298, 2008.

[106] O. Dirsch, N. Madrahimov, N. Chaudri, M. Deng, F. Madrahimova, A. Schenk, and U. Dahmen. Recovery of liver perfusion after focal outflow obstruction and liver resection. *Transplantation*, 85(5):748–756, 2008.

[107] G. Donati, G. La Manna, G. Cianciolo, V. Grandinetti, E. Carretta, M. Cappuccilli, L. Panicali, M. Iorio, F. Piscaglia, L. Bolondi, L. Coli, and S. Stefoni. Extracorporeal detoxification for hepatic failure using molecular adsorbent recirculating system: Depurative efficiency and clinical results in a long-term follow-up. *Artificial Organs*, e-publication ahead of print, 2013.

[108] R.E. Drake, S.J. Allen, J. Katz, J.C. Gabel, and G.A. Laine. Equivalent circuit technique for lymph flow studies. *American Journal of Physiology*, 251(5 Pt 2):H1090–H1094, 1986.

[109] P. Dutkowski, O. de Rougemont, and P.A. Clavien. Alexis Carrel: Genius, innovator and ideologist. *American Journal of Transplantation*, 8(10):1998–2003, 2008.

[110] P. Dutkowski, O. de Rougemont, and P.A. Clavien. Machine perfusion for 'marginal' liver grafts. *American Journal of Transplantation*, 8(5):917–924, 2008.

[111] P. Dutkowski, K. Furrer, Y.H. Tian, R. Graf, and P.A. Clavien. Novel short-term hypothermic oxygenated perfusion (HOPE) system prevents injury in rat liver graft from non-heart beating donor. *Annals of Surgery*, 244(6):968–977, 2006.

[112] P. Dutkowski, B. Odermatt, T. Heinrich, S. Schonfeld, M. Watzka, V. Winkelbach, M. Krysiak, and T. Junginger. Hypothermic oscillating liver perfusion stimulates ATP synthesis prior to transplantation. *Journal of Surgical Research*, 80(2):365–372, 1998.

[113] P. Dutkowski, S. Schonfeld, B. Odermatt, T. Heinrich, and T. Junginger. Rat liver preservation by hypothermic oscillating liver perfusion compared to simple cold storage. *Cryobiology*, 36(1):61–70, 1998.

[114] C. Eipel, K. Abshagen, J. Ritter, D. Cantre, M.D. Menger, and B. Vollmar. Splenectomy improves survival by increasing arterial blood supply in a rat model of reduced-size liver. *Transplant International*, 23(10):998–1007, 2010.

[115] R.M. Eisele, W. Meissner, N.C. Nussler, K.P. Platz, U. Settmacher, and P. Neuhaus. Hepatic artery resistance as a marker for preservation/reperfusion injury. *Transplantation Proceedings*, 33(1-2):959–961, 2001.

[116] W. Ekataksin. Microanatomy of the bile secretory epithelium and vasculature: The identification of mammalian livers. In M.P. Manns, J.L. Boyer, P.L.M. Jansen, and J. Reichen, editors, *Cholestatic liver diseases*, pages 46–61. Kluwer Academic Publishers, Dordrecht, 1998.

[117] W. Ekataksin. The isolated artery: An intrahepatic arterial pathway that can bypass the lobular parenchyma in mammalian livers. *Hepatology*, 31:269–279, 2000.

[118] W. Ekataksin and K. Wake. Liver units in 3 dimensions: 1. Organization of argyrophilic connective-tissue skeleton in porcine liver with particular reference to the compound hepatic lobule. *American Journal of Anatomy*, 191(2):113–153, 1991.

[119] W. Ekataksin and K. Wake. New concepts in biliary and vascular anatomy of the liver. *Progress in Liver Diseases*, 15:1–30, 1997.

[120] S. Ekins, A.J. Williams, and J.J. Xu. A predictive ligand-based bayesian model for human drug-induced liver injury. *Drug Metabolism and Disposition*, 38(12):2302–2308, 2010.

[121] B. Ekser, B. Gridelli, M. Veroux, and D.K.C. Cooper. Clinical pig liver xenotransplantation: How far do we have to go? *Xenotransplantation*, 18(3):158–167, 2011.

[122] H. Ellis. Anatomy of the liver. *Surgery (Oxford)*, 29(12):589–592, 2011.

[123] B.G. Ericzon, M. Larsson, and H.E. Wilczek. Domino liver transplantation: Risks and benefits. *Transplantation Proceedings*, 40(4):1130–1131, 2008.

[124] European Association for the Study of the Liver. EASL postgraduate course: Alcoholic liver disease, 2012.

[125] Eurotransplant International Foundation. Annual report, 2008.

[126] Eurotransplant International Foundation. Annual report, 2010.

[127] Eurotransplant International Foundation. Annual report, 2012.

[128] R. Fahraeus and T. Lindqvist. The viscosity of the blood in narrow capillary tubes. *American Journal of Physiology – Legacy Content*, 96(3):562–568, 1931.

[129] S.T. Fan. Live donor liver transplantation in adults. *Transplantation*, 82(6):723–732, 2006.

[130] S.T. Fan. *Living donor liver transplantation*. World Scientific Publishing Co. Pte. Ltd., Singapore, 2nd edition, 2007.

[131] Y.D. Fan, E. Vanheule, D. Meester, J. Van Huysse, K. Olievier, M. Praet, I. Colle, and B. de Hemptinne. Hepatic stellate cell activation: An important contributor to persistent hepatic resistance in small-for-size livers after extended partial hepatectomy in the rat. *Journal of Hepatology*, 52:S59–S60, 2010.

[132] G.C. Farrell and C.Z. Larter. Nonalcoholic fatty liver disease: From steatosis to cirrhosis. *Hepatology*, 43(S1):S99–S112, 2006.

[133] J.H.D. Fasel. Portal venous territories within the human liver: An anatomical reappraisal. *Anatomical Record-Advances in Integrative Anatomy and Evolutionary Biology*, 291(6):636–642, 2008.

[134] J. Fernandez and T. Gustot. Management of bacterial infections in cirrhosis. *Journal of Hepatology*, 56:S1–S12, 2012.

[135] P. Fiaschetti, R. Pretagostini, D. Stabile, D. Peritore, A. Oliveti, F. Gabbrielli, S. Cenci, A. Ricci, F. Vespasiano, and W.F. Grigioni. The use of neoplastic donors to increase the donor pool. *Transplantation Proceedings*, 44(7):1848–1850, 2012.

[136] D.R. Fine, D. Glasser, D. Hildebrandt, J. Esser, R.E. Lurie, and N. Chetty. An anatomic and physiological model of hepatic vascular system. *Journal of Applied Physiology*, 79(3):1008–1026, 1995.

[137] G. Finet, M. Gilard, B. Perrenot, G. Rioufol, P. Motreff, L. Gavit, and R. Prost. Fractal geometry of arterial coronary bifurcations: A quantitative coronary angiography and intravascular ultrasound analysis. *EuroInvention*, 3(4):490–498, 2007.

[138] C.D. Fingas, S. Wu, Y. Gu, J. Wohlschlaeger, A. Scherag, U. Dahmen, A. Paul, H. de Groot, and U. Rauen. Assessment of a chloride-poor versus a chloride-containing version of a modified histidine-tryptophan-ketoglutarate solution in a rat liver transplantation model. *Liver Transplantation*, 17(6):650–660, 2011.

[139] R.A. Fisher, L.M. Kulik, C.E. Freise, A.S.F. Lok, T.H. Shearon, Jr. R.S. Brown, R.M. Ghobrial, J.H. Fair, K.M. Olthoff, I. Kam, C.L. Berg, and the A2ALL Study Group. Hepatocellular carcinoma recurrence and death following living and deceased donor liver transplantation. *American Journal of Transplantation*, 7(6):1601–1608, 2007.

[140] C. Fondevila. Is extracorporeal support becoming the new standard for the preservation of DCD grafts? *American Journal of Transplantation*, 10(6):1341–1342, 2010.

[141] C. Fondevila, A.J. Hessheimer, M.-H.J. Maathuis, J. Munoz, P. Taura, D. Calatayud, H. Leuvenink, A. Rimola, J.C. Garcia-Valdecasas, and R.J. Ploeg. Hypothermic oxygenated machine perfusion in porcine donation after circulatory determination of death liver transplant. *Transplantation*, 94(1):22–29, 2012.

[142] S. Francque, W. Laleman, L. Verbeke, C. Van Steenkiste, C. Casteleyn, W. Kwanten, C. Van Dyck, M. D'Hondt, A. Ramon, W. Vermeulen, B. De Winter, E. Van Marck, V. Van Marck, P. Pelckmans, and P. Michielsen. Increased intrahepatic resistance in severe steatosis: endothelial dysfunction, vasoconstrictor overproduction and altered microvascular architecture. *Laboratory Investigation*, 92(10):1428–1439, 2012.

[143] S.L. Friedman. Molecular regulation of hepatic fibrosis, an integrated cellular response to tissue injury. *Journal of Biological Chemistry*, 275(4):2247–2250, 2000.

[144] P.J. Friend, C. Imber, S. St Peter, I. Lopez, A.J. Butler, and M.A. Rees. Normothermic perfusion of the isolated liver. *Transplantation Proceedings*, 33(7-8):3436–3438, 2001.

[145] T. Fukuchi, H. Hirose, A. Onitsuka, M. Hayashi, S. Senga, N. Imai, M. Shibata, K. Yamauchi, N. Futamura, and Y. Sumi. Effects of portal-systemic shunt following 90% partial hepatectomy in rats. *Journal of Surgical Research*, 89(2):126–131, 2000.

[146] B.J. Fuller and C.Y. Lee. Hypothermic perfusion preservation: The future of organ preservation revisited? *Cryobiology*, 54(2):129–145, 2007.

[147] L.A. Furchtgott, C.C. Chow, and V. Periwal. A model of liver regeneration. *Biophysical Journal*, 96(10):3926–3935, 2009.

[148] I.T. Gabe. Arterial blood flow by analogue solution of Navier-Stokes equation. *Physics in Medicine and Biology*, 10(2):271–280, 1965.

[149] E. Gabrys, M. Rybaczuk, and A. Kedzia. Fractal models of circulatory system. Symmetrical and asymmetrical approach comparison. *Chaos Solitons & Fractals*, 24(3):707–715, 2005.

[150] Z. Gao, K. Lister, and J.P. Desai. Constitutive modeling of liver tissue: Experiment and theory. *Annals of Biomedical Engineering*, 38(2):505–516, 2010.

[151] G. Garcea and G.J. Maddern. Liver failure after major hepatic resection. *Journal of Hepato-Biliary-Pancreatic Surgery*, 16(2):145–155, 2009.

[152] G. Garcea, H. Nabi, and G.J. Maddern. Russell strong and the history of reduced-size liver transplantation. *World Journal of Surgery*, 33(8):1575–1580, 2009.

[153] G. Garcea, S.L. Ong, and G.J. Maddern. Predicting liver failure following major hepatectomy. *Digestive and Liver Disease*, 41(11):798–806, 2009.

[154] G. Garcia-Tsao, S. Friedman, J. Iredale, and M. Pinzani. Now there are many (stages) where before there was one: In search of a pathophysiological classification of cirrhosis. *Hepatology*, 51(4):1445–1449, 2010.

[155] J.C. García-Valdecasas. Split and living donor liver transplantation. *Digestive and Liver Disease Supplements*, 3(4):93–95, 2009.

[156] J.C. Garcia-Valdecasas and C. Fondevila. In-vivo normothermic recirculation: An update. *Current Opinion in Organ Transplantation*, 15(2):173–176, 2010.

[157] C. Gennings, D. Heuman, O. Fulton, and A.J. Sanyal. Use of desirability functions to evaluate health status in patients with cirrhosis. *Journal of Hepatology*, 52(5):665–671, 2010.

[158] S. George. *Hemodynamic investigation of the liver using magnetic resonance imaging and computational fluid dynamics*. PhD thesis, Georgia Institute of Technology, 2008.

[159] R.M. Ghobrial, C.E. Freise, J.F. Trotter, L. Tong, A.O. Ojo, J.H. Fair, R.A. Fisher, J.C. Emond, A.J. Koffron, T.L. Pruett, K.M. Olthoff, and the A2ALL Study Group. Donor morbidity after living donation for liver transplantation. *Gastroenterology*, 135(2):468–476, 2008.

[160] C. Gille, C. Boelling, A. Hoppe, S. Bulik, S. Hoffmann, K. Huebner, A. Karlstaedt, R. Ganeshan, M. Koenig, K. Rother, M. Weidlich, J. Behre, and H.-G. Holzhuetter. HepatoNet1: A comprehensive metabolic reconstruction of the human hepatocyte for the analysis of liver physiology. *Molecular Systems Biology*, 6:411, 2010.

[161] P. Gines, J. Fernandez, F. Durand, and F. Saliba. Management of critically-ill cirrhotic patients. *Journal of Hepatology*, 56:S13–S24, 2012.

[162] I. Giuvarasteanu. Scanning electron microscopy of vascular corrosion casts–standard method for studying microvessels. *Romanian Journal of Morphology and Embryology*, 48(3):257–261, 2007.

[163] M. Glanemann, C. Eipel, A.K. Nussler, B. Vollmar, and P. Neuhaus. Hyperperfusion syndrome in small-for-size livers. *European Surgical Research*, 37(6):335–341, 2005.

[164] F. Glisson. *Anatomia hepatis*. London, 1654.

[165] N. Goldaracena, E. Quinonez, P. Mendez, M. Anders, F. Orozco Ganem, R. Mastai, and L. McCormack. Extremely marginal liver grafts from deceased donors have outcome similar to ideal grafts. *Transplantation Proceedings*, 44(7):2219–2222, 2012.

[166] R.F.M. Gomes and J.H.T. Bates. Geometric determinants of airway resistance in two isomorphic rodent species. *Respiratory Physiology & Neurobiology*, 130(3):317–325, 2002.

[167] Z. Gordon, D. Elad, R. Almog, Y. Hazan, A.J. Jaffa, and O. Eytan. Anthropometry of fetal vasculature in the chorionic plate. *Journal of Anatomy*, 211(6):698–706, 2007.

[168] D.N. Granger. Ischemia-reperfusion: Mechanisms of microvascular dysfunction and the influence of risk factors for cardiovascular disease. *Microcirculation*, 6(3):167–178, 1999.

[169] C.V. Greenway and R.D. Stark. Hepatic vascular bed. *Physiological Reviews*, 51(1):23–65, 1971.

[170] E. Gringeri, P. Bonsignore, D. Bassi, F.E. D'Amico, C. Mescoli, M. Polacco, M. Buggio, R. Luisetto, R. Boetto, G. Noaro, A. Ferrigno, E. Boncompagni, I. Freitas, M.P. Vairetti, A. Carraro, D. Neri, and U. Cillo. Subnormothermic machine perfusion for non-heart-beating donor liver grafts preservation in a swine model: A new strategy to increase the donor pool? *Transplantation Proceedings*, 44(7):2026–2028, 2012.

[171] M. Gronbaek, M.K. Jensen, D. Johansen, T.I.A. Sorensen, and U. Becker. Intake of beer, wine and spirits and risk of heavy drinking and alcoholic cirrhosis. *Biological Research*, 37(2):195–200, 2004.

[172] S. Gruttadauria, C.S. Foglieni, C. Doria, A. Luca, A. Lauro, and I.R. Marino. The hepatic artery in liver transplantation and surgery: Vascular anomalies in 701 cases. *Clinical Transplantation*, 15(5):359–363, 2001.

[173] J.V. Guarrera, J. Estevez, J. Boykin, R. Boyce, J. Rashid, S. Sun, and B. Arrington. Hypothermic machine perfusion of liver grafts for transplantation: Technical development in human discard and miniature swine models. *Transplantation Proceedings*, 37(1):323–325, 2005.

[174] J.V. Guarrera, S.D. Henry, B. Samstein, R. Odeh-Ramadan, M. Kinkhabwala, M.J. Goldstein, L.E. Ratner, J.F. Renz, H.T. Lee, Jr. R.S. Brown, and J.C. Emond. Hypothermic machine preservation in human liver transplantation: The first clinical series. *American Journal of Transplantation*, 10(2):372–381, 2010.

[175] J.V. Guarrera and N.A. Karim. Liver preservation: Is there anything new yet? *Current Opinion in Organ Transplantation*, 13(2):148–154, 2008.

[176] S.C. Gupta, C.D. Gupta, and A.K. Arora. Subsegmentation of the human liver. *Journal of Anatomy*, 124(2):413–423, 1977.

[177] S.C. Gupta, C.D. Gupta, and S.B. Gupta. Hepatovenous segments in the human liver. *Journal of Anatomy*, 133(1):1–6, 1981.

[178] H.K. Hahn, C.J.G. Evertsz, H.-O. Peitgen, and J.H.D. Fasel. Fractal properties, segment anatomy, and interdependence of the human portal vein and the hepatic vein in 3D. *Fractals*, 11(01):53–62, 2003.

[179] H.K. Hahn, M. Georg, and H.-O. Peitgen. Fractal aspects of three-dimensional vascular constructive optimization. In G. Losa, D. Merlini, T. Nonnenmacher, and E. Weibel, editors, *Fractals in biology and medicine*, Mathematics and biosciences in interaction, chapter 5, pages 55–66. Birkhäuser Basel, 2005.

[180] J.T. Halavaara, L.M. Hamberg, F.S. Leong, G.J. Hunter, G.S. Gazelle, and G.L. Wolf. Functional CT with an experimental intravascular contrast agent in the assessment of liver vascular physiology. *Academic Radiology*, 3(11):946–952, 1996.

[181] H. Hano and S. Takasaki. Three-dimensional observations on the alterations of lobular architecture in chronic hepatitis with special reference to its angioarchitecture for a better understanding of the formal pathogenesis of liver cirrhosis. *Virchows Archiv*, 443(5):655–663, 2003.

[182] C. Hansen, S. Zidowitz, A. Schenk, K.J. Oldhafer, H. Lang, and H.O. Peitgen. Risk maps for navigation in liver surgery. In K.H. Wong and M.I. Miga, editors, *Proceedings of SPIE, Medical Imaging 2010: Visualization, Image-Guided Procedures, and Modeling*, 2010.

[183] T.R. Harring, C.A. O'Mahony, and J.A. Goss. Extended donors in liver transplantation. *Clinics in Liver Disease*, 15(4):879–900, 2011.

[184] K. Hashimoto, C.M. Miller, C. Quintini, F.N. Aucejo, K. Hirose, T.D. Uso, L. Trenti, D.M. Kelly, C.G. Winans, D.P. Vogt, B. Eghtesad, and J.J. Fung. Is impaired hepatic arterial buffer response a risk factor for biliary anastomotic stricture in liver transplant recipients? *Surgery*, 148(3):582–588, 2010.

[185] R.H. Haynes. Physical basis of the dependence of blood viscosity on tube radius. *American Journal of Physiology – Legacy Content*, 198(6):1193–1200, 1960.

[186] M. Hennenberg, J. Trebicka, T. Sauerbruch, and J. Heller. Mechanisms of extrahepatic vasodilation in portal hypertension. *Gut*, 57(9):1300–1314, 2008.

[187] S.D. Henry and J.V. Guarrera. Protective effects of hypothermic ex vivo perfusion on ischemia/reperfusion injury and transplant outcomes. *Transplantation Reviews*, 26(2):163–175, 2012.

[188] A.J. Hessheimer, C. Fondevila, and J.C. Garcia-Valdecasas. Extracorporeal machine liver perfusion: Are we warming up? *Current Opinion in Organ Transplantation*, 17(2):143–147, 2012.

[189] A.J. Hessheimer, C. Fondevila, P. Taura, J. Munoz, O. Sanchez, J. Fuster, A. Rimola, and J. Carlos Garcia-Valdecasas. Decompression of the portal bed and twice-baseline portal inflow are necessary for the functional recovery of a "small-for-size" graft. *Annals of Surgery*, 253(6):1201–1210, 2011.

[190] A.J. Hessheimer, D. Parramon, A. Guimera, I. Erill, A. Rimola, J.C. Garcia-Valdecasas, R. Villa, and C. Fondevila. A rapid and reliable means of assessing hepatic steatosis in vivo via electrical bioimpedance. *Transplantation*, 88(5):716–722, 2009.

[191] W. Hillewaert, Q. Liu, K. Vekemans, P. Segers, P. Verdonck, J. Pirenne, J. Brassil, and D. Monbaliu. Hepatic artery/portal vein flow competition during hypothermic machine perfusion of the liver. *European Society for Artificial Organs (ESAO) congress, International Journal of Artificial Organs*, 30(8):710, 2007.

[192] N. Hirooka, I. Iwasaki, H. Horie, and G. Ide. Hepatic microcirculation of liver cirrhosis studied by corrosion cast/scanning electron microscope examination. *Acta Pathologica Japonica*, 36(3):375–387, 1986.

[193] C.-M. Ho, R.-K. Lin, S.-F. Tsai, R.-H. Hu, P.-C. Liang, T.W.-H. Sheu, and P.-H. Lee. Simulation of portal hemodynamic changes in a donor after right hepatectomy. *Journal of Biomechanical Engineering-Transactions of the ASME*, 132(4):041002, 2010.

[194] H. Ho, A. Bartlett, and P. Hunter. Hemodynamic simulation for an anatomically realistic portal system. *Medical image computing and computer-assisted intervention, MICCAI 2011*, 14(Pt 1):347–354, 2011.

[195] H. Ho, K. Sorrell, A. Bartlett, and P. Hunter. Blood flow simulation for the liver after a virtual right lobe hepatectomy, MICCAI 2012. *Medical Image Computing and Computer-Assisted Intervention*, 15(Pt 3):525–532, 2012.

[196] H. Ho, K. Sorrell, A. Bartlett, and P. Hunter. Modeling the hepatic arterial buffer response in the liver. *Medical Engineering & Physics*, 35(8):1053–1058, 2013.

[197] H. Ho, K. Sorrell, L. Peng, Z. Yang, A. Holden, and P. Hunter. Hemodynamic analysis for transjugular intrahepatic portosystemic shunt (tips) in the liver based on a CT-image. *IEEE Transactions on Medical Imaging*, 32(1):92–98, 2013.

[198] S. Hoehme, M. Brulport, A. Bauer, E. Bedawy, W. Schormann, M. Hermes, V. Puppe, R. Gebhardt, S. Zellmer, M. Schwarz, E. Bockamp, T. Timmel, J.G. Hengstler, and D. Drasdo. Prediction and validation of cell alignment along microvessels as order principle to restore tissue architecture in liver regeneration. *Proceedings of the National Academy of Sciences of the United States of America*, 107(23):10371–10376, 2010.

[199] S. Hoehme and D. Drasdo. A cell-based simulation software for multicellular systems. *Bioinformatics*, 26(20):2641–2642, 2010.

[200] S. Hoehme, J.G. Hengstler, M. Brulport, M. Schaefer, A. Bauer, R. Gebhardt, and D. Drasdo. Mathematical modelling of liver regeneration after intoxication with CCl4. *Chemico-Biological Interactions*, 168(1):74–93, 2007.

[201] R.M. Hoffmann, J.H. Southard, M. Lutz, A. Mackety, and F.O. Belzer. Synthetic perfusate for kidney-preservation - its use in 72-hour preservation of dog kidneys. *Archives of Surgery*, 118(8):919–921, 1983.

[202] A. Hofmann. The choleohepatic circulation of unconjugated bile acids: An update. In G. Paumgartner, A. Stiehl, and W. Gerok, editors, *Bile acids and the hepatobiliary system: from basic science to clinical practice*, pages 143–160. Kluwer Academic Publishers, Dordrecht, 1993.

[203] J.P. Holt, E.A. Rhode, W.W. Holt, and H. Kines. Geometric similarity of aorta, venae cavae, and certain of their branches in mammals. *American Journal of Physiology*, 241(1):100–104, 1981.

[204] H.-G. Holzhütter, D. Drasdo, T. Preusser, J. Lippert, and A.M. Henney. The virtual liver: A multidisciplinary, multilevel challenge for systems biology. *Wiley Interdisciplinary Reviews: Systems Biology and Medicine*, 4(3):221–235, 2012.

[205] J.C. Hong, H. Yersiz, and R.W. Busuttil. Where are we today in split liver transplantation? *Current Opinion in Organ Transplantation*, 16(3):269–273, 2011.

[206] K. Horsfield and G. Cumming. Morphology of the bronchial tree in man. *Journal of Applied Physiology*, 24(3):373–383, 1968.

[207] K. Horsfield, G. Dart, D.E. Olson, G.F. Filley, and G. Cumming. Models of the human bronchial tree. *Journal of Applied Physiology*, 31(2):207–217, 1971.

[208] T.L. Hsu, H. Hsiu, P.T. Chao, S.P. Li, W.K. Wang, and Y.Y.L. Wang. Three-block electrical model of renal impedance. *Physiological Measurement*, 26(4):387–399, 2005.

[209] H. Huang, M. Deng, H. Jin, O. Dirsch, and U. Dahmen. Intraoperative vital and haemodynamic monitoring using an integrated multiple-channel monitor in rats. *Laboratory Animals*, 44(3):254–263, 2010.

[210] H. Huang, M. Deng, H. Jin, A. Liu, O. Dirsch, and U. Dahmen. Hepatic arterial perfusion is essential for the spontaneous recovery from focal hepatic venous outflow obstruction in rats. *American Journal of Transplantation*, 11(11):2342–2361, 2011.

[211] H. Huang, M. Deng, H. Jin, A. Liu, O. Dirsch, and U. Dahmen. A novel end-to-side anastomosis technique for hepatic rearterialization in rat orthotopic liver transplantation to accommodate size mismatches between vessels. *European Surgical Research*, 47(2):53–62, 2011.

[212] P.M. Huet, G. Pomier-Layrargues, J.P. Villeneuve, F. Varin, and A. Viallet. Intrahepatic circulation in liver-disease. *Seminars in Liver Disease*, 6(4):277–286, 1986.

[213] A. Humar, A.J. Matas, and W.D. Payne. *Atlas of organ transplantation*. Springer-Verlag, London, 2006.

[214] A. Humar and W.D. Payne. Liver transplantation. In A. Humar, A.J. Matas, and W.D. Payne, editors, *Atlas of organ transplantation*. Springer-Verlag, London, 2006.

[215] L. Huwart, C. Sempoux, E. Vicaut, N. Salameh, L. Annet, E. Danse, F. Peeters, L.C. ter Beek, J. Rahier, R. Sinkus, Y. Horsmans, and B.E. Van Beers. Magnetic resonance elastography for the noninvasive staging of liver fibrosis. *Gastroenterology*, 135(1):32–40, 2008.

[216] S. Hwang. Microcirculation of the liver. In D.C. Madoff, M. Makuuchi, M. Nagino, and J.-N. Vauthey, editors, *Venous embolization of the liver*, chapter 2, pages 9–13. Springer, London, 2011.

[217] S. Ijaz, W. Yang, M.C. Winslet, and A.M. Seifalian. Impairment of hepatic microcirculation in fatty liver. *Microcirculation*, 10(6):447–456, 2003.

[218] T. Ikegami, M. Shimada, S. Imura, Y. Arakawa, A. Nii, Y. Morine, and H. Kanemura. Current concept of small-for-size grafts in living donor liver transplantation. *Surgery Today*, 38(11):971–982, 2008.

[219] C.J. Imber, S.D. St Peter, I.L. de Cenarruzabeitia, D. Pigott, T. James, R. Taylor, J. McGuire, D. Hughes, A. Butler, M. Rees, and P.J. Friend. Advantages of normothermic perfusion over cold storage in liver preservation. *Transplantation*, 73(5):701–709, 2002.

[220] C.M. Ionescu, I. Muntean, J.A. Tenreiro-Machado, R. De Keyser, and M. Abrudean. A theoretical study on modeling the respiratory tract with ladder networks by means of intrinsic fractal geometry. *IEEE Transactions on Biomedical Engineering*, 57(2):246–253, 2010.

[221] Y. Ito, K.K. Sorensen, N.W. Bethea, D. Svistounov, M.K. McCuskey, B.H. Smedsrod, and R.S. McCuskey. Age-related changes in the hepatic microcirculation in mice. *Experimental Gerontology*, 42(8):789–797, 2007.

[222] Y. Iwakiri. Endothelial dysfunction in the regulation of cirrhosis and portal hypertension. *Liver International*, 32(2):199–213, 2012.

[223] H. Iwamoto, N. Matsuno, Y. Narumi, M. Uchiyama, K. Kozaki, H. Degawa, K. Hama, K. Kikuchi, H. Takeuchi, M. Kozaki, and T. Nagao. Beneficial effect of machine perfusion preservation on liver transplantation from non-heart-beating donors. *Transplantation Proceedings*, 32(7):1645–1646, 2000.

[224] J. Jack, J.F. Wambaugh, and I. Shah. Simulating quantitative cellular responses using asynchronous threshold boolean network ensembles. *BMC Systems Biology*, 5:109, 2011.

[225] G.N. Jager, N. Westerhof, and A. Noordergraaf. Oscillatory flow impedance in electrical analog of arterial system - representation of sleeve effect and non-Newtonian properties of blood. *Circulation Research*, 16(2):121–133, 1965.

[226] S. Jain, C.Y. Lee, S. Baicu, H. Duncan, H. Xu, J.W. Jones, M.G. Clemens, J. Brassil, M.J. Taylor, and K.G.M. Brockbank. Hepatic function in hypothermically stored porcine livers: Comparison of hypothermic machine perfusion vs cold storage. *Transplantation Proceedings*, 37(1):340–341, 2005.

[227] S. Jain, H.Z. Xu, H. Duncan, J.W. Jones, J.X. Zhang, M.G. Clemens, and C.Y. Lee. Ex-vivo study of flow dynamics and endothelial cell structure during extended hypothermic machine perfusion preservation of livers. *Cryobiology*, 48(3):322–332, 2004.

[228] R.W. Jamieson, M. Zilvetti, D. Roy, D. Hughes, A. Morovat, C.C. Coussios, and P.J. Friend. Hepatic steatosis and normothermic perfusion-preliminary experiments in a porcine model. *Transplantation*, 92(3):289–295, 2011.

[229] L. Jerby, T. Shlomi, and E. Ruppin. Computational reconstruction of tissue-specific metabolic models: Application to human liver metabolism. *Molecular Systems Biology*, 6:401, 2010.

[230] Z.L. Jiang, G.S. Kassab, and Y.C. Fung. Diameter-defined Strahler system and connectivity matrix of the pulmonary arterial tree. *Journal of Applied Physiology*, 76(2):882–892, 1994.

[231] H. Jin, U. Dahmen, A. Liu, H. Huang, Y. Gu, and O. Dirsch. Prolonged cold ischemia does not trigger lethal rejection or accelerate the acute rejection in two allogeneic rat liver transplantation models. *Journal of Surgical Research*, 175(2):322–332, 2012.

[232] I. Jochmans, C. Moers, J.M. Smits, H.G.D. Leuvenink, J. Treckmann, A. Paul, A. Rahmel, J.P. Squifflet, E. van Heurn, D. Monbaliu, R.J. Ploeg, and J. Pirenne. The prognostic value of renal resistance during hypothermic machine perfusion of deceased donor kidneys. *American Journal of Transplantation*, 11(10):2214–2220, 2011.

[233] L.C. Junqueira and J. Carneiro. *Functionele histologie*. Elsevier Gezondheidszorg, 10th edition, 2004.

[234] K. Jurczuk, M. Kretowski, and J. Bezy-Wendling. Vascular system modeling in parallel environment - distributed and shared memory approaches. *IEEE Transactions on Information Technology in Biomedicine*, 15(4):668–672, 2011.

[235] A. Kamarainen, I. Virkkunen, and J. Tenhunen. Hypothermic preconditioning of donor organs prior to harvesting and ischaemia using ice-cold intravenous fluids. *Medical Hypotheses*, 73(1):65–66, 2009.

[236] P.S. Kamath, R.H. Wiesner, M. Malinchoc, W. Kremers, T.M. Therneau, C.L. Kosberg, G. D'Amico, E.R. Dickson, and W.R. Kim. A model to predict survival in patients with end-stage liver disease. *Hepatology*, 33(2):464–470, 2001.

[237] Z. Kan and D.C. Madoff. Liver anatomy: Microcirculation of the liver. *Seminars in Interventional Radiology*, 25(2):77–85, 2008.

[238] M. Kanamoto, M. Shimada, T. Utsunomiya, S. Imura, Y. Morine, T. Ikemoto, H. Mori, and J. Hanaoka. Impact of a new refrigerator on the preservation of hepatic grafts. *Hepatology Research*, 42(8):798–805, 2012.

[239] A.N. Kandilis, J. Koskinas, D.G. Tiniakos, N. Nikiteas, and D.N. Perrea. Liver regeneration: Focus on cell types and topographic differences. *European Surgical Research*, 44(1):1–12, 2010.

[240] M.K. Kapanen, J.T. Halavaara, and A.M. Hakkinen. Open four-compartment model in the measurement of liver perfusion. *Academic Radiology*, 12(12):1542–1550, 2005.

[241] M.M. Kaplan and M.E. Gershwin. Primary biliary cirrhosis. *New England Journal of Medicine*, 353(12):1261–1273, 2005.

[242] S.J. Karran, C.J. Eagles, J.S. Fleming, and D.M. Ackery. In vivo measurement of liver perfusion in the normal and partially hepatectomized rat using TC-99M sulfur colloid. *Journal of Nuclear Medicine*, 20(1):26–31, 1979.

[243] M. Kasahara, Y. Takada, K. Kozaki, K. Uryuhara, Y. Ogura, K. Ogawa, Y. Fujimoto, and K. Tanaka. Functional portal flow competition after auxiliary partial orthotopic living donor liver transplantation in noncirrhotic metabolic liver disease. *Journal of Pediatric Surgery*, 39(7):1138–1141, 2004.

[244] G.S. Kassab. Scaling laws of vascular trees: Of form and function. *American Journal of Physiology-Heart and Circulatory Physiology*, 290(2):H894–H903, 2006.

[245] G.S. Kassab and Y.C.B. Fung. The pattern of coronary arteriolar bifurcations and the uniform shear hypothesis. *Annals of Biomedical Engineering*, 23(1):13–20, 1995.

[246] I. Kassissia, A. Brault, and P.M. Huet. Hepatic-artery and portal-vein vascularization of normal and cirrhotic rat-liver. *Hepatology*, 19(5):1189–1197, 1994.

[247] R. Kavlock and D. Dix. Computational toxicology as implemented by the US EPA: Providing high throughput decision support tools for screening and assessing chemical exposure, hazard and risk. *Journal of Toxicology and Environmental Health-Part B-Critical Reviews*, 13(2-4):197–217, 2010.

[248] E.B. Keeffe. Liver transplantation: Current status and novel approaches to liver replacement. *Gastroenterology*, 120(3):749–762, 2001.

[249] A.R. Kemper, A.C. Santago, J.D. Stitzel, J.L. Sparks, and S.M. Duma. Biomechanical response of human liver in tensile loading. *Annals of Advances in Automotive Medicine*, 54:15–26, 2010.

[250] A.S. Kennedy, C. Kleinstreuer, C.A. Basciano, and W.A. Dezarn. Computer modeling of yttrium-90-microsphere transport in the hepatic arterial tree to improve clinical outcomes. *International Journal of Radiation Oncology Biology Physics*, 76(2):631–637, 2010.

[251] V.O. Kheyfets, W. O'Dell, T. Smith, J.J. Reilly, and E.A. Finol. Considerations for numerical modeling of the pulmonary circulation - a review with a focus on pulmonary hypertension. *Journal of Biomechanical Engineering*, 135(6):061011, 2013.

[252] F. Kiernan. The anatomy and physiology of the liver. *Transactions of the royal society of London*, 123:711–770, 1883.

[253] R.D. Kim, J.-S. Kim, and K.E. Behrns. Liver regeneration and the atrophy-hypertrophy complex. In D.C. Madoff, M. Makuuchi, M. Nagino, and J.-N. Vauthey, editors, *Venous embolization of the liver*, chapter 6, pages 37–47. Springer, London, 2011.

[254] Y. Kishi, T. Hashimoto, and M. Makuuchi. Portal and hepatic vein anatomy. In D.C. Madoff, M. Makuuchi, M. Nagino, and J.-N. Vauthey, editors, *Venous embolization of the liver*, chapter 3, pages 15–22. Springer, London, 2011.

[255] Y. Kishi, H. Imamura, Y. Sugawara, K. Sano, J. Kaneko, N. Kokudo, and M. Makuuchi. Evaluation of donor vasculobiliary anatomic variations in liver graft procurements. *Surgery*, 147(1):30–39, 2010.

[256] T.L. Kline, M. Zamir, and E.L. Ritman. Relating function to branching geometry: A micro-CT study of the hepatic artery, portal vein, and biliary tree. *Cells Tissues Organs*, 194(5):431–442, 2011.

[257] K. Kogure, M. Ishizaki, M. Nemoto, H. Kuwano, and M. Makuuchi. A comparative study of the anatomy of rat and human livers. *Journal of Hepato-Biliary-Pancreatic Surgery*, 6(2):171–175, 1999.

[258] A. Koo, I.Y.S. Liang, and K.K. Cheng. Terminal hepatic microcirculation in the rat. *Quarterly Journal of Experimental Physiology and Cognate Medical Sciences*, 60(4):261–266, 1975.

[259] G. Kootstra, J.H. Daemen, and A.P. Oomen. Categories of non-heart-beating donors. *Transplantation Proceedings*, 27(5):2893–2894, 1995.

[260] R.G. Kratky and M.R. Roach. Shrinkage of Batsons and its relevance to vascular casting. *Atherosclerosis*, 51(2-3):339–341, 1984.

[261] M. Kretowski, J. Bezy-Wendling, and P. Coupe. Simulation of biphasic CT findings in hepatic cellular carcinoma by a two-level physiological model. *IEEE Transactions on Biomedical Engineering*, 54(3):538–542, 2007.

[262] M. Kretowski, Y. Rolland, J. Bezy-Wendling, and J.L. Coatrieux. Fast algorithm for 3-D vascular tree modeling. *Computer Methods and Programs in Biomedicine*, 70(2):129–136, 2003.

[263] A. Kribben, G. Gerken, S. Haag, S. Herget-Rosenthal, U. Treichel, C. Betz, C. Sarrazin, E. Hoste, H. Van Vlierberghe, A. Escorsell,

C. Hafer, O. Schreiner, P.R. Galle, E. Mancini, P. Caraceni, C.J. Karvellas, H. Salmhofer, M. Knotek, P. Gines, J. Kozik-Jaromin, and K. Rifai. Effects of fractionated plasma separation and adsorption on survival in patients with acute-on-chronic liver failure. *Gastroenterology*, 142(4):782–789, 2012.

[264] W. Kroon, W. Huberts, M. Bosboom, and F. van de Vosse. A numerical method of reduced complexity for simulating vascular hemodynamics using coupled 0D lumped and 1D wave propagation models. *Computational and Mathematical Methods in Medicine*, 2012.

[265] J.W.C. Kung, I.S. Currie, S.J. Forbes, and J.A. Ross. Liver development, regeneration, and carcinogenesis. *Journal of Biomedicine and Biotechnology*, 2010:984248, 2010.

[266] Q. Lai, F. Melandro, G.B.L. Sandri, G. Mennini, S.G. Corradini, M. Merli, P.B. Berloco, and M. Rossi. Use of elderly donors for liver transplantation: Has the limit been reached? *Journal of Gastrointestinal and Liver Diseases*, 20(4):383–387, 2011.

[267] W. Laleman. *Role of hepatic stellate cells and vascular mediators in the pathophysiology of cirrhotic portal hypertension*. PhD thesis, Katholieke Universiteit Leuven, 2006.

[268] W. Laleman, I.V. Elst, M. Zeegers, R. Servaes, L. Libbrecht, T. Roskams, J. Fevery, and F. Nevens. A stable model of cirrhotic portal hypertension in the rat: Thioacetamide revisited. *European Journal of Clinical Investigation*, 36(4):242–249, 2006.

[269] W. Laleman, L. Van Landeghem, A. Wilmer, J. Fevery, and F. Nevens. Portal hypertension: From pathophysiology to clinical practice. *Liver International*, 25(6):1079–1090, 2005.

[270] P. Lamata, A. Jalote-Parmar, F. Lamata, and J. Declerck. The resection map, a proposal for intraoperative hepatectomy guidance. *International Journal of Computer Assisted Radiology and Surgery*, 3(3-4):299–306, 2008.

[271] W.H. Lamers, A. Hilberts, E. Furt, J. Smith, G.N. Jonges, C.J.F. Vannoorden, J.W.G. Janzen, R. Charles, and A.F.M. Moorman. Hepatic enzymic zonation - a reevaluation of the concept of the liver acinus. *Hepatology*, 10(1):72–76, 1989.

[272] B.H. Landing and T.R. Wells. Considerations of some architectural properties of the biliary tree and liver in childhood. *Perspectives in pediatric pathology*, 14:122–142, 1991.

[273] M. Lara, C.Y. Chen, P. Mannor, O. Dur, P.G. Menon, A.P. Yoganathan, and K. Pekkan. Hemodynamics of the hepatic venous three-vessel confluences using particle image velocimetry. *Annals of Biomedical Engineering*, 39(9):2398–2416, 2011.

[274] H. Lauschke, M. Kotting, S. Akbar, and T. Minor. Use of taurine as antioxidant in resuscitating livers from non-heart-beating donors by gaseous oxygen persufflation. *Journal of Investigative Surgery*, 16(1):7–11, 2003.

[275] W.W. Lautt. Mechanism and role of intrinsic regulation of hepatic arterial blood flow: Hepatic arterial buffer response. *American Journal of Physiology*, 249(5):G549–G556, 1985.

[276] W.W. Lautt. Regulatory processes interacting to maintain hepatic blood flow constancy: Vascular compliance, hepatic arterial buffer response, hepatorenal reflex, liver regeneration, escape from vasoconstriction. *Hepatology Research*, 37(11):891–903, 2007.

[277] W.W. Lautt. *Hepatic circulation: Physiology and pathophysiology*. Morgan & Claypool Life Sciences., San Rafael CA, 2010.

[278] W.W. Lautt and C.V. Greenway. Conceptual review of the hepatic vascular bed. *Hepatology*, 7(5):952–963, 1987.

[279] C.Y. Lee, J.X. Zhang, J.W. Jones, J.H. Southard, and M.G. Clemens. Functional recovery of preserved livers following warm ischemia: Improvement by machine perfusion preservation. *Transplantation*, 74(7):944–951, 2002.

[280] S.S. Lee, A. Hadengue, C. Girod, A. Braillon, and D. Lebrec. Reduction of intrahepatic vascular space in the pathogenesis of portal-hypertension - invitro and invivo studies in the rat. *Gastroenterology*, 93(1):157–161, 1987.

[281] T.C. Lee, K.F. Huang, M.L. Hsiao, S.T. Tang, and S.T. Young. Electrical lumped model for arterial vessel beds. *Computer Methods and Programs in Biomedicine*, 73(3):209–219, 2004.

[282] K. Lehmann and P.-A. Clavien. History of hepatic surgery. *Surgical Clinics of North America*, 90(4):655–664, 2010.

[283] J. Lemasters, H. Bunzendahl, and R. Thurman. Preservation of the liver. In W.C. Maddrey and M.F. Sorrell, editors, *Transplantation of the liver*. Appleton & Lange, Connecticut, 1991.

[284] J. Li, Y. Hou, J. Liu, B. Liu, and L. Li. A better way to do small-for-size liver transplantation in rats. *Frontier Medical*, 5(1):106–110, 2011.

[285] Q. Li, D.-W. Liu, L.-M. Zhang, B. Zhu, Y.-T. He, and Y.-H. Xiao. Effects of augmentation of liver regeneration recombinant plasmid on rat hepatic fibrosis. *World Journal of Gastroenterology*, 11(16):2438–2443, 2005.

[286] A.C. Liakopoulos. Darcy's coefficient of permeability as symmetric tensor of second rank. *International Association of Scientific Hydrology*, 10(3):41–48, 1965.

[287] R.-H. Lin and C.-L. Chuang. A hybrid diagnosis model for determining the types of the liver disease. *Computers in Biology and Medicine*, 40(7):665–670, 2010.

[288] K.D. Lindor, M.E. Gershwin, R. Poupon, M. Kaplan, N.V. Bergasa, and E.J. Heathcote. Primary biliary cirrhosis. *Hepatology*, 50(1):291–308, 2009.

[289] A. Liu, H. Fang, O. Dirsch, H. Jin, and U. Dahmen. Early release of macrophage migration inhibitory factor after liver ischemia and reperfusion injury in rats. *Cytokine*, 57(1):150–157, 2012.

[290] J.P. Liu, L.L. Gluud, B. Als-Niesen, and C. Gluud. Artificial and bioartificial support systems for liver failure. *Cochrane Database of Systematic Reviews*, 2004(1):CD003628, 2004.

[291] G.J. Lueck, T.K. Kim, P.N. Burns, and A.L. Martel. Hepatic perfusion imaging using factor analysis of contrast enhanced ultrasound. *IEEE Transactions on Medical Imaging*, 27(10):1449–1457, 2008.

[292] Y. Ma, G.D. Wang, L.W. Wu, and R.D. Hu. Dynamical changing patterns of histological structure and ultrastructure of liver graft undergoing warm ischemia injury from non-heart-beating donor in rats. *World Journal of Gastroenterology*, 12(30):4902–4905, 2006.

[293] R. Maass-Moreno and C.F. Rothe. Contribution of the large hepatic veins to postsinusoidal vascular resistance. *American Journal of Physiology*, 262(1 Pt 1):G14–G22, 1992.

[294] R. Maass-Moreno and C.F. Rothe. Nonlinear resistances in hepatic microcirculation. *American Journal of Physiology*, 269(6 Pt 2):H1922–H1930, 1995.

[295] R. Maass-Moreno and C.F. Rothe. Distribution of pressure gradients along hepatic vasculature. *American Journal of Physiology-Heart and Circulatory Physiology*, 272(6):H2826–H2832, 1997.

[296] M.-H.J. Maathuis, H.G.D. Leuvenink, and R.J. Ploeg. Perspectives in organ preservation. *Transplantation*, 83(10):1289–1298, 2007.

[297] M.H.J. Maathuis, S. Manekeller, A. van der Plaats, H.G.D. Leuvenink, N.A. 't Hart, A.B. Lier, G. Rakhorst, R.J. Ploeg, and T. Minor. Improved kidney graft function after preservation using a novel hypothermic machine perfusion device. *Annals of Surgery*, 246(6):982–991, 2007.

[298] N. Madrahimov, O. Dirsch, C. Broelsch, and U. Dahmen. Marginal hepatectomy in the rat - from anatomy to surgery. *Annals of Surgery*, 244(1):89–98, 2006.

[299] F. Maes, P. Ransbeeck, H. Van Oosterwyck, and P. Verdonck. Modeling fluid flow through irregular scaffolds for perfusion bioreactors. *Biotechnology and Bioengineering*, 103(3):621–630, 2009.

[300] J.F. Magliocca, J.C. Magee, S.A. Rowe, M.T. Gravel, R.H. Chenault, R.M. Merion, J.D. Punch, R.H. Bartlett, and M.R. Hemmila. Extracorporeal support for organ donation after cardiac death effectively expands the donor pool. *Journal of Trauma-Injury Infection and Critical Care*, 58(6):1095–1101, 2005.

[301] A.V. Maker, W.R. Jarnagin, and A.M. Covey. Liver anatomy: Variant venous anatomy and implications for resection. In D.C. Madoff, M. Makuuchi, M. Nagino, and J.-N. Vauthey, editors, *Venous embolization of the liver*, chapter 5, pages 29–36. Springer, London, 2011.

[302] S.M. Maksan, H. Paulo, E. Ryschich, C. Kuntz, M.M. Gebhard, E. Klar, and J. Schmidt. In vivo assessment of angioarchitecture and microcirculation in experimental liver cancer - a new model in rats. *Digestive Diseases and Sciences*, 48(2):279–290, 2003.

[303] D.E. Malarkey, K. Johnson, L. Ryan, G. Boorman, and R.R. Maronpot. New insights into functional aspects of liver morphology. *Toxicologic Pathology*, 33(1):27–34, 2005.

[304] M. Malinchoc, P.S. Kamath, F.D. Gordon, C.J. Peine, J. Rank, and P.C.J. ter Borg. Model to predict poor survival in patients undergoing transjugular intrahepatic portosystemic shunts (TIPS). *Hepatology*, 43(2):S11–S12, 2000.

[305] F.P. Mall. A study of the structural unit of the liver. *American Journal of Anatomy*, 5:244–249, 1906.

[306] J. Mann and D.A. Mann. Transcriptional regulation of hepatic stellate cells. *Advanced Drug Delivery Reviews*, 61(7-8):497–512, 2009.

[307] R.E. Mann, R.G. Smart, and R. Govoni. The epidemiology of alcoholic liver disease. *Alcohol Research & Health*, 27(3):209–219, 2003.

[308] S. Marchesseau, T. Heimann, S. Chatelin, R. Willinger, and H. Delingette. Fast porous visco-hyperelastic soft tissue model for surgery simulation: Application to liver surgery. *Progress in Biophysics & Molecular Biology*, 103(2-3):185–196, 2010.

[309] G. Mareels. *Experimental and numerical modeling of flow and mass transport in a bio-artificial liver*. PhD thesis, Ghent University, 2008.

[310] Y.K. Mariappan, K.J. Glaser, and R.L. Ehman. Magnetic resonance elastography: A review. *Clinical Anatomy*, 23(5):497–511, 2010.

[311] E. N. Marieb and K. Hoehn. *Anatomy & physiology*. Pearson Education, San Francisco, 3rd edition edition, 2008.

[312] P.N.A. Martins and P. Neuhaus. Surgical anatomy of the liver, hepatic vasculature and bile ducts in the rat. *Liver International*, 27(3):384–392, 2007.

[313] P.N.A. Martins, T.P. Theruvath, and P. Neuhaus. Rodent models of partial hepatectomies. *Liver International*, 28(1):3–11, 2008.

[314] S. Marubashi, M. Sakon, H. Nagano, K. Gotoh, K. Hashimoto, M. Kubota, S. Kobayashi, S. Yamamoto, A. Miyamoto, K. Dono, S. Nakamori, K. Umeshita, and M. Monden. Effect of portal hemodynamics on liver regeneration studied in a novel portohepatic shunt rat model. *Surgery*, 136(5):1028–1037, 2004.

[315] T.V. Masyuk, E.L. Ritman, and N.F. LaRusso. Hepatic artery and portal vein remodeling in rat liver - vascular response to selective cholangiocyte proliferation. *American Journal of Pathology*, 162(4):1175–1182, 2003.

[316] P. Mathurin and M.R. Lucey. Management of alcoholic hepatitis. *Journal of Hepatology*, 56:S39–S45, 2012.

[317] T. Matsumoto and M. Kawakami. The unit-concept of hepatic parenchyma - a re-examination based on angioarchitectural studies. *Acta Pathologica Japonica*, 32(2):285–314, 1982.

[318] T. Matsumoto, R. Komori, T. Magara, T. Ui, M. Kawakami, T. Tokuda, S. Takasaki, H. Hayashi, K. Jo, H. Hano, H. Fujino, and H. Tanaka. A study on the normal structure of the human liver, with special reference to its angioarchitecture. *Jikeikai Medical*, 26:1–40, 1979.

[319] E. Mazza, A. Nava, D. Halmloser, W. Jochum, and M. Bajka. The mechanical response of human liver and its relation to histology: An in vivo study. *Medical Image Analysis*, 11(6):663–672, 2007.

[320] R. McCuskey. Hepatic microcirculation. In P. Bioulac-Sage and C. Balabaud, editors, *Sinusoids in human liver: Health and disease*, pages 151–164. Kupffer Cell Foundation, Rijswijk, 1988.

[321] R.S. McCuskey. A dynamic and static study of hepatic arterioles and hepatic sphincters. *American Journal of Anatomy*, 119(3):455–477, 1966.

[322] R.S. McCuskey. Morphological mechanisms for regulating blood flow through hepatic sinusoids. *Liver*, 20(1):3–7, 2000.

[323] R.S. McCuskey, W. Ekataksin, A.V. LeBouton, J. Nishida, M.K. McCuskey, D. McDonnell, C. Williams, N.W. Bethea, B. Dvorak, and O. Koldovsky. Hepatic microvascular development in relation to the morphogenesis of hepatocellular plates in neonatal rats. *The anatomical record. Part A, Discoveries in molecular, cellular, and evolutionary biology*, 275(1):1019–30, 2003.

[324] R.S. McCuskey and F.D. Reilly. Hepatic microvasculature: Dynamic structure and its regulation. *Seminars in Liver Disease*, 13(1):1–12, 1993.

[325] T.J. McKenzie, J.B. Lillegard, and S. Nyberg. Artificial and bioartificial liver support. *Seminars in liver disease*, 28:210–217, 2008.

[326] A.J. McLaren and P.J. Friend. Trends in organ preservation. *Transplant International*, 16(10):701–708, 2003.

[327] M. Meguro, T. Katsuramaki, H. Kimura, M. Isobe, M. Nagayama, K. Kukita, A. Nui, and K. Hirata. Apoptosis and necrosis after warm ischemia-reperfusion injury of the pig liver and their inhibition by ONO-1714. *Transplantation*, 75(5):703–710, 2003.

[328] M. Mescam, M. Kretowski, and J. Bezy-Wendling. Multiscale model of liver DCE-MRI towards a better understanding of tumor complexity. *IEEE Transactions on Medical Imaging*, 29(3):699–707, 2010.

[329] G.K. Michalopoulos. Liver regeneration. *Journal of Cellular Physiology*, 213(2):286–300, 2007.

[330] G.K. Michalopoulos. Liver regeneration after partial hepatectomy critical analysis of mechanistic dilemmas. *American Journal of Pathology*, 176(1):2–13, 2010.

[331] G.K. Michalopoulos and M.C. DeFrances. Liver regeneration. *Science*, 277(5331):1423–1423, 1997.

[332] V. Milisic and A. Quarteroni. Analysis of lumped parameter models for blood flow simulations and their relation with 1D models. *ESAIM-Mathematical Modelling and Numerical Analysis*, 38(4):613–632, 2004.

[333] J.M. Millis, D.C. Cronin, R. Johnson, H. Conjeevaram, C. Conlin, S. Trevino, and P. Maguire. Initial experience with the modified extracorporeal liver-assist device for patients with fulminant hepatic failure: System modifications and clinical impact. *Transplantation*, 74(12):1735–1746, 2002.

[334] G. Millonig, S. Friedrich, S. Adolf, H. Fonouni, M. Golriz, A. Mehrabi, P. Stiefel, G. Poeschl, M.W. Buechler, H.K. Seitz, and S. Mueller. Liver stiffness is directly influenced by central venous pressure. *Journal of Hepatology*, 52(2):206–210, 2010.

[335] T. Minor, P. Olschewski, R.H. Tolba, S. Akbar, M. Kocalkova, and F. Dombrowski. Liver preservation with HTK: Salutary effect of hypothermic aerobiosis by either gaseous oxygen or machine perfusion. *Clinical Transplantation*, 16(3):206–211, 2002.

[336] G.Y. Minuk. Hepatic regeneration: If it ain't broke, don't fix it. *Canadian Journal of Gastroenterology*, 17(7):418–424, 2003.

[337] N. Mittal, Y. Zhou, S. Ung, C. Linares, S. Molloi, and G.S. Kassab. A computer reconstruction of the entire coronary arterial tree based on detailed morphometric data. *Annals of Biomedical Engineering*, 33(8):1015–1026, 2005.

[338] C. Moers, J.M. Smits, M.H.J. Maathuis, J. Treckmann, F. van Gelder, B.P. Napieralski, M. van Kasterop-Kutz, J.J.H. van der Heide, J.P. Squifflet, E. van Heurn, G.R. Kirste, A. Rahmel, H.G.D. Leuvenink, A. Paul, J. Pirenne, and R.J. Ploeg. Machine perfusion or cold storage in deceased-donor kidney transplantation. *New England Journal of Medicine*, 360(1):7–19, 2009.

[339] M.M. Molla and M.C. Paul. LES of non-Newtonian physiological blood flow in a model of arterial stenosis. *Medical Engineering & Physics*, 34(8):1079–1087, 2012.

[340] D. Monbaliu. *Tolerance of livers to warm ischemia in a preclinical model of liver transplantation from non-heart-beating donors*. PhD thesis, Katholieke Universiteit Leuven, 2007.

[341] D. Monbaliu and J. Brassil. Machine perfusion of the liver: Past, present and future. *Current Opinion in Organ Transplantation*, 15(2):160–166, 2010.

[342] D. Monbaliu, C. Debbaut, W. Hillewaert, J. Brassil, W. Laleman, M. Sainz-Barriga, D. Kravitz, J. Pirenne, and P. Segers. Flow competition between hepatic arterial and portal venous flow during hypothermic machine perfusion preservation of porcine livers. *International Journal of Artificial Organs*, 35(2):119–131, 2012.

[343] D. Monbaliu, Q. Liu, L. Libbrecht, R. De Vos, K. Vekemans, C. Debbaut, O. Detry, T. Roskams, J. van Pelt, and J. Pirenne. Preserving the morphology and evaluating the quality of liver grafts by hypothermic machine perfusion: A proof-of-concept study using discarded human livers. *Liver Transplantation*, 18(12):1495–1507, 2012.

[344] D. Monbaliu, Q. Liu, K. Vekemans, T. Roskams, and J. Pirenne. Potentiation of adverse effects of cold by warm ischemia in circulatory death donors for porcine liver transplantation. *Transplantation Proceedings*, 44(9):2874–2879, 2012.

[345] D. Monbaliu, J. Pirenne, and D. Talbot. Liver transplantation using donation after cardiac death donors. *Journal of Hepatology*, 56(2):474–485, 2012.

[346] D. Monbaliu, L. Qiang, K. Vekemans, and J. Pirenne. History of organ perfusion in organ transplantation. In D. Talbot and A. D'Alessandro, editors, *Organ donation and transplantation after cardiac death*, chapter 3, pages 31–49. Oxford press, 2009.

[347] D. Monbaliu, J. Vandersmissen, G. De Hertogh, G. Van Assche, I. Hoffman, N. Knops, C. Debbaut, S. Heye, J. Pirenne, and G. Maleux. Portal hypertension after combined liver and intestinal transplantation, a diagnostic and therapeutic challenge? *Pediatric Transplantation*, 16(7):E301–E305, 2012.

[348] E. Morsiani, A. Aleotti, and D. Ricci. Haemodynamic and ultrastructural observations on the rat liver after two-thirds partial hepatectomy. *Journal of Anatomy*, 192:507–515, 1998.

[349] K.E. Mortensen, L.N. Conley, J. Hedegaard, T. Kalstad, P. Sorensen, C. Bendixen, and A. Revhaug. Regenerative response in the pig liver remnant varies with the degree of resection and rise in portal pressure. *American Journal of Physiology-Gastrointestinal and Liver Physiology*, 294(3):G819–G830, 2008.

[350] U. Motosugi, T. Ichikawa, F. Amemiya, H. Sou, K. Sano, A. Muhi, N. Enomoto, and T. Araki. Cross-validation of MR elastography and ultrasound transient elastography in liver stiffness measurement: Discrepancy in the results of cirrhotic liver. *Journal of Magnetic Resonance Imaging*, 35(3):607–610, 2012.

[351] P.M. Motta. The three-dimensional microanatomy of the liver. *Archivum Histologicum Japonicum*, 47(1):1–30, 1984.

[352] M.F. Mozes, R.B. Skolek, and B.C. Korf. Use of perfusion parameters in predicting outcomes of machine-preserved kidneys. *Transplantation Proceedings*, 37(1):350–351, 2005.

[353] S. Mueller, G. Millonig, L. Sarovska, S. Friedrich, F.M. Reimann, M. Pritsch, S. Eisele, F. Stickel, T. Longerich, P. Schirmacher, and H.K. Seitz. Increased liver stiffness in alcoholic liver disease: Differentiating fibrosis from steatohepatitis. *World Journal of Gastroenterology*, 16(8):966–972, 2010.

[354] S.A. Müller, F. Pianka, M. Schoebinger, A. Mehrabi, H. Fonouni, B. Radeleff, H.-P. Meinzer, and B.M. Schmied. Computer-based liver volumetry in the liver perfusion simulator. *Journal of Surgical Research*, 171(1):87–93, 2011.

[355] B. Mullhaupt, D. Dimitroulis, J.T. Gerlach, and P.A. Clavien. Hot topics in liver transplantation: Organ allocation – extended criteria donor – living donor liver transplantation. *Journal of Hepatology*, 48 Suppl 1:S58–67, 2008.

[356] D. Mutter, B. Dallemagne, C. Bailey, L. Soler, and J. Marescaux. 3D virtual reality and selective vascular control for laparoscopic left hepatic lobectomy. *Surgical Endoscopy and Other Interventional Techniques*, 23(2):432–435, 2009.

[357] J.P. Mynard. *Computer modelling and wave intensity analysis of perinatal cardiovascular function and dysfunction*. PhD thesis, University of Melbourne, 2011.

[358] K. Nakata, G.F. Leong, and R.W. Brauer. Direct measurement of blood pressures in minute vessels of the liver. *American Journal of Physiology*, 199(6):1181–1188, 1960.

[359] K. Naruse. Artificial liver support: Future aspects. *Journal of Artificial Organs*, 8:71–76, 2005.

[360] K. Naruse, W. Tang, and M. Makuuchi. Artificial and bioartificial liver support: A review of perfusion treatment for hepatic failure patients. *World Journal of Gastroenterology*, 13(10):1516–1521, 2007.

[361] P. Neuhaus and G. Blumhardt. Extracorporeal liver perfusion - applications of an improved model for experimental studies of the liver. *International Journal of Artificial Organs*, 16(10):729–739, 1993.

[362] J.O. Neumann, M. Thorn, L. Fischer, M. Schobinger, T. Heimann, B. Radeleff, J. Schmidt, H.P. Meinzer, M.W. Buehler, and P. Schemmer. Branching patterns and drainage territories of the middle hepatic vein in computer-simulated right living-donor hepatectomies. *American Journal of Transplantation*, 6(6):1407–1415, 2006.

[363] F. Nevens and W. Laleman. Artificial liver support devices as treatment option for liver failure. *Best Practice & Research in Clinical Gastroenterology*, 26(1):17–26, 2012.

[364] G.A. Nibourg, R. Hoekstra, T.V. van der Hoeven, M.T. Ackermans, T.B. Hakvoort, T.M. van Gulik, and R.A. Chamuleau. Increased hepatic functionality of the human hepatoma cell line hepaRG cultured in the AMC bioreactor. *International Journal of Biochemistry & Cell Biology*, 45(8):1860–1868, 2013.

[365] D.A. Nordsletten, S. Blackett, M.D. Bentley, E.L. Ritman, and N.P. Smith. Structural morphology of renal vasculature. *American Journal of Physiology-Heart and Circulatory Physiology*, 291(1):H296–H309, 2006.

[366] P.G. Northup and C.L. Berg. Living donor liver transplantation: The historical and cultural basis of policy decisions and ongoing ethical questions. *Health Policy*, 72(2):175–185, 2005.

[367] S. Ogawa and S. Miyagawa. Potentials of regenerative medicine for liver disease. *Surgery Today*, 39(12):1019–1025, 2009.

[368] H. Ohno, Y. Naito, H. Nakajima, and M. Tomita. Construction of a biological tissue model based on a single-cell model: A computer simulation of metabolic heterogeneity in the liver lobule. *Artificial Life*, 14(1):3–28, 2008.

[369] O. Ohtani and Y. Ohtani. Lymph circulation in the liver. *Anatomical Record-Advances in Integrative Anatomy and Evolutionary Biology*, 291(6):643–652, 2008.

[370] J.G. O'Leary, R. Lepe, and G.L. Davis. Indications for liver transplantation. *Gastroenterology*, 134(6):1764–1776, 2008.

[371] P. Olschewski, P. Gass, V. Ariyakhagorn, K. Jasse, G. Hunold, M. Menzel, W. Schoening, V. Schmitz, P. Neuhaus, and G. Puhl. The influence of storage temperature during machine perfusion on preservation quality of marginal donor livers. *Cryobiology*, 60(3):337–343, 2010.

[372] M.S. Olufsen and A. Nadim. On deriving lumped models for blood flow and pressure in the systemic arteries. *Mathematical Biosciences and Engineering*, 1(1):61–80, 2004.

[373] R.C. Ooi, X.Y. Luo, S.B. Chin, A.G. Johnson, and N.C. Bird. The flow of bile in the human cystic duct. *Journal of Biomechanics*, 37(12):1913–1922, 2004.

[374] G.D. Pan and L.N. Yan. Problems in adult living donor liver transplantation using the right hepatic lobe. *Hepatobiliary & Pancreatic Diseases International*, 5(3):345–9, 2006.

[375] V. Papp, K. Dezso, V. Laszlo, P. Nagy, and S. Paku. Architectural changes during regenerative and ontogenic liver growth in the rat. *Liver Transplantation*, 15(2):177–183, 2009.

[376] D. Parramon, I. Erill, A. Guimera, A. Ivorra, A. Munoz, A. Sola, C. Fondevila, J.C. Garcia-Valdecasas, and R. Villa. In vivo detection of liver steatosis in rats based on impedance spectroscopy. *Physiological Measurement*, 28(8):813–828, 2007.

[377] A.W. Paulsen. Hepatic anatomy, physiology, and assessment of hepatic function. In W.B. Ronald and B.K. Goran, editors, *Transplantation of the liver*, pages 43–64. Saunders, Philadelphia, 1996.

[378] S.D. St Peter, C.J. Imber, and P.J. Friend. Liver and kidney preservation by perfusion. *Lancet*, 359(9306):604–613, 2002.

[379] T.C. Peterson and M. Neumeister. Effect of pentoxifylline in rat and swine models of hepatic fibrosis, role of fibroproliferation in its mechanism. *Immunopharmacology*, 31(2-3):183–193, 1996.

[380] S. Petkova, A. Hossain, J. Naser, and E. Palombo. CFD modelling of blood flow in portal vein hypertension with and without thrombosis. *Third International Conference on CFD in the Minerals and Process Industries*, 2006.

[381] J. Phua and K.H. Lee. Liver support devices. *Current Opinion in Critical Care*, 14(2):208–215, 2008.

[382] M. Pinzani and F. Vizzutti. Anatomy and vascular biology of the cells in the portal circulation. In A.J. Sanyal and V.H. Shah, editors, *Portal hypertension: Pathobiology, evaluation and treatment*, Clinical gastroenterology, chapter 2. Humana Press, Totowa, New Jersey, 2005.

[383] J. Pirenne, F. Van Gelder, R. Aerts, D. Monbaliu, D. Van Hees, J. de Roey, B. Desschans, L. De Pauw, and W. Coosemans. Abdominal transplant surgery and transplant coordination university hospitals leuven 1997-2007: An overview. *Acta Chirurgica Belgica*, 108(1):15–21, 2008.

[384] J. Pirenne, F. Van Gelder, W. Coosemans, R. Aerts, B. Gunson, T. Koshiba, I. Fourneau, D. Mirza, W. Van Steenbergen, J. Fevery, F. Nevens, and P. McMaster. Type of donor aortic preservation solution and not cold ischemia time is a major determinant of biliary strictures after liver transplantation. *Liver Transplantation*, 7(6):540–545, 2001.

[385] A. Plessier, P.-E. Rautou, and D.-C. Valla. Management of hepatic vascular diseases. *Journal of Hepatology*, 56:S25–S38, 2012.

[386] E. Polat, S. Topaloglu, C. Sokmensuer, E. Topaloglu, F.M. Avsar, H. Ozel, O. Saygun, I. Yildiz, G. Ucar, and S. Hengirmen. Heterogeneity of damage between segments of rat liver after inflow-outflow obstruction. *Transplantation Proceedings*, 38(9):3075–3081, 2006.

[387] I.C.J.H. Post, M.C. Dirkes, M. Heger, R. Bezemer, J. van 't Leven, and T.M. van Gulik. Optimal flow and pressure management in machine perfusion systems for organ preservation. *Annals of Biomedical Engineering*, 40(12):2698–2707, 2012.

[388] T. Poynard, P. Bedossa, and P. Opolon. Natural history of liver fibrosis progression in patients with chronic hepatitis C. *Lancet*, 349(9055):825–832, 1997.

[389] M.Y. Rady, J.L. Verheijde, and J. McGregor. Organ donation after circulatory death: The forgotten donor? *Critical Care*, 10(5):166, 2006.

[390] S. Raghunathan, D. Evans, and J.L. Sparks. Poroviscoelastic modeling of liver biomechanical response in unconfined compression. *Annals of Biomedical Engineering*, 38(5):1789–1800, 2010.

[391] G. Ramadori, F. Moriconi, I. Malik, and J. Dudas. Physiology and pathophysiology of liver inflammation, damage and repair. *Journal of Physiology and Pharmacology*, 59:107–117, 2008.

[392] S. Ran, T.-F. Wen, L.-N. Yan, B. Li, Y. Zeng, Z.-Y. Chen, Y. Zhang, Z.-X. Liao, G.-L. Liang, G. Li, and X.-H. Zhang. Risks faced by donors of right lobe for living donor liver transplantation. *Hepatobiliary & Pancreatic Diseases International*, 8(6):581–585, 2009.

[393] H.P. Rani, T.W.H. Sheu, T.M. Chang, and P.C. Liang. Numerical investigation of non-Newtonian microcirculatory blood flow in hepatic lobule. *Journal of Biomechanics*, 39(3):551–563, 2006.

[394] A.M. Rappaport, Z.J. Borowy, W.M. Lougheed, and W.N. Lotto. Subdivision of hexagonal liver lobules into a structural and functional unit; role in hepatic physiology and pathology. *Anatomical record*, 119(1):11–33, 1954.

[395] S.P. Reddy, J. Brockmann, and P.J. Friend. Normothermic perfusion: A mini-review. *Transplantation*, 87(5):631–632, 2009.

[396] B. Reitinger, A. Bornik, R. Beichel, and D. Schmalstieg. Liver surgery planning using virtual reality. *IEEE Computer Graphics and Applications*, 26(6):36–47, 2006.

[397] M.Y. Rennie, J. Detmar, K.J. Whiteley, J. Yang, A. Jurisicova, S.L. Adamson, and J.G. Sled. Vessel tortuousity and reduced vascularization in the fetoplacental arterial tree after maternal exposure to polycyclic aromatic hydrocarbons. *American Journal of Physiology-Heart and Circulatory Physiology*, 300(2):H675–H684, 2011.

[398] J.F. Renz, H. Yersiz, P.R. Reichert, G.M. Hisatake, D.G. Farmer, J.C. Emond, and R.W. Busuttil. Split-liver transplantation: A review. *American Journal of Transplantation*, 3(11):1323–1335, 2003.

[399] A.L. Richards, C. Kleinstreuer, A.S. Kennedy, E. Childress, and G.D. Buckner. Experimental microsphere targeting in a representative hepatic artery system. *IEEE Transactions on Biomedical Engineering*, 59(1):198–204, 2012.

[400] P.D.I. Richardson and P.G. Withrington. Liver blood flow. 1. Intrinsic and nervous control of liver blood flow. *Gastroenterology*, 81(1):159–173, 1981.

[401] S. Richter, B. Vollmar, I. Mucke, S. Post, and M.D. Menger. Hepatic arteriolo-portal venular shunting guarantees maintenance of nutritional microvascular supply in hepatic arterial buffer response of rat livers. *Journal of Physiology-London*, 531(1):193–201, 2001.

[402] T. Ricken and J. Bluhm. Remodeling and growth of living tissue: A multiphase theory. *Archive of Applied Mechanics*, 80(5):453–465, 2010.

[403] K.J. Riehle, Y.Y. Dan, J.S. Campbell, and N. Fausto. New concepts in liver regeneration. *Journal of Gastroenterology and Hepatology*, 26 Suppl 1:203–12, 2011.

[404] E. Roan and K. Vemaganti. Strain rate-dependent viscohyperelastic constitutive modeling of bovine liver tissue. *Medical & Biological Engineering & Computing*, 49(4):497–506, 2011.

[405] D.C. Rockey. Cell and molecular mechanisms of increased intrahepatic resistance and hemodynamic correlates. In A.J. Sanyal and V.H. Shah, editors, *Portal hypertension*. Humana Press, New Jersey, 2005.

[406] L. Roffi. Liver in mythology: A different version of Tityos' myth. *Journal of Hepatology*, 57(3):710–711, 2012.

[407] A. Rojas-Pena, J.L. Reoma, E. Krause, E.L. Boothman, N.P. Padiyar, K.E. Cook, R.H. Bartlett, and J.D. Punch. Extracorporeal support: Improves donor renal graft function after cardiac death. *American Journal of Transplantation*, 10(6):1365–1374, 2010.

[408] S. Rosenstengel, S. Stoeppeler, R. Bahde, H.U. Spiegel, and D. Palmes. Type of steatosis influences microcirculation and fibrogenesis in different rat strains. *Journal of Investigative Surgery*, 24(6):273–282, 2011.

[409] T. Roskams, V.J. Desmet, and C. Verslype. Development, structure and function of the liver. In A.D. Burt, B.C. Portmann, and L.D. Ferrell, editors, *MacSween's pathology of the liver*, chapter 1, pages 1–72. Churchill Livingstone, 2007.

[410] Jr. R.S. Brown. Live donors in liver transplantation. *Gastroenterology*, 134(6):1802–1813, 2008.

[411] E.B. Rypins, K.M. Rosenberg, I.J. Sarfeh, J. Houck, R.M. Conroy, and N. Milne. Computer-analysis of portal hemodynamics after small-diameter portacaval H-grafts - the theoretical basis for partial shunting. *Journal of Surgical Research*, 42(4):354–361, 1987.

[412] M.E. Safar and P. Laurent. Pulse pressure and arterial stiffness in rats: Comparison with humans. *American Journal of Physiology-Heart and Circulatory Physiology*, 285(4):H1363–H1369, 2003.

[413] S. Sahin and M. Rowland. Application of the dispersion model to describe disposition kinetics of markers in the dual perfused rat liver. *Drug Metabolism and Disposition*, 35(7):1119–1125, 2007.

[414] S. Saito, J. Yamanaka, K. Miura, N. Nakao, T. Nagao, T. Sugimoto, T. Hirano, N. Kuroda, Y. Iimuro, and J. Fujimoto. A novel 3D hepatectomy simulation based on liver circulation: Application to liver resection and transplantation. *Hepatology*, 41(6):1297–1304, 2005.

[415] Y. Sato, K. Tsukada, and K. Hatakeyama. Role of shear stress and immune responses in liver regeneration after a partial hepatectomy. *Surgery Today-the Japanese Journal of Surgery*, 29(1):1–9, 1999.

[416] I.M. Sauer and J.C. Gerlach. Modular extracorporeal liver support. *Artificial Organs*, 26(8):703–706, 2002.

[417] R. Saxena, N.D. Theise, and J.M. Crawford. Microanatomy of the human liver - exploring the hidden interfaces. *Hepatology*, 30(6):1339–1346, 1999.

[418] A. Schenk, S. Zidowitz, H. Bourquain, M. Hindennach, C. Hansen, H.K. Hahn, and H.-O. Peitgen. Clinical relevance of model based computer-assisted diagnosis and therapy. In M.L. Giger and N. Karssemeijer, editors, *Medical imaging 2008: Computer-aided diagnosis*, Proceedings of the society of photo-optical instrumentation engineers (spie), page 91502, 2008.

[419] A. Schlegel, O.d. Rougemont, R. Graf, P.-A. Clavien, and P. Dutkowski. Protective mechanisms of end-ischemic cold machine perfusion in DCD liver grafts. *Journal of Hepatology*, 58(2):278–286, 2013.

[420] M.R. Schon, O. Kollmar, S. Wolf, H. Schrem, M. Matthes, N. Akkoc, N.C. Schnoy, and P. Neuhaus. Liver transplantation after organ preservation with normothermic extracorporeal perfusion. *Annals of Surgery*, 233(1):114–123, 2001.

[421] K. Schregel, E. Wuerfel née Tysiak, P. Garteiser, I. Gemeinhardt, T. Prozorovski, O. Aktas, H. Merz, D. Petersen, J. Wuerfel, and R. Sinkus. Demyelination reduces brain parenchymal stiffness quantified in vivo by magnetic resonance elastography. *Proceedings of the National Academy of Sciences of the United States of America*, 109(17):6650–6655, 2012.

[422] P. Segers, E.R. Rietzschel, M.L. De Buyzere, N. Stergiopulos, N. Westerhof, L.M. Van Bortel, T. Gillebert, and P.R. Verdonck. Three- and four-element windkessel models: Assessment of their fitting performance in a large cohort of healthy middle-aged individuals. *Proceedings of the Institution of Mechanical Engineers Part H-Journal of Engineering in Medicine*, 222(H4):417–428, 2008.

[423] D. Selle, B. Preim, A. Schenk, and H.-O. Peitgen. Analysis of vasculature for liver surgical planning. *IEEE Transactions on Medical Imaging*, 21(11):1344–1357, 2002.

[424] D. Selle, W. Spindler, B. Preim, and H.-O. Peitgen. Mathematical methods in medical imaging: Analysis of vascular structures for liver surgery planning. In B. Enquist and W. Schmid, editors, *Mathematics unlimited - 2001 and beyond*. Springer Verlag, Berlin, 2000.

[425] M.A. Selver, A. Kocaoglu, G.K. Demir, H. Dogan, O. Dicle, and C. Guezelis. Patient oriented and robust automatic liver segmentation for pre-evaluation of liver transplantation. *Computers in Biology and Medicine*, 38(7):765–784, 2008.

[426] H. Shah, K. Kuehl, and A.H. Sherker. Liver disease after the Fontan procedure what the hepatologist needs to know. *Journal of Clinical Gastroenterology*, 44(6):428–431, 2010.

[427] V. Shah, G. Garcia-Cardena, W.C. Sessa, and R.J. Groszmann. The hepatic circulation in health and disease: Report of a single-topic symposium. *Hepatology*, 27(1):279–288, 1998.

[428] Y. Shi, P. Lawford, and R. Hose. Review of zero-D and 1-D models of blood flow in the cardiovascular system. *Biomedical Engineering Online*, 10, 2011.

[429] T. Shigeta, N. Matsuno, H. Huai-Che, H. Obara, H. Mizunuma, T. Hirano, S. Uemoto, and S. Enosawa. A basic consideration for porcine liver preservation using a novel continuous machine perfusion device. *Transplantation Proceedings*, 44(4):942–945, 2012.

[430] K.C. Shih and K. Man. Small-for-size liver graft injury–impact on tumor behavior. *Transplantation Reviews (Orlando)*, 24(1):1–10, 2010.

[431] T. Shimamura, M. Taniguchi, M.B. Jin, T. Suzuki, M. Matsushita, H. Furukawa, and S. Todo. Excessive portal venous inflow as a cause of allograft dysfunction in small-for-size living donor liver transplantation. *Transplantation Proceedings*, 33(1-2):1331, 2001.

[432] W. Shirai, T. Sato, H. Shibuya, K. Naito, and A. Tsukise. Three-dimensional vasculature of the bovine liver. *Anatomia Histologia Embryologia-Journal of Veterinary Medicine Series C*, 34(6):354–363, 2005.

[433] J.H. Siggers, A. Bonfiglio, K. Leungchavaphongse, and R. Repetto. Mathematical modeling of blood circulation in the liver. *6th World Congress of Biomechanics (WCB 2010) in conjunction with 14th International Conference on Biomedical Engineering (ICBME) and 5th Asia Pacific Conference on Biomechanics (APBiomech): IFMBE Proceedings*, 31:454–457, 2010.

[434] S. Silbernagl and A. Despopoulos. *Atlas van de fysiologie*. HB uitgevers, Baarn, Nederland, 2007.

[435] M. Silveira and K. Lindor. Primary sclerosing cholangitis. In S.P.S. Monga, editor, *Molecular pathology of liver diseases*, volume 5 of *Molecular pathology library*, chapter 50, pages 741–752. Springer US, 2011.

[436] C. Skagen, M. Lucey, and A. Said. Liver transplantation: An update 2009. *Current Opinion in Gastroenterology*, 25(3):202–208, 2009.

[437] J.E. Skandalakis, L.J. Skandalakis, P.N. Skandalakis, and P. Mirilas. Hepatic surgical anatomy. *Surgical Clinics of North America*, 84(2):413–435, 2004.

[438] S.W. Smye, C.J. Evans, M.P. Robinson, and B.D. Sleeman. Modelling the electrical properties of tissue as a porous medium. *Physics in Medicine and Biology*, 52(23):7007–7022, 2007.

[439] V. Smyrniotis, G. Kostopanagiotou, A. Kondi, E. Gamaletsos, K. Theodoraki, D. Kehagias, K. Mystakidou, and J. Contis. Hemodynamic interaction between portal vein and hepatic artery flow in small-for-size split liver transplantation. *Transplant International*, 15(7):355–360, 2002.

[440] J.H. Southard and M. Ametani. Organ preservation. In L.C. Ginns and A.B. Cosimi, editors, *Organ transplantation*. Wiley-Blackwell, 1999.

[441] J.H. Southard and F.O. Belzer. Principles of organ preservation. In R.W. Busuttil and G.B. Klintmalm, editors, *Transplantation of the liver*. Elsevier Saunders, 1996.

[442] J.H. Southard, S. Lindell, M. Ametani, J.P. Richer, and A.W.F. Vos. Kupffer cell activation in liver preservation: Cold storage vs machine perfusion. *Transplantation Proceedings*, 32(1):27–28, 2000.

[443] P. Soyer. Segmental anatomy of the liver: Utility of a nomenclature accepted worldwide. *American Journal of Roentgenology*, 161(3):572–573, 1993.

[444] M.M. Spannbauer, A. Oleszczuk, A. Tannapfel, M. Bluher, U.C. Pietsch, J. Hengstler, B. Donaubauer, P. Madaj-Sterba, M. Furll, A. Schuhmacher, J. Thiery, J.P. Hauss, and M.R. Schon. Micro- and macrovesicular steatotic liver model for transplantation induced by ethanol and protein-deficient diet. *Transplantation Proceedings*, 37(1):210–211, 2005.

[445] B. Spronck, E.G. Martens, E.D. Gommer, and F.N. van de Vosse. A lumped parameter model of cerebral blood flow control combining cerebral autoregulation and neurovascular coupling. *American Journal of Physiology - Heart and Circulatory Physiology*, 303(9):H1143–53, 2012.

[446] T.E. Starzl. The long reach of liver transplantation. *Nature Medicine*, 18(10):1489–1492, 2012.

[447] T.E. Starzl and J.J. Fung. Themes of liver transplantation. *Hepatology*, 51(6):1869–1884, 2010.

[448] T.E. Starzl, C.G. Groth, L. Brettschneider, I. Penn, V.A. Fulginiti, J.B. Moon, H. Blanchard, Jr. A.J. Martin, and K.A. Porter. Orthotopic homotransplantation of the human liver. *Annals of Surgery*, 168(3):392–415, 1968.

[449] T.E. Starzl, G.B. Klintmalm, K.A. Porter, S. Iwatsuki, and G.P. Schroter. Liver transplantation with use of cyclosporin A and prednisone. *New England Journal of Medicine*, 305(5):266–269, 1981.

[450] T.E. Starzl, T.L. Marchioro, K.N. Vonkaulla, G. Hermann, R.S. Brittain, and W.R. Waddell. Homotransplantation of the liver in humans. *Surgery, gynecology & obstetrics*, 117:659–676, 1963.

[451] N. Stergiopulos, B.E. Westerhof, and N. Westerhof. Total arterial inertance as the fourth element of the windkessel model. *American Journal of Physiology-Heart and Circulatory Physiology*, 276(1):H81–H88, 1999.

[452] R.H. Stewart and G.A. Laine. Flow in lymphatic networks: Interaction between hepatic and intestinal lymph vessels. *Microcirculation*, 8(4):221–227, 2001.

[453] A.N. Strahler. Quantitative analysis of watershed geomorphology. *Transactions of the American Geophysical Union*, 8(6):913–920, 1957.

[454] M.L. Sturdevart and A. Human. Multiorgan procurement from the deceased donor. In A. Humar, A.J. Matas, and W.D. Payne, editors, *Atlas of organ transplantation*. Springer-Verlag, London, 2006.

[455] K.C. Sudhamshu, S. Matsutani, H. Maruyama, T. Akiike, and H. Saisho. Doppler study of hepatic vein in cirrhotic patients: Correlation with liver dysfunction and hepatic hemodynamics. *World Journal of Gastroenteroly*, 12(36):5853–5858, 2006.

[456] T.M. Suszynski, M.D. Rizzari, III W.E. Scott, L.A. Tempelman, M.J. Taylor, and K.K. Papas. Persufflation (or gaseous oxygen perfusion) as a method of organ preservation. *Cryobiology*, 64(3):125–143, 2012.

[457] N.A. 't Hart, A. van der Plaats, A. Faber, H.G.D. Leuvenink, P. Olinga, J. Wiersema-Buist, G.J. Verkerke, G. Rakhorst, and R.J. Ploeg. Oxygenation during hypothermic rat liver preservation: An in vitro slice study to demonstrate beneficial or toxic oxygenation effects. *Liver Transplantation*, 11(11):1403–1411, 2005.

[458] N.A. 't Hart, A. van der Plaats, H.G.D. Leuvenink, H. van Goor, J. Wiersema-Buist, G.J. Verkerke, G. Rakhorst, and R.J. Ploeg. Determination of an adequate perfusion pressure for continuous dual vessel hypothermic machine perfusion of the rat liver. *Transplant International*, 20(4):343–352, 2007.

[459] L. Taelman, J. Degroote, P. Verdonck, J. Vierendeels, and P. Segers. Modeling hemodynamics in vascular networks using a geometrical multiscale approach: Numerical aspects. *Annals of Biomedical Engineering*, 41(7):1445–1458, 2013.

[460] K. Takasaki and M. Yamamoto. Surgical anatomy of the liver in the glissonean pedicle approach: What we need to know. In D.C. Madoff, M. Makuuchi, M. Nagino, and J.-N. Vauthey, editors, *Venous embolization of the liver*, chapter 4, pages 23–27. Springer, London, 2011.

[461] H.K. Tan. Molecular adsorbent recirculating system (MARS). *Annals Academy of Medicine Singapore*, 33(3):329–335, 2004.

[462] K. Tanaka and Y. Ogura. "Small-for-size graft" and "small-for-size syndrome" in living donor liver transplantation. *Yonsei Medical Journal*, 45(6):1089–1094, 2004.

[463] L. Tariciotti, C. Rocha, M.T.P.R. Perera, B.K. Gunson, S.R. Bramhall, J. Isaac, J.A.C. Buckels, A.D. Mayer, P. Muiesan, and D.F. Mirza. Is it time to extend liver acceptance criteria for controlled donors after cardiac death? *Transplantation*, 92(10):1140–1146, 2011.

[464] R. Taub. Liver regeneration: From myth to mechanism. *Nature Reviews Molecular Cell Biology*, 5(10):836–847, 2004.

[465] H.F. Teutsch. The modular microarchitecture of human liver. *Hepatology*, 42(2):317–325, 2005.

[466] H.F. Teutsch, D. Schuerfeld, and E. Groezinger. Three-dimensional reconstruction of parenchymal units in the liver of the rat. *Hepatology*, 29(2):494–505, 1999.

[467] D. Thabut and V. Shah. Intrahepatic angiogenesis and sinusoidal remodeling in chronic liver disease: New targets for the treatment of portal hypertension? *Journal of Hepatology*, 53(5):976–980, 2010.

[468] D.G. Tiniakos, A. Kandilis, and S.A. Geller. Tityus: a forgotten myth of liver regeneration. *Journal of Hepatology*, 53(2):357–361, 2010.

[469] T. Tojimbara, W.N. Wicomb, R. Garcia-Kennedy, W. Burns, M. Hayashi, G. Collins, and C.O. Esquivel. Liver transplantation from non-heart beating donors in rats: Influence of viscosity and temperature of initial flushing solutions on graft function. *Liver Transplantation and Surgery*, 3(1):39–45, 1997.

[470] U. Töx, I. Scheller, N. Kociok, M.A. Kern, D. Klanac, S.M. Daudi, O. Laue, P. Schirmacher, T. Goeser, S. Schulte, and H.M. Steffen. Expression of angiotensin II receptor type 1 is reduced in advanced rat liver fibrosis. *Digestive Diseases and Sciences*, 52(8):1995–2005, 2007.

[471] G. Troianowski, C.A. Taylor, J.A. Feinstein, and I.E. Vignon-Clementel. Three-dimensional simulations in Glenn patients: Clinically based boundary conditions, hemodynamic results and sensitivity to input data. *Journal of Biomechical Engineering*, 133(11):111006, 2011.

[472] R. Troisi, S. Ricciardi, P. Smeets, M. Petrovic, G. Van Maele, I. Colle, H. Van Vlierberghe, and B. de Hemptinne. Effects of hemi-portocaval shunts for inflow modulation on the outcome of small-for-size grafts in living donor liver transplantation. *American Journal of Transplantation*, 5(6):1397–1404, 2005.

[473] J.E. Tsitlik, H.R. Halperin, A.S. Popel, A.A. Shoukas, F.C.P. Yin, and N. Westerhof. Modeling the circulation with 3-terminal electrical networks containing special nonlinear capacitors. *Annals of Biomedical Engineering*, 20(6):595–616, 1992.

[474] O.N. Tucker and N. Heaton. The 'small for size' liver syndrome. *Current Opinion in Critical Care*, 11(2):150–155, 2005.

[475] M. Uchiyama, K. Kozaki, T. Nemoto, H. Degawa, N. Matsuno, K. Kubota, H. Takeuchi, E. Sakurai, M. Kozaki, T. Ikeda, N. Asuwa, S. Masuda, and T. Nagao. Liver transplantation from non-heart-beating donors: Effect of machine perfusion preservation and pentoxifylline. *Transplantation Proceedings*, 30(7):3798–3800, 1998.

[476] M. Uchiyama, N. Matsuno, K. Hama, H. Iwamoto, Y. Narumi, K. Kikuchi, H. Degawa, K. Kozaki, K. Kubota, H. Takeuchi, E. Sakurai, N. Asuwa, S.M.T. Hirano, and T. Nagao. Comparison between non-pulsatile and pulsatile machine perfusion preservation in liver transplantation from non-heart-beating donors. *Transplantation Proceedings*, 33(1-2):936–938, 2001.

[477] M. Vairetti, A. Ferrigno, F. Carlucci, A. Tabucchi, V. Rizzo, E. Boncompagni, D. Neri, E. Gringeri, I. Freitas, and U. Cillo. Subnormothermic machine perfusion protects steatotic livers against preservation injury: A potential for donor pool increase? *Liver Transplantation*, 15(1):20–29, 2009.

[478] A. van der Plaats. *The Groningen hypothermic liver perfusion system for improved preservation in organ transplantation*. PhD thesis, University of Groningen, 2005.

[479] A. van der Plaats, M.H.J. Maathuis, N.A. 't Hart, A.A. Bellekom, H.S. Hofker, E.B. van der Houwen, G.J. Verkerke, H.G.D. Leuvenink, P. Verdonck, R.J. Ploeg, and G. Rakhorst. The Groningen hypothermic liver perfusion pump: Functional evaluation of a new machine perfusion system. *Annals of Biomedical Engineering*, 34(12):1924–1934, 2006.

[480] A. van der Plaats, N.A. 't Hart, A.M. Morariu, G.J. Verkerke, H.G.D. Leuvenink, R.J. Ploeg, and G. Rakhorst. Effect of University of Wisconsin organ-preservation solution on haemorheology. *Transplant International*, 17(5):227–233, 2004.

[481] A. van der Plaats, N.A. 't Hart, G.J. Verkerke, H.G.D. Leuvenink, R.J. Ploeg, and G. Rakhorst. Hypothermic machine preservation in liver transplantation revisited: Concepts and criteria in the new millennium. *Annals of Biomedical Engineering*, 32(4):623–631, 2004.

[482] A. van der Plaats, N.A. 't Hart, G.J. Verkerke, H.G.D. Leuvenink, P. Verdonck, R.J. Ploeg, and G. Rakhorst. Numerical simulation of the hepatic circulation. *International Journal of Artificial Organs*, 27(3):222–230, 2004.

[483] C. Van Steenkiste. *The role of placental growth factor (PlGF) in the pathophysiology of portal hypertension and cirrhosis*. PhD thesis, Ghent University, 2011.

[484] C. Van Steenkiste, B. Trachet, C. Casteleyn, D. Van Loo, L. Van Hoorebeke, P. Segers, A. Geerts, H. Van Vlierberghe, and I. Colle. Vascular corrosion casting: Analyzing wall shear stress in the portal vein and vascular abnormalities in portal hypertensive and cirrhotic rodents. *Laboratory Investigation*, 90(11):1558–1572, 2010.

[485] E. Vanheule, Y.-D. Fan, J. Van Huysse, D. Meester, K. Olievier, M. Praet, B. de Hemptinne, and I. Colle. Expression of placental growth factor in regenerating livers after partial hepatectomy in the rat. *European Journal of Gastroenterology & Hepatology*, 23(1):66–75, 2011.

[486] E. Vanheule, A.M. Geerts, J. Van Huysse, D. Schelfhout, M. Praet, H. Van Vlierberghe, M. De Vos, and I. Colle. An intravital microscopic study of the hepatic microcirculation in cirrhotic mice models: Relationship between fibrosis and angiogenesis. *International Journal of Experimental Pathology*, 89(6):419–432, 2008.

[487] K. Vekemans, Q. Liu, J. Brassil, M. Komuta, J. Pirenne, and D. Monbaliu. Influence of flow and addition of oxygen during porcine liver hypothermic machine perfusion. *Transplantation Proceedings*, 39(8):2647–2651, 2007.

[488] K. Vekemans, Q. Liu, J. Pirenne, and D. Monbaliu. Artificial circulation of the liver: Machine perfusion as a preservation method in liver transplantation. *Anatomical Record-Advances in Integrative Anatomy and Evolutionary Biology*, 291(6):735–740, 2008.

[489] J. Vermehren, A. Polta, O. Zimmermann, E. Herrmann, T. Poynard, W.P. Hofmann, J. Bojunga, C. Sarrazin, S. Zeuzem, and M. Friedrich-Rust. Comparison of acoustic radiation force impulse imaging with transient elastography for the detection of complications in patients with cirrhosis. *Liver International*, 32(5):852–858, 2012.

[490] C. Vicas, M. Lupsor, R. Badea, and S. Nedevschi. Usefulness of textural analysis as a tool for noninvasive liver fibrosis staging. *Journal of Medical Ultrasonics*, 38(3):105–117, 2011.

[491] I.E. Vignon-Clementel, C.A. Figueroa, K.E. Jansen, and C.A. Taylor. Outflow boundary conditions for 3D simulations of non-periodic blood flow and pressure fields in deformable arteries. *Computer Methods in Biomechanics and Biomedical Engineering*, 13(5):625–640, 2010.

[492] I.E. Vignon-Clementel, A.L. Marsden, and J.A. Feinstein. A primer on computational simulation in congenital heart disease for the clinician. *Progress in Pediatric Cardiology*, 30(1-2):3–13, 2010.

[493] S. Vilarinho and Richard P. Lifton. Liver transplantation: From inception to clinical practice. *Cell*, 150(6):1096–1099, 2012.

[494] T. Vogel, J.G. Brockmann, C. Coussios, and P.J. Friend. The role of normothermic extracorporeal perfusion in minimizing ischemia reperfusion injury. *Transplantation Reviews*, 26(2):156–162, 2012.

[495] T. Vogel, J.G. Brockmann, and P.J. Friend. Ex-vivo normothermic liver perfusion: An update. *Current Opinion in Organ Transplantation*, 15(2):167–172, 2010.

[496] B. Vollmar and M.D. Menger. The hepatic microcirculation: Mechanistic contributions and therapeutic targets in liver injury and repair. *Physiological Reviews*, 89(4):1269–1339, 2009.

[497] B. Vollmar, B. Wolf, S. Siegmund, A.D. Katsen, and M.D. Menger. Lymph vessel expansion and function in the development of hepatic fibrosis and cirrhosis. *American Journal of Pathology*, 151(1):169–175, 1997.

[498] R. Wagner, D. Van Loo, F. Hossler, K. Czymmek, E. Pauwels, and L. Van Hoorebeke. High-resolution imaging of kidney vascular corrosion casts with nano-CT. *Microscopy and Microanalysis*, 17(2):215–219, 2011.

[499] J. Wambaugh and I. Shah. Simulating microdosimetry in a virtual hepatic lobule. *Plos Computational Biology*, 6(4):e1000756, 2010.

[500] S.Y. Wan, A.P. Kiraly, E.L. Ritman, and W.E. Higgins. Extraction of the hepatic vasculature in rats using 3-D micro-CT images. *IEEE Transactions on Medical Imaging*, 19(9):964–971, 2000.

[501] A. Warren, S. Chaberek, K. Ostrowski, V.C. Cogger, S.N. Hilmer, R.S. McCuskey, R. Fraser, and D.G. Le Couteur. Effects of old age on vascular complexity and dispersion of the hepatic sinusoidal network. *Microcirculation*, 15(3):191–202, 2008.

[502] E. Weibel. Mandelbrot's fractals and the geometry of life: A tribute to Benoît Mandelbrot on his 80th birthday. In G. Losa, D. Merlini, T. Nonnenmacher, and E. Weibel, editors, *Fractals in biology and medicine*, Mathematics and biosciences in interaction, chapter 1, pages 3–16. Birkhäuser Basel, 2005.

[503] M. Weiss, T.C. Krejcie, and M.J. Avram. A physiologically based model of hepatic ICG clearance: Interplay between sinusoidal uptake and biliary excretion. *European Journal of Pharmaceutical Sciences*, 44(3):359–65, 2011.

[504] C. Welch. A note on transplantation of the whole liver in dogs. *Transplant Bull*, 1955(2):54–55, 1955.

[505] M.J. Welsh, C.S. Rogers, D.A. Stoltz, D.K. Meyerholz, and R.S. Prather. Development of a porcine model of cystic fibrosis. *Transactions of the American Clinical and Climatological Association*, 120:149–162, 2009.

[506] J.R. Welty, C.E. Wicks, R.E. Wilson, and G.L. Rorrer. *Fundamentals of momentum, heat, and mass transfer*. John Wiley and sons, 4th edition, 2001.

[507] T.-F. Wen, Z.-Y. Chen, L.-N. Yan, B. Li, Y. Zeng, J.-C. Zhao, W.-T. Wang, J.-Y. Yang, Y.-K. Ma, M.-Q. Xu, J.-W. Liu, Z.-G. Deng, and H. Wu. Measures for increasing the safety of donors in living donor liver transplantation using right lobe grafts. *Hepatobiliary & Pancreatic Diseases International*, 6(6):590–595, 2007.

[508] D. Werner, T. Ricken, U. Dahmen, and O. Dirsch. A biphasic FEM model for the microperfusion in liver lobules. *Proceedings in Applied Mathematics and Mechanics*, 12(1):89–90, 2012.

[509] E. Wisse, F. Braet, D.Z. Luo, R. De Zanger, D. Jans, E. Crabbe, and A. Vermoesen. Structure and function of sinusoidal lining cells in the liver. *Toxicologic Pathology*, 24(1):100–111, 1996.

[510] A.M. Wolthuis, D. Monbaliu, W. Coosemans, and J. Pirenne. Deceased donor retrieval. In *Handbook of renal and pancreatic transplantation*, pages 91–107. John Wiley & Sons, Ltd, 2012.

[511] W. Xing, M. Deng, J. Zhang, H. Huang, O. Dirsch, and U. Dahmen. Quantitative evaluation and selection of reference genes in a rat model of extended liver resection. *Journal of Biomolecular Techniques*, 20(2):109–115, 2009.

[512] X. Xu, K. Man, S.S. Zheng, T.B. Liang, T.K. Lee, K.T. Ng, S.T. Fan, and C.M. Lo. Attenuation of acute phase shear stress by somatostatin improves small-for-size liver graft survival. *Liver Transplantation*, 12(4):621–627, 2006.

[513] S. Yagi, T. Lida, K. Taniguchi, T. Hori, T. Hamada, K. Fujii, S. Mizuno, and S. Uemoto. Impact of portal venous pressure on regeneration and graft damage after living-donor liver transplantation. *Liver Transplantation*, 11(1):68–75, 2005.

[514] J. Yamanaka, S. Saito, Y. Iimuro, T. Hirano, T. Okada, N. Kuroda, T. Sugimoto, and J. Fujimoto. The impact of 3-D virtual hepatectomy simulation in living-donor liver transplantation. *Journal of Hepato-Biliary-Pancreatic Surgery*, 13(5):363–369, 2006.

[515] L.N. Yan, B. Li, Y. Zeng, T.F. Wen, J.C. Zhao, W.T. Wang, J.Y. Yang, M.Q. Xu, Y.K. Ma, Z.Y. Chen, J.W. Liu, and H. Wu. Modified techniques for adult-to-adult living donor liver transplantation. *Hepatobiliary & Pancreatic Diseases International*, 5(2):173–9, 2006.

[516] Y. Yang, S. George, D.R. Martin, A.R. Tannenbaum, and D.P. Giddens. 3D modeling of patient-specific geometries of portal veins using MR images, 2006.

[517] H. Yokomori, M. Oda, K. Yoshimura, and T. Hibi. Recent advances in liver sinusoidal endothelial ultrastructure and fine structure immunocytochemistry. *Micron*, 43(2-3):129–134, 2012.

[518] F. Yuan, Y. Chi, S. Huang, and J. Liu. Modeling n-furcated liver vessels from a 3-D segmented volume using hole-making and subdivision methods. *IEEE Transactions on Biomedical Engineering*, 59(2):552–561, 2012.

[519] X. Yuan, A.J. Theruvath, X. Ge, B. Floerchinger, A. Jurisch, G. Garcia-Cardena, and S.G. Tullius. Machine perfusion or cold storage in organ transplantation: Indication, mechanisms, and future perspectives. *Transplant International*, 23(6):561–570, 2010.

[520] T. Yzet, R. Bouzerar, J.-D. Allart, F. Demuynck, C. Legallais, B. Robert, H. Deramond, M.-E. Meyer, and O. Baledent. Hepatic vascular flow measurements by phase contrast MRI and Doppler echography: A comparative and reproducibility study. *Journal of Magnetic Resonance Imaging*, 31(3):579–588, 2010.

[521] M. Zambelli, E. Andorno, L. De Carlis, G. Rossi, U. Cillo, T. De Feo, A. Carobbio, A. Giacomoni, G. Bottino, and M. Colledan. Full-right-full-left split liver transplantation: The retrospective analysis of an early multicenter experience including graft sharing. *American Journal of Transplantation*, 12(8):2198–2210, 2012.

[522] M. Zamir. On fractal properties of arterial trees. *Journal of Theoretical Biology*, 197(4):517–526, 1999.

[523] M. Zamir. Arterial branching within the confines of fractal L-system formalism. *Journal of General Physiology*, 118(3):267–275, 2001.

[524] M. Zamir. Fractal dimensions and multifractility in vascular branching. *Journal of Theoretical Biology*, 212(2):183–190, 2001.

[525] M. Zamir and S. Phipps. Network analysis of an arterial tree. *Journal of Biomechanics*, 21(1):25–34, 1988.

[526] D.J. Zanchet and E.F. de Souza Montero. Pig liver sectorization and segmentation and virtual reality depiction. *Acta Cirúrgica Brasileira*, 17(6):381–387, 2002.

[527] J.J. Zhang, X.K. Meng, C. Dong, J.L. Qiao, R.F. Zhang, G.Q. Yue, and H.Y. Zhong. Development of a new animal model of liver cirrhosis in swine. *European Surgical Research*, 42(1):35–39, 2009.

[528] L. Zhang, J. Yin, Y. Duan, Y. Yang, L. Yuan, and T. Cao. Assessment of intrahepatic blood flow by Doppler ultrasonography: Relationship between the hepatic vein, portal vein, hepatic artery and portal pressure measured intraoperatively in patients with portal hypertension. *BMC Gastroenterology*, 11, 2011.

[529] W. Zhang, L. Tucker-Kellogg, B.C. Narmada, L. Venkatraman, S. Chang, Y. Lu, N. Tan, J.K. White, R. Jia, S.S. Bhowmick, S. Shen, Jr. C.F. Dewey, and H. Yu. Cell-delivery therapeutics for liver regeneration. *Advanced Drug Delivery Reviews*, 62(7-8):814–826, 2010.

[530] Y. Zhang, Y. He, R.K. Praseedom, S. Zheng, J. Dong, and H. Chen. Establishment of animal model of dual liver transplantation in rat. *PLoS One*, 7(7):e40818, 2012.

[531] A. Zipprich, M.R. Loureiro-Silva, I. D'Silva, and R.J. Groszmann. The role of hepatic arterial flow on portal venous and hepatic venous wedged pressure in the isolated perfused CCl4-cirrhotic liver. *American Journal of Physiology-Gastrointestinal and Liver Physiology*, 295(1):G197–G202, 2008.

[532] Z. Zou, W. Ekataksin, and K. Wake. Zonal and regional differences identified from precision mapping of vitamin A-storing lipid droplets of the hepatic stellate cells in pig liver : A novel concept of addressing the intralobular area of heterogeneity. *Hepatology*, 27(4):1098–1108, 1998.

[533] R. Zuchini, H.W. Tsai, C.Y. Chen, C.H. Huang, S.C. Huang, G.B. Lee, C.F. Huang, and X.Z. Lin. Electromagnetic thermotherapy using fine needles for hepatoma treatment. *European Journal of Surgical Oncology (EJSO)*, 37(7):604–610, 2011.